Millimeter-Wave and Terahertz Reconfigurable Apertures for Imaging and Wireless Communication Applications

by

Panagiotis C. Theofanopoulos

A Dissertation Presented in Partial Fulfillment
of the Requirements for the Degree
Doctor of Philosophy

Approved November 2020 by the
Graduate Supervisory Committee:

Georgios Trichopoulos, Chair
Constantine Balanis
James Aberle
Dan Bliss
Chris Groppi

ARIZONA STATE UNIVERSITY

May 2021

ABSTRACT

This work focuses on the analysis and design of large-scale millimeter-wave and terahertz (mmWave/THz) beamforming apertures (e.g., reconfigurable reflective surfaces–RRSs). As such, the small wavelengths and ample bandwidths of these frequencies enable the development of high-spatial-resolution imaging and high-throughput wireless communication systems that leverage electrically large apertures to form high-gain steerable beams.

For the rigorous evaluation of these systems' performance in realistic application scenarios, full-wave simulations are needed to capture all the exhibited electromagnetic phenomena. However, the small wavelengths of mmWave/THz bands lead to enormous meshes in conventional full-wave simulators. Thus, a novel numerical decomposition technique is presented, which decomposes the full-wave models in smaller domains with less meshed elements, enabling their computationally efficient analysis. Thereafter, this method is leveraged to study a novel radar configuration that employs a rotating linear antenna with beam steering capabilities to form 3D images. This imaging process requires fewer elements to carry out high-spatial-resolution imaging compared to traditional 2D phased arrays, constituting a perfect candidate in low-profile, low-cost applications.

Afterward, a high-yield nanofabrication technique for mmWave/THz graphene switches is presented. The measured graphene sheet impedances are incorporated into equivalent circuit models of coplanar switches to identify the optimum mmWave/THz switch topology that would enable the development of large-scale RRSs.

Thereon, the process of integrating the optimized graphene switches into large-scale mmWave/THz RRSs is detailed. The resulting RRSs enable dynamic beam steering achieving 4-bits of phase quantization –for the first time in the known literature– eliminating the parasitic lobes and increasing the aperture efficiency. Furthermore, the devised multi-bit configurations use a single switch-per-bit topology retaining low system complexity and RF losses. Finally, single-bit RRSs are modified to offer single-lobe patterns by employing a surface randomization technique. This approach allows for the use of low-complexity single-bit configurations to suppress the undesired quantization lobes without residing to the use of sophisticated multi-bit topologies.

The presented concepts pave the road toward the implementation and proliferation of large-scale reconfigurable beamforming apertures that can serve both as mmWave/THz imagers and as relays or base stations in future wireless communication applications.

ACKNOWLEDGMENTS

This work has been the result of the continuous collaboration between me and my advisor Professor Trichopoulos, to whom I am deeply appreciative. His continuous support and understanding, along with our endless interactions, have helped me shape the scope of my research, and have immensely contributed to my findings. Moreover, I would like to thank him for his enormous patience during our heated discussions on matters of research. Additionally, I would like to thank my advisory committee, and specifically Professors Balanis, Aberle, Bliss, and Groppi, with whom I have interacted all these years, either through courses or personally, and have helped me evolve both as a person and as a researcher.

Additionally, in this world we do not come alone, but as a part of a family. Thus, I offer my sincere gratitude to my family, whose constant support has enabled me to pursue my goals and aspirations. Besides biological family, friends are a vital part of our lives, thus I would like to state that this would be impossible without the support of my dear friends Stefanos P., Konstantinos A., and George K., whose ears were always there to absorb the tension, alleviate the pressure, and share unforgettable moments. I would also like to deeply thank my dear friend and mentor Christos L., whose words of wisdom at the start of my research career have always been the compass that steers me toward the correct direction.

Furthermore, I would like to thank my dear lab mates and colleagues, Yiran, Subramanian, and Bharath, whose support has been vital to the completion of this work. Our daily interactions have enabled me to expand my horizons and achieve my research goals.

Finally, this dissertation is dedicated to my late grandfather Panagiotis. He still is the beacon in my life, and I wish I become a small fraction of the person he was.

Παππού σε ευχαριστώ που υπήρξες στη ζωή μου.

TABLE OF CONTENTS

LIST OF TABLES

LIST OF FIGURES

Figure Page

Figure Page

Figure Page

Figure Page

Figure Page

Figure Page

Figure Page

Figure Page

Figure Page

CHAPTER 1

Millimeter-wave and Terahertz Systems for Imaging, Sensing, and Wireless Communication Applications

This work focuses on the development and design of novel efficient low-profile millimeter-wave/terahertz (mmWave/THz) beamforming apertures that can be used for several applications including imaging and communications. MmWave/THz waves typically range from ~30 GHz to ~10 THz ('terahertz gap') in the electromagnetic spectrum between microwave and infrared bands (Fig. 1.1). This frequency region remained unused in the better part of the last century until the advances in semiconductor and nanofabrication techniques enabled the development of various systems that can be exploited in imaging and communication applications. Namely, these frequencies are utilized in the 5G communication systems since the available bandwidth (BW) is huge compared to microwaves, enabling the development of high-throughput wireless communications [1]. For instance, a system with a 3% fractional BW (e.g., a typical printed patch antenna [2]) has an absolute BW of 150 MHz at 5 GHz, while the same absolute BW at 300 GHz is 9 GHz, allowing for a significant increase in the achieved data-rates [4].

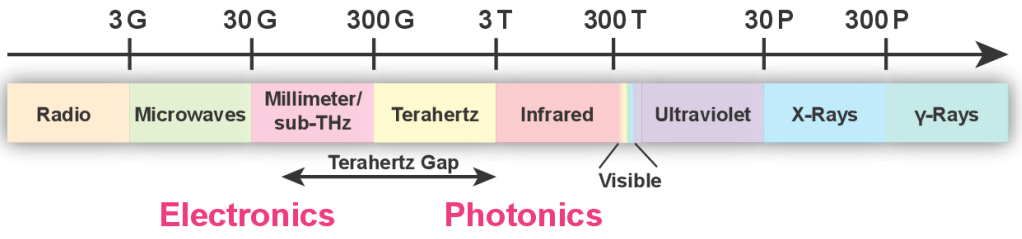

Fig. 1.1 The electromagnetic spectrum and the THz gap (0.1-10 THz) [4].

Moreover, the non-ionizing nature of these frequencies, their penetration abilities (e.g., through cloth), small wavelength, and ample bandwidths, allow for the development of high-spatial-resolution 2D/3D imaging systems for security, automotive, and biomedical applications [5]-[13]. Finally, the small wavelengths of mmWave/THz bands, enable the design and development of compact/high-gain apertures which are crucial both in imaging and communication applications providing narrow beams. For example, a 36×36 cm^2 aperture offers a maximum gain of 22 dB (half-power-beamwidth-HPBW=8^o) at 5 GHz, while the same aperture at 300 GHz offers a maximum gain of 58 dB (HPBW=0.15^o) [2]. In the following sections, indicative examples of mmWave/THz systems for imaging and communication applications are presented alongside a brief description of the employed configurations.

I. Millimeter-wave/terahertz systems for imaging and sensing applications

Imaging systems in mmWave/THz bands are typically used in security/surveillance, as well as earth and space observation applications since they can penetrate a plethora of materials including cloth and clouds [5]-[13]. As such, these applications require high-spatial-resolution images, thus the employed sensors are required to have electrically large apertures that form high-gain steerable beams [5]-[13]. On the one hand, such sensors can leverage high-gain quasi-optical systems (e.g., paraboloid reflector or lenses [5][6]) leading to simple but bulky designs with slow image acquisition speed (framerate) due to the incorporated mechanical beam steering mechanisms. On the other hand, low-profile systems consisting of a plethora of printed antennas (e.g., phased arrays [7]) can offer high-gain, electronically steerable beams, and fast image acquisition speeds; however, the use of multiple antenna elements/RF-channels leads to increased RF-

front-end complexity. Therefore, to decrease the system's size and complexity and increase the image acquisition speed, a combination of the aforementioned approaches can be exploited [9], and/or synthetic aperture imaging techniques can be used that require a handful of antenna elements [8][11]. Nevertheless, such approaches constitute a compromise between imaging speed, beam gain, system size, and RF-front-end complexity. In this section, mmWave/THz imaging systems are briefly presented to emphasize the current state-of-the-art.

A quasi-optical, high-resolution THz imaging system implemented by Cooper et al. [5], is presented in Fig. 1.2. This imaging system operates at 675 GHz and consists of a horn antenna coupled to a large paraboloid reflector forming a very narrow pencil beam. This high-gain beam is scanned across the whole field-of-view (FOV) by mechanically steering one of the feeding sub-reflectors. Even though this setup allows for relatively high-speed imaging (~2Hz) with a significant spatial resolution (~0.5mm), it constitutes an extremely bulky solution due to the quasi-optical setup used.

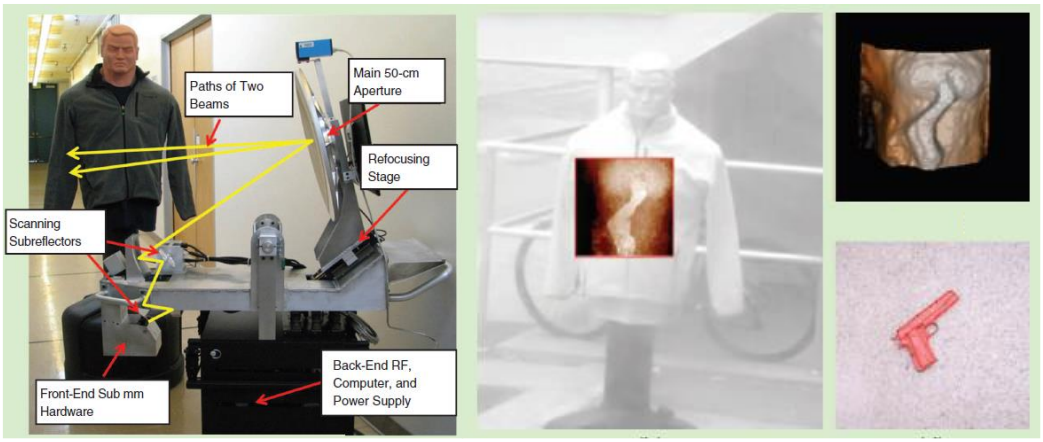

(a) (b)

Fig. 1.2 (a) The monostatic THz imaging system proposed by Cooper et al. [5] comprised a quasi-optical setup and a horn antenna and (b) imaging results of concealed weapon examples.

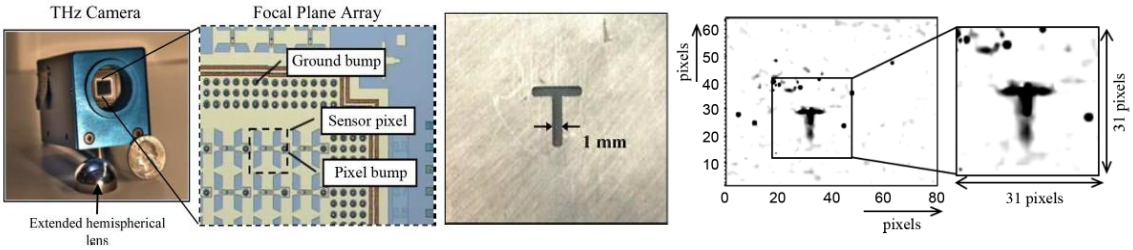

(a) (b)

Fig. 1.3 (a) The THz camera implemented by Trichopoulos et al. [6]. This camera comprises an on-wafer multi-pixel direct detection sensor that is coupled to a hemispherical silicon lens. (b) An imaging example with the THz camera of (a).

Another example of a THz imaging system is given in Fig. 1.3. This passive system, proposed by Trichopoulos et al. [6], operates at the 0.6-1.1 THz band and implements a combination of quasi-optical components and multi-element antenna sensors with integrated direct detectors (Schottky-diodes), leading to a focal plane array (FPA) that acquires real-time images (due to the absence of mechanical scanning), with enhanced

spatial resolution. However, the use of a dielectric lens to achieve high-spatial-resolution leads to bulky designs that are incompatible with applications where size is critical.

The aforementioned setups require quasi-optical components to perform mmWave/THz imaging for security and other applications, leading to bulky designs. Conversely, mmWave/THz imaging systems that employ planar sensors comprised of antennas (e.g., phased arrays) lead to low-profile topologies that can be leveraged for real-time high-spatial-resolution imaging [7]-[13]. For example, Gonzalez-Valdez et al. [7], presented a Ka-band imaging system that uses a multistatic setup comprised of a handful of transmitters and thousands of receiver antennas, as shown in Fig. 1.4. The design and development of this setup constitute a herculean engineering task, since, embedding thousands of mmWave antennas with their respected RF-frond-end circuity in a setup is not trivial; however, such sensors retain a low-profile and provide fast image acquisition speeds due to the absence of mechanical scanning.

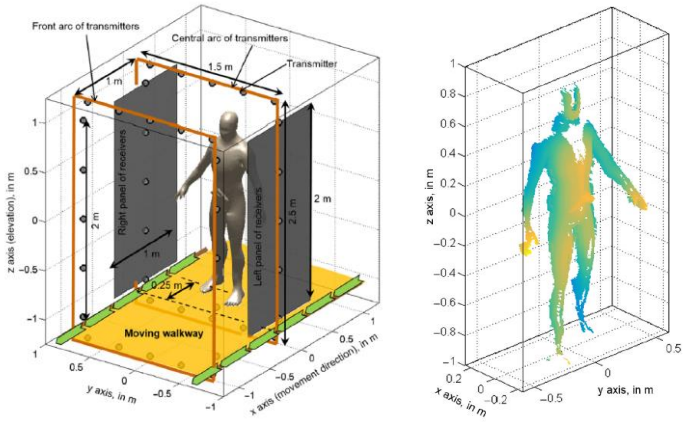

(a) (b)

Fig. 1.4 (a) The multistatic imaging system proposed by Gonzalez-Valdez et al [7]. The system comprises thousands of antenna receivers to acquire images with high-spatial-resolution. (b) A simulated imaging example of a human body using the design of (a).

Alternatively, to reduce the RF-front-end complexity, Ahmed et al. [8] proposed a sparse multistatic system that performs imaging at 78 GHz. This system significantly reduces the number of used elements compared to [7] by leveraging multistatic sparsity techniques [14], leading to sparsely populated apertures with a handful of antennas. Specifically, the proposed sensor consists of 768 receiving and 768 transmitting antennas leading to 7,682 (768^2) effective antenna elements, though the actual number of channels/elements is only 1,536 (768×2). Even though this sparse-multistatic approach is preferable compared to [7], the total number of integrated antennas with their respective RF-channels still leads to a complicated RF-front-end circuitry (e.g. mixers, phase-shifters, local-oscillators, etc.).

To further reduce RF-front-end complexity, Baccouche et al. [10] proposed a W-Band multistatic imaging system comprising of two linear arrays (12 receiving and 12 transmitting horn antennas), as shown in Fig. 1.5. However, this system acquires images by performing a synthetic aperture technique, where a physical displacing of the sensor is necessary to illuminate the whole FOV (raster-scanning), thus significantly limiting image acquisition speed. A similar design was proposed by Nowok et al. [9], where a multiple-input-multiple-output (MIMO) 3D imaging system at 360 GHz, implemented by two linear arrays. However, the proposed system comprises a combination of sparse-multistatic phased arrays (like [7]) and quasi-optical components (like [5]) (cylindrical reflector), resulting in a simple, though, low-framerate bulky design.

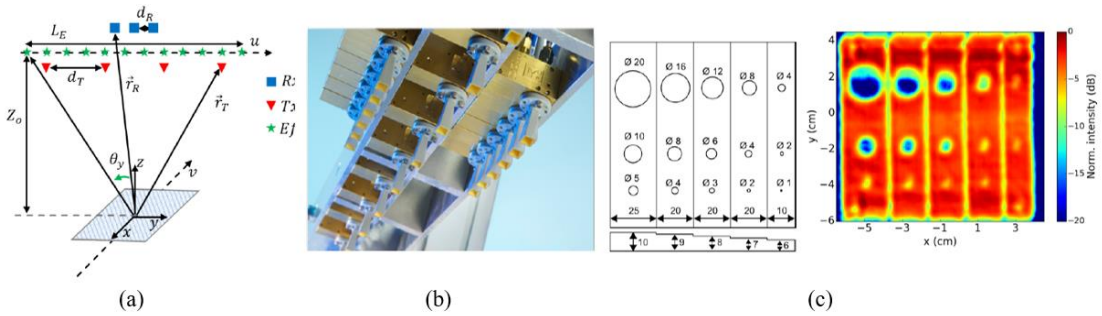

Fig. 1.5 (a) The multistatic imaging setup as proposed by Baccouche et al. in [10], (b) the implemented system comprises a series of horn antennas that perform 1-D multistatic imaging, while mounted on a stage that is moved to scan the whole 2-D FOV(raster-scanning), and (c) a measured image of a standard target.

Alongside security imaging, mmWaves/THz frequencies have been used in automotive imaging radars [11], since they offer enhanced spatial resolution by employing small aperture sensors that can be easily embedded in vehicles. An automotive radar/imaging system operating at 77 GHz is presented in Fig. 1.6 [11], where a single wide-beam antenna is used to illuminate the FOV and a linear receiving array is used to record the backscattered signals. Unlike the arrays of the previous examples, this configuration reduces the RF-front-end complexity by leveraging a coded aperture approach to record all the necessary information from the backscattered signals. As such, by modulating the binary phase shifters integrated with each antenna (Fig. 1.6b), a series of orthogonal patterns is recorded at the receiver. Then, after all the patterns are recorded, the final image is reconstructed using a mathematical back-projection method. This approach significantly reduces the RF-front-end complexity though the framerate is reduced since multiple orthogonal patterns, which are sequentially recorded, are required to accurately reconstruct the final image.

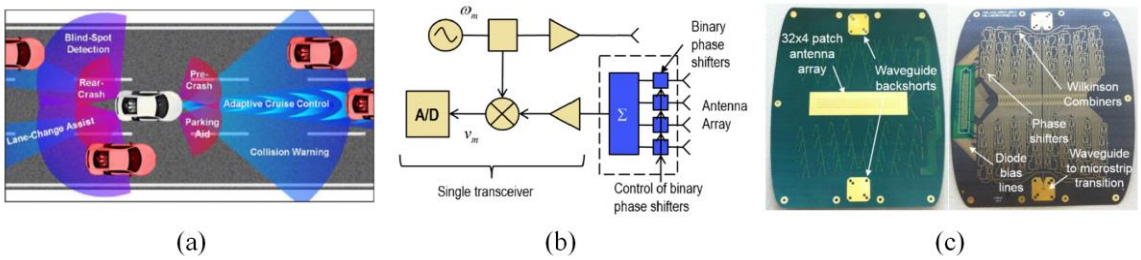

Fig. 1.6 (a) Automotive radars eliminate the blind spots while driving [11]. (b) A coded array automotive radar paradigm and (c) the implemented prototype [11].

Another example of THz imaging is given in Fig. 1.7 [12]. This system exploits the THz camera proposed in [6], along with a mathematical image reconstruction algorithm used in tomography systems, to obtain 3D images of different objects. This THz tomography imaging technique can be used for security and pharmaceutical imaging applications, allowing for non-invasive imaging of the targets.

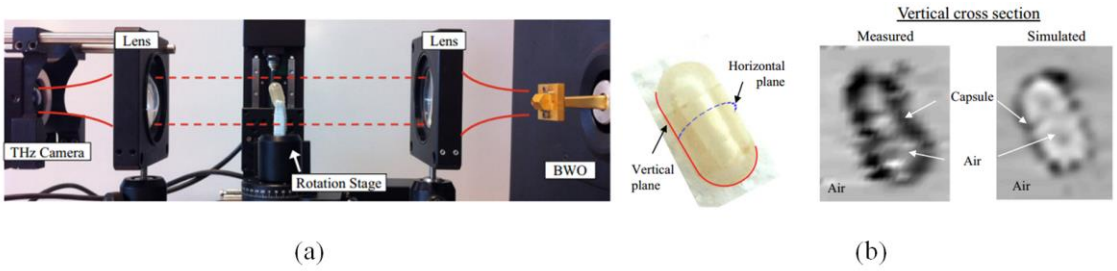

Fig. 1.7 (a) The tomography imaging setup using a THz camera [12] and (b) the imaging results for a vitamin capsule.

Finally, mmWave/THz frequencies can be exploited in medical imaging applications [13], as presented in Fig. 1.8. Specifically, in [13], THz images of skin burns on a rat were obtained using a 0.525 THz raster-scanning system. The images reveal the changes in the skin tissue's humidity with time. This kind of THz imaging can be proven

extremely valuable for medical applications since it provides additional information about the damaged tissue compared with conventional imaging devices (e.g. optical, infrared, and X-rays).

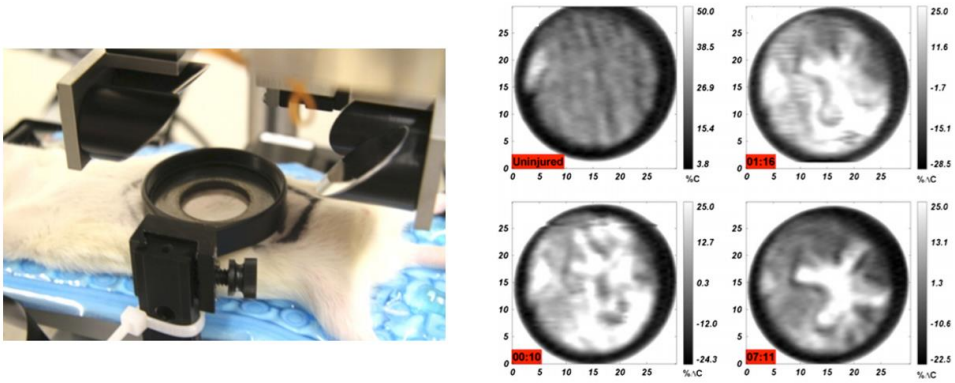

(a) (b)

Fig.1.8 (a) The setup used to image skin burns on rats [13]. The setup consists of a horn antenna and quasi-optical components and (b) the images are obtained by raster-scanning the FOV at different times after the initial burn.

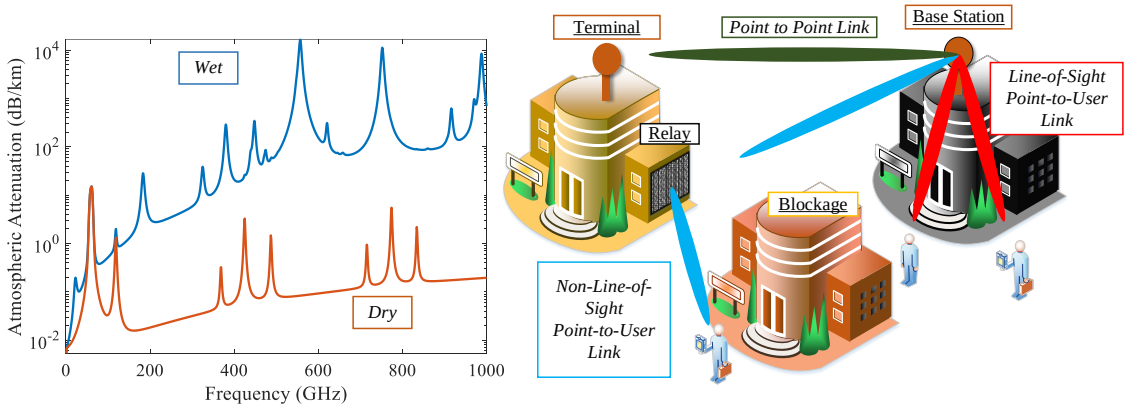

(a) (b)

Fig.1.9 (a) The atmospheric losses versus frequency for low and high humidity environments, and (b) a 5G and beyond communication system paradigm.

II. Wireless communications using millimeter-wave/terahertz systems

Alongside imaging applications, mmWave/THz frequencies have attracted the interest of the research community for communication purposes due to the ample bandwidths that enable high-throughputs reaching up to 120 Gbits/sec [15]-[17]. In general, mmWave/THz frequencies have higher atmospheric losses compared to microwaves (Fig. 1.9a), thus the throughput is expected to decrease due to low signal-to-noise ratio (SNR). Moreover, diffuse scattering caused by common –electrically-rough– surfaces in these frequencies (e.g., walls), leads to shadowing that reduces coverage in urban environments.

To overcome these limitations, electrically large apertures can be employed offering high-gains that compensate for the atmospheric losses and blockage, thus enabling high-throughput wireless communications [15]-[20]. Typically, mmWave/THz communication systems are classified into two major categories, as illustrated in Fig. 1.9b: 1) point-to-point communications (e.g. between base-stations and terminals) (backbone network), and 2) base-station to user links.

Point-to-point communications in THz bands are still in their infant stages, though some works that propose such systems are found in the existing literature [15]-[17]. Specifically, point-to-point wireless THz links require high-throughputs to accommodate multiple data streams (from multiple users), thus high operation frequencies are necessary [3]. These systems, typically, employ quasi-optical components (e.g. lenses, mirrors, etc.) that form highly-directive beams to achieve decent SNR in the communication channels, thus increasing the archived data-rates. Examples of point-to-point mmWave/THz systems

are given in Fig. 1.10. As such, in Fig. 10a, a photonics-based system is presented that performs wireless data transmission at 350 GHz, reaching 120 Gbits/sec of throughput. Alternatively, 'all-electronic' systems have been proposed for point-to-point communications, as shown in Fig. 1.10b [15]. However, these systems cannot reach the throughputs of their photonics-based competitors, due to the limitations of the integrated electronics achieving a maximum channel capacity up to 100 Gbits/sec [16][17].

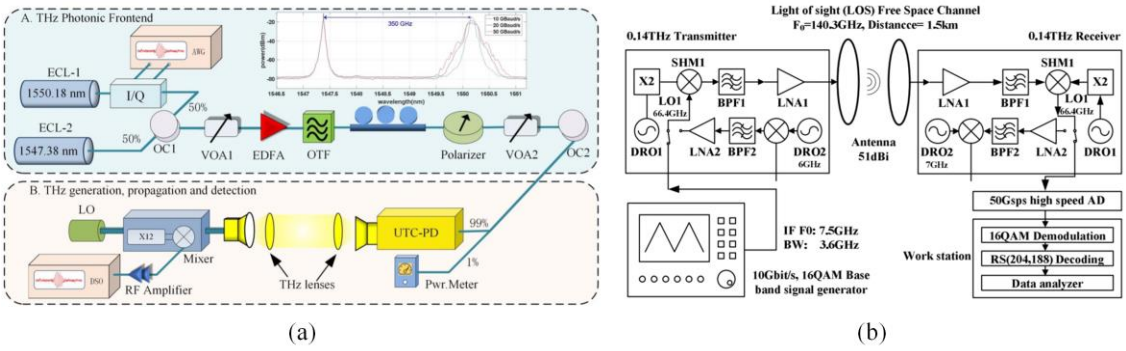

Fig.1.10 (a) A photonic based point-to-point communication link example proposed in [15] and (b) its fully electronic equivalent, proposed in [16].

Besides point-to-point mmWave/THz communications, a great effort is devoted by the research community on the base-station to user communication links for cells that serve a small number of users, though with high data-rates (Fig. 1.9b) [18]-[21]. Such applications require lower data-rates than point-to-point links, though they should offer coverage over a considerable area to include as many users as possible. Typically, in microwaves (4G and below), the user coverage is assured by employing low-gain antennas with high RF power as base-stations. However, the atmospheric losses and blockage of mmWave/THz bands (Fig. 1.9a), and the RF power limitations, demand for higher-gain antennas to achieve similar SNR performance as microwave systems. Thus, to increase the

provided data-rates the use of space-division-multiple-access (SDMA) is preferred [18], where multiple high-gain beams track the user's position (Fig. 1.9b), offering an acceptable SNR performance leading to increased data-rates.

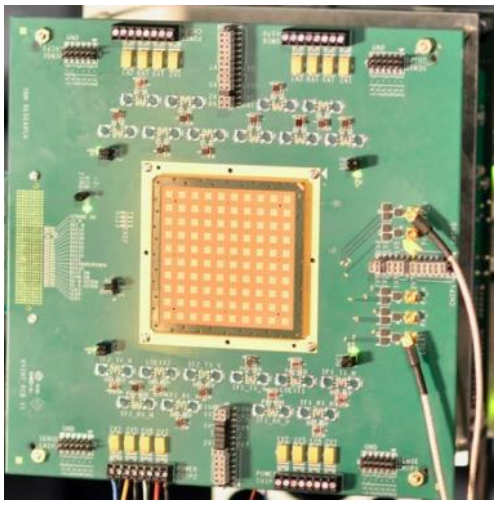

Fig.1.11 A 64-element mmWave MIMO array for 5G applications operating at 28 GHz [19].

Such systems are usually implemented by deploying MIMO arrays as the one depicted in Fig. 1.11 and carry out beam steering in the digital processing domain [18][19]. This approach is versatile in terms of beam scanning capabilities; however, in cases where the user is in the non-line-of-sight of the base station (Fig. 1.9b), the performance of these links decreases dramatically, due to the mmWave/THz dispersion losses of common construction materials (e.g., concrete, drywall, etc.) [1]. To overcome this issue, the use of relays (intelligent reconfigurable surfaces–IRSs) is preferred as shown in Fig. 1.9b. These relays consist of a plethora of antennas with integrated RF switches that modulate the impinging waves (from the base station) and redirect the beam toward the user [20][21]. In

this manner, the communication link performance remains high, and a greater coverage is achieved without increasing the transmitted RF power on the base station.

III. Contributions of this research

The scope of this work is the study, analysis, and design of mmWave/THz beamforming systems for imaging and wireless communication applications. Specifically, the goal is to devise low-complexity, low-loss systems that offer solutions for high-spatial-resolution imaging and wireless communication applications. The first step in the design process is a thorough analysis of the proposed system. As such, full-wave simulations are necessary to reveal all the exhibited electromagnetic phenomena and allow the case study of complex application scenarios; however, simulating large-scale mmWave/THz antenna systems that incorporate hundreds or thousands of elements with conventional full-wave tools is burdensome computationally. For that purpose, in Chapter 4, a novel decomposition numerical method based on the premise of conjugate field coupling is presented. This novel method alleviates the computation roadblock toward the study and analysis of mmWave/THz antenna systems by significantly reducing the necessary computational resources.

Then, in Chapter 5, a novel imaging technique that employs both mechanical and electronic beam scanning to reduce the number of incorporated antennas in the imaging system is presented. Leveraging the proposed approach, the number of antennas can be significantly reduced by a factor of $N^{3/2}/2$ (compared to an $N \times N$ traditional phased array), while high-spatial-resolution is achieved. As such, fewer antennas are used to carry out the imaging leading to less incorporated electronics, power consumption, and real estate.

Moreover, the devised low-profile, lightweight systems could be mounted in drones or CubeSats, enabling high spatial resolution imaging in applications where size and weight are crucial.

This work also focuses on the hardware implementation of systems. As such, employing large-scale reconfigurable reflective surfaces (RRSs) consisting of antennas with integrated single-pole-single-throw (SPST) graphene switches is a promising solution that could be utilized both in imaging and wireless communication systems. Specifically, these surfaces modulate the impinging waves beamforming them toward the desired directions/angles, while tunning the state of the switches to enable dynamic beam tilting. Herein, to achieve the necessary wavefront modulation, low-cost switches consisting of 2D materials (e.g., graphene) are promoted. However, integrating graphene switches over large areas is not trivial; thus, in Chapter 6, a novel nanofabrication technique based on sacrificial layers is presented that enables graphene switches incorporation in large-scale mmWave apertures with more than 90 % yield for the first time. The fabrication process is evaluated by comparing the on-wafer measured graphene material properties with the existing literature. Afterward, in Chapter 7, the measured graphene properties are used to analyze, and design various graphene loaded switch topologies and identify the one that provides optimum RF performance. This thorough analysis is carried out for the first time in this work and constitutes the roadmap of the analysis and design not only of graphene loaded switches but for various switch topologies that incorporate tunable thin-film or 2D material.

The proposed graphene switches are the cornerstone in the implementation of reconfigurable reflective surfaces that can be leveraged both in imaging and wireless communication applications. Particularly, existing RRS designs typically offer a single bit

of phase modulation (e.g., 0^o and 180^o) that leads to low aperture efficiency and high-level parasitic lobes. These issues are tackled in Chapters 8-10, where novel reconfigurable unit-cell topologies for reconfigurable reflective surfaces are thoroughly presented. In Chapter 8, the process of integrating the SPST graphene switches in the RRS unit-cells is detailed. However, the performance of the single-bit graphene actuated RRS designs is degraded due to the high quantization errors that lead to low aperture efficiency and high parasitic lobes. Thus, in Chapter 9, novel multi-bit RRS topologies are presented that integrate up to 4 switches, within the limited space of the unit-cell, to acquire 4 bits of phase quantization for the modulation of the impinging waves. This is the first time in known literature that more than 2 bits of phase quantization are achieved with SPST switches. Additionally, the proposed configurations use a single SPST switch per bit, offering low system complexity, while significantly increasing aperture efficiency and eliminating the undesired lobes. Finally, in Chapter 10, a novel alternative RRS design is presented that utilizes a single bit of phase quantization to acquire single lobe performance (no parasitic quantization lobes) by employing a surface randomization technique.

All the aforementioned innovations are thoroughly presented in the following Chapters paving the road for future mmWave/THz wireless communication and high-resolution imaging systems.

IV. Conclusion of Chapter 1

In this Chapter, a variety of mmWave/THz systems alongside their applications were presented. As such, mmWave/THz systems can consist of quasi-optical components, antenna arrays, reconfigurable surfaces, and combinations, and are used either for

communication and/or imaging applications. Moreover, the contributions of this work were summarized. Next, in Chapter 2, the beamforming principles of mmWave/THz systems are presented.

CHAPTER 2

Beamforming Topologies for Millimeter-wave and Terahertz Imaging and Communication Systems

This Chapter presents the beamforming topologies used in the mmWave/THz systems for imaging and wireless communication applications. As such, these systems employ steerable high-gain beams to carry out their operation. The systems are classified based on their beamforming approach and their principles of operation are briefly presented. Specifically, mmWave/THz systems form steerable collimated beams, either by using focusing components (mirrors, lenses) [5][6], a plethora of antennas [7][8], or a combination of both [9]. The gain of the aperture is proportional to its size [2] and beam steering can be carried out with mechanical components and/or electronically.

I. Phased arrays

Phased arrays consist of several antenna elements that are fed by an RF-front-end circuitry and are desirable topologies in several mmWave/THz applications due to the achieved high-gains and beam shaping versatility. The radiation pattern of a planar array (Fig. 2.1.) is given by [2]

$$E_{rad}(\theta,\varphi) = E_{ele}(\theta,\varphi)AF \quad (2.1)$$

where

$$AF(\theta,\varphi) = \sum_{i=1}^{N_x}\sum_{l=1}^{N_y} w_{(i,l)}e^{j\psi_{(i,l)}} \quad (2.2)$$

and

$$\psi_{(i,l)} = b_{(i,l)} + k\left[x_{(i,l)}\sin(\theta)\cos(\varphi) + y_{(i,l)}\sin(\theta)\sin(\varphi)\right] \qquad (2.3)$$

where E_{rad} are the radiated fields of the array in spherical coordinates (θ,φ), E_{ele} is the radiation pattern of the individual antenna element (assuming identical antennas) in spherical coordinates, $w_{(i,k)}$ is the amplitude coefficient of each element, $b_{(i,k)}$ is the feeding phase of each element, θ is the elevation angle, φ is the azimuth angle, $x_{(i,k)}$ element position along the ***x*** axis, $y_{(i,k)}$ is the element position along the ***y*** axis, k is the free-space wavenumber, and N_x and N_y, are the numbers of antenna elements along the ***x*** and ***y*** axes, respectively.

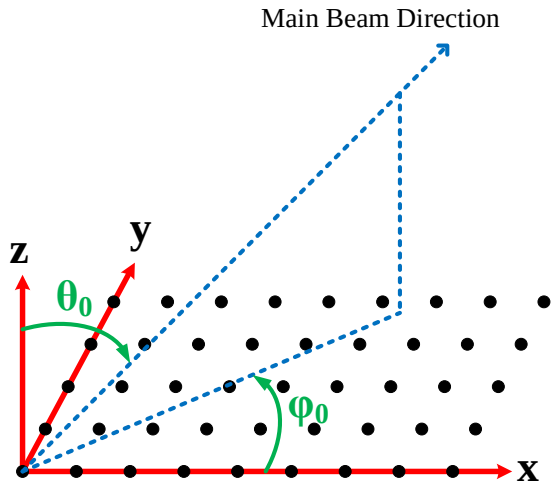

Fig. 2.1 A planar array of antenna elements located on the ***x***-***y*** plane. Black dots represent the antenna elements.

To steer the beam at the desired direction (θ_0, φ_0), as shown in Fig 2.1, the introduced phase at each antenna element is given by [2]

$$b_{(i,l)} = -k\left[x_{(i,l)}\sin(\theta_0)\cos(\varphi_0) + y_{(i,l)}\sin(\theta_0)\sin(\varphi_0)\right] \quad (2.4)$$

The element phase given in (2.4) is introduced at the radiation elements using two major approaches: 1) analog beamforming [22] and 2) digital beamforming [23]. In the case of analog beamforming, the necessary phase is introduced on the antenna elements through a corporate RF feeding network comprised of couplers, splitters, phase shifters, etc. [22]. This approach introduces the required phase delay in the RF signals directly, as illustrated in Fig. 2.2a, and then the signals down-converted and digitized using an analog-to-digital converter (ADC); however, the incorporated circuitry leads to high RF-front-end complexity and losses. Alternatively, beamforming can be carried out in the digital domain, where the RF signals are directly down-converted after the antennas and the beamforming is implemented in the post-processing/digital domain (Fig. 2.2b). This approach is more versatile in terms of beamforming since the introduced phase delay can be digitally assigned any value and is independent of incorporated hardware components (e.g., phase shifters). However, a single mixer and local-oscillator signal are needed at the feed of each element leading again to a complex system. As shown in Fig. 2.2c, both systems form high-gain steerable beams with a single main lobe. Moreover, these systems can operate in receiving, transmitting, transceiving, or hybrid modes depending on the application.

In both digital and analog beamforming approaches, as the number of incorporated antennas increases, system complexity, RF losses, and DC power consumption skyrocket [24] due to the incorporated components (mixers, LOs, couplers, phase-shifters, etc.). Moreover, the real-estate cost of the circuit components is significant [25], thus hindering the proliferation of such topologies in the mmWave/THz bands. To reduce the number of

integrated antennas elements, thus alleviate the RF-front-end complexity, topologies that use multistatic sparsity approaches have been proposed in the literature [14] (discussed in Chapter 5).

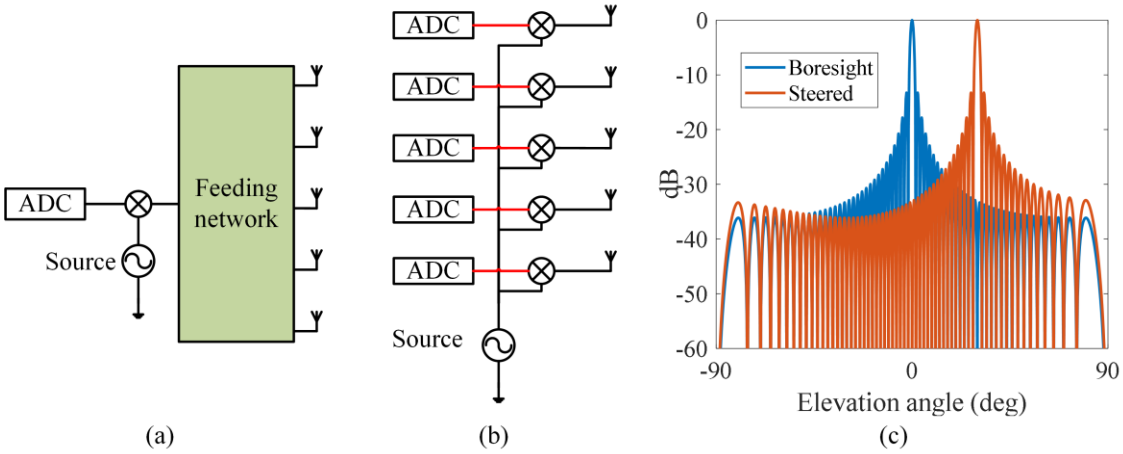

Fig. 2.2 (a) The schematic of a basic analog beamforming receiving system comprising of a corporate feeding network, (b) its digital beamforming counterpart, and (c) an example of beam steering for a 50×1 ($\lambda_0/2$ spacing) linear antenna array.

Another alternative to reduce the RF-front-end complexity in phased array imaging systems are coded phased arrays. As such, these configurations utilize a single source to distribute (or record) the signals to the antennas as illustrated in Fig. 2.3. At the RF channel of each antenna element, a switch is embedded modulating the RF signals in phase and/or amplitude. In such systems a simple modulation scheme is utilized [11][26]; for example, the feeding phase of the antenna element can be tuned to either 0^o or 180^o. Similar modulation schemes can be carried out on the amplitude of the feeding signals [11][26]. In this manner, these systems form multiple spatiotemporally orthogonal radiation patterns to illuminate the FOV (or detect from it). Such configurations are usually implemented in multistatic configurations, where a separate single-antenna receiver (or transmitter) is used

alongside the coded array [11][26]. The decoding process is carried out in the post-processing domain, by using the recorded signals of the various orthogonal patterns [26].

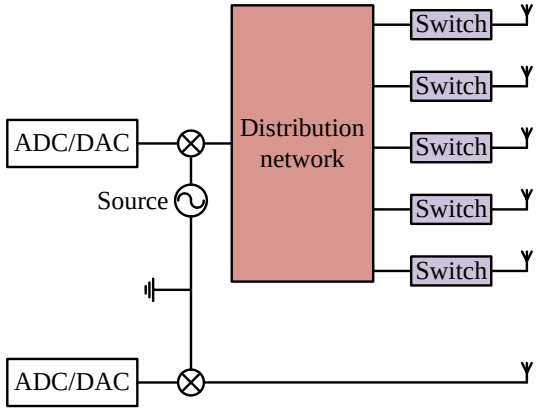

Fig. 2.3 The schematic of a coded phased array using switches at the feed of each element.

II. Reconfigurable reflective surfaces

Phased arrays presented in section II, incorporate a hundred or even thousands of antennas to form high-gain steerable beams required for imaging and/or communication applications. However, as the number of antennas and the operating frequency increase, the efficiency drops in terms of RF losses and DC power consumption due to the RF-front-end complexity [24]. Moreover, the use of complex RF-front-end networks that comprise multiple mmWave/THz active components (mixers, LOs, etc.) leads to increased implementation costs. Therefore, solutions that simplify the RF-front-end circuitry are necessary without compromising the total gain and the beam steering abilities of the system. As such, reconfigurable reflective surfaces have been promoted as an alternative solution to phased arrays [27]. These configurations use external sources that illuminate the RRS consisting of a plethora of tunable antennas elements with integrated switches

(e.g., PIN diodes [28]), as shown in Fig. 2.4a. To steer the beam at the desired direction, the state of the switches is tuned, modulating the phase of the reflected waves. The total system gain is similar to the phased array systems (assuming same aperture size) and the beam steering speed depends only on the incorporated electronics as in the case of phased arrays [27]. Therefore, RRSs can serve as an alternative to phased arrays both in imaging (e.g., imaging sensors) and wireless communication applications (e.g., base stations, relays, etc.).

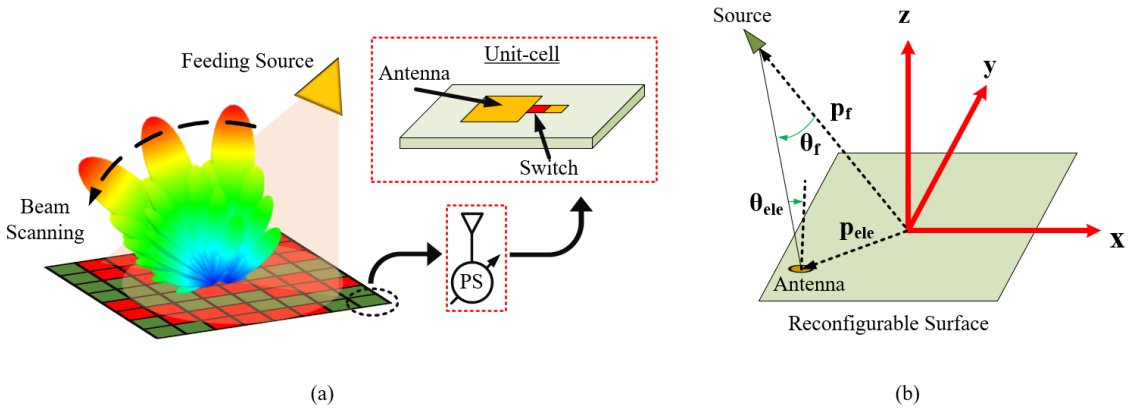

Fig. 2.4 (a) The basic principle of operation for RRSs and (b) the analytical configuration of the design.

The feeding scheme of RRSs can vary depending on the application, though generally it can be approximated using the model of Fig. 2.4b. As such, assuming that a spherical wave source is placed at a certain distance from the surface, the total radiation pattern of the RRS is given by [27]

$$E_{rad}(\theta,\varphi) = \sum_{i=1}^{N_x}\sum_{l=1}^{N_y} A_{(i,l)} I_{(i,l)} \quad (2.5)$$

where N_x and N_y are the numbers of elements across the $\boldsymbol{x}$ and $\boldsymbol{y}$ axes, respectively, $A_{(i,l)}$ is the element radiation pattern, and $I_{(i,l)}$ is the illumination pattern caused by the source on the surface. The element radiation pattern of (2.5) is approximated by

$$A_{(i,l)} \approx cos^{q_e}(\theta) e^{jk(\boldsymbol{p_{ele}}_{(i,l)} \cdot \boldsymbol{u})} \quad (2.6)$$

where q_e is the factor that controls the normalized gain of the reconfigurable surface antennas (assuming a cosine model with rotational symmetry for the surface elements [27]) –typically varying from 0.5 to 2 for patch antennas [27]–, $\boldsymbol{p_{ele}}$ is the position vector of each antenna (Fig. 2.4b), k is the free-space wavenumber, and $\boldsymbol{u}$ is the observation position vector given by

$$\boldsymbol{u} = \boldsymbol{x} sin(\theta)\cos(\varphi) + \boldsymbol{y} sin(\theta) si\, n(\varphi) + \boldsymbol{z} cos(\theta) \quad (2.7)$$

where θ and φ are the spherical coordinate system's angles. Thus, (2.5) assumes that the impinging waves on the elements ($I_{(i,l)}$) are re-radiated from the RRS antennas as a summation of spherical waves. The illumination components at each (i,l) antenna of the reconfigurable surface are given by [27]

$$I_{(i,l)} \approx cos^{q_f}(\theta_{f(i,l)}) \frac{e^{-jk(|\boldsymbol{p_{ele}}_{(i,l)} - \boldsymbol{p_f}|)}}{|\boldsymbol{p_{ele}}_{(i,l)} - \boldsymbol{p_f}|} M_{(i,l)} \quad (2.8)$$

and

$$M_{(i,l)} = cos^{q_e}\left(\theta_{e(i,l)}\right) e^{j\varphi_{mod(i,l)}} \quad (2.9)$$

where $\boldsymbol{p_f}$ is the position vector of the source, q_f is the gain factor of the source (typically ranging between 10 to 50 for feed-horn antennas [27]), θ_f is the angle the source "sees"

each antenna element, θ_{ele} is the angle that each antenna element "sees" the source, and $\varphi_{mod(i,k)}$ is the modulation phase inserted by the reconfigurable (i,l) antenna element. As such, the first term of (2.8) expresses the spherical wave produced by the illumination source (assuming cosine approximation with rotational symmetry), and $M_{(i,l)}$ is the modulation factor introduced by each reconfigurable antenna element. The modulation angle of each element to steer the beam toward the (θ_0,φ_0) direction is given by [28]

$$\varphi_{mod(i,l)} = -k\left[x_{(i,l)}sin(\theta_0)\cos(\varphi_0) + y_{(i,l)}sin(\theta_0)sin(\varphi_0)\right] + k\left|\boldsymbol{p_{ele}}_{(i,l)} - \boldsymbol{p_f}\right| \quad (2.10)$$

where ($x_{(i,l)}$, $y_{(i,l)}$) is the position of the (i,l) antenna element on the RRS. The modulation phase of (2.10) is a continuous function and can take any value within the [-180^o, 180^o] locus. However, reconfigurable systems typically utilize a handful of reflection phases due to hardware limitations [27]-[38]. Namely, one or two single-pull-single-throw switches (e.g., PIN diodes) are usually integrated with the antennas to tune the phase of the reflected waves, thus the number of available phase states generally varies from 2 to 4. For single-bit quantization, the phase states are ideally 0 and 180^o, and for the dual-bit quantization, the available states are 0^o, 90^o, 180^o, and 270^o. Generally, the phase states are 2^B, where B is the number of bits, and are equispaced in the 0^o-360^o range. Thus, the phase of each element given by (2.10) is quantized based on the available phase states. This quantization process causes phase errors that lead to increased side-lobe-levels, as shown in Fig. 2.5 [REF]. The effects of the quantization process on the radiation patterns, alongside methods to mitigate the quantization lobes, are discussed in Chapters 8-10.

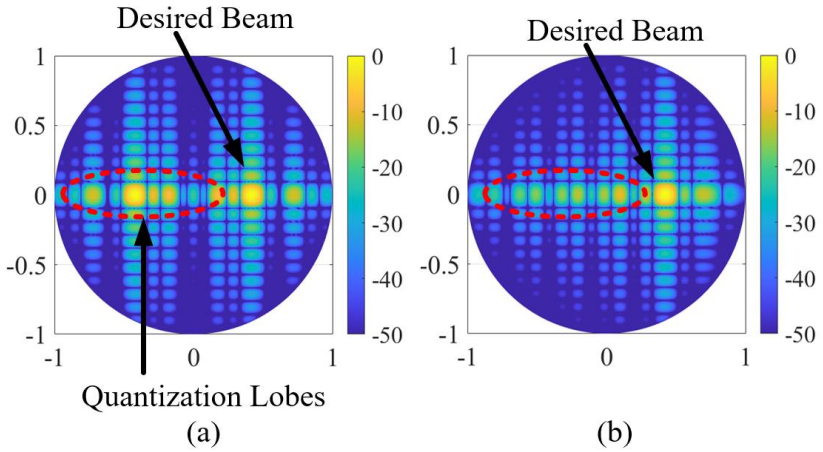

Fig. 2.5 (a) The radiation pattern of a 20×20 element ($\lambda_0/2$ sampling) RRS with: (a) 1-bit and (b) 2-bit phase quantization. The source is a boresight plane-wave.

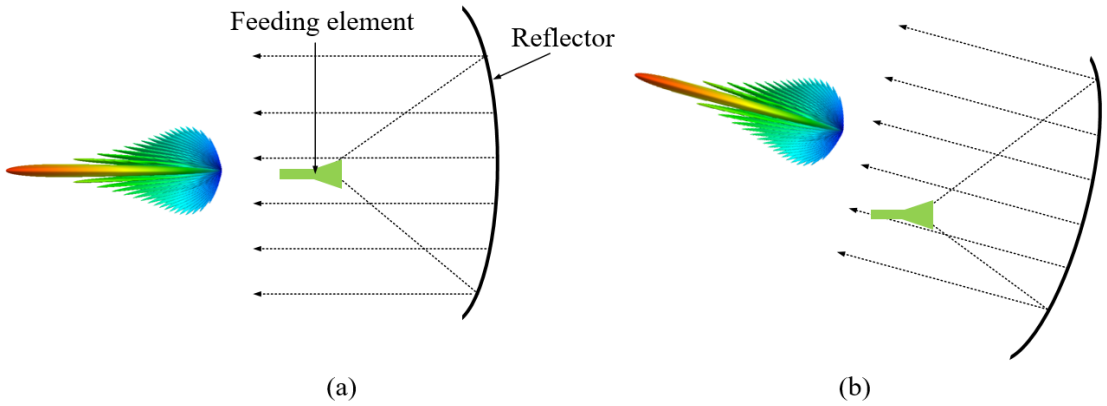

Fig. 2.6 (a) The main concept of the quasi-optical setups and (b) the beam steering approach followed in [5].

III. Quasi-optical systems

Another popular category of mmWave/THz systems incorporates quasi-optical components (e.g., lenses, reflectors, etc.). Such configurations offer high-gain beams without including multiple antennas as in the case of phased arrays, thus the RF-front end

complexity is significantly reduced. Namely, a single antenna can be used to illuminate a large aperture reflector (or lens), creating a highly directive beam, as shown in Fig. 2.6a. This approach can offer extremely high-gain beams for both imaging and communications applications with a simplistic design since the directivity of the system depends on the dimensions of the reflector [2].

Quasi-optical systems usually comprise one or a series of reflectors and a single feeding antenna correctly placed at the focal point of the reflector. The feeding antennas are usually horn antennas, due to their radiation pattern properties [2][5]. Namely, the high directivity and symmetrical radiation pattern are key factors that horn antennas are preferred. The use of these elements leads to highly focused beams that can be studied using the Gaussian beam theory [39].

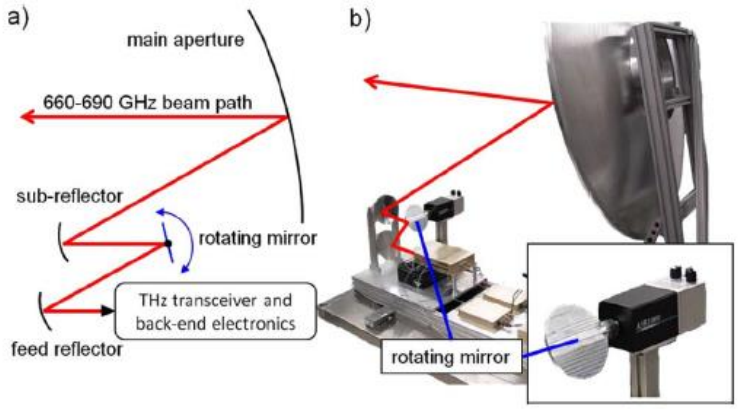

Fig. 2.7 The design proposed by Cooper et al. [5] to perform THz imaging for stand-off security applications. A series of sub-reflectors is used to form the feeding beam of the main reflector and the beam steering is achieved by manipulating one of the sub-reflectors.

Although this approach can use a single feeding antenna (e.g., horn antenna), the beam scanning is not a trivial procedure. To explain the beam steering procedure, let us

consider Fig. 2.6b. To steer the main beam of the system in a certain direction, the relative position of the reflector and the feeding antenna change accordingly. An example of a system that performs imaging in the 600-700 GHz band, using quasi-optical components and a feed-horn antenna, is given in Fig. 2.7 [5]. Beam steering is achieved by mechanically rotating one of the sub reflectors. Although this simplistic approach offers high-gain beams, the mechanical motion compromises the beam steering speed. Additionally, the design is extremely bulky which is a common aspect of all quasi-optical setups.

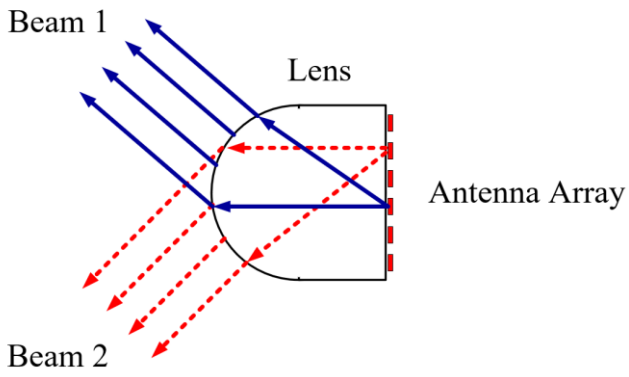

Fig. 2.8 The fundamental principle of beam steering in focal place arrays. A different beam corresponds to each antenna, depending on the position of the antenna.

Another category of quasi-optical sensors that combines the advantages of phased arrays and optical topologies to form high-gain beams with beam steering capabilities are focal plane arrays (e.g., [6]). Namely, FPAs consist of quasi-optical components and sensor arrays, as depicted in Fig. 2.8. This design consists of two parts: 1) the focusing element (e.g., hemispherical lens) and 2) the antenna array. To steer the beam at the desired direction, different antenna elements on the array are activated. Therefore, there is no need

for steering the beam of the feeding antennas using a complex feeding network or with a mechanical movement.

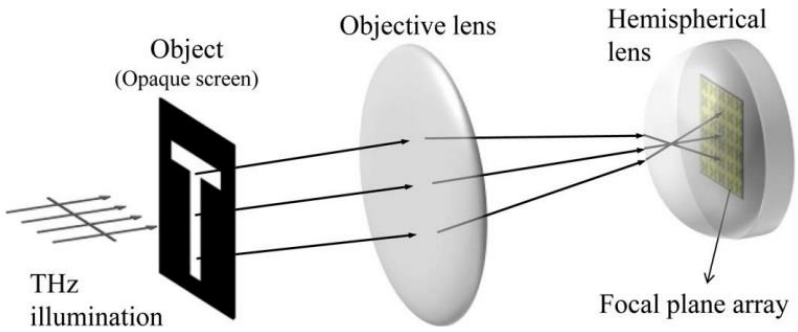

Fig. 2.9 The imaging system proposed in [12]. The system consists of a THz illumination source, an objective lens, and a focal plane array.

An example of such a FPA system is given in Fig. 2.9 [12]. In this system, the array consists of antennas with integrated direct detectors, and the illumination of the object is achieved by an external source. The object is initially illuminated by a plane-wave and the scattered fields are focused on the focal plane sensor using an objective lens (Fig. 2.9). Then, each of the direct detectors records the signal that corresponds to a single pixel of the image. The use of coherent detection is avoided due to complexity reasons.

IV. Directivity and efficiency of beamforming systems

All the aforementioned beamforming systems are non-omnidirectional radiators, meaning that the energy is focused on specific angles instead of equally distributed toward all directions/angles. As such, if $E_{rad}(\theta,\varphi)$ is the radiation pattern of the beamformer, then the directivity (D) and the maximum directivity (D_0) are defined as [2]

$$D(\theta,\varphi) = 4\pi \frac{E_{rad}(\theta,\varphi)}{\int_0^{2\pi}\int_0^{\pi} E_{rad}(\theta,\varphi)sin(\theta)d\theta d\varphi} \qquad (2.11a)$$

$$D_0 = 4\pi \frac{E_{rad}(\theta,\varphi)|_{max}}{\int_0^{2\pi}\int_0^{\pi} E_{rad}(\theta,\varphi)sin(\theta)d\theta d\varphi} \qquad (2.11b)$$

where θ and φ are the elevation and azimuth angles of the spherical coordinate system, respectively. Higher directivity values translate to greater energy focusing on certain directions/angles and it is proportional to the size of the aperture of the radiator [2]. However, (2.11) does not incorporate any losses associated with the beamformer since it depends solely on the shape of the radiation pattern and not on its absolute values.

To account for these losses the beamformer efficiency is considered. As such, the beamformer efficiency is the ratio of the delivered power over the available source power defined as [2]

$$e_b = \frac{P_{radiated}}{P_{available}} = e_c e_d e_m e_{etc} \qquad (2.12)$$

where e_c is the efficiency due to conductor losses, e_d represents the efficiency due to dielectric losses, e_m is the efficiency due to mismatches, and e_{etc} is the efficiency associated with miscellaneous loss mechanisms (e.g., spillover efficiency in reflectarrays [27]). For example, in the case of a phased array, if the source provides 1 Watt of power, if the total radiated power is 0.2 Watt, then the beamformer efficiency is 20 %.

V. Signal-to-noise-ratio in antenna systems

Typically, antennas operate in non-absolute-zero temperature conditions (273 Kelvin is the typical room-temperature), thus the collisions of the molecules and the loss mechanisms (dielectric and conductor losses) of the incorporated materials lead to the

generation of noise at the output port of the antenna [40][41]. Moreover, at the same physical port, the captured signal is present; thus, both these signals are recorded by the receiver. The ratio of the signal power (P_{signal}) over the noise power (P_{noise}) at the antenna port, define the signal-to-noise-ratio [40]

$$SNR_{ant} = \frac{P_{signal}}{P_{noise}} \quad (2.13)$$

The noise power can be reduced by either reducing the physical temperature of the antenna and/or by mitigating the losses. Alternatively, the noise could be reduced by integrating for more time at the receiver since the noise at the antenna output port is a random waveform in time [41].

In the case of a phased array (e.g., Fig. 2.1), the noise signals at every antenna port are uncorrelated quantities since they originate from individual uncorrelated noise sources [41]. On the other hand, the signals originated by the impinging waves on the antennas are correlated quantities since they result from the coherent sampling of the imping wave [41]. Leveraging this effect, the phased array ($\lambda_0/2$ sampled) SNR is given by [41]

$$SNR_{array} = N \cdot SNR_{ele} \quad (2.14)$$

where SNR_{ele} is the SNR at the port of each antenna of the array (assumed identical) and N is the number of the antennas in the array.

VI. Conclusion of Chapter 2

This Chapter presented mmWave/THz beamforming systems including phased arrays, reconfigurable reflective surfaces, and quasi-optical setups. These systems can be

used wither in wireless communication applications or as imagers. In Chapter 3, the imaging architectures used in mmWave/THz bands are classified based on their principles of operation.

CHAPTER 3

Millimeter-wave and Terahertz Imaging Architectures

This Chapter presents the principles of imaging topologies used in the mmWave/THz bands. As such, the illumination scheme of the field-of-view and the image reconstruction method, classify the mmWave/THz configurations of Chapter 1 into various categories.

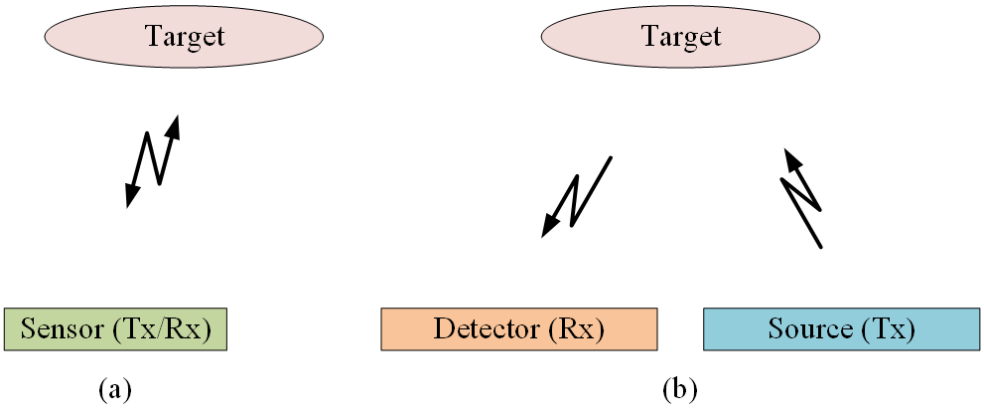

Fig. 3.1 Architectures of active imaging: (a) The monostatic illumination approach carried out by transmit/receive elements that are closely located and (b) the multistatic illumination scheme, in which the source(s) (illumination) and the detector(s) are separated by a large distance.

I. Monostatic and multistatic imaging sensor topologies

Active imaging systems consist of an aperture that transmits electromagnetic (E/M) waves to illuminate a scene, a receiving aperture that records the backscattered signals, and a processing unit that implements an image reconstruction algorithm. Succinctly, active imaging systems can be classified as: 1) monostatic or 2) multistatic, as shown in Fig. 3.1. Monostatic systems consist of sources that illuminate the FOV with a mmWave/THz beam

and the scattered fields are collected by the receivers. Moreover, the distance between the transmitting and receiving antenna elements is considerably smaller than the distance between the imaging system and the target (even zero in the case of transceiving antennas). These configurations comprise compact system solutions; however, since the illumination source and the receiver are closely located, the imaging capabilities of this configuration are limited due to the monostatic radar-cross-section (RCS) properties of the target(s) [42]. For example, if the target is a smooth metallic sheet located off-center from the monastic imager (Fig. 3.1a), the transmitted signals from the source would scatter toward the specular reflection away from the receiver, leading to poor image quality.

To overcome this limitation, multistatic configurations have been proposed in the existing literature, as illustrated in Fig. 3.1b. These systems use a source(s) to illuminate the FOV and a series of detectors to record the scattered (or transmitted) signals from the targets (e.g., [7][8]). This approach alleviates the monostatic RCS issues mentioned in the previous paragraph since the receivers can observe the targets from multiple angles, achieving better image quality in scenarios dominated by specular reflections. The main drawback of the multistatic approach is the need for large-aperture systems that accommodate several sources and receivers located at physically large distances, to carry out bistatic imaging. Finally, as the distance between the imager and the target increases, bistatic setups tend to operate as monostatic. Finally, both monostatic and bistatic imaging approaches can use beamformers as the ones presented in Chapter 2.

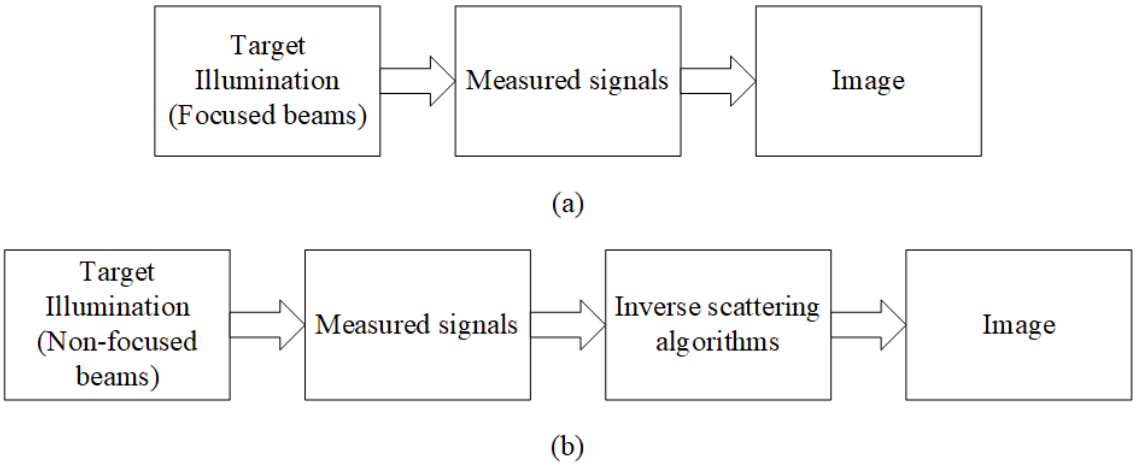

Fig. 3.2 The flow-charts of: (a) focused imaging systems, where the detected signals directly correspond to the pixel values of the final image, and (b) systems that employ field inversion techniques to reconstruct the image using the recorded signals.

II. Classification based on the imaging process

Imaging systems can be classified not only based on the FOV illumination scheme but also on the image reconstruction process. Namely, systems are typically split into two categories: 1) focused and b) inverse scattering algorithm systems. Firstly, focused systems utilize a sensor that forms a narrow high-gain beam that is scanned across the FOV and the recorded signals are arranged accordingly to form the image (e.g., [5]), as described in Fig. 3.2a. Specifically, in these systems, there is a one-to-one relationship between the direction of the beam and the pixels of the final image. Typically, monostatic systems are treated as focused systems and their main advantage is the simplicity in the image formation process.

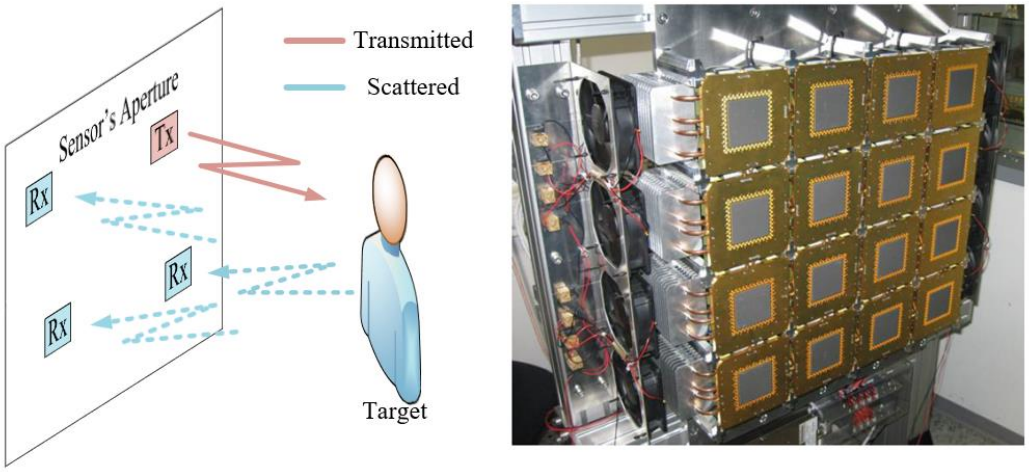

Fig. 3.3 The multistatic system presented in [8]. (a) The data acquisition procedure, where each transmitter is serially activated, and the scattered signals are detected by the receivers and (b) the actual multistatic array.

On the contrary, imaging systems that use non-focused beams to image the FOV, employ field inversion techniques to reconstruct the final image (e.g., [8]). This approach is suitable for bistatic imaging systems; however, the data acquisition process due to the sequential illumination scheme and the post-processing are time-consuming, leading to slow image acquisition. The imaging procedure followed by non-focused systems is given in Fig. 3.2b. Namely, to reconstruct the image, these systems illuminate the FOV by serially activating the transmitter antennas (low-directivity elements) and the scattered fields are recorded by the detectors. Afterward, the image is obtained using inverse scattering methods (e.g., [8]). An example of such a system is given in Fig. 3.3 [8]. This multistatic system comprises 768 transmitting elements and 768 receiving elements. To image the desired field-of-view, the transmitters are sequentially activated, and all the backscattered signals are detected by the receivers. After activating all the transmitters, the recorded signals are used to reconstruct the image using a back-projection algorithm [8]. Even

though this approach does not require a complex feeding network, the post-processing time is not negligible compromising the real-time imaging performance of the design.

III. Conclusion of Chapter 3

In this Chapter mmWave/THz imaging systems were briefly categorized based on their principles of operation as:

1) Imaging systems based on the field-of-view illumination scheme:
    a) Multistatic
    b) Monostatic
2) Imaging systems based on the image reconstruction method:
    a) Focused systems
    b) Inverse scatting systems

In Chapter 4, a technique to study mmWave/THz systems is presented. The proposed method can be leveraged to estimate the performance of an imaging system with the use of complex targets. Typically, configurations that include both the imaging sensor (e.g., quasi-optical setup) and the target (e.g., a mannequin), lead to resource-hungry simulation setups. Therefore, Chapter 4 presents a decomposition scheme that can numerically estimate the imaging performance of various hardware topologies and simplify the design process of radar imagers.

CHAPTER 4

Modeling of Large-Format Millimeter-wave and Terahertz Imaging Systems

The scope of this work is the development of efficient mmWave/THz systems that can serve both for imaging and communication applications. However, the study and modeling of such mmWave/THz systems, especially in imaging applications, is not trivial due to the small wavelengths that lead to extremely large electromagnetic models that include both the sensors and the complex test targets. These models are usually studied using semi-analytical techniques, but these approaches mask the actual performance of the system due to the incorporated mathematical approximations. Therefore, this Chapter presents, a numerical decomposition algorithm that enables the study of these complex systems using full-wave models, shedding light on their actual performance.

I. Existing techniques for modeling of large-format systems

Evaluating the performance of large-format multi-dimensional imaging systems requires the accurate modeling and simulation of the imaging sensor. Although, revealing the actual performance of such systems demands their evaluation in the presence of various targeting scenarios before proceeding with fabrication. However, modeling large-format imaging sensors in the presence of electrically large targets is not trivial computationally. For instance, calculating the scattered fields of a human phantom at 70 GHz requires at least a few million meshing elements for a single full-wave simulation [43]. To compensate for these computational obstacles hybrid and semi-analytical techniques are incorporated in the study of imaging systems, to reduce the required computational resources

[7][44][45]. Namely, in [7] a microwave metamaterial Synthetic Aperture Radar (SAR) was studied using a semi-analytical approach. Specifically, the fields of the sensor are initially calculated using an arbitrary linear array consisting of ideal point sources; then, these fields are propagated using the Born approximation and ideal point scatterers are considered as targets. Additionally, in [44] the performance of a standoff imaging system operating in the Ka-band is evaluated using a human body as a target. The simulation results presented in [44], were obtained using a Physical Optics (PO) simulator, which does not account for all the exhibited physical phenomena. Another study case for the evaluation of large format imaging systems is presented in [45], where a THz camera's performance is evaluated using hybrid algorithms that incorporate full-wave, semi-analytical, and analytical approaches. However, all the aforementioned examples are approximating scattering and propagation phenomena. Namely, when the object scene includes multiple internal reflections, speckle reflections, lossy materials, multiple dielectrics, and/or multi-layered materials, these approaches become inaccurate. Therefore, being able to use full-wave numerical tools in a computationally efficient method will benefit the design of several mmWave/THz imaging systems.

In the remainder of this Chapter, a hybrid computational algorithm is presented that incorporates the necessary full-wave numerical methods along with a domain decomposition approach, to accurately model large-format imaging systems aiming towards their performance evaluation.

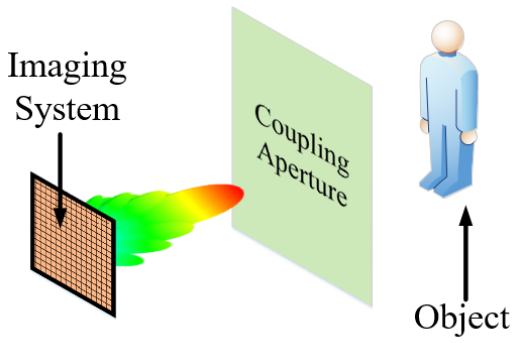

Fig. 4.1 The domains utilized to algorithm's schematic configuration. The fields are recorded on a fictitious aperture where the conjugate field coupling coefficient is computed.

II. Analysis of large-format imaging systems using a decomposition method

To overcome the aforementioned computational bottlenecks, an analysis algorithm is proposed that can be exploited for the study of large aperture imaging systems with multiple sensors (>100) and electrically large targets (e.g. $40\lambda_0 \times 40\lambda_0$). The mmWave/THz imaging system is modeled by an imaging sensor, an object, and a fictitious coupling aperture, as depicted in Fig. 4.1. Initially, the target is illuminated by an incident wave (e.g., plane wave) and the scattered fields are computed on the coupling aperture using a full-wave electromagnetic tool (MLFMM) [46]. Similarly, the fields formed by the imaging aperture (e.g., antenna array) are computed on the same aperture. Then, the image is synthesized by calculating the conjugate field coupling coefficient of the two field distributions on the coupling aperture using the following formula [39]

$$C_{(i,j)} = \int_S E_{rad(i,j)} \cdot E^*_{scat} dS \qquad (4.1)$$

where $C_{(i,j)}$ corresponds to the coupling coefficient of a certain beam (i,j), $E_{rad(i,j)}$ are the radiated fields of the (i,j) beam, and E_{scat} are the scattered fields of the object. As such, the image is formed by computing all conjugate coupling coefficients for every (i,j) beam direction/position

$$[\text{Image}] = \begin{bmatrix} C_{1,1} & . & C_{1,m} \\ . & . & . \\ C_{n,1} & . & C_{n,m} \end{bmatrix} \qquad (4.2)$$

This approach reduces the computational effort towards reconstructing the image since the scattered fields from the electrically large object are computed once. Moreover, the interaction between the imaging sensor and the target is assumed negligible.

The conjugate field coupling is well known in the electromagnetics community. Specifically, the conjugate field coupling coefficient is used in quasi-optical systems to evaluate the coupling between different Gaussian beams [39].

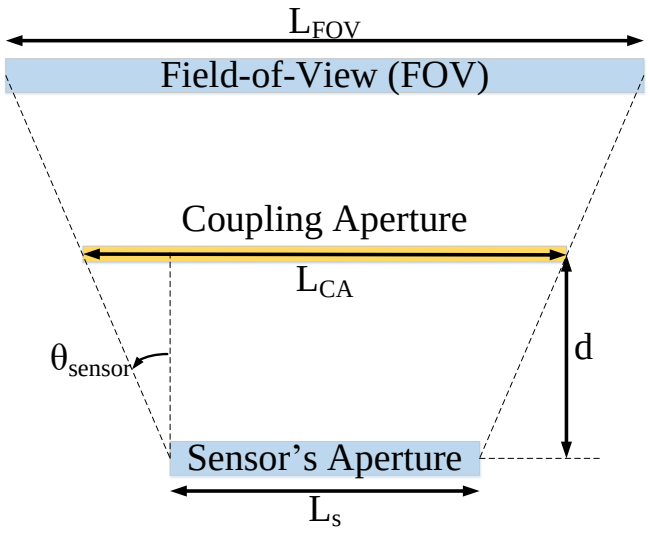

Fig. 4.2 The proposed algorithm's geometric configuration.

Furthermore, proper field sampling on the coupling aperture is crucial for robust computation of the conjugate coupling coefficients. For most imaging scenarios, the coupling aperture can be placed farther from the near-field of both the target and the sensor. However, according to [47], when the coupling aperture is in the near field region of a radiator ($L \leq D/\lambda_0$, where L is the distance from the radiator and D is the targeted aperture's diameter), field sampling must be $\lambda_0/2$ or denser. For large aperture imaging systems the objects can be within that limit, thus field sampling needs to be denser than $\lambda_0/2$. Namely, if the coupling aperture is within a few λ from the target or the sensor, the sampling should be much denser to account for the scattered evanescent fields [47]. Additionally, the size of the coupling aperture is directly related to the dimensions of the sensor's aperture and the FOV, as depicted in Fig. 4.2. As such, the diameter of the coupling aperture L_{CA} is defined by the subtended angle formed between the FOV and the sensor ($L_{CA}=L_S+2d\cdot\tan(\theta_{sensor})$), [47]. Finally, the distance and size of the coupling aperture do not affect the acquired coupling coefficient in (4.1), as long as, the aforementioned field sampling criteria are met.

A. Imaging sensor modeling

This section uses the proposed decomposition method to investigate systems that synthesize images mechanically using a raster scanning method, or systems that employ electronic beam scanning.

In raster scanning systems, a single pencil beam mechanically scans the object scene by physical displacement and synthesizes the image. The beam is typically formed by coupling a single mmWave/THz sensor with optical components (e.g., [5]). To carry

out the imaging process, the system's fields ($E_{rad(i,j)}$) are computed on the coupling aperture once. Moreover, the object is illuminated by a plane wave, and the backscattered fields (E_{scat}) are also computed on the coupling aperture. Then, the single-pixel response of the system is calculated using the conjugate field coupling (4.1). Finally, this step is repeated by translating the sensor's fields ($E_{rad(i,j)}$) to every position of the sensor, thus forming a 2D image using (4.2). This raster scanning process is carried out in post-processing since the radiated/receiving beam of the system ($E_{rad(i,j)}$), is irrelevant to its position.

On the other hand, electronic scanning systems, synthesize the image by electronically scanning the beam direction of the fixed-positioned sensor to achieve the illumination of each pixel (e.g. [7][8]). For such systems, the image reconstruction is achieved by: 1) calculating the radiated fields of the sensor ($E_{rad(i,j)}$) on the coupling aperture for every angle/pixel to account for beam aberrations, 2) calculating the backscattered fields (E_{scat}) form the target scene once, and 3) computing the conjugate field coupling (4.1) for every beam direction. Finally, the image is reconstructed using (4.2).

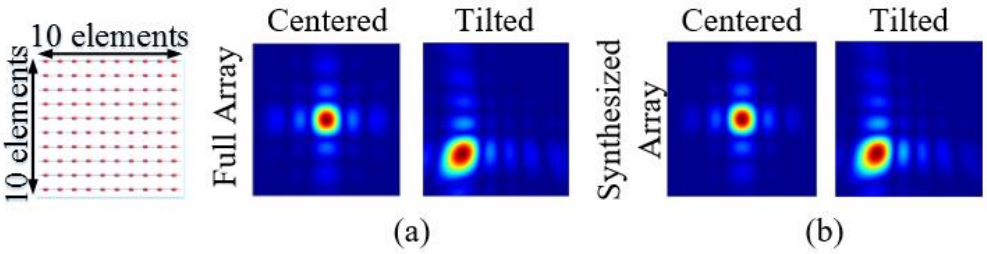

Fig. 4.3 Field distribution on the coupling aperture located $50\lambda_0$ for (a) a 10×10 planar phased array and (b) a synthesized 10×10 phased array.

Imaging systems comprise large aperture sensors typically consisting of multi-element sensors (phased arrays [9]) or quasi-optical components (mirrors, reflectors, etc.

[5]). The study and modeling of quasi-optical sensors is more computationally demanding than the study of phased arrays. However, in the latter case, where multi-element phased arrays are involved, the computational method must account for the beam deformation that occurs at wide tilt angles.

This Chapter focuses on large scale 2D planar phased arrays consisting of dipoles. However, simulating a multielement array (e.g., 80×80) is very resource demanding. Thus, the radiated fields on the coupling aperture are synthesized using a single antenna's fields, based on the array factor as

$$E_{rad} = E_{element} \cdot AF = E_{element} \cdot AF_x \cdot AF_y \qquad (4.3)$$

where, $E_{element}$ are the radiated fields of the single element antenna and AF_x and AF_y the array factors in $\boldsymbol{x}$ and $\boldsymbol{y}$ axes, respectively, given by (2.1). This approach does not account for the mutual coupling between the elements of the full array; however, this effect has a minimal impact on the field calculation and can be considered negligible for most imaging applications.

The computed radiated fields of a 10×10 planar phased array are presented in Fig. 4.3, alongside the synthesized radiated fields using (4.3). The synthesized radiated fields are in excellent agreement with the fields of the full phased array. Using (4.3), large-format phased arrays can be simulated allowing the study of large aperture imaging systems.

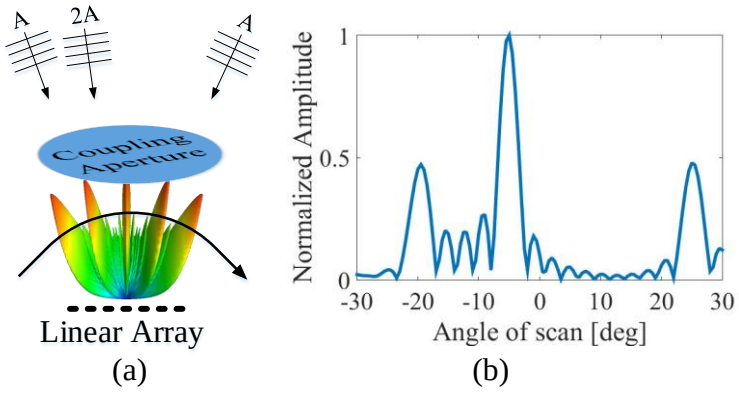

Fig. 4.4 Proof of concept for 1D imaging. (a) Three plane waves are incident on an antenna array from directions -20º, -5º, and 25º and with magnitudes *A*, *2A*, and *A*, respectively. (b) The plot of the conjugate coupling coefficient along the ±30º FOV. The magnitude and position of the three peaks are directly related to the corresponding incident plane waves.

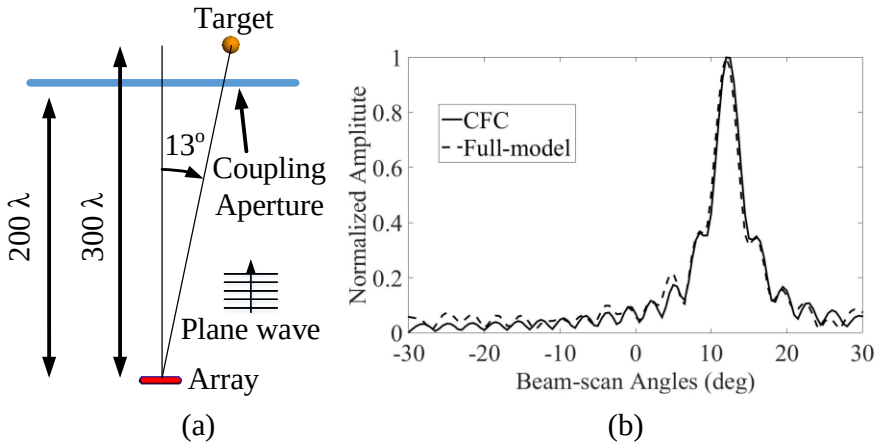

Fig. 4.5 1D imaging example. (a) One sphere is located at 13º from the broadside direction of the antenna array. (b) Comparison of CFCC for the ±30º FOV and the received signal using the full-model simulation for a 40-element array.

B. Imaging discrete illumination sources

To evaluate the validity of the concept two one-dimensional imaging examples are studied. As such, in the first case, the magnitude and direction of three incidence plane-

waves are tracked, as depicted in Fig. 4.4. A 40-element (Nyquist sampled), 300 GHz, linear phased array is used to scan a fan beam within a 60^o FOV. Firstly, the radiated fields are computed for every beam angle (121 beams in total) on the coupling aperture located $90\lambda_0$ from the array. Afterward, the fields of three plane waves are calculated on the same aperture. Using (4.1) the coupling coefficients C_i for all 121 directions are calculated as plotted in Fig. 4.4b. The location and magnitude of the three peaks correspond to the three incident plane-waves.

In another example, the afore used linear 40-element array is utilized in a single sphere imaging scenario, as shown in Fig. 4.5. To carry out the imaging, the radiated fields for every beam angle (121 beams) are initially computed on the coupling aperture located $200\lambda_0$ from the array. Afterward, the object scene is illuminated by the plane wave and the scattered E-field distribution on the same aperture is calculated. Using (4.1) the coupling coefficients C_i for all 121 directions are calculated and plotted in Fig. 4.5b. In the same figure, the results obtained using the full-model simulation, where both the sphere and the imaging array are included, are presented. As shown, the results are in very good agreement with the full-model simulations (average absolute error of 0.0237).

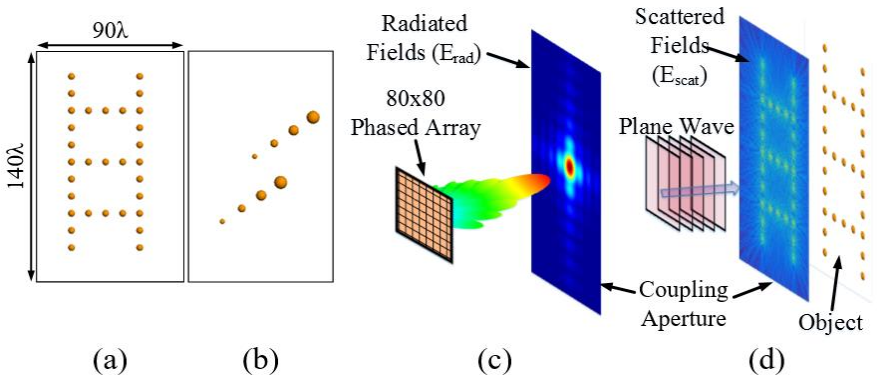

Fig. 4.6 Imaging of an electrically large field of view: (a) 32 PEC spheres and (b) 8 variable sized spheres. The imaging system model decomposed into: (d) the imaging sensor simulations and (c) the illumination of the object with a plane wave.

III. Computed images of large-format imaging systems

This section presents imaging examples of electrically large FOVs for electronic beam scanning and mechanical raster scanning systems. In the first example, a 60 GHz phased antenna array system that utilizes electronic beam scanning to image phantom objects is investigated, as depicted in Figs. 4.6a and 4.6b. The FOV is $140\lambda_0 \times 90\lambda_0$ sampled by 735 beams, which also corresponds to the total number of pixels in the mmWave image. The imaging sensor is comprised of an 80×80 2D phased array of dipoles with $\lambda_0/2$ spacing. The radiated fields of the array are calculated using (4.3) and the coupling aperture is placed $400\lambda_0$ from the array and the object, respectively. The field sampling on the coupling aperture is $\lambda_0/2$ to satisfy the criteria given in [47]. The exemplary target consists of 31 PEC spheres of $6\lambda_0$ in diameter spaced every $8\lambda_0$, as shown in Fig. 4.6a. The image is computed using two steps, as shown in Fig. 4.6c and 4.6d. Initially, the phased array is simulated using the synthesis approach discussed in section 4-II-A, and the radiated fields

on the coupling aperture are calculated using (4.3) (Fig. 4.6c). Also, the target scene is illuminated by a plane wave and the scattered fields are calculated on the same aperture (Fig. 4.6d).

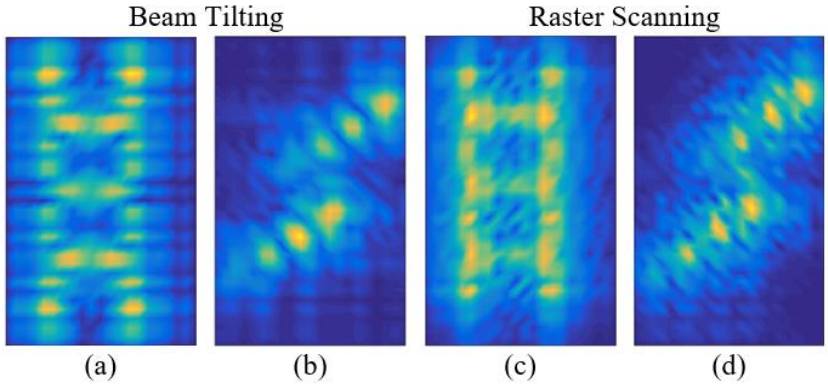

Fig. 4.7 Imaging of the objects shown in Fig. 4.6: (a) and (b) Using beam steering. (c) and (d) Using raster-scanning.

The simulated image is depicted in Fig. 4.7a and is synthesized by calculating the conjugate coupling (4.2) between the fields of the target and the array for each pixel. Similarly, the image for the target of Fig. 4.6b is acquired and presented in Fig. 4.7b. In this case, the object scene (Fig. 4.6b) consists of 8 spheres of various sizes ($4\lambda_0$, $6\lambda_0$, $8\lambda_0$, and $12\lambda_0$) to test the imaging performance of the system. As expected, the smaller sphere is hardly visible due to its small radar cross-section (RCS). The interference pattern artifacts presented in Fig. 4.7 are a result of the complex wave propagation and diffraction phenomena and are accurately modeled because of the full-wave numerical computations.

The second case study is a raster scanning system that uses a single narrow beam to mechanically scan the FOV (raster-scanning). A fixed direction beam is formed by an 80×80 2D phased array, though optical components can also be used to form a pencil beam.

Thus, the array beam fields are calculated once on the coupling aperture for broadside illumination. Afterward, the simulated fields are translated across the FOV with a pitch of $8\lambda_0$ and the conjugate coupling coefficient is calculated for each position (4.2), leading to 735 pixels. Finally, the resulting images of the objects are depicted in Figs. 4.7c and 4.7d. As expected, the raster scanning artifacts are substantially different than using beam-tilting systems due to the beam aberrations and angle of incidence.

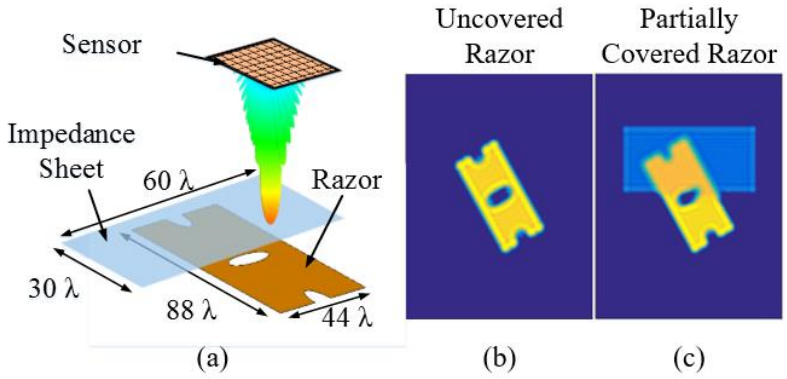

Fig. 4.8 (a) The imaging scenario of partially covered a metallic (PEC) razor at 600 GHz using raster scanning. (b) The radiated fields of the imaging sensor (c) and (d) The final reconstructed image of the uncovered and the partially covered razor, respectively.

In another raster-scanning example, the image of a partially covered metallic razor at 600 GHz is recorded, as shown in Fig. 4.8. The implemented pencil beam's HPBW is 5^o on both E- and H- planes and the beam fields are calculated using (4.3). Similarly, in this scenario, the image is acquired by displacing the sensor's fields and calculating the conjugate field coupling coefficients (4.2). The synthesized images of the uncovered and the partially covered razor are given in Fig. 4.8b and 4.8c, respectively, and highlight the proposed technique's capability to model complex imaging scenarios with multiple lossy reflectors.

Finally, a 3D imaging example is presented, similar to frequency-modulated-continuous-wave (FMCW) radars, to highlight the capability of the method to efficiently model multi-dimensional imaging systems. As such, two metallic spheres are placed at different distances from an 80×80 2D beam scanning phased array sensor, as shown in Fig. 4.9a and 4.9b. Following the aforementioned computation steps, the images are synthesized for several frequency points in the 55-65 GHz band (every 250 MHz). Applying the inverse Fourier Transform on the multi-spectral images, the relevant position of the spheres is obtained, and a 3D representation of the scenery, as depicted in Fig. 3.9c-d.

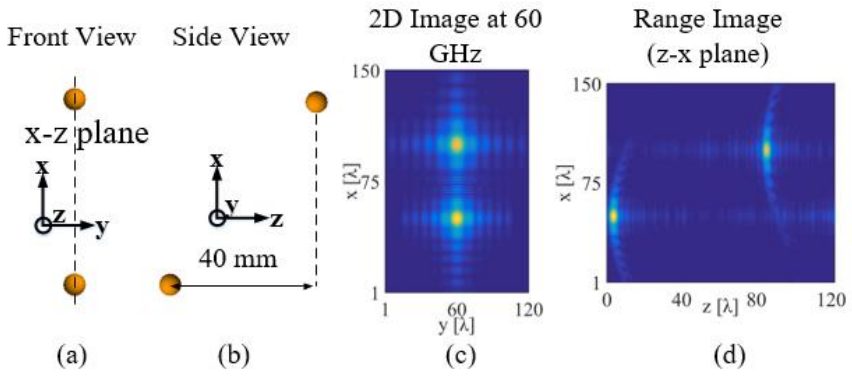

Fig. 4.9 (a) The 3D imaging scenario (front view) consisting of two PEC spheres ($6\lambda_0$ radius). (b) The side view of the same configuration, the spheres separation distance is 40 mm. (c) The 2D reconstructed image at the center frequency (60 GHz) and (d) The reconstructed range image (**z-x** plane).

The efficiency of the presented method is summarized in Table 4.1 with a comparison between the proposed technique and the classical approach. In the classical approach, the total system comprised of the sensor and the target is simulated for each pixel using a full-wave tool, leading to a series of computationally intensive simulations. The tabulated data suggest that using a classical approach to study multi-pixel imaging systems

can be prohibitive, especially when multiple frequency points or multiple frames need to be computed. The total number of hours needed using full-wave simulations was extracted by solving just a handful of the total 735 pixels to estimate the per-pixel simulation time.

Table 4.1

Comparison between the conventional and the proposed method for the object of Fig. 4.4a

Quantity	Conventional Simulation	Proposed Technique	
Pixels	735	735	
Mesh Size	421,124	Array	1,120
		Target	415,524
Total Simulation Time	1,249.5 hours (estimated)	Array	3 hours
		Target	1.6 hours
Improvement Factor	271		

IV. Conclusion of Chapter 4

In this Chapter, a novel method for the analysis of large-format mmWave/THz imaging systems is presented and validated through a series of numerical results. Computational accuracy is achieved using full-wave numerical methods only for solving the most complex electromagnetic phenomena, such as beam formation and wave scattering on the objects. Therefore, the imaging sensor radiated fields and object scattered fields are computed using a full-wave electromagnetic solver (MLFMM). Finally, the image is synthesized by finding conjugate field coupling coefficients on a fictitious aperture between the object and the imaging sensor. By decoupling the two domains 721

times faster analysis is achieved for FOVs larger than $140\lambda_0 \times 90\lambda_0$ sampled by 735 pixels. Therefore, the proposed technique constitutes a robust tool for the analysis of multi-dimensional, large format imaging systems. This algorithm enables the full-wave study of broadband-video imaging systems in mmWave/THz frequencies. As such, the proposed method is used for the study of a multistatic, compact, imaging system, presented in Chapter 5.

CHAPTER 5

Multistatic Terahertz Imaging Using the Radon Transform

This Chapter presents a low-profile configuration that performs high-spatial-resolution 3D imaging while retaining a simplified-compact RF front-end. The recent advances in integrated circuits for mmWave/THz applications [48]-[50], along with sparsity techniques [14], and efficient image reconstruction algorithms [51][52], can be exploited to design a low-profile, compact imaging system, as the one proposed herein. Unlike the imaging systems presented in Chapter 1, the proposed imaging configuration utilizes a combination of mechanical rotation and electronic beam scanning to synthesize a large aperture, thus performing fast high-spatial-resolution imaging. The proposed configuration can be used in security, surveillance, and earth observation applications.

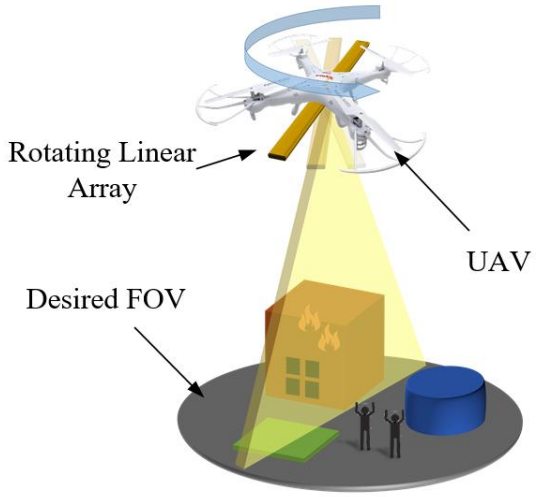

Fig. 5.1 An application example of the proposed system, comprised of a rotating linear phased array.

Specifically, the proposed system carries out imaging by mechanically rotating the linear antenna around its center, while electronically scanning the fan-beam on the radial direction (Fig. 5.1). Then, the image is synthesized by applying a back-projection algorithm [52] on the recorded signals. As such, the imaging approach allows for a low-profile, lightweight, and cost-effective topology that can be attractive for several mmWave and THz imaging applications. As depicted in Fig. 5.1, the proposed sensor can utilize the capability of certain UAVs to rotate (yaw axis) and provide rapid image acquisition. This Chapter thoroughly describes the theoretical background of the imaging method and presents the incorporated sparsity approaches to further reduce the total number of antenna elements. Finally, a signal-to-noise ratio study is carried out to compare the performance of the proposed imaging system with conventional phased array setups.

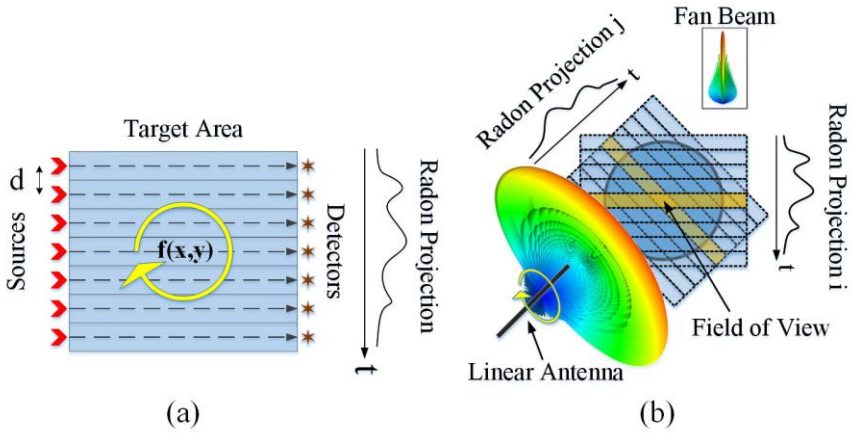

Fig. 5.2 The analogy between CT and THz imaging. (a) Tomography utilizes parallel beams propagating through the object and (b) the proposed imaging radar configuration uses a highly directive fan beam to record the backscattered signals from the FOV. Using a linear phased array, the fan-beam is electronically scanned across the FOV. In both configurations, mechanical rotation is required to record the necessary Radon projections.

I. Radar image synthesis using the projection slice theorem

The proposed radar-imaging configuration employs the projection-slice theorem to reconstruct 2D and 3D images exploiting the radiation characteristics of a rotational linear antenna array. The imaging process and the mathematical reconstruction algorithm of the proposed method are inspired by computerized tomography (CT) systems. Thus, it was decided to present the proposed configuration alongside the basics of CT systems to help with comprehension. Initially, the image reconstruction procedure followed in X-ray CT is presented, as illustrated in Fig. 5.2. As such, in a simplified version of CT systems, a set of parallel X-rays propagate through the object under test (OUT) and a linear detector array records the signals on the opposite side [52]. Each ray is attenuated depending on the material properties along the straight propagation path and the recorded signals comprise the Radon Transform for a given angle. Mathematically this is described by the following equations [52]

$$P_\theta(t) = \int_{(\theta,t)line} f(x,y)\, ds \;\forall\; \theta \qquad (5.1)$$

and

$$\begin{bmatrix} t \\ s \end{bmatrix} = \begin{bmatrix} \cos\theta & \sin\theta \\ -\sin\theta & \cos\theta \end{bmatrix} \begin{bmatrix} x \\ y \end{bmatrix} \qquad (5.2)$$

where *f(x,y)* represents the OUT reflectivity, $P_\theta(t)$ is the Radon Transform (RT) at projection angle θ, and *t* is the axis of the projection (Fig. 5.2a). Note that the rotation is performed from 0^o to 180^o since additional projections will result in redundant information. In CT systems, the integration corresponds to the ray attenuation along the propagation path. As such, the detected signals are strictly correlated with the properties of each path

and correspond to the Radon projection (RP) of the object for a given observation angle (Fig. 5.2a).

After obtaining a single projection, the system is rotated, and another projection is recorded. For a properly sampled image, the number of parallel rays (N_{rays}) should be approximately equal to the number of projections ($N_{projections}$) [52].

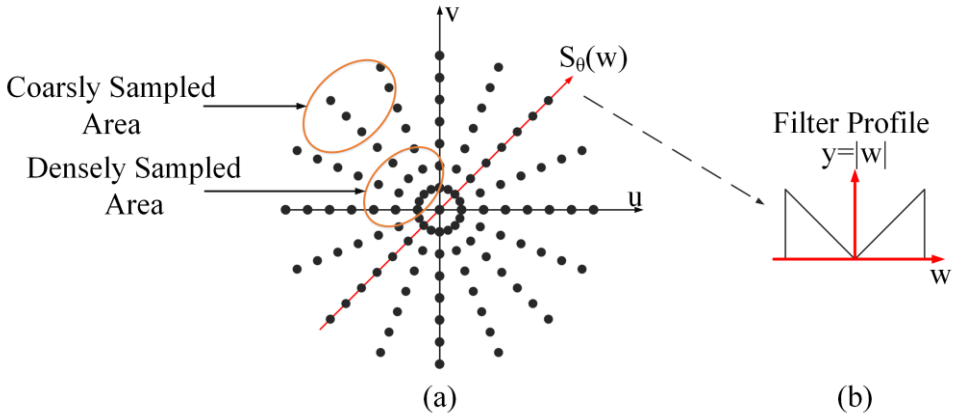

Fig. 5.3 After recording the Radon projections, the Fourier Transform of each RP $S_\theta(w)$ is calculated, which lies along different radial directions (red line), thus, resulting in a non-uniform sampling of the frequency space ($u=w\cdot cos\theta$ and $v=w\cdot sin\theta$). The frequency-domain image is corrected by filtering, as depicted, in (b) [52].

After recording all the necessary Radon projections, the Fourier Transform on the acquired projections is performed [52]

$$S_\theta(w) = \int_{-\infty}^{\infty} P_\theta(t)\, e^{-j2\pi wt} dt \;\; \forall \;\; \theta \qquad (5.3)$$

where $P_\theta(t)$ is the projection for an angle of θ, w is the spatial frequency, and t is the projection axis. Equation (5.3), corresponds to a slice on the original 2D Fourier Transform of the image $f(x,y)$. Reconstructing the image using the Inverse Fourier Transform on the

frequency domain will result in image artifacts due to the non-uniform sampling of the frequency space, as depicted in Fig. 5.3a. Thus, to ensure the accurate image reconstruction, a filtered back-projection (FBP) technique is used [52]

$$f(x,y) = \int_0^{\pi}\left[\int_{-\infty}^{\infty} S_\theta(w)|w|e^{j2\pi wt}dw\right]d\theta \quad (5.4)$$

where the term in the brackets represents the filtered Inverse Fourier Transform of $S_\theta(w)$. Using a uniform weighting along the irregularly spaced frequency points, the artifacts on the reconstructed image are reduced [52]. The profile of the ramp filter (Ram-Lak [52]) is depicted in Fig. 5.3b.

Although the projection-slice theorem has been mainly used for cross-sectional or 3D imaging in medical diagnosis [52], it has also found applications in 2D radar imaging. For example, spotlight synthetic aperture radars (SARs) [53], employ a modified Inverse Radon Transform to reconstruct terrain images based on the scattered wavefronts. However, spotlight SAR is a slow image acquisition method that uses spectral information of the scattered fields to apply the projection-slice theorem and reconstruct 2D images, thus limiting the performance of the system in 2D terrain imaging. Conversely, the proposed imaging method can perform single frequency 2D imaging or 3D cross-range imaging by exploiting the spectral information as shown in the latter sections.

Contrary to CT systems, the proposed method images the FOV using waves that are scattered on the object's surface. As such, a linear antenna array produces a highly directive steerable fan-beam that illuminates only strips on the object and receives the backscattered signal, as shown in Fig. 5.2b. Such highly directive fan-beams can be produced by multi-element linear phased arrays, reflective surfaces, leaky wave antennas

(LWAs), etc. The parallel strip scan is performed by electronically sweeping the fan-beam and each measured signal corresponds to a single projection point for a given rotation angle (Fig. 5.2b). After the electronic beam scan is completed, the array is rotated, and the beam sweep is repeated. As such, the proposed active radar imaging method corresponds to the Radon Transform of the FOV reflectivity, $f(x,y)$, as in (5.1).

Although the configuration requires both electronic and mechanical scans, this combination can provide fast image acquisition compared to strictly mechanical scanning systems (e.g., [5]), since the electronic sweep is completed much faster than the mechanical, while reducing the RF front-end complexity.

II. Radar imaging using a multistatic linear array

In this section, the numerical analysis of the proposed imaging scheme is presented, alongside a series of computational images is generated, using a multistatic linear antenna array.

A. Imaging system topology

To test the performance of the proposed imaging configuration a rotating multistatic linear antenna is used to produce a steerable fan beam. The beamforming of the fan beam is carried out in the digital domain (DBF) as explained in Chapter 2-I. Multistatic configurations perform imaging by deploying transmitting elements that illuminate the FOV and a series of receiving antennas that capture the backscattered signals. Then the image is reconstructed using DBF, by numerically scanning the beam at different

directions. Accordingly, in this case study, a multistatic setup that uses a single element to illuminate the desired FOV and a series of antennas for the receiving array is deployed.

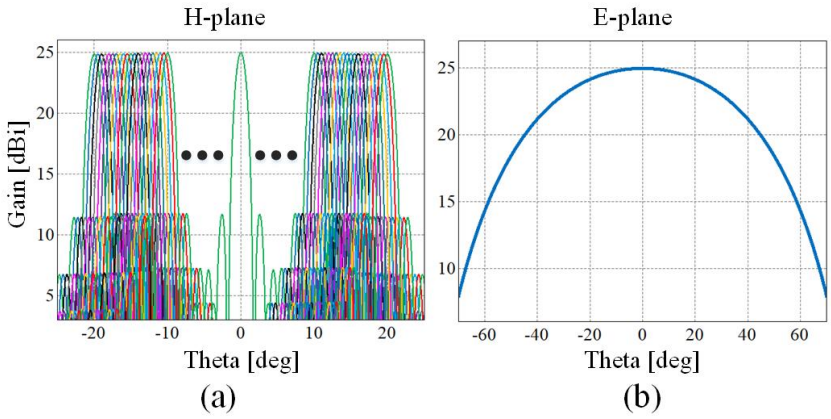

Fig. 5.4 (a) The H-plane radiation patterns of the 64-element receiving linear phased array. The horizontal axis represents the elevation angle (0^o for boresight illumination) and the vertical the gain in dBi. The 81 beams are obtained by appropriately scanning the inter-element phase difference. (b) The E-plane radiation pattern of the 64-element linear phased array.

The aperture sensor in this case study is comprised of a uniform linear phased antenna array of 64 half-wavelength dipoles placed $\lambda_0/4$ on top of an infinite ground plane. The interelement distance is $\lambda_0/2$ (Nyquist sampling) and the design frequency is 300 GHz. As such, a highly directive fan beam is formed, as depicted in Fig. 5.4. Namely, the H-plane and E-plane HPBWs are ~1.68^o and ~72.43^o, respectively. A single transmitting dipole antenna is used for scene illumination and the fan beam is scanned from $\pm 20^o$, leading to a circular FOV of 40^o in diameter.

B. 1D projection imaging

To test the angular resolution of the proposed configuration, the Radon projection of a perfect-electric-conductor (PEC) sphere is captured for a single rotational angle θ from

the center of the linear antenna array. The 1D imaging configuration is depicted in Fig. 4.5a and is simulated using MLFMM [46] along with the hybrid algorithm for the analysis of large-format imaging systems presented in Chapter 4. To extract the information within the FOV, a set of 30 orthogonal beams [54] could be used, however, to accurately extract the position of all targets in the reconstructed image it was decided to use denser sampling with 81 beams [55][56]. By increasing the number of sampling beams, the position of small targets is accurately detected (e.g. point scatterers), since, the probability of aligning the maximum of the scanned beams with the direction of the target is higher [56] (more than 80% in this case study). This increase in the number of beams is not translated to an increase in the hardware complexity since the beam scanning is carried out in post-processing domain using DBF. If the angular resolution is limited by hardware (e.g. digital phase shifters in analog beamforming), the minimum number of orthogonal beams should be used (31 for this case study), to retain low RF-front-end complexity.

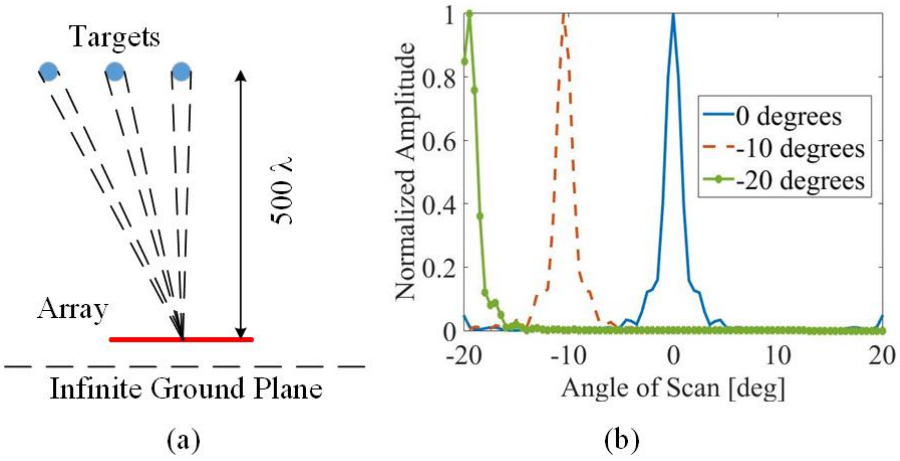

Fig. 5.5 (a) 1D imaging of $20\lambda_0$ diameter PEC spheres. The objects are placed on the H-plane at $500\lambda_0$ above the dipole array. Three different configurations are simulated: centered, -10 degrees, and -20 degrees at the edge of the FOV. (b) The acquired 1D projections.

In this case study, imaging is performed by scanning the fan-beam using DBF and directly calculating the data points at different angles. Figure 5.5b shows the 1-D image reconstruction (Radon Projection) of a sphere placed at three different positions within the 40-degree FOV.

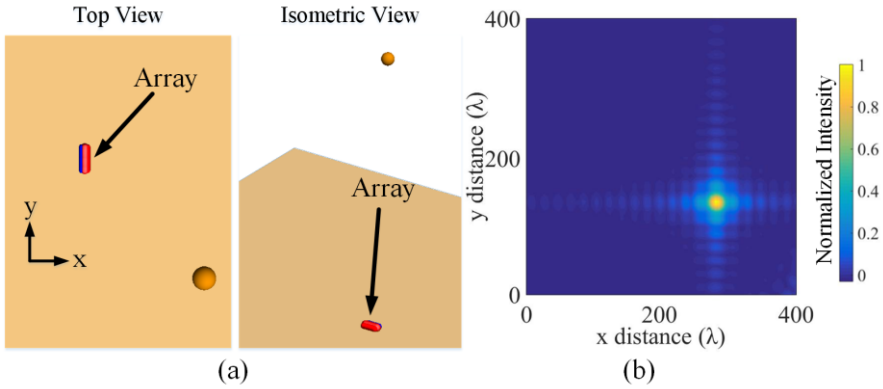

Fig. 5.6 (a) The top and the isometric view of the 2D scene containing a single PEC sphere at a distance of $500\lambda_0$ and (b) image acquired using a 64×64 2D planar phased array.

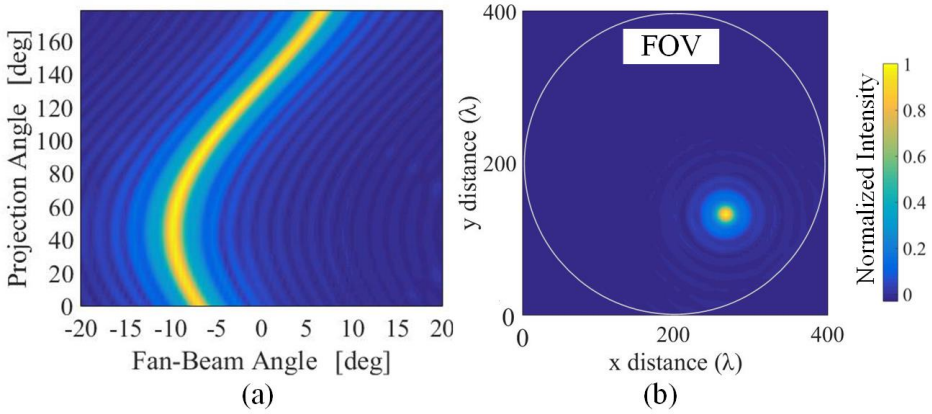

Fig. 5.7 Full multistatic linear array imaging: (a) The sinogram of the single sphere imaging setup (Fig. 5.6a). The horizontal axis corresponds to the projection axis t and the vertical to the projection angles θ (Fig. 5.2). (b) The reconstructed image using the FBP (5.4).

III. 2D imaging using a full multistatic linear array

To study the 2D imaging performance of the proposed technique, the scenario of Fig. 5.6a is simulated. In this setup, a $10\lambda_0$-radius PEC sphere is placed $500\lambda_0$ above the array plane. Each projection is comprised of 81 beam scans and the total number of projections is 81, resulting in 81×81=6,561 data points. These points are depicted in the sinogram of Fig. 5.7a, where the beam scans of all 0^o-180^o projections are plotted.

Finally, the acquired projections are used to synthesize the 2-D image of the sphere using the FBP (5.4), as depicted in Fig. 5.7b. The shape and correct location of the target is imaged inside the FOV, the diameter of which is determined by the fan-beam scanning range (-20^o to $+20^o$).

Additionally, to validate the proposed system's imaging performance, the scenario of Fig. 5.6a was imaged using a 2D multistatic phased array consisting of 64×64 receiving ($\lambda_0/2$ spacing) and one transmitting antenna. The imaging scheme is performed by illuminating the FOV with the transmitting antenna and recording the backscattered signals at every receiving element. Then, the pencil beam is electronically scanned at different directions using DBF and the calculated signals are directly used to reconstruct the image shown in Fig. 5.6b. In total, 812 beam directions are simulated, leading to 6,561 pixels.

Hence, from observing Figs. 5.6b and 5.7b it is concluded that the imaging resolution of the proposed system, comprised by a rotating linear array of 64 elements, is the same as the one using a 2D planar phased array of 64^2 elements. Thus, the reduction of the total number of elements achieved is N, where N is the number of elements across the linear array.

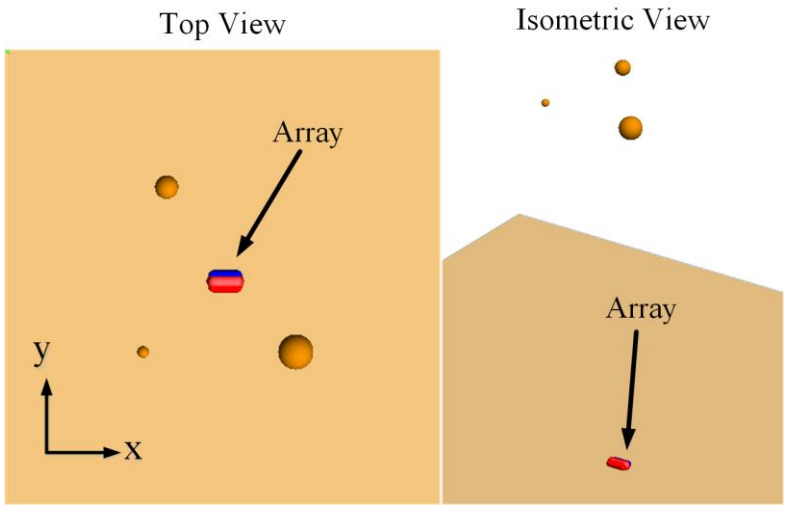

Fig. 5.8 (a) The top view of the 2D scene with three PEC spheres at $500\lambda_0$ and (b) the isometric view of the system.

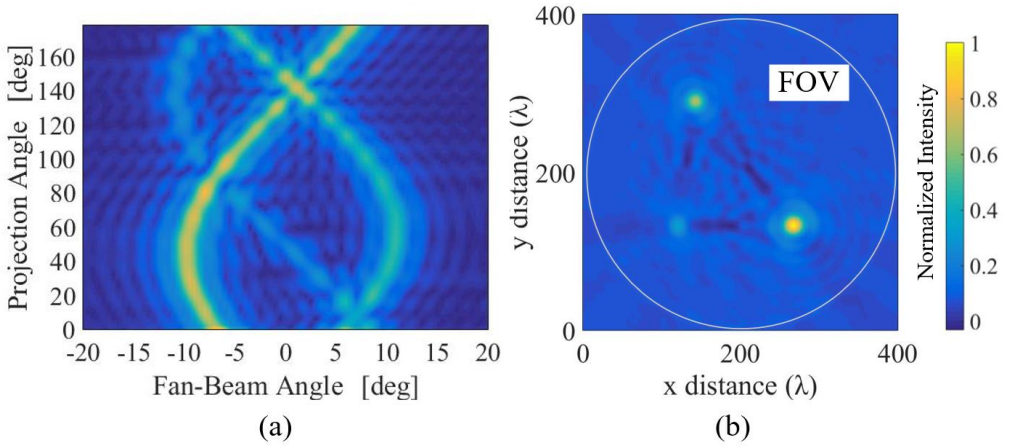

Fig. 5.9 Full multistatic linear array imaging: (a) The sinogram of three PEC spheres (Fig. 5.8a). The horizontal axis corresponds to the projection axis t and the vertical to the projection angles θ (Fig. 5.2). (b) The reconstructed image using the RT (5.4).

Finally, a multiple sphere scenario is analyzed to study the imaging performance for multiple objects with variable dimensions, as depicted in Fig. 5.8. Therefore, three spheres are used in this scenario with a diameter of $10\lambda_0$, $20\lambda_0$, and $30\lambda_0$, respectively. Fig.

5.9 depicts the respective sinogram of the FOV and the reconstructed image. As expected, the reflected signal strength and radius of the reconstructed objects correspond to the size variation of the spheres.

IV. 3D image reconstruction using the Radon Transform

Depth information can be recovered in continuous-wave imaging systems by acquiring 2D images at multiple frequency points. As such, applying the Inverse Fast Fourier Transform (IFFT) on the 2D images results in a 3D image reconstruction [41]

$$f_{3D}(x,y,z) = IFFT_{1D}\{f_{2D}(x,y,\omega)\} \qquad (5.5)$$

where $f_{2D}(x,y,\omega)$ is the complex-valued 2D image at radial frequency ω. However, the 2D images reconstructed using the Radon Transform are real-valued [52], hence, (5.5) cannot be directly used. To address this issue, the procedure illustrated in Fig. 5.10 is followed. As such, the multi-frequency Radon Transform (5.1) of the FOV (Fig. 5.10a) is initially acquired, where each of the measured points on the sinogram is a complex number. Then, the sinograms are Transformed from the frequency domain to range using IFFT (5.5). Finally, the 3D image is reconstructed using the 2D back-projection algorithm (5.4) for every range point as shown in Fig. 5.10c. The depth spatial resolution is determined by the bandwidth $dz=c/2\cdot BW$ (c is the speed of light), and the maximum resolvable distance by the frequency step $Z_{max}=c/2\cdot df$ [41].

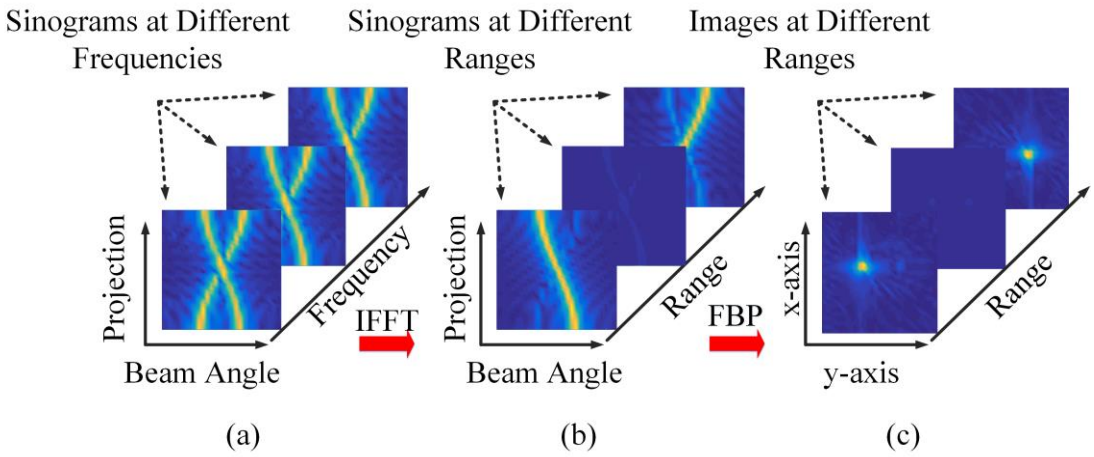

Fig. 5.10 The procedure followed to reconstruct 3D images using the Radon Transform. (a) The 2D sinograms for multiple frequency points, (b) the 2D sinograms for different ranges, and (b) the reconstructed images using filtered back-projection.

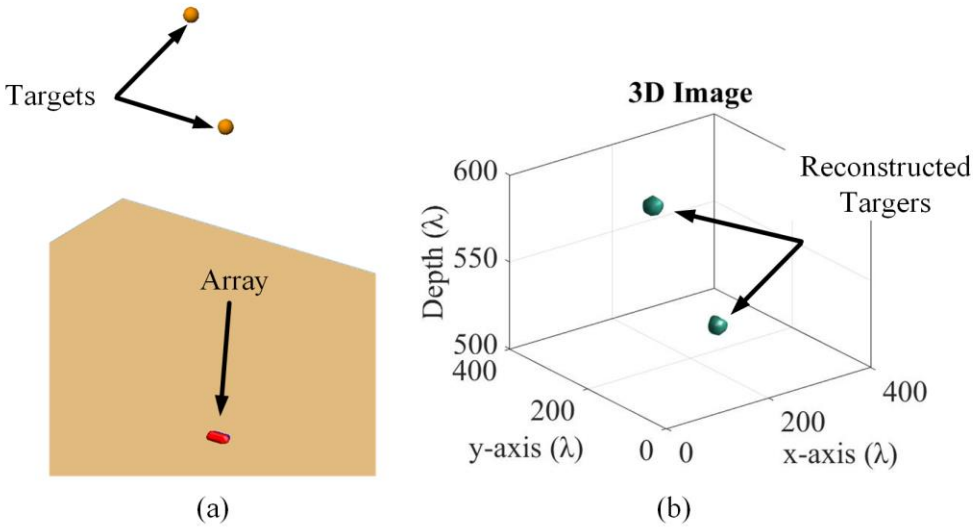

Fig. 5.11 (a) The 3D imaging configuration consisting of two spheres as targets at different distances ($520\lambda_0$ and $570\lambda_0$, respectively) from the linear sensor and (b) the 3D reconstructed image.

To demonstrate the 3D imaging capabilities of the proposed scheme, a case study imaging is carried out consisting of two spheres located at different distances within the FOV, as depicted in Fig. 5.11. To reconstruct the range of the FOV, we recorded the images for 11 different frequencies within the 295-305 GHz spectrum (1 GHz step). After acquiring the 2D complex sonograms for each frequency, (5.5) was used to Transform them into range. Finally, the 3D was reconstructed using Radon Transform on each of the sinograms.

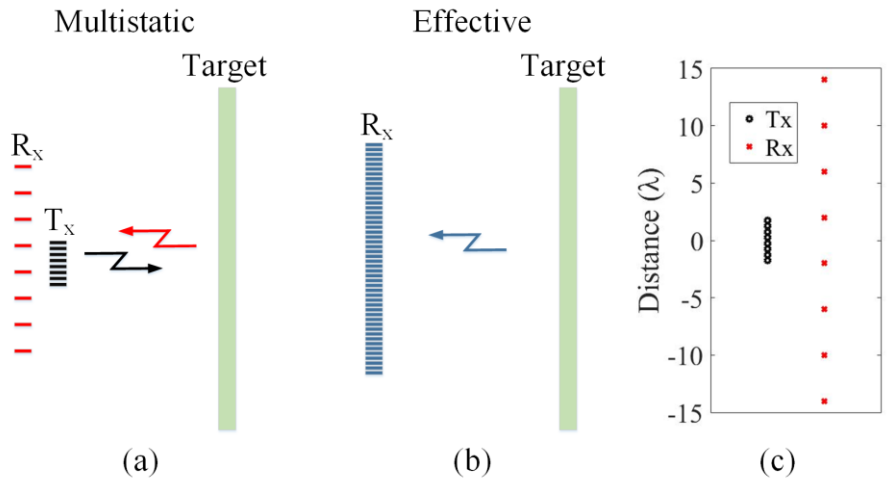

Fig. 5.12 (a) The proposed multistatic sparse imaging system configuration, (b) the effective array (Nyquist sampling), and (c) the simulated sparse multistatic setup consisting of 8 transmitting and 8 receiving elements.

V. Radar imaging using rotating sparse multistatic arrays

The aforementioned configuration is capable of performing 2D and 3D high-spatial-resolution imaging using full multistatic linear arrays. However, implementing a compact, integrated system in the mmWave/THz range using multiple antenna elements (e.g., slot dipoles or other low-profile radiators) is non-trivial as explained in Chapter 2,

due to the incorporated RF circuitry. Therefore, reducing the total number of used elements in the array, while retaining the same spatial resolution, is critical. For this purpose, the full multistatic setup used in section 5-II is replaced by a sparse multistatic setup as shown in Fig. 5.12a and 5.12b. In this example, the sparse setup is implemented by two uniform arrays comprised of 8 transmitting ($\lambda_0/2$ spacing) and 8 receiving ($4\lambda_0$ spacing) elements, respectively (Fig. 5.12c). In Fig. 5.13 the array factor (AF) patters for the sparse multistatic and the full multistatic are given. The effective array is composed by applying the spatial convolution between the transmitting and the receiving array [14], resulting in an equivalent 64 element uniform linear array ($\lambda_0/2$ spacing)

$$E_{eff}(\theta,\varphi) = E_{transmitter}(\theta,\varphi)\cdot E_{receiver}(\theta,\varphi) \qquad (5.6)$$

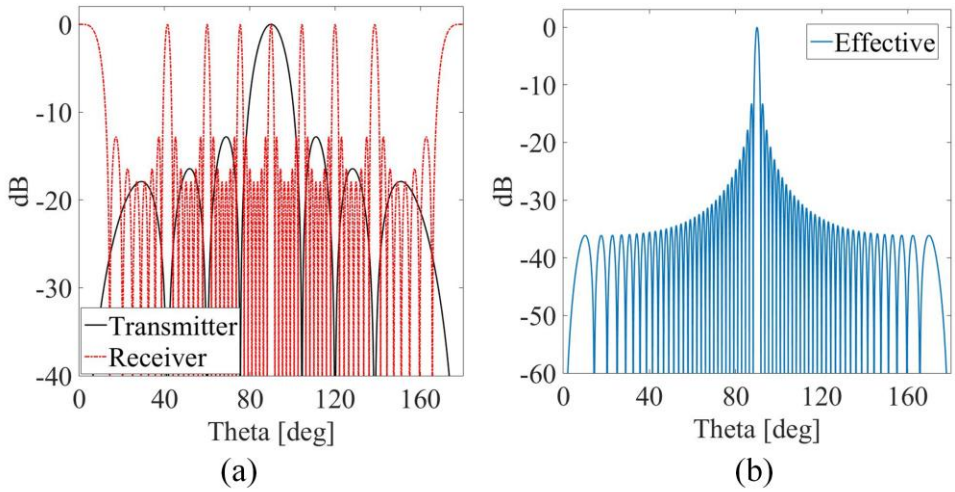

Fig. 5.13 (a) The AF of the multistatic setup. It is important to note that the maximums of the grating lobes of the sparsely populated receiving array coincide with the nulls of the Nyquist sampled ($\lambda_0/2$) linear array. (b) The AF of the effective monostatic 64 element linear array ($\lambda_0/2$ spacing).

By applying this sparse multistatic approach, the total number of elements is reduced to 16 (8 transmitting and 8 receiving) from the original 64 in the full multistatic array case (section 5-II). This reduction enables the implementation of a low-profile compact imaging sensor that provides high-spatial-resolution images while maintaining a handful of elements compared to the full multistatic 2D planar array consisting of 64^2 elements or the 64-element rotating linear array.

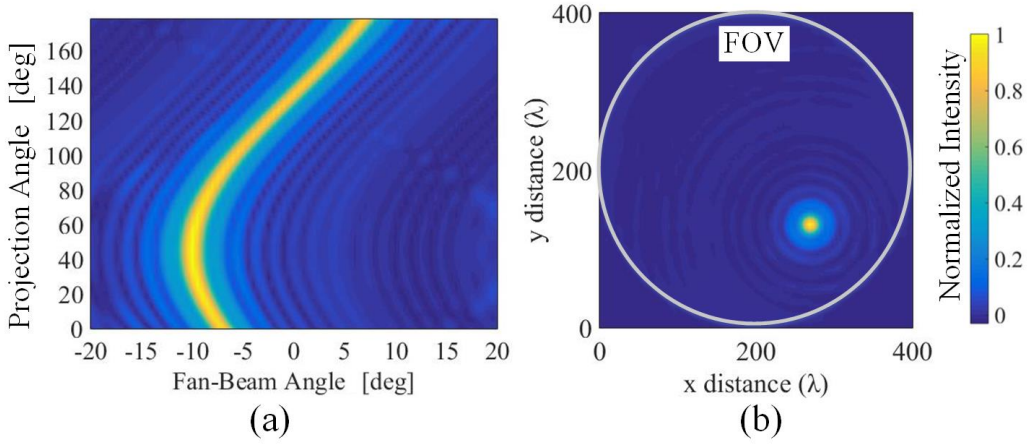

Fig. 5.14 (a) The sinogram of the target in Fig. 5.6a, recorded using the sparse multistatic array of Fig. 5.12c. The horizontal axis represents the projection axis t and the vertical is the projection angle θ (Fig. 5.2). (b) The reconstructed image applying the FBP (5.4) on the sinogram.

To acquire the image of the FOV of Fig. 5.6a, the same rotational scheme, as in the full multistatic array case is followed. The measured Radon projections are shown in the sinogram of Fig. 5.14a. The image is reconstructed from the recorded data using the FBP (5.4) and it is depicted in Fig. 5.14b. As in the full multistatic array case, an excellent agreement between the images acquired using the 2D 64×64 planar array (Fig. 5.6b) and the multistatic 16-element system, is observed.

Additionally, the multiple sphere imaging scenario (Fig. 5.8) is studied using the sparse multistatic setup, and the extracted results are given in Fig. 5.15.

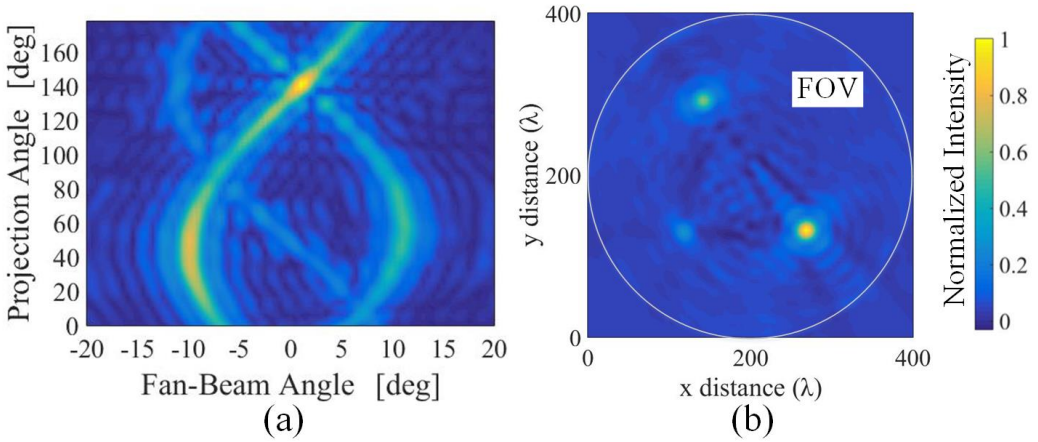

Fig. 5.15 (a) The sinogram of Fig. 5.8a, recorded using the sparse multistatic array of Fig. 5.12c. (b) The reconstructed image using the FBP (5.4).

In the presented examples, the overall reduction of elements is 4,080 (from 4,096 to 16) without compromising the spatial resolution. The angular resolution of the proposed configuration depends on the HPBW of the fan beam and is given by $a_r = tan(HPBW^o/2)$. Accordingly, the spatial resolution of the imaging configuration depends on the angular resolution and the distance from the array. The pixel width will then be $w_p = 2 \cdot d \cdot tan(HPBW^o/2)$, where d is the distance from the array. Higher spatial resolution can be achieved by increasing the sensor aperture and decreasing the fan-beam HPBW on the small dimension (H-plane in this case study). In this case study, the total length of the imaging aperture is 28 mm and can achieve a spatial resolution of ~13 cm at the distance of 5 meters at 300 GHz (the FOV extends to 4 meters in diameter).

VI. Signal-to-noise ratio analysis of the proposed imaging system

The previous sections have demonstrated that a rotating fan-beam antenna can produce 3D radar images with a comparable spatial resolution to a full 2D array, by using only a fraction of the antenna elements, thus significantly reducing the RF-front-end complexity. However, the use of less antenna elements leads to lower received signal power, thus a reduction in the signal-to-noise ratio is expected. The goal of this section is to compare the SNR of the presented rotational configuration to the traditional beam scanning method (e.g., phased array) and quantify the effect of SNR on the reconstructed images.

A. Image signal-to-noise-ratio

In this sub-section, the SNR performance of a multistatic antenna array is described, but the analysis can be similarly extended to other rotating apertures that form fan beams (e.g., RRSs or leaky-wave antennas).

In this example, the SNR of each antenna element is assumed to be identical (SNR_{ele}) and that the imaging is carried out by a 2D planar multistatic imaging array with a single transmitting antenna $N_t=1$, and multiple receivers $N_r=64\times64$. To reconstruct the image, the transmitter illuminates the FOV and the backscattered signals are simultaneously recorded on the receivers with an integration time t_s. Thus, the SNR of the 2D multistatic imaging array is given by [41]

$$SNR_{tot}^{2D} = SNR_{ele} + 10\,log_{10}(N_t N_r) \qquad (5.7)$$

The rotating linear antenna uses N_t transmitting and N_r receiving elements and (5.7) becomes

$$SNR_{tot}^{Rotating} = SNR_{ele} + 10\,log_{10}(N_t N_r) + 10\,log_{10}\left(N_{proj}\right) \quad (5.8)$$

where, N_t and N_r are the numbers of transmitting and receiving antennas of the linear multistatic array, respectively, and N_{proj} is the number of projections needed to acquire the image.

For a fully multistatic (not sparse) configuration ($N_t=1$ and $N_r=64$), the acquisition speed is $t_s \times N_{proj}$, where t_s is the integration time per projection (simultaneous reception). On the contrary, the sparse array configuration ($N_t=8$ transmitting and $N_r=8$ receiving antennas) requires, a data acquisition time of $t_s \cdot N_{proj} \cdot N_t$, since, the FOV is sequentially illuminated by activating successively all the available transmitters and record the backscattered signals at the receivers. After all the received signals are acquired, DBF is performed as described in Chapter 2-I. The acquisition time for a multi-transmitter imaging configuration can be reduced to $t_s \cdot N_{proj}$, with the use of orthogonal modulation codes on the transmitted signals [57].

The SNR comparison of the aforementioned configurations is presented in Table 5.1. For analysis simplicity, $SNR_{ele}=0$ *dB,* and same integration time $t_s \cdot N_{proj}$ is assumed for all configurations.

To fairly compare the SNR of the proposed imaging configuration with the 2D planar array, the total integration time is also assumed $t_s \cdot N_{proj}$, resulting in

$$SNR_{tot}^{2D} = SNR_{ele} + 10\,log_{10}(N_t N_r) + 10\,log_{10}\left(N_{proj}\right) \quad (5.9)$$

The renormalized SNR of the 2D multistatic planar array is given in Table 5.1. As expected, using fewer antennas results in lower system SNR than fully populating the aperture with antennas. However, the spatial resolution of the proposed configuration is the same compared to 2D antenna arrays as shown in the previous sections.

Table 5.1

System SNR of the imaging topologies assuming identical integration time ($t_s \cdot N_{proj}$)

Imaging configuration	T_x	R_x	N_{proj}	*SNR (dB)*
64×64	1	4096	-	55
64×1	1	64	81	37
64(sparse)×1	8	8	81	37

B. Image reconstruction in the presence of receiver noise

To comprehend the actual performance of the proposed imaging scheme compared to 2D planar arrays, the images are reconstructed in the presence of receiver noise. Namely, the target scenario shown in Fig. 5.8 is used, and the FOV is imaged with a rotating linear configuration (1×64 receiving antennas) and a 2D planar array (64×64 receiving antennas). In both cases, the FOV is illuminated with a single antenna and then the backscattered signals are recorded by the receivers. Then, the recorded signals of each antenna receiver are perturbed with identical SNR_{ele} for both topologies. Finally, the respective image reconstruction process is carried out. The computed images in Fig. 5.16 show a slight difference in the image artifacts, however, the 2D array images are more sensitive to smearing due to sidelobe level.

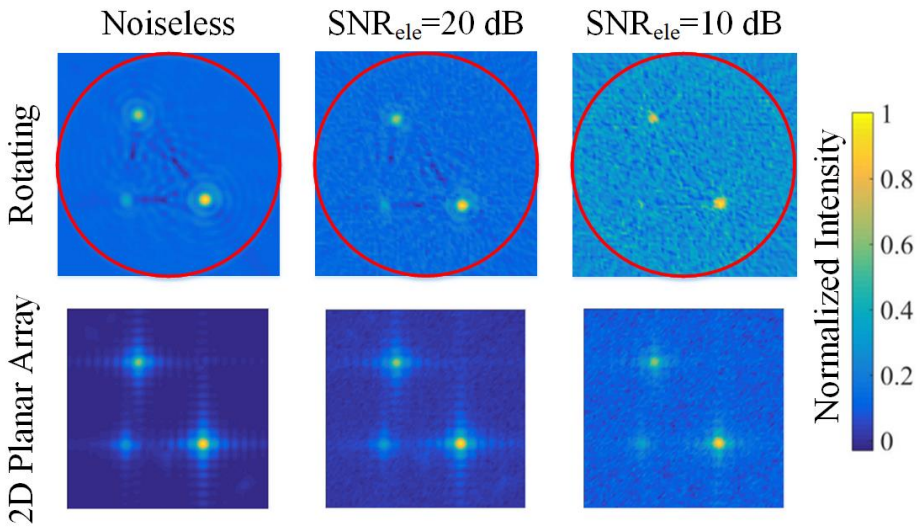

Fig. 5.16 The reconstructed images of three spheres using the proposed rotating and the 2D planar array configurations for different receiver noise. For the rotating array, the FOV is marked with a red circle. In both cases, the FOV extends to 40 degrees in diameter.

VII. Applications of the proposed imaging method

The proposed configuration is compatible with low-profile and lightweight mmWave/THz imaging hardware and requires both electronic and mechanical scanning mechanisms to acquire 2D or 3D images. Due to the rotational motion, the proposed method could enable real-time or near real-time image acquisition depending on the embedded platform. For example, a realistic one rotation-per-second (rps) will result in a 2 frame-per-second (fps) rate and similarly, 10 rps can enable 20 fps. Besides, the proposed method could be attractive for platforms that inherently feature rotational motion, or it can be supported with minor design effort and cost. Such applications could be envisioned in UAVs (quadcopters) and CubeSats, where size and weight are at a premium. In an application scenario, the proposed imaging topology requires mechanical motion. As such, future work would require evaluating the effect of possible vibrations of the imaging array

on the image quality and implementing methods to correct for the anticipated artifacts. Namely, different platforms suffer from various vibration effects; hence, a detailed study needs to be carried out for each platform. For example, quadcopters have a tumbling motion that could affect the images, since the reference position of the imaging sensor is not fixed, however, in the case of CubeSats, this tumbling motion is negligible. Similar problems occur in spotlight SAR, where corrections are applied to the received signals to account for the irregular flight path of the aircraft [53]. In addition, the small aberrations caused by the micro-vibrations should be studied, in cases where motors are deployed to achieve the rotational scanning.

VIII. Conclusions of Chapter 5

In this Chapter, a novel image reconstruction method based on the Radon Transform that enables the development of compact high-spatial-resolution imaging topologies was presented. This imaging configuration provides 2D or 3D images at the mmWave/THz spectrum while retaining a low-profile design due to the reduced number of elements used. The proposed imaging scheme records the Radon Transform of the given FOV and the images are reconstructed using the Fourier Slice Theorem. Initially, the proposed technique is studied using a multistatic array of 1 transmitting and 64 receiving antennas and is compared to a more conventional multistatic beam-steering aperture populated with 1 transmitting and 64×64 receiving antennas. Then, to further simplify the imaging configuration, a sparsity technique was incorporated into the proposed design, leading to a compact setup, capable of performing high-resolution imaging. The total reduction of active elements achieved by a factor of $N^{3/2}/2$ (assuming a conventional 2D antenna array of N×N elements). For the examples presented in this Chapter, the rotational

imaging scheme and the multistatic approach reduced the number of active elements by 256 (from 4,096 to 16). In addition, to 2D imaging examples, a procedure to reconstruct 3D images using the Radon Transform was presented for the first time in the known literature. Finally, an SNR analysis was carried out for the presented configuration and the results were compared with traditional 2D planar multistatic imaging topologies.

A. Alternative sensor topologies

In this Chapter a novel imaging technique is thoroughly validated through a series of results. However, there are still other aspects of the imaging system that should be investigated. Namely, the proposed sensor demands a multistatic sparse array comprising of a handful of elements. However, the design and development of this mmWave/THz antenna array are not trivial, since, monolithically integrating (on-wafer) 16 antenna elements with their respected RF-front-end circuit is a difficult and costly task as described in Chapter 2. Therefore, alternative imaging sensor topologies should be explored.

An alternative sensor consisting of a leaky-wave antenna is illustrated in Fig. 5.17a. As such, substate integrated LWAs form narrow fan beams that can be scanned using a frequency sweep. Specifically, the direction of the formed fan-beam depends on the operating frequency of the signals that propagate through the antenna [2]. However, frequency scanned LWAs restrict the ability of the presented method to reconstruct 3D images since the recorded frequency signals will correspond to certain fan-beam angles.

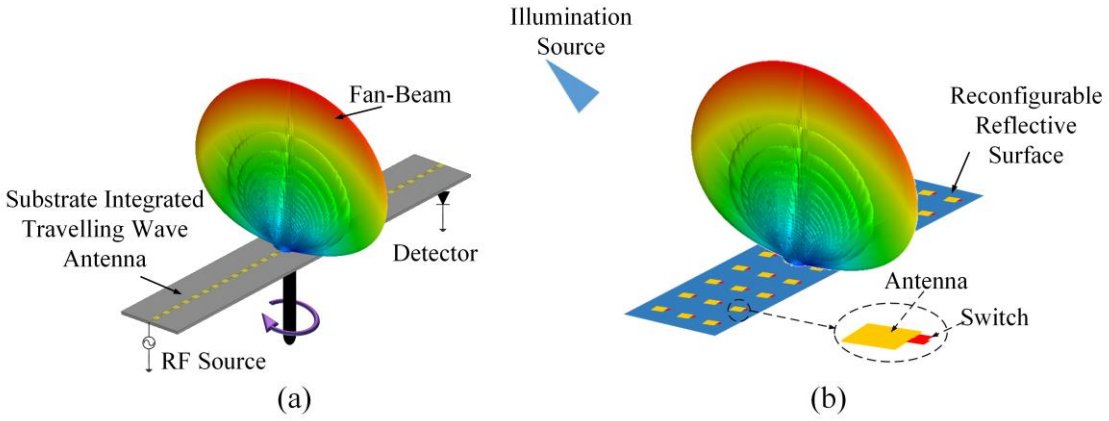

Fig. 5.17 The proposed system implemented using: (a) a rotating substrate integrated LWA and (b) a rotating RRS.

On the other hand, the use of RRSs (Chapter 2-II) as the sensors could be a viable alternative that limits the use of complex hardware and does not mitigate the 3D imaging performance of the presented method. As such, a "thin" rectangular reflective surface consisting of a plethora of elements with integrated switches could be employed, as illustrated in Fig. 5.17b. The surface illumination could be carried out by an external source (e.g. horn antenna) and the beam steering would be achieved by modulating the imaging waves' phases, by tuning the integrated switches on the antennas.

Finally, multistatic coded aperture phased arrays (Chapter 2-II) could be employed as the sensors of this imaging method. Namely, a multistatic setup consisting of a single transmitter and a linear array of receiving antennas with integrated phase or amplitude switches at each element (e.g., [11]), could serve as the sensor of the proposed imaging configuration. These coded antenna arrays that are typically used in automotive radars, reduce the RF-font-end significantly compared to classical phased arrays [11] and can be exploited to obtain 3D images.

These alternative sensor topologies emphasize the need for cost-efficient mmWave/THz switches that can be monolithically integrated with multiple antenna elements on electrically large apertures, to form narrow steerable beams. These systems would enable 3D high-spatial-resolution imaging using the proposed and/or other imaging methods. However, the fabrication and design of such mmWave/THz switching topologies is not a trivial task. Thus, in Chapters 6 and 7, such mmWave/THz switches that use graphene and can be monolithically integrated on printed antennas, are thoroughly presented.

CHAPTER 6

Large-Area Graphene Nanofabrication and On-Wafer Characterization for Reconfigurable Millimeter-wave and Terahertz Devices

The proliferation of promising mmWave/THz applications, including the novel imaging method presented in Chapter 5, requires large-format arrays with hundreds or even thousands of devices. Specifically, large apertures that form high-gain steerable beams can alleviate the propagation losses in wireless communication systems and enable high-spatial-resolution 3D imaging as discussed in the previous Chapters. In these applications, reconfiguration, especially through switching, is crucial in enabling RF signal processing including carrier modulation/encoding or beam steering in antenna arrays.

In microwave frequencies (< 30 GHz), a variety of off-the-shelf switches and components is available (e.g., PIN and varactor diodes, phase shifters, couplers, etc.), enabling the design of complex large-scale reconfigurable apertures. However, in mmWave/THz bands, many of these traditional switching topologies are unavailable due to fabrication and loss constraints. Thus, alternative topologies are required that can form high-gain beams and retain the necessary beam steering capabilities. As such, at mmWave/THz frequencies, single-pole-single-throw switches can provide many practical reconfiguration solutions without residing to the complexity of more traditional devices; for example, an SPST switch can be integrated on an antenna to enable direct signal control and provide 1-bit quantized phase and/or amplitude modulation on the RF signals [28]. These configurations are mainly categorized as either coded phased arrays (e.g., 1-bit

digital phased arrays [58][59]) or RRSs (e.g., reflectarrays [27]-[38]). Such reconfigurable apertures carry out frequency-independent beamforming while retaining low DC power consumption and RF losses compared to traditional phased array systems, due to the simplified RF-front-end complexity [24]. Moreover, these reconfigurable multi-element apertures, which are expected to dominate in at mmWave/THz bands, are less prone to phase quantization errors compared to smaller ones, as observed in [35]. Finally, switches can typically achieve simpler modulation schemes (e.g., 1-bit phase or amplitude modulation); however, spectral efficiency is not necessarily a requirement at mmWave/THz bands, where bandwidth can be orders of magnitude larger than lower RF.

Initially in this Chapter, the available mmWave/THz switching topologies are presented, varying from traditional technologies (e.g., CMOS) to novel 2D materials. Moreover, their advantages and disadvantages concerning the maximum frequency of operation, large-area integration, fabrication complexity, and cost, are summarized. This study focuses on graphene actuated switches since graphene is a cost-efficient, off-the-shelf, tunable material that offers a steady performance over a wide frequency range up to 2 THz. However, the main drawback of graphene is the low fabrication yield over large areas, due to its delicate nature. Thus, herein, a novel nanofabrication method that achieves high-yield over large areas is presented. The proposed nanofabrication process enables the proliferation of graphene-actuated reconfigurable mmWave/THz apertures, for imaging and communication applications.

I. Switching topologies for millimeter-wave/terahertz reconfigurable devices

State-of-the-art switches based on CMOS, SiGe, GaAs, InP, and other technologies operate up to 350 GHz and can provide viable solutions for reconfigurable mmWave/THz applications [60]-[66]. For example, state-of-the-art SiGe SPST switches, offer insertion loss (IL) less than 3 dB with switching ratios (R) up to 15 dB at 300 GHz. However, the downside is that the fabrication cost increases dramatically when integrated into large arrays with thousands of elements because of the chip's real-estate cost [25]. Specifically, the performance of the aforementioned switches is limited by the parasitics and mobility constraints exhibited in mmWave/THz frequencies (at room temperatures) [67]. To compensate for these limitations, more advanced technology nodes are required, thus increasing the fabrication cost significantly when it comes to large-scale reconfigurable apertures. For example, a mmWave/THz RRS with an aperture of 20 mm × 20 mm can host more than 1,600 antenna elements at 300 GHz ($\lambda_0/2$ sampling). To implement such an array with state-of-the-art methods requires at least 1,600 switches (one per antenna), which can be manually assembled as chips on the aperture (to reduce the cost) or have an entire wafer of 400 mm^2 with all the switches integrated. Therefore, scaling CMOS, SiGe, GaAs, InP, and other similar technologies becomes a cost and fabrication challenge for mmWave/THz multi-element large-format apertures.

Conversely, switching can be achieved with the use of alternative tunable thin-film (2D or 2.5D) materials; the electromagnetic properties of which (e.g. sheet resistance or permittivity/permeability) can be tuned over a large bandwidth by external mechanism (e.g. field biasing or heating). Such materials include ferrite [68], liquid crystals [69], molybdenum disulfide (MoS_2) [70], black phosphorus (BlPh) [71], vanadium dioxide

(VO_2) [72]-[74], and graphene (GR) [75]-[83]. In the literature, MoS_2 and BlPh switches are currently limited to lower frequencies (< 100 GHz) due to their high intrinsic impedances (MΩ) that demand for thin and long active device shapes to avoid excess losses. However, these long configurations are highly affected by parasitics (e.g., coupling capacitance) that become pronounced in the mmWave/THz high frequencies [70][71]. Alternatively, VO_2 switches have been proposed in mmWave/THz bands with good performance (low insertion loss and switching ratio –more than 1,000) [72][73]. VO_2 conductivity is thermally regulated, thus it has been mostly exploited in power limiting switching topologies. Nevertheless, VO_2 switching is sensitive to ambient temperature changes [73], a limiting factor for reliable compact multi-element designs that exhibit strong heat dissipation. In addition, the heaters of VO_2 switches require at least 20-50 mW per element [72], thus power consumption is expected to skyrocket in multielement configurations with hundreds or even thousands of integrated switches.

Another 2D tunable material is graphene whose sheet impedance can be regulated with the use of external biasing as in field-effect transistors [75]-[83]. In addition, the graphene sheet resistance values are significantly lower than those of MoS_2 and BlPh thus it is preferred in mmWave/THz devices due to the mitigated RF parasitics [75]. In table 6.1, the existing technologies for mmWave/THz switches are summarized.

Table 6.1

Existing mmWave/THz Switching Configurations

Technology	Maximum Frequency (GHz)	Switching Performance (IL and R)	Cost per mm^2	References
CMOS	300	High	Extremely High	[62]
SiGe	320	High	Extremely High	[60][61][67]
InPh, GaNi, etc.	330	High	High	[63]-[65]
VO_2	1000	High	Low	[72]-[74]
Graphene	2000	Good	Low	[75]-[83]

II. Graphene as a tunable 2D resistor

This work focuses on the devise of graphene switches for mmWave/THz applications. Graphene is a versatile 2D material formed by a hexagonal carbon atom lattice as depicted in Fig. 6.1a. As such, each carbon atom is bonded with three neighboring carbon atoms through an σ-bond (two-electron bond – one from each atom [84]) and the remaining one (1) outer shell electron of the carbon atom is available for electronic conduction [84]. When an external electric field biasing is applied, this electron is energized, escaping from the valence into the conduction band, enabling the flow of currents through the monolayer [85]. Thus, the graphene sheet impedance can be regulated by applying an external field biasing as in field-effect-transistors [85].

(a) Graphene

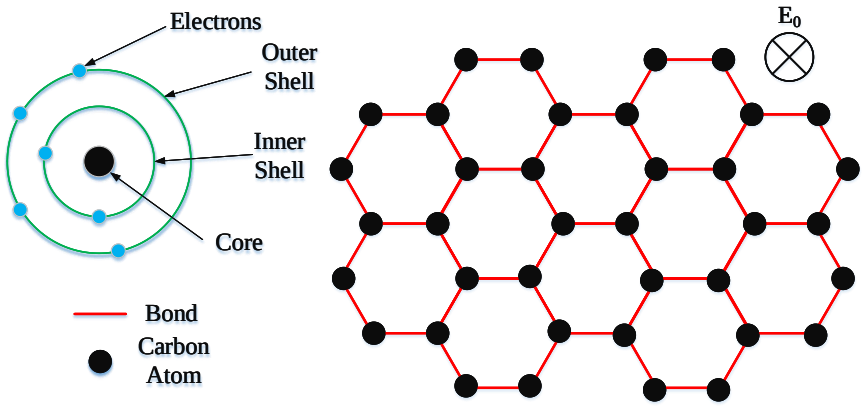

(b) Graphene Conductivity

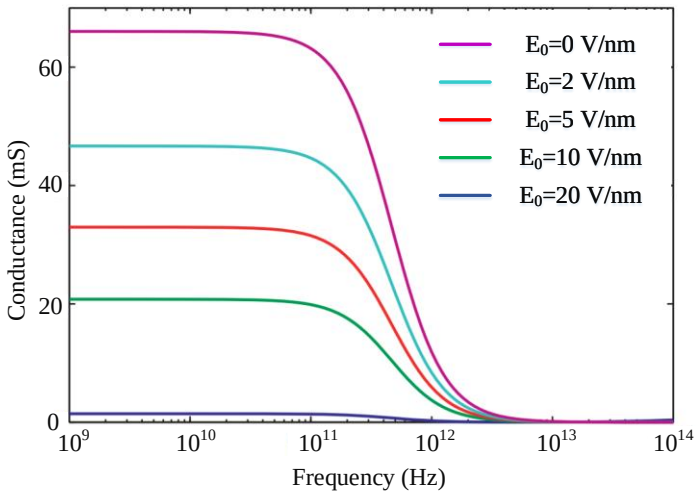

Fig. 6.1 (a) The graphene hexagonal structure and the carob atom. (b) the graphene monolayer sheet conductance versus frequency for various biasing voltage [85].

The tunable sheet conductivity/impedance can be described using quantum theory and is detailed in [85]. The conductance tunability under various external biasing voltages versus frequency is plotted in Fig. 6.1b. As clearly shown from this plot, graphene can be used as a tunable sheet resistor until 1.5 THz since after that frequency plasmonic effects limit the conductivity tunability [85]. From Fig. 6.1b is evident that graphene sheet impedance (one over the conductivity) can be tuned with the use of an external electric

field ranging from a few Ω to a few kΩ. The ideal sheet impedance ratio exceeds 60, however in reality the biased/unbiased ratio is limited to 10 or lower since the graphene layer exhibits impurities and limited grain sizes that reduce the switching performance. These intrinsic impedance values are not as high as in the case of MoS_2 and BlPh, thus the designed devices are smaller leading to less parasitic effects in the mmWave/THz bands. Moreover, the tuning mechanism can be implemented with a simple biasing gate instead of complex heating devices as in the case of VO_2 switches. Thus, graphene-loaded devices have attracted great interest in the research community, varying from microwaves (e.g., [75]), to THz bands (e.g., [76]). Such graphene-actuated switches can enable a plethora of setups including reconfigurable apertures for communication and imaging applications.

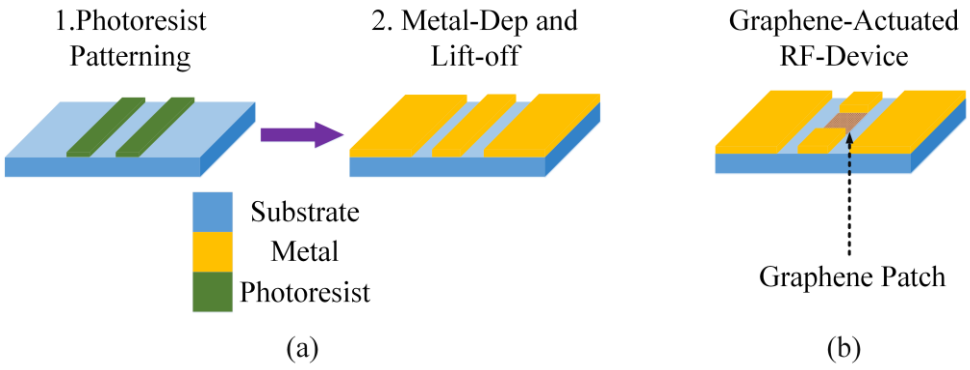

Fig. 6.2 (a) The steps for fabricating a metal CPW line using standard nano-fabrication procedures. (b) Graphene-actuated RF-switch.

III. Existing graphene nanofabrication processes

Implementation of large-area graphene-based electronics is hindered by the existing nanofabrication approaches that are unable to achieve high-yield over large-areas (> 1 cm × 1 cm). Owing to its delicate nature, graphene easily delaminates during the

fabrication processes, even with the use of common chemicals [86][87]. Graphene delamination is exacerbated when thick metal layers are required to reduce ohmic losses. For example, at 300 GHz the skin depth of gold (Au) is 140 nm [88], hence the Au thickness for a 300 GHz transmission line should be at least 280 nm to minimize ohmic losses. However, developing thick metal layers (> 0.2 μm) with integrated graphene patches is non-trivial, due to the compatibility of graphene with the chemicals used during the fabrication steps. Thick metal layers require double layer lift-off photoresists that allow fine resolution patterning with higher yield [89]; though, the strong chemicals used during this process dramatically increase graphene delamination. Therefore, the existing nanofabrication technologies provide low yield, which is prohibitive for the design of large-scale mmWave/THz systems, including coded antenna arrays and reconfigurable surfaces.

Figure 6.2a depicts the steps for the fabrication of coplanar-waveguide (CPW) transmission line using thick metal layers [90]: 1) Spin coat a double layer photoresist (3-4 times the metal thickness), pattern it using photolithography followed by development, and 2) Deposit a metal layer using electron-beam evaporation deposition (EVD) and pattern it using lift-off. The aforementioned process is a well-known procedure used for the development of high-frequency RF devices. Contrary, Fig. 6.2b presents a graphene-actuated RF-device configuration with a graphene patch intersecting the center conductor of the CPW. To develop this configuration the substrate is covered with a delicate graphene sheet and then the metal topology is patterned using the aforementioned steps. However, the wet processes of development and lift-off used for metal patterning, often lead to graphene delamination due to its delicate nature [86][87]. This becomes a significant

roadblock for large-format arrays of devices where yield is crucial [91], including reconfigurable surfaces and coded phased arrays.

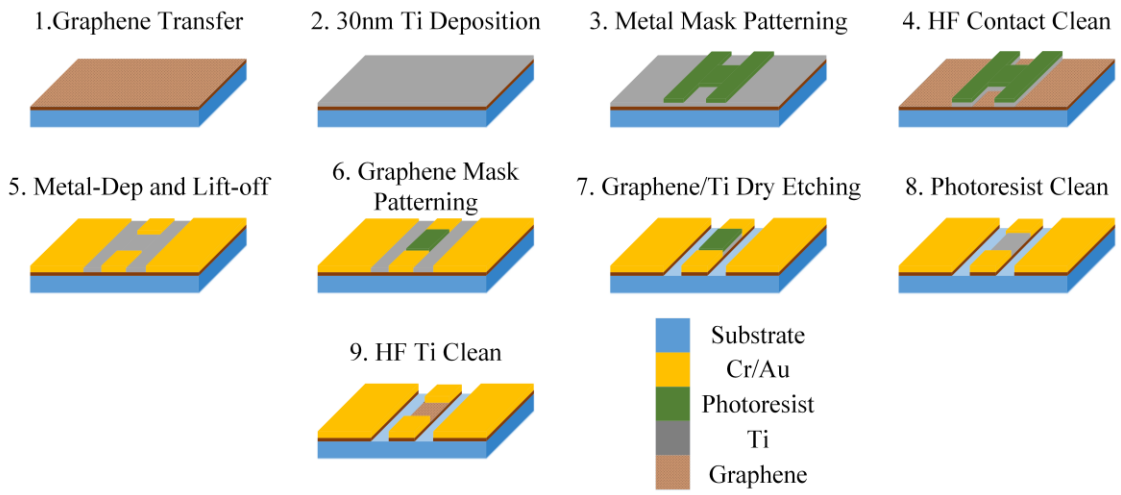

Fig. 6.3 The proposed fabrication procedure for the development of on-wafer mmWave/THz graphene devices with Ti sacrificial layer to protect the graphene.

In this Chapter, a high-yield fabrication procedure is presented (Fig. 6.3). The proposed method uses titanium (Ti) sacrificial layers to cover graphene during the fabrication procedure and prevent delamination. Besides, using Ti layers cleans the graphene monolayer by bonding to organic residues, leading to intrinsic performance [86]. Hence, the development of large-scale mmWave/THz graphene reconfigurable devices is enabled with the proposed high-yield nanofabrication process. A similar procedure using yttrium (Y) sacrificial layers has been proposed recently [87]; although this work presents promising results, the use of a rare element like Y is not compatible with the development of a high-yield standardized process. Namely, such processes demand low-cost materials, but Y is typically six times more expensive than Ti. In addition, Ti is a well-known material used in industrial procedures; hence, no adaptation is needed for the existing equipment to

the new material properties (melting point, sputtering profiles, etc.). Moreover, the fabrication residues of Y and its oxides are damaging to human health and the environment in contrast to Ti [92][93]. Hence, Ti was selected instead of Y as a sacrificial layer for the presented high-yield fabrication process.

IV. Nanofabrication method for large-area graphene devices

The proposed fabrication process followed to develop graphene-based switches is illustrated in Fig. 6.3. Initially, a high resistivity (> 10,000 Ω·cm) silicon wafer that serves as the substrate and is commonly used in mmWave/THz RF applications, is cleaned using a 1:10 hydrofluoric acid (HF): deionized (DI) water solution. In this step, the native oxide layer of the silicon surface is removed before the graphene transfer and the silicon surface is passivated with hydrogen (H) atoms. The advantages of this clean are twofold. Firstly, the H-passivated surface minimizes the effects of the graphene-silicon interaction leading to intrinsic graphene performance [94]. Secondly, the native oxide of the silicon is hydrophilic [95], hence, by removing and replacing it with a hydrophobic H-passivated surface the risk of delaminating the transferred graphene monolayer during the wet processes is minimized. Also, transferring the graphene onto a hydrophobic surface hinders doping and other effects that undermine the graphene performance [96].

After the cleaning is completed, the graphene monolayer is transferred onto the silicon substrate using wet transfer [97] (this step was carried out by ACS Materials [98]). The Raman spectrum [99] of the graphene monolayer on the high resistivity silicon substrate is shown in Fig. 6.4 (acquired on a WITec alpha300R system with 532 nm excitation laser), where the clear G and 2D peaks for monolayer graphene are observed.

These peaks reveal the condition of the graphene monolayer and are typically used to examine the atomic structure of monolayer materials, including graphene [99]. Finally, the absence of the D peak suggests that there are very few defects on the graphene monolayer before the nanofabrication process.

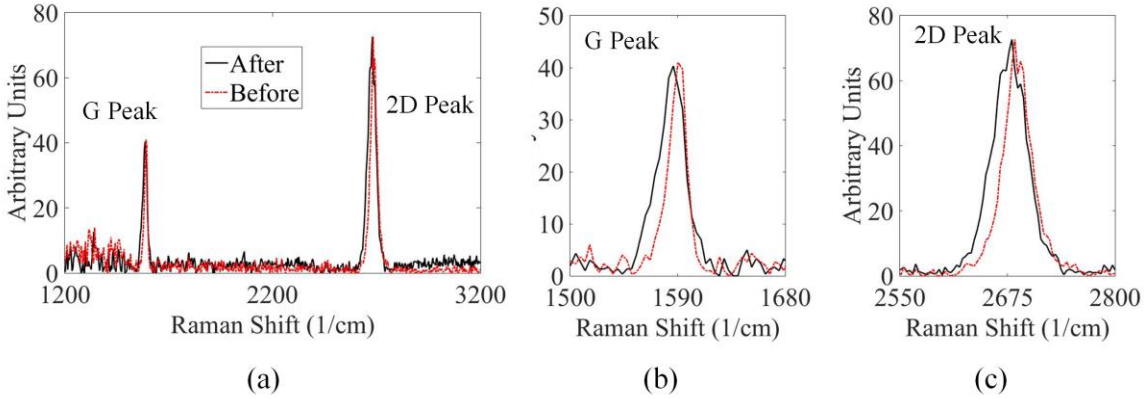

Fig. 6.4 (a) The Raman spectra of the graphene monolayer acquired before and after the fabrication procedure focusing on the (b) G and (c) 2D peaks (60 sec total accumulation time).

Even though the wet transfer procedure is robust, due to the use of poly(methyl methacrylate) (PMMA), residual polymer, and other particles tend to adhere to the graphene monolayer leading to deteriorated performance [87]. Hence, using a Ti sacrificial layer also helps remove those residual contaminants and achieve intrinsic performance [86]. After the transfer is completed, a 30 nm Ti sacrificial layer is deposited using EVD at a rate of 1 Å/sec (chamber pressure less than 5×10-7 m-torr). A reasonably thick (> 20 nm) blanketing layer is used to ensure uniform coverage, thus minimizing graphene exposure to the strong chemicals used during the fabrication procedure that might lead to its delamination. This step could also be carried out at the beginning of the process before the graphene monolayer transfer. After the Ti deposition, the double layer photoresist

(MIR-701 and LOR-10A) for the metal mask is spin-coated on the wafer. Then the photoresist is exposed at 63 m-J/cm^2 using a 365 nm light and developed using AZ-300 MIF (45-60 seconds). The two layers of the photoresist develop at different rates in the base solution, creating an undercut that is necessary to perform the lift-off process that follows [89]. Afterward, to clean the Ti from the metal contact areas, the wafers are submerged in a 1:72 HF:DI water solution for 2 minutes.

Next, the Cr/Au (10 nm/300 nm) metal layer is deposited using EVD, with a rate of 1 Å/sec and 1.4 Å/sec, respectively (chamber pressure less than 5×10-7 m-torr). After the deposition, the metal mask is patterned with a lift-off process using heated Remover PG at 80^{o}C. Thereafter, the double layer photoresist (MIR-701 and LOR-10A) with the mask to pattern the graphene into rectangular patches is spin-coated, exposed at 63 m-J/cm^2 using 365 nm light, and developed using AZ-300 MIF (45-60 seconds). After the dry etching, the hardened fluorinated single layer photoresist cannot be removed completely without the use of 400T, which is an aggressive tetramethylammonium hydroxide (TMAH) based chemical that delaminates graphene even when covered with a 30 nm Ti layer. Therefore, instead of using a single layer of photoresist, which is common in dry etching procedures, a double layer photoresist [89] is used, which is easily removed by Remover PG. After the development of the graphene patch mask, a dry-etching process is carried out with SF_6/Ar (20/5 sccm) plasma (75 W, 10 m-torr) for 7 minutes. Figure 6.3 (step 6), shows that the photoresist covers only the graphene patches since the Cr/Au layer is not etched by the plasma, hence it acts as a self-aligned hard mask. In addition, the DC-bias of the dry etching procedure was optimized to minimize the resputtering of the gold, while retaining an acceptable etching rate. After the dry etching is completed, the remaining

photoresist is cleaned using a fast (less than a minute) O2 plasma dry-etch and heated Remover PG at 80 ^{o}C. Then, the Ti sacrificial layer is removed by submerging the wafers in a 1:36 HF:DI water solution for 2 minutes. Finally, Fig. 6.4, presents a representative Raman spectrum of the monolayer graphene pieces on the final devices, establishing the fabrication process. The G and the 2D peaks before and after the full fabrication process are similar in height and position, indicating no significant changes in doping, while there is no D peak, indicating the graphene remains intact and free of defects [99].

Graphene is transferred at the beginning of the process, to increase the overlapping metal-graphene area achieving good ohmic contact and providing mechanical rigidity by robustly anchoring the graphene on the substrate. The final wafer is shown in Fig. 6.5a, where the total graphene dimensions are 2 cm × 2 cm, and the wafer has more than 280 graphene RF-devices.

To demonstrate the robustness of the proposed method, Fig. 6.5b depicts a wafer with graphene-actuated devices, fabricated with the standard no-Ti process. In this example, the lift-off process was carried out in a heated Remover PG solution as in the Ti process, to ensure the success of the metallization mask. However, the graphene monolayer is delaminated by the used lift-off chemicals leading to a nearly 0 % yield, as depicted in Fig. 6.5b.

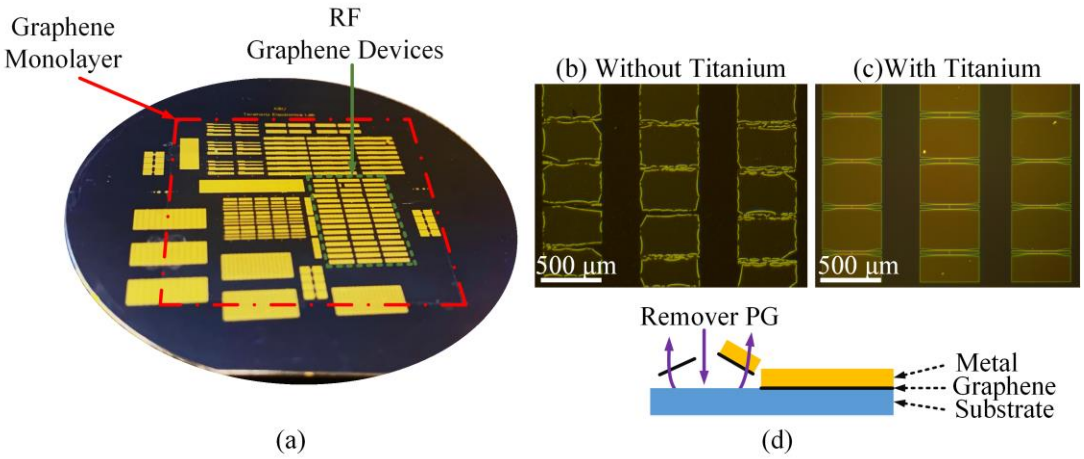

Fig. 6.5 (a) Photograph of the fabricated on-wafer RF-devices. (b) Optical microscope images of an array of graphene devices for the standard no-Ti wafer after the lift-off procedure, (c) the final wafer with the use of Ti sacrificial layer. (d) Graphene delamination during lift-off in Remover PG solution (metal pattering), leading to excessive deformation of the metal layer.

This section presented a novel nanofabrication method that achieves more than 92 % yield for large-area graphene devices. The graphene monolayers were examined before and after the fabrication process with the use of Raman spectroscopy to reveal any possible defects due to the proposed method. Even though these results suggest that the atomic structure of the graphene monolayer remains intact, the scope of this work is to utilize mmWave/THz graphene switches; thus, the graphene properties should be investigated in the mmWave/THz bands. Therefore, the following sections present an on-wafer mmWave/THz graphene characterization process that is used to measure the graphene sheet impedance in the 220-300 GHz bands.

V. On-wafer calibration process

In this section, the fabricated graphene-loaded switches are characterized in the sub-mmWave bands. As such, the measurement set-up of Fig. 6.6, along with the thru-

reflect-line (TRL) calibration procedure, are used to calculate the graphene sheet impedance of the fabricated devices. Specifically, this setup consists of a Rohde & Schwarz (R&S) vector-network-analyzer (VNA) that feeds two Virginia Diodes (VDI) frequency extenders covering the WR-3.4 band (220-330 GHz). The extension modules measure only the forward scattering parameters (S_{21} and S_{11}) [100]. On the port of each of the frequency extender, a (ground-signal-ground, GSG) contact probe is mounted [101], feeding the RF signal to the on-wafer devices (Fig. 6.6).

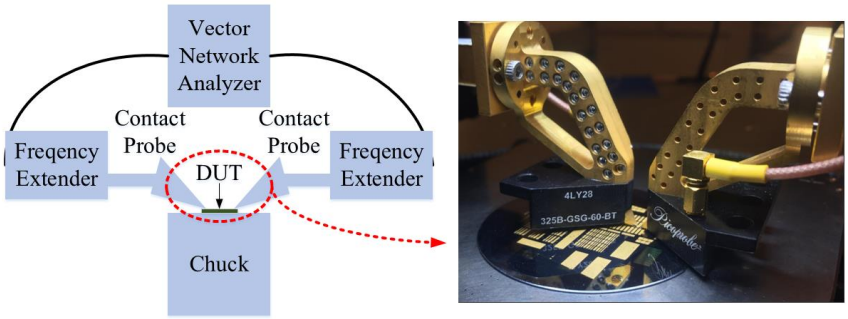

Fig. 6.6 The setup used to carry out the on-wafer measurements in the 220-330 GHz band.

To characterize graphene sheet impedance, a two-tier calibration is carried out. Initially, the waveguide ports of the VNA extenders are calibrated using a thru-short-shifted-short-match (TRRM) calibration process [103], and then an on-wafer 8-term TRL calibration is utilized [102] to shift the measurement reference plane on the graphene devices. The top-view of the on-wafer TRL calibration standards is shown in the microscope images in Fig. 6.7. The landing pads have a characteristic impedance of 50 Ohms to match the GSG contact probes, while the transmission lines that lead to the DUT, are smaller in size to minimize the losses due to radiation.

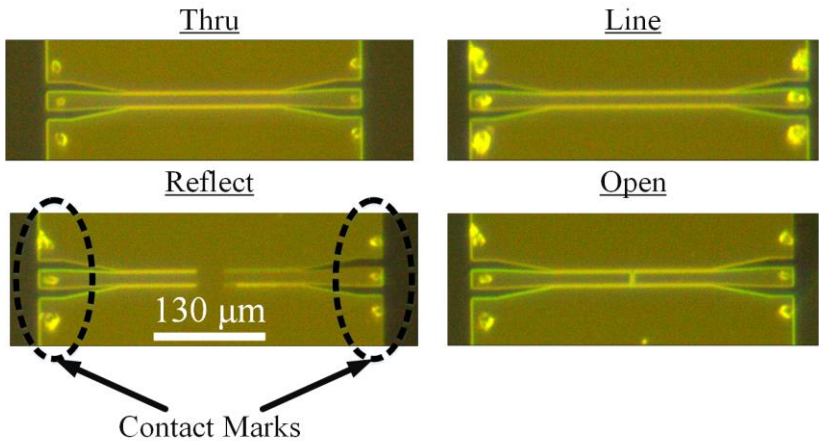

Fig. 6.7 The on-wafer TRL calibration standards (thru-short-line), and the open discontinuity (no-graphene). The line is 35 µm longer than the thru standard. Each device is measured multiple times, hence the pronounced RF contact probe scuff marks.

On-wafer contact probe measurements are challenging due to non-systemic errors, including: 1) the contact force between the probe's tips and the CPW contact pads is non-repeatable, due to the manual handling of the micromanipulators, metal wear, and planarity, leading to varying contact parasitics, 2) the landing position varies for different measurements, thus arbitrarily shifting the reference plane, and 3) the standards can feature small defects due to localized nanofabrication aberrations. Additionally, this setup measures only the forward scattering parameters, thus symmetry is assumed in the S-matrix, further hindering the calibration process.

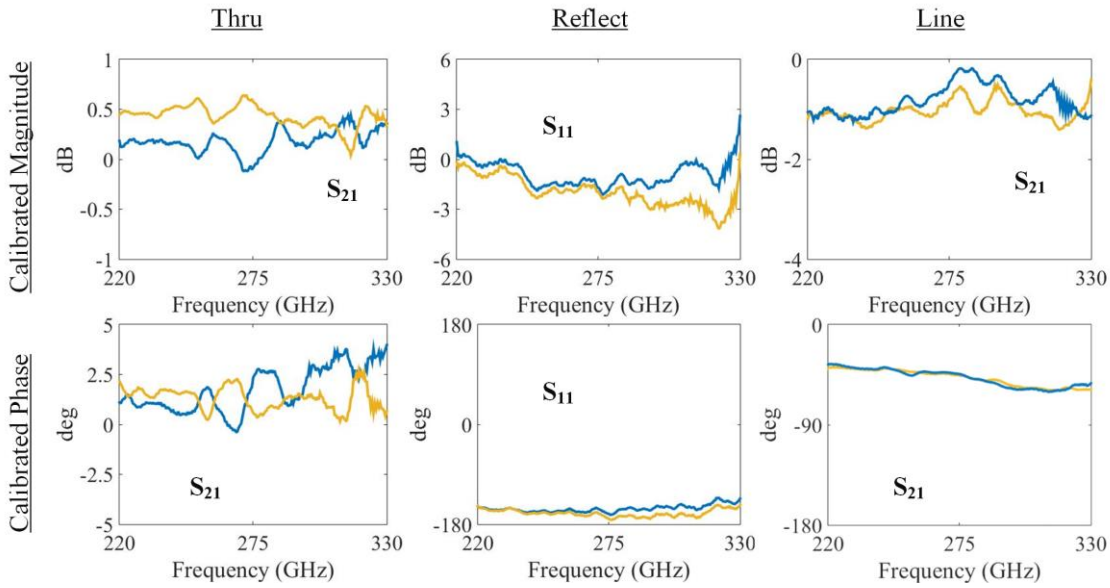

Fig. 6.8 The sensitive contact probe measurements lead to different responses for identical calibration standards.

All the aforementioned factors contribute to low-measurement repeatability leading to errors that are common in mmWave/THz contact probe measurements [104]-[106]. To quantify the effect of these factors on the measurement process, in Fig. 6.8 the calibrated results between different TRL standards are presented. Specifically, for each of the calibration standards (Thru-Reflect-Line), three identical copies are fabricated (9 in total). Then, one of each is used to form a TRL calibration set; the remaining two are used as the as devices-under-test (DUTs) and their calibrated S-parameters are given in Fig. 6.8. As clearly shown, the calibrated S-parameters vary in both phase and magnitude between different identical devices, affected by the expected non-systemic errors. To mitigate this uncertainty, in the rest of the measurements, the three standards are averaged, thus minimizing the variations in the calibration process.

Table 6.2

Fabricated Graphene Switch Configurations

Configuration	Z_o (Ω)	S (μm)	W (μm)	L (μm)	N (S/L)
1	36	20	4	5	4
2	32	40	5	5	8
3	32	24	3	3	8

The next step is testing the accuracy of the TRL calibration process by characterizing the well-known open discontinuity along the signal path of the CPW (Fig. 6.9). Specifically, the open discontinuity is modeled using the Π network of lumped capacitors [107], as depicted in Fig. 6.9. For this measurement process, three CPW configurations are used (Table 6.2).

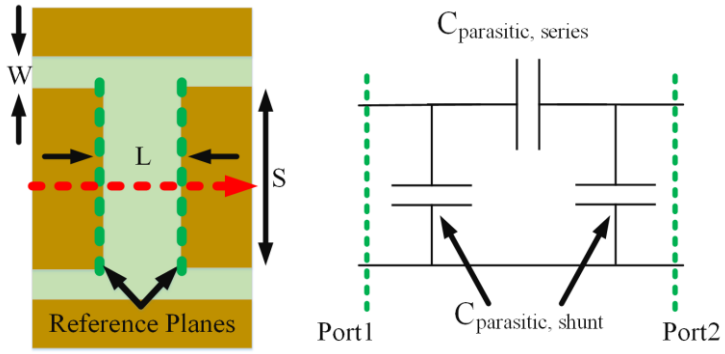

Fig. 6.9 The top view schematic of the CPW open discontinuity and its equivalent circuit.

The measured calibrated S_{21} of the open discontinuity (no-graphene) is shown in Fig. 6.10. Alongside the measured data, the theoretical values are given, obtained by the

analytical models of [107], validating the calibration process. Similarly, in this experiment, two different devices are measured to demonstrate the variability of the measured scattering parameters. Therefore, to obtain the parasitic capacitances needed for the extraction of the graphene sheet impedance, as discussed in the following section 6-VI, the different open devices' measurements, are averaged.

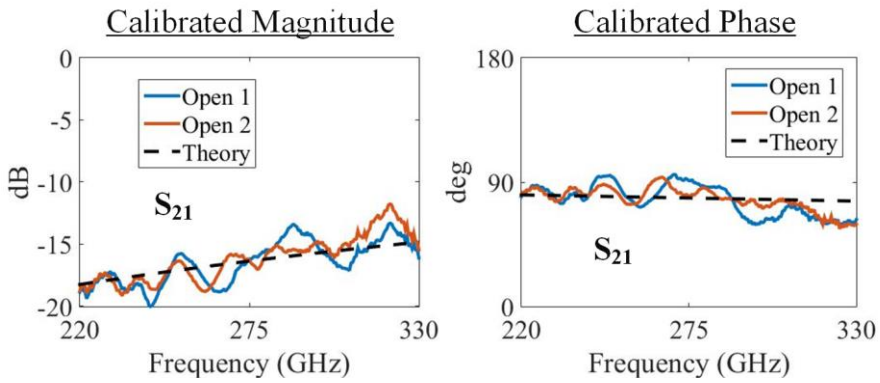

Fig. 6.10 Measured versus theoretical open CPW discontinuity for the 3rd configuration.

VI. On-wafer graphene characterization

In this section, the on-wafer graphene characterization process is presented. To extract the graphene sheet impedance in the mmWave/THz bands, the TRL method of the previous section 6-V is leveraged. As such, in this section, the graphene sheet impedances are measured both for the unbiased and biased cases to verify that the graphene monolayer properties remained unaltered during the proposed nanofabrication method of section 6-VI.

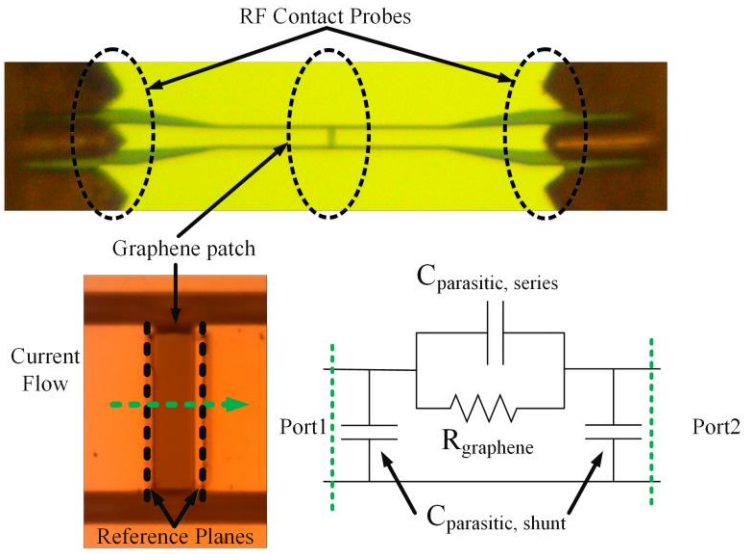

Fig. 6.11 The fabricated CPW lines integrated with graphene patches (without the biasing gate), and the equivalent circuit model. The landing pads of the contact probes are designed at 50 Ohms.

A. Graphene sheet characterization

This sub-section presents the unbiased graphene sheet impedance measurements in the 220-330 GHz band. The top-view of the graphene DUT is given in Fig. 6.11. The un-calibrated and calibrated data (S_{21}) for the DUT discontinuity with and without (open) graphene are given in Fig. 6.12. As expected, when the CPW discontinuity contains graphene, the coupled signal to the second port increases, since the graphene acts as a parallel resistor to the series parasitic capacitance (Fig. 6.11). To carry out the TRL calibration the averaged standards of the previous section 6-V are used, thus shifting the reference plane on the graphene devices, as shown in Fig. 6.11.

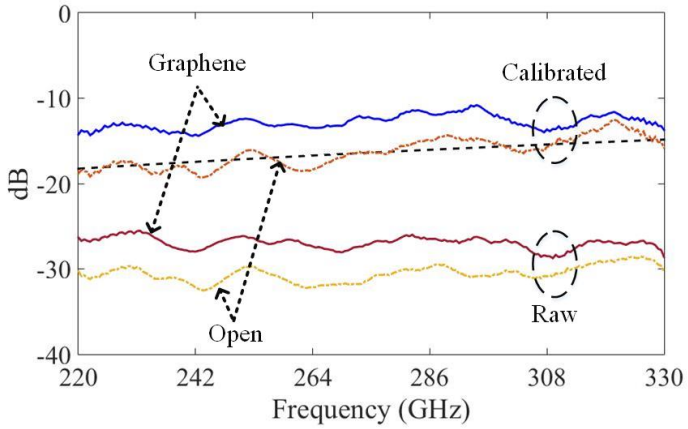

Fig. 6.12 The raw and calibrated $|S_{21}|$ of the devices (3rd configuration) with and without (open) graphene. As expected, the presence of graphene increases the signal coupling to the second port. In addition, the black dotted line represents the theoretical $|S_{21}|$ value expected for the CPW open discontinuity.

The graphene patch is in the open discontinuity of the CPW and the equivalent circuit of the device is depicted in Fig. 6.11. As such, the graphene is in parallel with the series parasitic capacitance. To calculate the graphene sheet impedance from the calibrated measurements, the parasitic series capacitance's S-matrix is measured and then transformed to ABCD parameters [88]

$$ABCD_m = \begin{bmatrix} A_{meas} & B_{meas} \\ C_{meas} & D_{meas} \end{bmatrix} \qquad (6.1)$$

Since the open discontinuity is modeled with a Π network (Fig. 6.9), the reactance of the series capacitance of the open discontinuity (no graphene), is approximated by the following formula [88]

$$Z_{C,parasitic,series} = B_{open} \qquad (6.2)$$

where B_{open} is the parameter of the $ABCD_m$ matrix of the open discontinuity. Afterward, the total series impedance is calculated in the presence of graphene using again the ABCD parameters

$$Z_{series} = B_{graphene} \quad (6.3)$$

where $B_{graphene}$ is the parameter of the $ABCD_m$ matrix of the graphene-loaded open discontinuity. Then the graphene sheet impedance is extracted by the following formula

$$Z_{graphene,square} = \frac{Z_{C,parasitic,series} Z_{series}}{Z_{C,parasitic,series} - Z_{series}} \times N \quad (6.4)$$

where $N=S/L$ is the number of parallel squares the current flows through the device (Fig. 6.9).

The averaged graphene sheet resistance is plotted in Fig. 6.13. In this graph, 18 averaged measurements are presented, collected from 6 identical devices for each one the 3 different configurations (Table 6.2). The imaginary part of the calculated graphene impedance is negligible; hence, disregarded. Each of the three CPW configurations (Table 6.2) exhibits different $Z_{capacitance}$ values due to different geometrical features, thus measured S-parameters are expected to differ for the various configurations. However, the calculated graphene sheet resistance should be the same for all devices across the measurement band, since graphene properties are independent of the switches' topological configurations. Using different switch variations reduces the measurement uncertainty since the samples are considered less correlated [108]. Additionally, Table 6.3 presents the measured sheet resistance in comparison with already published results, thus verifying the robustness of the proposed nanofabrication process and measurement setup.

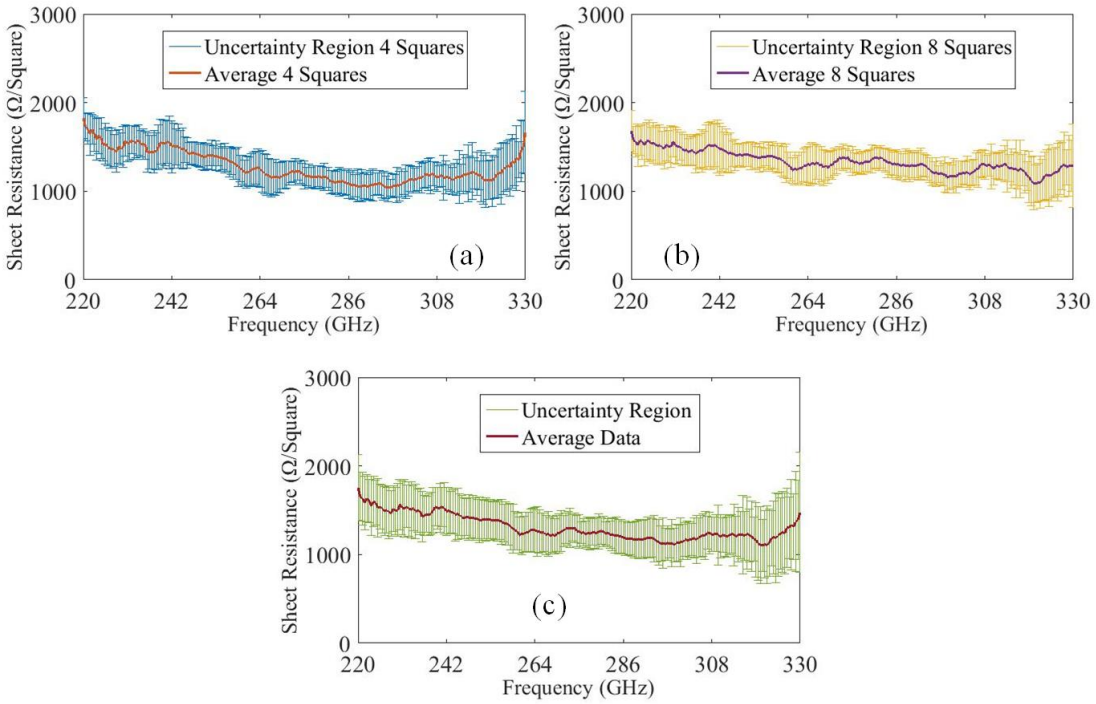

Fig. 6.13 The acquired sheet resistance of graphene in the 220-330 GHz range: (a) 4 squares, (b) 8 squares, and (c) averaged data. The uncertainty region in all figures includes both the measurement error and the device variability.

Table 6.3

Reported Graphene Sheet Resistances

Sheet Resistance (Ω/□)	Frequency Range (GHz)	Measurement Configuration	Reference
1100	1-20	In-plane	[81]
1260	0-110	In-plane	[109]
1452	220-330	In-plane	This Work
1600	200-1000	Out-of-plane	[77]

1490	250-2000	Out-of-plane	[78]

B. Tuning graphene sheet impedance using ion gel gating

In this sub-section, the graphene sheet resistance is characterized under various external DC biasing voltages. As shown in Fig. 6.14, ion-gel is a polymer that contains a high concentration of ions [110]. Using external DC biasing between the ground and the signal conductors of the CPW, a thin layer of ions is created on the top of the graphene shifting the Fermi energy level, thus changing its sheet resistance. Ion-gel has been exploited mostly in out-of-plane THz metasurfaces [77][78], due to its low losses and fabrication simplicity. However, none of these studies characterizes the ion-gel properties in these frequencies. Specifically, identifying the losses of ion-gel in the mmWave/THz spectrum is important for the design of graphene-controlled devices that utilize ion gel gating. In Fig. 6.14c the measured ion-gel losses are given versus frequency measured in the 220-330 GHz band for the first time. To measure the ion-gel losses, a thin ion-gel layer was deposited over a CPW transmission line and the data was normalized using the empty CPW line measurement (response calibration). The measured ion-gel loss is approximately 5 dB/mm across the W.R 3.4 band.

For the fabrication of the ion-gel, a three-part recipe was used. Specifically, a polymer {Poly(styrene-b-ethylene oxide-b-styrene)}, an ionic liquid {1-Ethyl-3-methylimidazolium bis(trifluoromethylsulfonyl)imide}, and a solvent (ethyl acetate), were mixed, with a weight ratio of 1%-9%-90%. Afterward, the mixture was stirred on top of a hotplate (50-60^{o}C) at 300 rounds-per-minute approximately for 30 minutes. The final

solution has the viscosity of water (1 cp). After the mixture is stirred, a fine (80 μm diameter) syringe was used to deposit the solution over the graphene devices. The ion gel gates were left one day at room temperature to ensure the evaporation of any excess liquids.

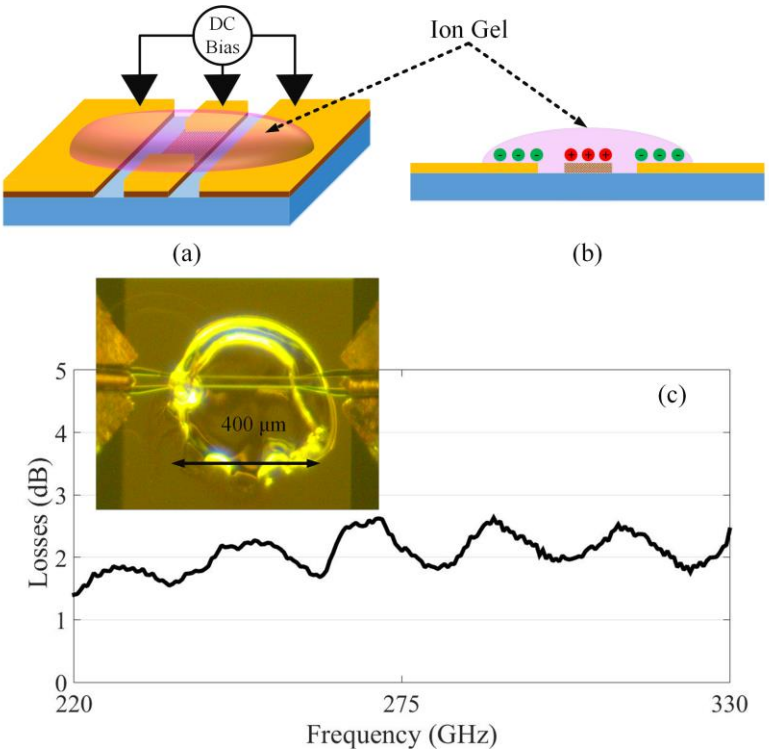

Fig. 6.14 The ion-gel biasing scheme: (a) The biasing is applied through the ground and center conductors of the CPW line and (b) the ion distribution when the external biasing is applied. Ions form a thin layer over the graphene, creating a vertical biasing electric field. (c) Measured insertion losses of the ion-gel in the 220-330 GHz band for the first time. The diameter of the deposited ion-gel is approximately 400 μm. The ripples on the measured losses are caused by the multiple reflections caused by the ion-gel. Inset: The on-wafer measurement configuration.

Using ion-gel gating the graphene sheet impedance is tuned leading to different S_{21} responses, as shown in Fig. 6.15. As expected, the scattering parameters of each configuration vary due to the different parasitics. In addition, the measured graphene sheet impedances were extracted by the different configurations and averaged. The averaged graphene sheet impedances versus the biasing voltage are given in Fig. 6.15c. Alongside

the on-wafer data obtained by the proposed setup, the sheet impedance acquired in [77][78] using out-of-plane configurations are presented, validating the robustness of the proposed nanofabrication method.

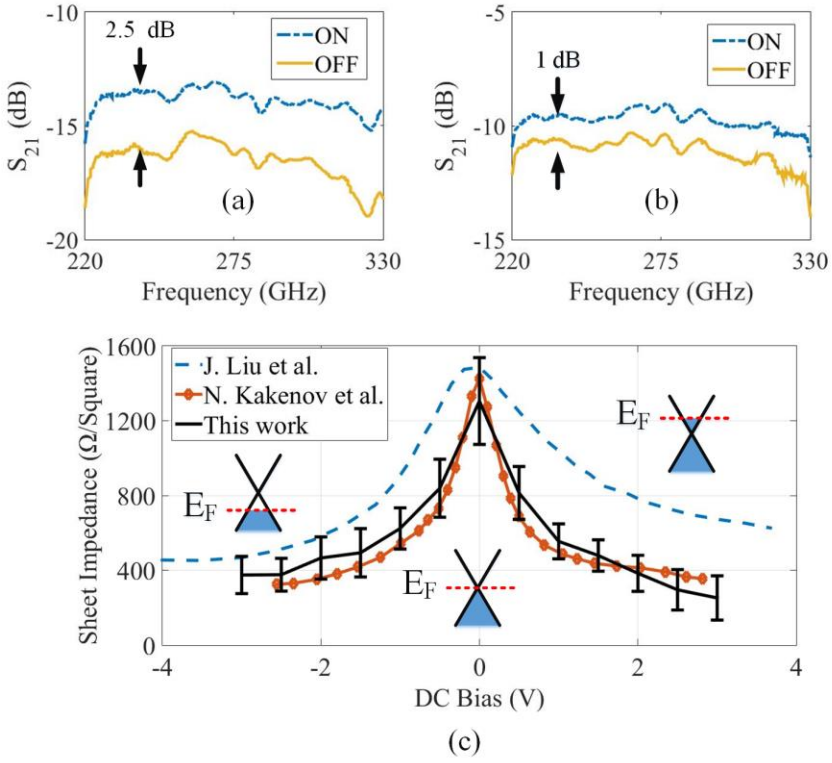

Fig. 6.15 (a)-(b) The measured calibrated S_{21} values for different graphene switch configurations under biasing. (c) The measured sheet impedance values in comparison with out-of-plane measurements.

VII. Conclusions of Chapter 6

In this Chapter, a high-yield nanofabrication process for the development of large-scale, tunable, graphene-based devices was presented, and an on-wafer graphene characterization process in the 220-330 GHz band, was carried out. Such graphene switches could be embedded in large-scale configurations with relatively low system

complexity and cost, compared to CMOS and SiGe technologies. Using the proposed nanofabrication method, more than 90% yield over a 1.5cm^2 area is acquired (1 cm × 1.5 cm) for the development of electrically large graphene-modulated apertures. Additionally, by using an in-house on-wafer TRL calibration, the graphene sheet impedance was measured in the W.R 3.4 band, both with and without external DC biasing. The presented data are in good agreement with the already published results, thus validating the proposed nanofabrication and measurement processes. Further steps towards devising graphene-actuated switches would include the patterning of ion gel gates using photolithography and/or stencil masks.

The measurements reveal that the graphene intrinsic performance is plagued by fabrication imperfections, limiting the exhibited biased/unbiased sheet impedance ratio. Specifically, as shown through a series of mmWave/THz on-wafer measurements, graphene's sheet impedance ratio does not exceed 4-5. To accurately design graphene-loaded devices (e.g. switches) the measured sheet impedances for various biasing schemes should be considered. Moreover, when implemented in a switching device, the performance of the switch is affected by the parasitic components (e.g. capacitances) of the device. These parasitics depend solely on the geometrical features of the device (Z_o, S, W, and N) and not on the graphene sheet impedance. Therefore, in Chapter 7, the measured graphene sheet impedance values are used in a parametric study of graphene-actuated switches realized on coplanar transmission lines. The analysis of Chapter 7 proposes accurate equivalent circuit models for the simulation of graphene switching topologies. These models incorporate the measured sheet resistance values (presented in this Chapter), to identify the optimum switch design. The optimized configurations enable the

development of efficient reconfigurable mmWave/THz devices (e.g. phase shifters) and RRSs (reflectarrays).

CHAPTER 7

Modeling of Millimeter-wave and Terahertz Thin-Film Switches for On-Wafer Coplanar Transmission Lines

This Chapter focuses on the study of graphene loaded (GL) coplanar transmission line (TL) switches, as illustrated in Fig. 7.1. As discussed in Chapter 6, graphene is a 2D material that exhibits sheet resistance tunability over a great bandwidth (DC-2 THz) with the use of external biasing fields, similar to field-effect-transistors. Additionally, the implementation of large-scale graphene-loaded RRSs has been enabled with the development of the high-yield nanofabrication process presented in Chapter 6. This novel nanofabrication method offers more than 90% yield over a large area. Moreover, as demonstrated through a series of on-wafer measurements, graphene exhibits sheet impedance tunability between $R_{biased}=300\ \Omega/\square$ and $R_{unbiased}=1{,}500\ \Omega/\square$. This sheet impedance modulation can be leveraged to implement mmWave/THz graphene-actuated switches that can be monolithically integrated with large-format reconfigurable apertures. However, as observed from the measurements of Chapter 6-VI, the geometrical features of the switch topology severely affect its performance due to the incorporated parasitics. Thus, this Chapter investigates the graphene switch performance based on the topological parameters (e.g. device width/length and configuration: series/shunt), aiming to identify the optimum switch configuration that would enable the devise of large-format efficient mmWave/THz reconfigurable apertures.

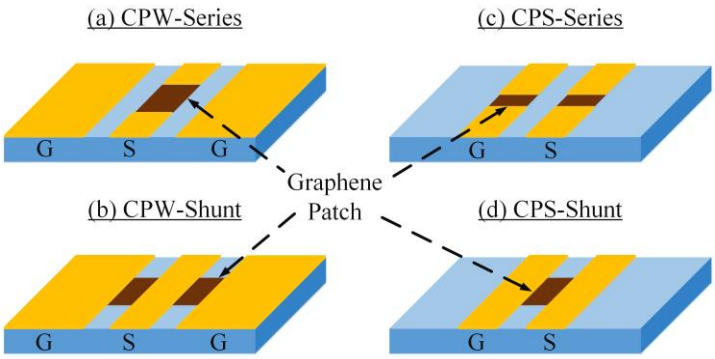

Fig. 7.1 The proposed CPW and CPS graphene loaded transmission line configurations.

I. Millimeter-wave/terahertz graphene switches

Several studies propose graphene-loaded topologies including attenuators, switches, and reconfigurable power dividers [75]-[83]. These works present both experimental designs and/or theoretical studies for series or shunt configurations. However, insight on the expected performance based on the configuration (series versus shunt topology) and the design parameters (e.g. characteristic impedance−Z_0 and graphene shape) is missing from the existing literature. Specifically, the achievable ON/OFF ratio and insertion loss, when graphene is embedded in a switching topology, can differ from the sheet impedance ratio. For example, in [79], measurements up to 110 GHz of a shunt coplanar waveguide (CPW) graphene switch are presented, demonstrating the switching performance does not exceed 2 dB (IL ≈ 10 dB). Conversely, in [81], a tunable graphene-based series microstrip attenuator is measured up to 20 GHz achieving a switching ratio of 3-5 dB (IL ≈ 5 dB). Moreover, in Chapter 6-VI-B, two different series graphene switch configurations were measured at the 220-300 GHz band, exhibiting ratios of 1 and 2.5 dB,

respectively. Thus, what is the maximum performance of graphene-based switches, and under what limitations?

II. Modeling methods for graphene switches

This Chapter methodically studies mmWave/THz GL TL switches and reveals the dependence of their performance on design parameters, including transmission line characteristic impedance, graphene patch geometry, scaling effects, and topology (series versus shunt). This is not the first-time equivalent circuit models are used to study graphene-actuated switches. Specifically, existing studies use equivalent models for graphene devices, though without presenting any parametric analysis [81]-[83] that would help identify the optimum graphene-switch topology. Namely, in [81] an equivalent model is used to extract the graphene sheet impedance values from the measured S-parameters of a microstrip attenuator. Moreover, in [82], an equivalent model approach is exploited to identify the losses in GL TLs, by carrying out full-wave simulations and then using the ABCD parameters to extract the complex TL characteristics (complex-propagation constant and -characteristic impedance) for different frequencies. Finally, in [83] a one-port GL device is proposed, and an equivalent model is used to extract the graphene sheet impedance values without investigating the effects of patch geometry on device performance. Nevertheless, no study examines in-depth the mmWave/THz switching performance with respect to the affecting parameters.

In this Chapter, graphene is modeled using the measured (220-330 GHz) sheet impedance values of Chapter 6 (R_{biased}*=300 Ω/□* and $R_{unbiased}$*=1,500 Ω/□*), instead of theoretical models, to include all the physical phenomena that affect the switching

performance (e.g. lattice defects, grain size, etc.). As such, this study identifies the optimal GL TL geometry that offers the best switching performance with limited graphene biased/unbiased ratio. This is achieved by incorporating the measured graphene sheet resistance in the theoretical equivalent models of the CPW and CPS TLs. This study is focused on GL coplanar waveguides and striplines (CPW and CPS) switches since these TLs are frequently used in mmWave/THz integrated circuits (ICs) [111]. Finally, modeling the GL TL CPW and CPS switches, with the use of accurate equivalent models, accounts for all the frequency-dependent parasitic effects, thus revealing the actual performance of the proposed mmWave/THz switches.

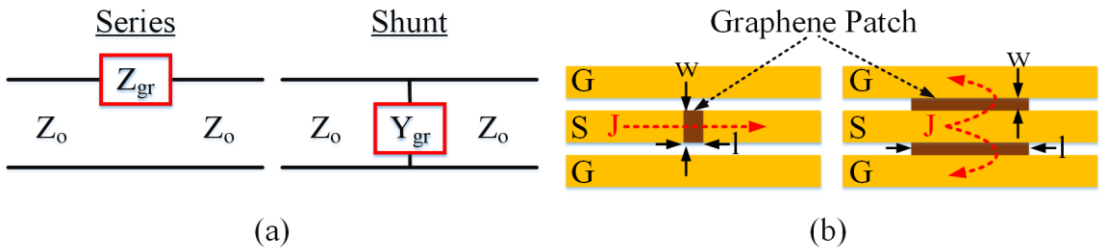

Fig. 7.2 (a) Graphene switches as lumped models (series and shunt) without parasitics and (b) the equivalent CPW topology paradigm (top view).

A. Scale-less modeling of graphene switches

This section demonstrates the performance dependence of graphene-loaded transmission line switches based on graphene shape, characteristic impedance, and topology (series versus shunt). The equivalent circuits of the series and shunt graphene switches are depicted in Fig. 7.2a and their respective scattering parameters [88] are given by

$$S_{11}^{series} = \frac{\frac{Z_{gr,\,sheet}}{N}}{2Z_o + \frac{Z_{gr,\,sheet}}{N}} = S_{22}^{series} \qquad (7.1.1)$$

$$S_{21}^{series} = \frac{2Z_o}{2Z_o + \frac{Z_{gr,\,sheet}}{N}} = S_{12}^{series} \qquad (7.1.2)$$

$$S_{11}^{shunt} = \frac{-Z_o}{\frac{2Z_{gr,\,sheet}}{N + Z_o}} = S_{22}^{shunt} \qquad (7.2.1)$$

$$S_{21}^{shunt} = \frac{2\frac{Z_{gr,\,sheet}}{N}}{\frac{2Z_{gr,\,sheet}}{N + Z_o}} = S_{12}^{shunt} \qquad (7.2.2)$$

where $Z_{gr,sheet}$ is the sheet impedance of graphene in Ω/□ (R_{biased}*=300 Ω/□* and $R_{unbiased}$*=1,500 Ω/□*) and *N* is the number of graphene squares oriented in a line vertical to the current flow (N_{series}*=w/l* and N_{shunt}*=l/w*). Considering that the graphene gate has a uniform current distribution due to small electrical size, the number of squares defines the total lumped impedance; for example, if graphene is 5 squares, then R_{biased}*=60 Ω* and $R_{unbiased}$*=300 Ω*. Moreover, in (7.1) and (7.2) the S-parameters depend only on the number of squares *N* (ratio of *w* over *l*); thus, these equations do not account for any scaling effects, which are thoroughly presented in the following sections.

The series (shunt) topology is in ON (OFF) state when graphene is biased and exhibits low impedance, thus leading to high (low) S_{21}. On the opposite, the series (shunt) switch is OFF (ON) when graphene is unbiased-(high impedance) and the S_{21} is low (high). The two switching performance metrics of interest are: 1) insertion loss (S_{21}) for the ON state and 2) the S_{21} ratio between the ON and OFF states. Typically, improving the former reduces the latter and vice-versa. Therefore, switch design becomes a compromise between insertion loss and ON/OFF ratio.

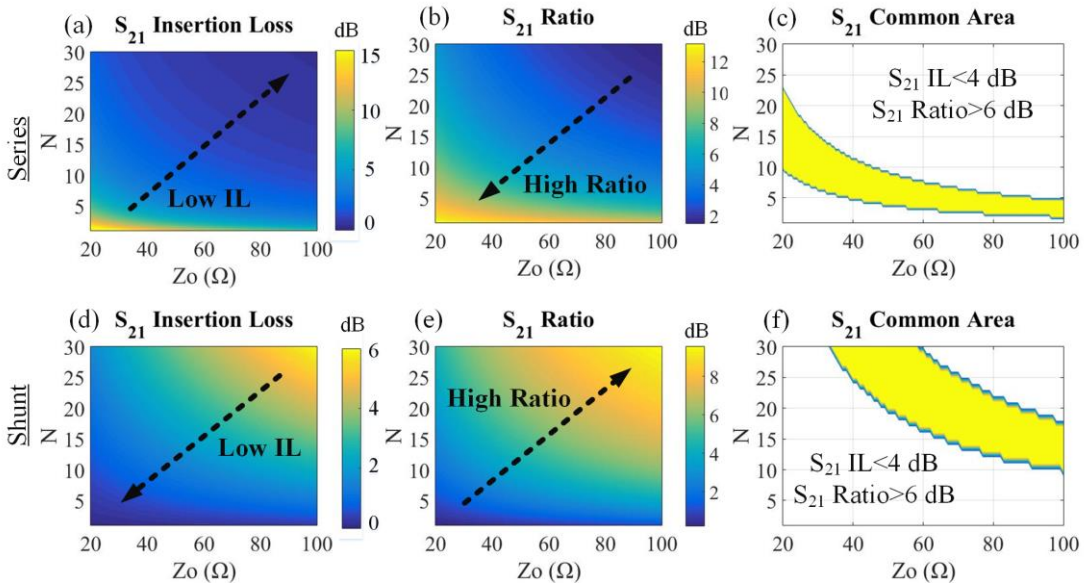

Fig. 7.3 The series/shunt switch topology (lumped): (a)/(d) Insertion loss, (b)/(e) ON/OFF ratio, and (c)/(f) the common area for given specifications.

The inverse proportionality between the switching ratio and the IL is also evident when simulating the topologies for variable N and Z_0, as depicted in Figs. 7.3a-b,d-e. Moreover, for specific switch operation (e.g. IL < 4 dB and R > 6 dB), the range of {N, Z_0} which satisfies these conditions, is identified in Fig. 7.3c and f.

The results of Fig. 7.3 demonstrate that both topologies can exhibit similar performance for the same graphene sheet impedance ratio (5 in this case). For example, if Z_0=*60 Ω* and IL = 3 dB, both configurations can exhibit a maximum ON/OFF ratio of 7 dB (for different squares – N). However, as shown in the latter sections, the comparison is not always accurate, since the modeling of this section does not include any scaling effects that limit the performance due to the presence of parasitics. The effects of these parasitics are pronounced in the mmWave/THz frequencies since they offer a better path for the currents that flow through the switch, thus mitigating the performance.

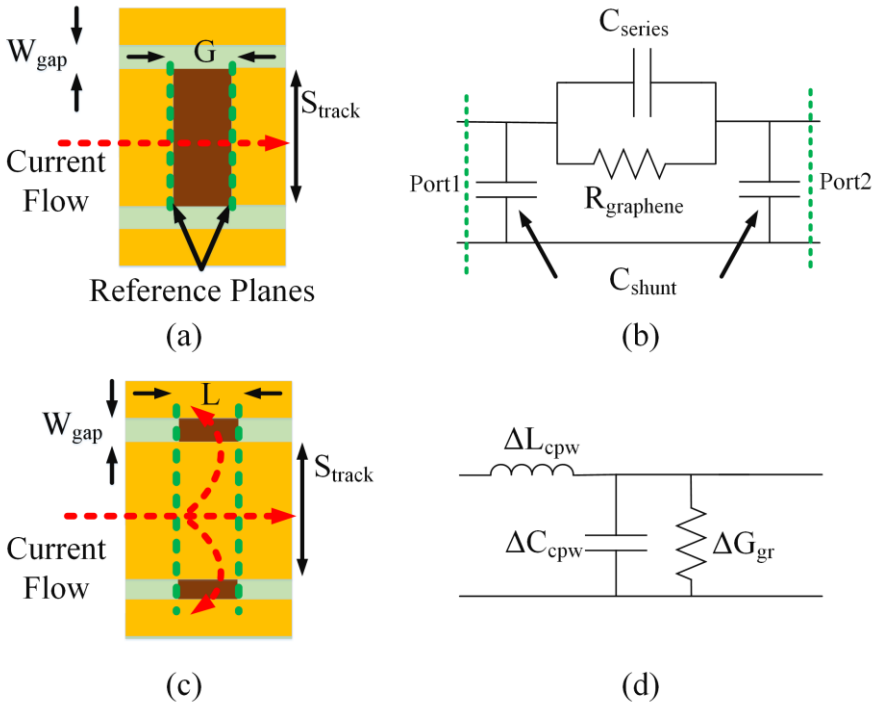

Fig. 7.4 The CPW (a) series and (c) shunt switch configurations (top-view) and in (b) and (d) the respective equivalent circuits.

III. Graphene loaded CPW switches

In this section, the study of section-7-II is expanded for series and shunt CPW switch topologies, by including the scaling factors in the equivalent circuit models. The scaling factor affects the device parasitics (neglected in section-7-II). Thus, this extended investigation reveals the effects of the parasitics on the switching performance. The topologies of the CPW switches are depicted in Fig. 7.4.

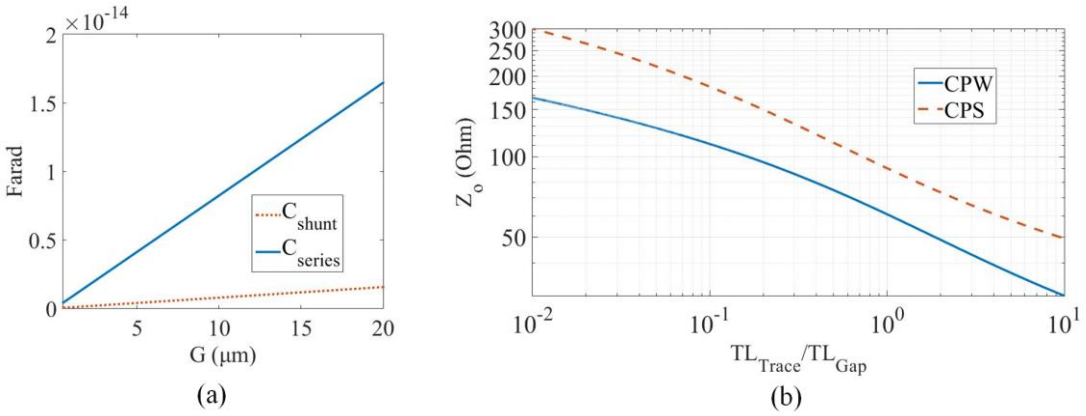

Fig. 7.5 (a) The calculated C_{series} and C_{shunt} versus G for a 50 (Ω) CPW line −S_{track}/ W_{gap}=*1.67* and N=*5* (N=S_{track}/G)− and (b) the CPW and CPS characteristic impedance versus the TL trace over gap ratio [112].

A. Series CPW Topology

The series GL-CPW switch is modeled with an equivalent Π-network, as shown in Fig. 7.4b. The parasitic capacitances of the configuration depend on the geometrical features of the discontinuity [107]. The graphene sheet is modeled using a lumped resistor (Fig. 7.4b). The ABCD parameters of the series GL-CPW switch are [88]

$$ABCD = \begin{bmatrix} 1 + \frac{Y_p}{Y_s} & \frac{1}{Y_p} \\ 2Y_p + \frac{Y_p^2}{Y_s} & 1 + \frac{Y_p}{Y_s} \end{bmatrix} \qquad (7.3)$$

where,

$$Y_s = \frac{X_s + R_{gr}}{X_s R_{gr}}, \quad Y_p = \frac{1}{X_p} \qquad (7.4)$$

and,

$$X_s = \frac{1}{i\omega C_{series}}, \quad X_p = \frac{1}{i\omega C_{shunt}}, \; and \; R_{gr} = \frac{Z_{gr,sheet}}{N} \qquad (7.5)$$

where, C_{series} and C_{shunt} are the parasitic capacitances of the switch (Fig. 7.4a-b) and depend on the geometrical features of the device (N, G, S_{track}, and W_{gap}). Their closed-form expressions are given by [107]

$$C_{shunt} = 4\varepsilon_0\varepsilon_{eff}\left[\frac{K(k_3)}{K(k_3')}K(k)\frac{S}{2} - \frac{K(k)}{K(k')}L_m\right] \qquad (7.6a)$$

$$C_{shunt} = 4\varepsilon_0\varepsilon_{eff}\left[\frac{K(k_2)}{K(k_2')} - \frac{K(k_3)}{K(k_3')}\right]K(k)\frac{S}{2} \qquad (7.6b)$$

where $K(k)$, L_m, S, and ε_{eff} depend on the geometry of the CPW discontinuity and are detailed in [107]. Figure 7.5a shows the dependence of the parasitic capacitances for the series CPW switch versus G. As such, the capacitance values are decreasing as the device is scaled down. This scaling effect enables better performance for smaller G values in series topologies, as shown in the latter parts of this section. However, the fabrication of small devices requires costly nanofabrication methods that hinder their proliferation.

To evaluate the accuracy of the models, full-wave simulations are carried out using a commercial finite element method (FEM) solver [113]. In these simulations, the number of graphene squares (N) and CPW Z_0 are fixed (fixed ratio of S_{track}/W_{gap} as shown in Fig. 7.5b), and device length/scaling factor (G) is varied. The obtained results of Fig. 7.6 verify that the model has good performance for various gap size (G) values. The discrepancy observed in Fig. 7.6c for high G values is due to the model inaccuracies of the parasitic capacitances obtained from [107]. Namely, the effect of fringing fields is neglected in the models of [107], thus they become inaccurate for greater G values. Moreover, if the

simplistic approach of section 7-II was followed, the S-parameters (thus IL and ON/OFF ratio) of the devices would be constant regardless of the scaling factor *G*, since (7.1)-(7.2) depend only on *N* and Z_0.

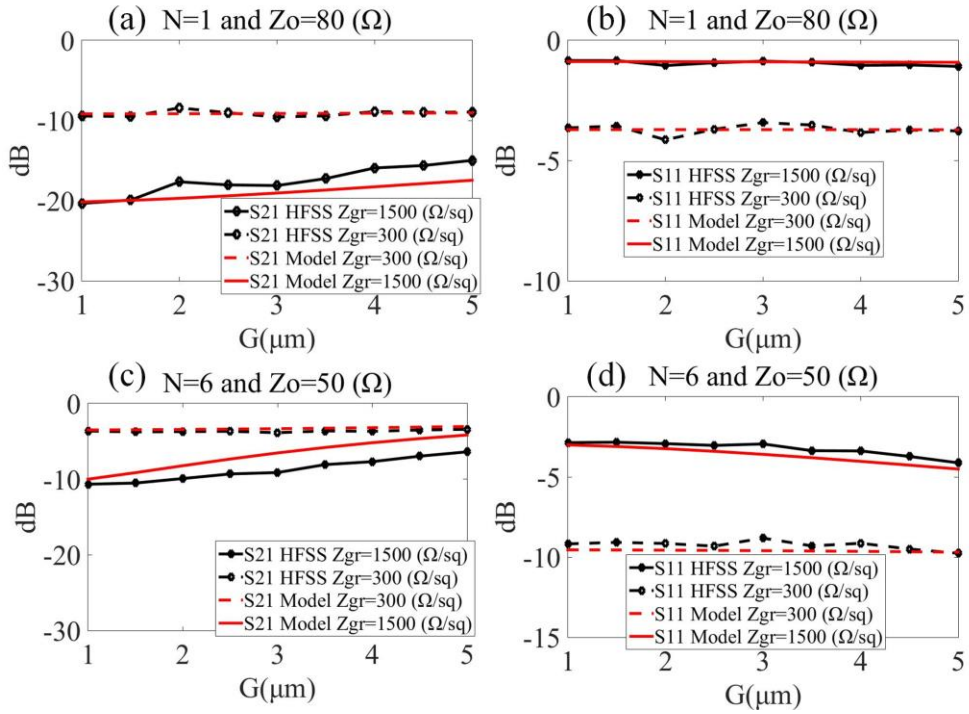

Fig. 7.6 The S_{21} and S_{11} comparison between the proposed series GL-CPW switch model and full-wave simulations for various configurations.

The simulation results are de-embedded using a thru-reflect-line (TRL) calibration, eliminating any mismatch effects of the FEM solver's ports. As such, for each of the *G* values, four configurations are simulated (3 TRL standards and 1 series GL-CPW switch). These simulations are carried out at 300 GHz and the substrate is high resistivity silicon ($\varepsilon_r=11.9$, $h=200\ \mu m$) (as for the rest of the Chapter), leading to dense meshes that increase the total simulation time. Namely, to obtain the S-matrix for each *G*-step of Fig. 7.6, approximately 3 minutes are needed (on a system with an Intel Xeon 6-core processor and

64 GB RAM). Therefore, if a design demands optimization based on N, Z_0, and G, with a fine step, the total full-wave simulation time becomes a bottleneck. Thus, the proposed models are an invaluable tool for the design of GL switches.

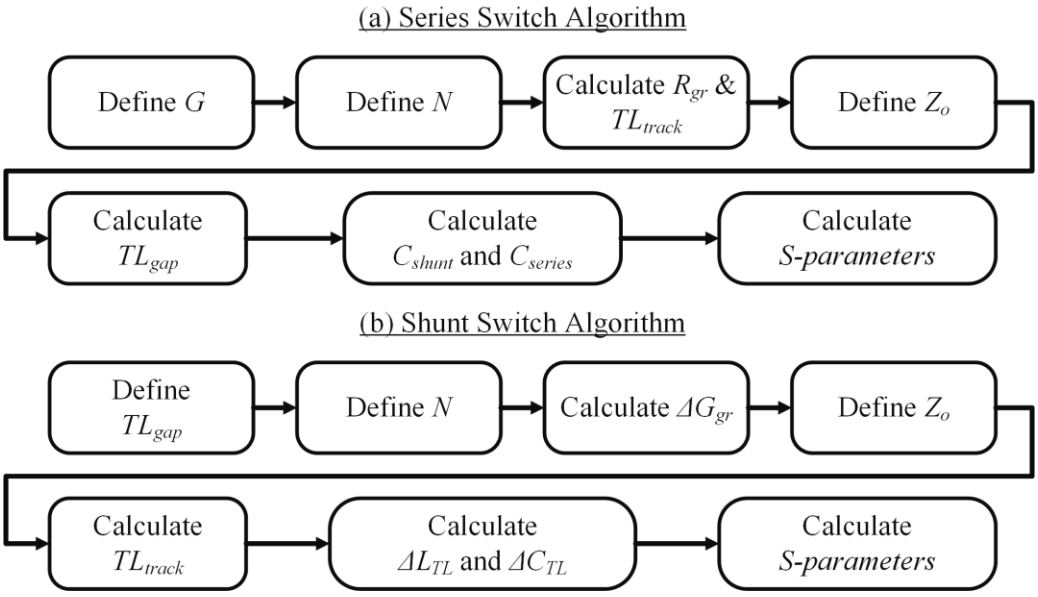

Fig. 7.7 The algorithms (a) series and (b) shunt, used to analyze the multi-dimensional problems based on the scaling factors, graphene squares, and Z_0.

The results of Fig. 7.6 are a small subset of the available topologies based on Z_0, N, and G parameters. Hence, to identify the performance based on all the incorporated parameters; a scan for all the available combinations {G, N, Z_0} needs to be carried out. Explicitly, using the algorithm given in Fig. 7.7a, the S-parameters of the series GL-CPW switch are calculated for all the available variations. Z_0 (Fig. 7.5) is scanned between 20 and 120 Ω (S_{track}/W_{gap} ratio from 0.05 to 12), leading to low radiation losses and practically sized features [112]. The obtained results are a 5-dimensional matrix (assuming the devices

are reciprocal) that contains all the S-parameters for each available combination of {G, N, Z_0}, one for every switch state (ON/OFF).

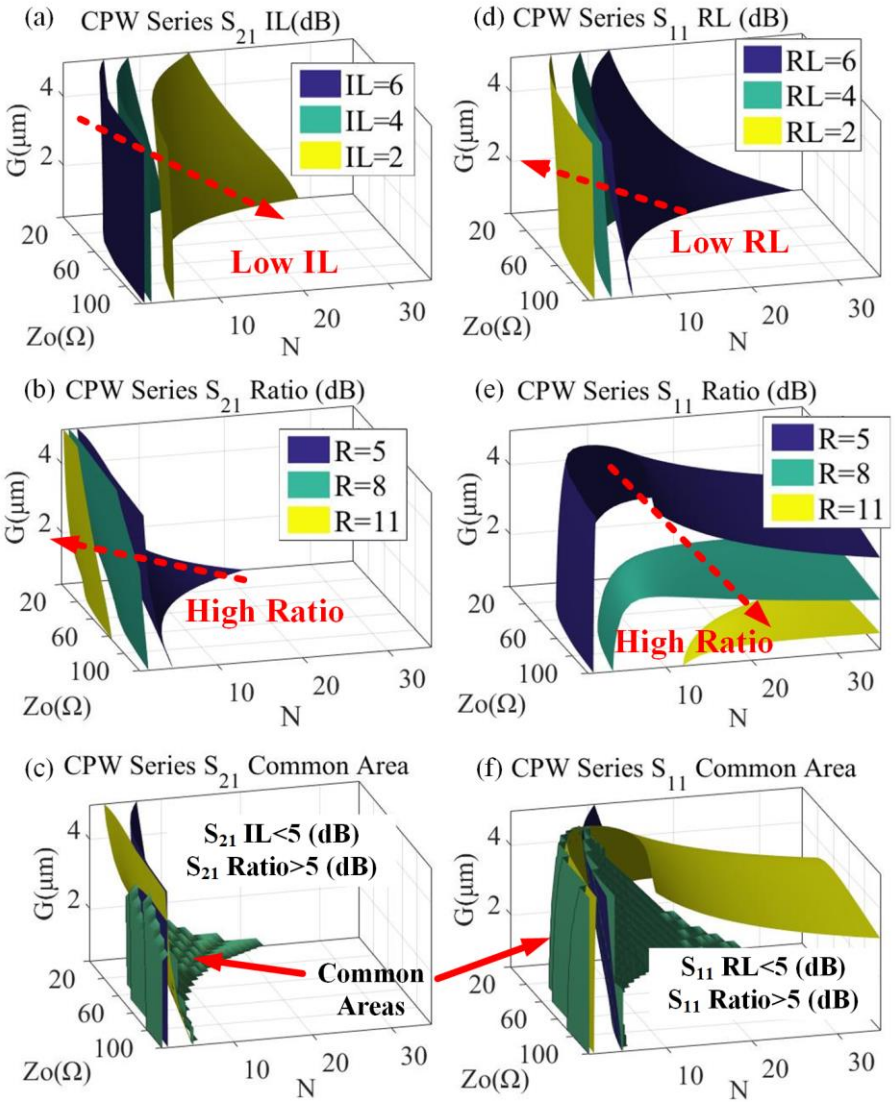

Fig. 7.8 The S_{21}/S_{11} parameters of the series GL-CPW switch: (a)/(d) insertion/return loss, (b)/(e) ON/OFF ratio, and (c)/(f) common locus for given criteria.

To observe the dependence of the series switch performance on the topological features, the IL and switching ratio are examined (Fig. 7.8). For example, in Fig. 7.8a, the surfaces of constant IL (S_{21} ON) values are plotted; each point on these surfaces provides

a combination of {G, N, Z_0}. Similarly, in Fig. 7.8b, surfaces of constant S_{21} ON/OFF ratio values determine the respective combination of {G, N, Z_0}. These results reveal that increasing the number of graphene squares N, decreases the IL but also worsens the switching ratio. Similar trends are noticed for the other two parameters G and Z_0, indicating that there is large design flexibility to achieve the desired specifications.

Figure 7.8c depicts the common area of {G, N, Z_0} that follows the exemplary specifications of IL<5 dB and switching ratio greater than 5 dB. These results suggest that the performance of the series GL-CPW switch depends on the gap size/scaling factor (G). Namely, slices of the common area (Fig. 7.8c) for different G values are given in Fig. 7.9. As expected, scaling the device size to smaller gap values decreases the parasitic effects, therefore, increasing the common area.

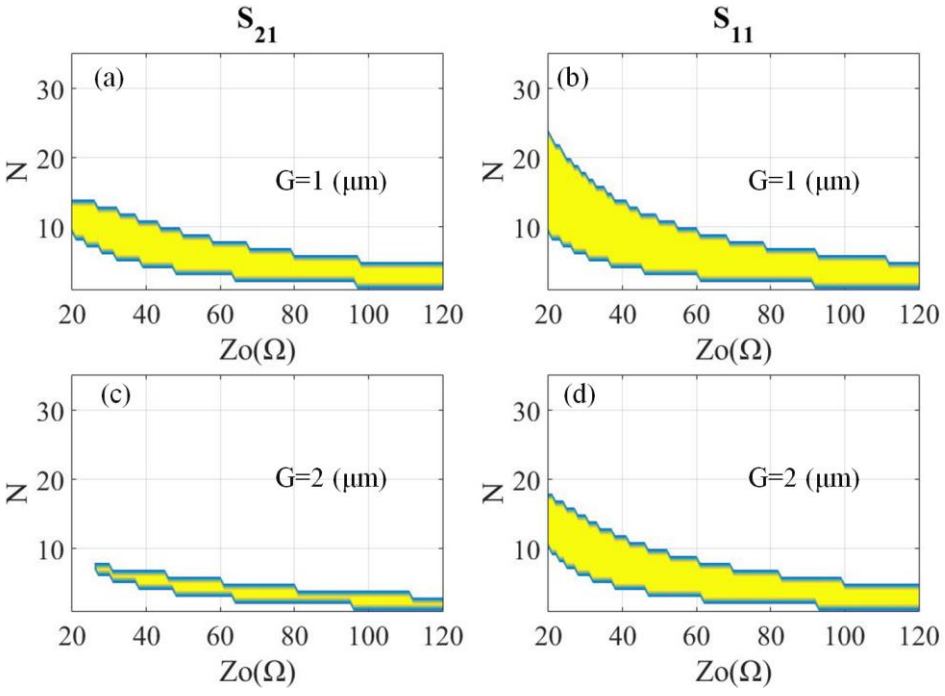

Fig. 7.9 The slices of the common areas of Fig. 7.8c and f, for different G values.

Examining the multi-dimensional data can be challenging to the designer and prioritizing specific parameters can help arrive faster in the desired switching topology. For example, by defining a desired/acceptable IL, the parameter space that satisfies the performance goal can be obtained. As such, Fig. 7.10 presents the ON/OFF ratio with respect to {G, N, Z_0} for fixed IL values, observing a tradeoff between the IL and ON/OFF ratio. These maps are very useful since the designer can identify the desired ON/OFF ratio for a given IL and obtain the geometrical characteristics of the topology. Additionally, using the proposed models more than 600,000 S-matrices are calculated, for all the {G, N, Z_0} combinations. These results are calculated in less than 15 minutes using the proposed equivalent models; however, the same time using full-wave simulations would result in several months of run time.

In the following sub-section, the case study of the shunt GL-CPW switches is presented and a comparison between the series and the shunt topology is carried out in terms of switching performance.

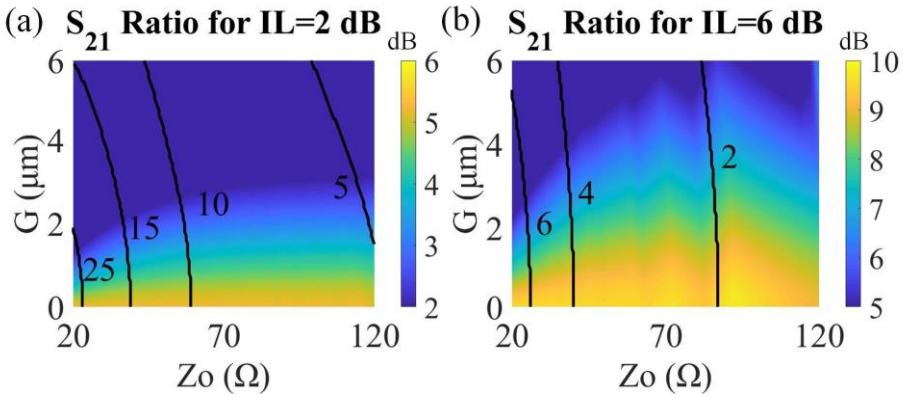

Fig. 7.10 The series GL-CPW switch 2D maps of the ON/OFF ratio for fixed IL. With black contour, the number of squares is noted.

B. Shunt CPW topology

This section presents the models for the shunt GL-CPW switch shown in Fig. 7.4c. In this design, the graphene monolayer is incorporated in the gaps of the CPW, and the switch is modeled as a distributed transmission line. Graphene is represented as a distributed admittance of $\Delta G_{gr}=2NL/Z_{gr,sheet}$. The complex propagation constant and Z_0 of the GL-CPW are given by [82]

$$\gamma_{gr} = \sqrt{(j\omega\Delta L)\left(\Delta G_{gr} + j\omega\Delta C\right)} \quad \text{and} \quad Z_{o,gr} = \sqrt{\frac{(j\omega\Delta L)}{(\Delta G_{gr}+j\omega\Delta C)}} \qquad (7.7)$$

where ΔL and ΔC are the distributed CPW (or CPS) components obtained by [112]. Thus, the ABCD parameters of the GL-CPW switch are [88]

$$ABCD = \begin{bmatrix} cosh(\gamma L) & Z_{o,gr}\, sinh(\gamma L) \\ \frac{sinh(\gamma L)}{Z_{o,gr}} & cosh(\gamma L) \end{bmatrix} \qquad (7.8)$$

To validate the accuracy of the proposed model, the analytical results are compared with full-wave simulations, as shown in Fig. 7.11. Similarly, to the series case, N and Z_0 are kept fixed and W_{gap} (scaling factor) is varied. The results of Fig. 7.11 verify the accuracy of the proposed shunt GL-CPW switch models since they are in good agreement with the full-wave simulations.

Following the algorithm given in Fig. 7.7b, the S-matrices for all the available $\{W_{gap}, N, Z_0\}$ combinations are obtained, and in Fig. 7.12 the 3D isosurfaces of the S_{21} are presented. Conversely, to the series case, the IL has an opposite trend with respect to N.

The common region of the S_{21} is given in Fig. 7.12c and is significantly larger for the shunt GL-CPW switch compared to the series topology.

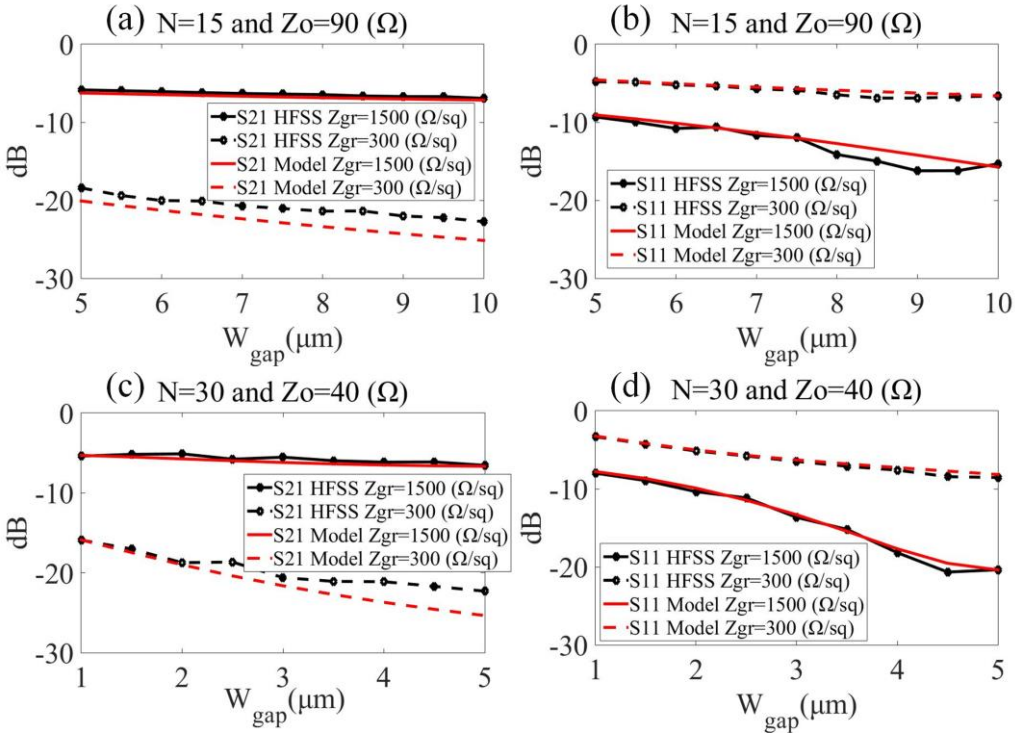

Fig. 7.11 The S_{21} and S_{11} comparison between the proposed shunt GL-CPW switch model and full-wave simulations for various configurations.

In Fig. 7.13 the slices of the common areas (Fig. 7.12c) for different W_{gap} values are given. Contrary to the series case (Fig. 7.9), the common area is not significantly limited by parasitics (series and shunt capacitances of Fig. 7.4b), hence offering greater flexibility for the design of GL switches. Besides, in Fig. 7.14 the S_{21} ON/OFF ratio for fixed IL values is given with respect to $\{W_{gap}, N, Z_0\}$. The results indicate that the switching performance improves with the larger scale of the devices, conversely to the series topology. Overall, the shunt topology offers better performance when considering

fabrication limitations. For example, for IL = 6 dB, the maximum achieved ratio is 19 dB for the shunt case, while the series is less than 10 dB. Hence, the results establish that the shunt switch design is preferable over the series in terms of IL and ON/OFF ratio.

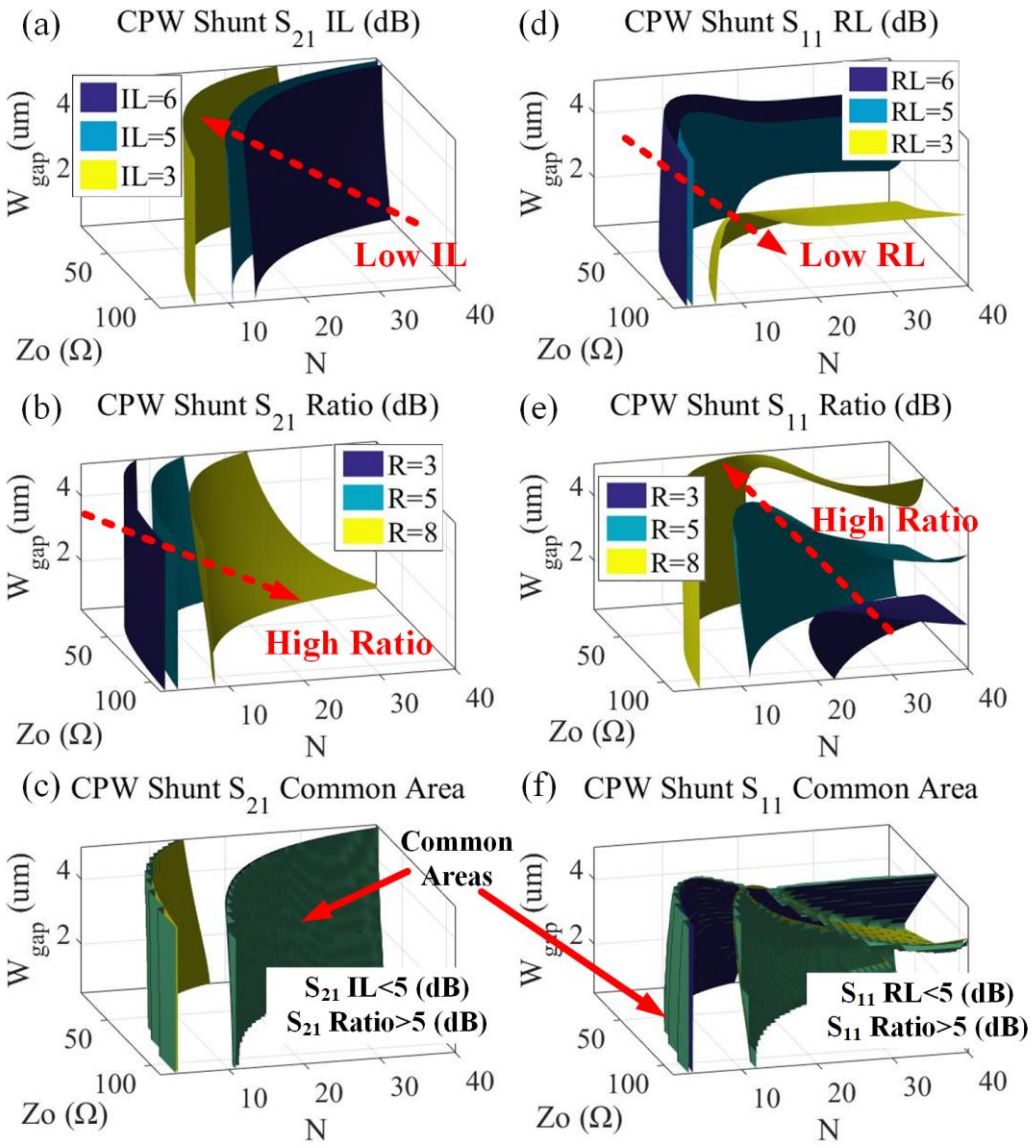

Fig. 7.12 The S_{21}/S_{11} parameters of the shunt GL-CPW switch: (a)/(d) insertion/return loss, (b)/(e) ON/OFF ratio, and (c)/(f) common locus for given criteria.

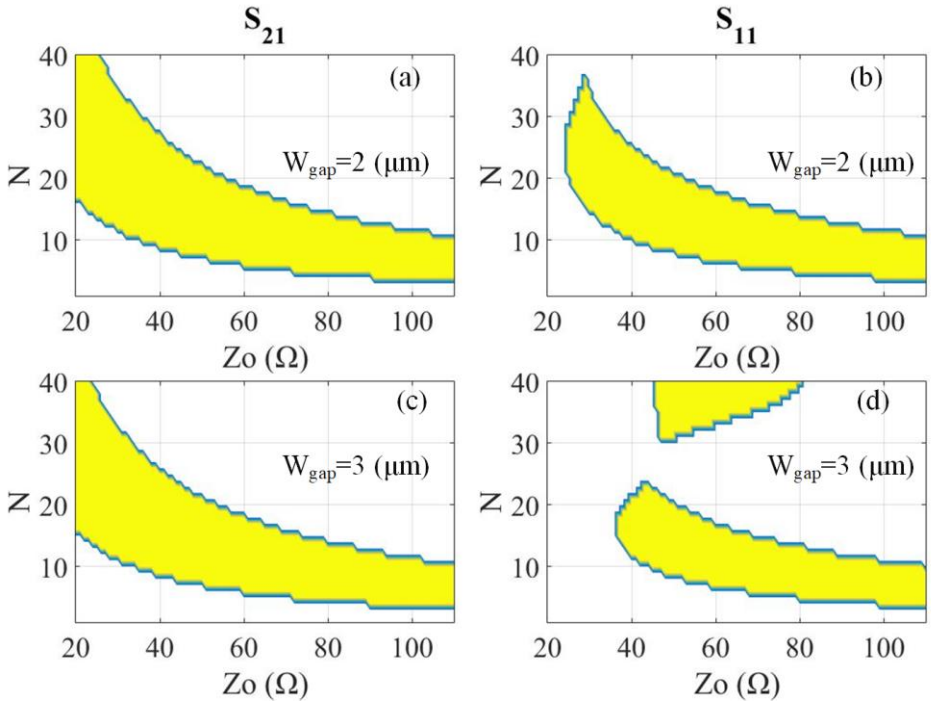

Fig. 7.13 The slices of the common areas of Fig. 7.12 for different W_{gap} values.

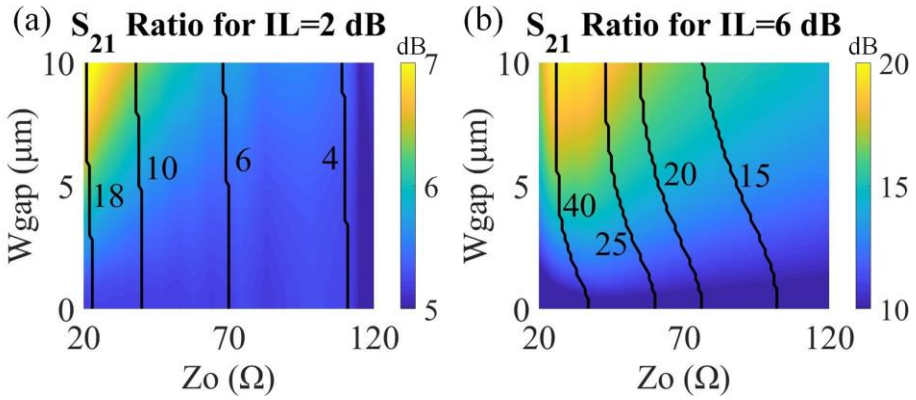

Fig. 7.14 The shunt GL-CPW switch 2D maps of the ON/OFF ratio for fixed IL. With black contour, the number of squares is noted.

All the results of this section are obtained using the proposed equivalent models and suggest that the shunt topology outperforms the series. Nevertheless, the following should be mentioned regarding the proposed designs: 1) The series case has better performance for smaller gap (G) sizes (< 1 μm), which requires advanced/costly nanolithography processes (e.g. electron beam lithography−EBL) for fabrication. On the other hand, the performance of the shunt increases proportionally to the scaling factor, thus alleviating the cost of complex fabrication processes. However, as the CPW TL W_{gap} size increases, radiation and higher-order mode losses become pronounced. As shown in Fig. 7.11, the proposed shunt CPW switch model has good agreement with the full-wave simulations that include all these losses, but for electrically larger designs, radiation losses and higher-order modes (not accounted for herein) are expected to limit the switching performance.

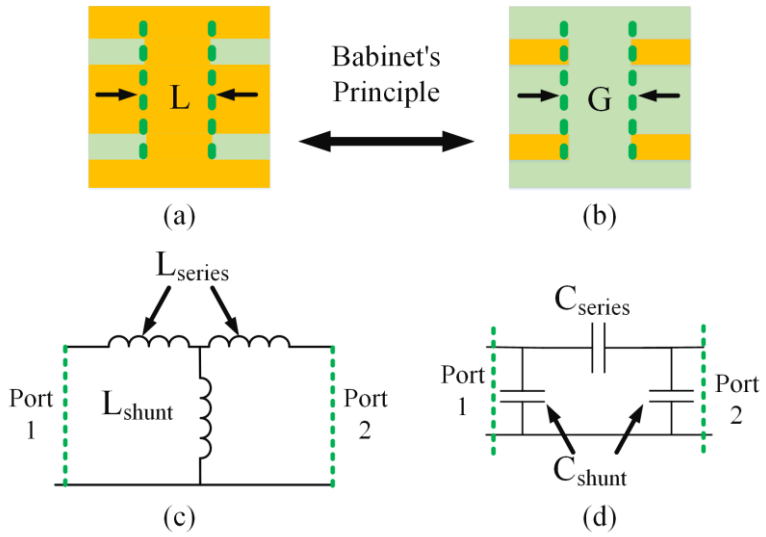

Fig. 7.15 (a) The CPW short discontinuity and (c) the equivalent circuit. Contrary, using Babinet's principle (b) the CPS gap discontinuity and (d) the equivalent circuit.

IV. Graphene loaded CPS switches

Another type of TL that is used in mmWave/THz planar ICs is coplanar stripline, especially for cases where a higher Z_0 is preferred (see Fig. 7.5). In this section, the theoretical modeling proposed in section 7-III is expanded for the study of series and shunt GL-CPS switches. Similarly, to the CPW topology, the switching performance is characterized based on the scaling factor, characteristic impedance, and graphene shape (squares).

A. Series CPS topology

To formulate the series GL-CPS switch, its equivalent circuit needs to be derived in the absence of graphene (parasitics), namely the series gap discontinuity. Unlike the CPW gap discontinuity, the CPS gap discontinuity's equivalent circuit models are not available in the existing literature in closed form. Nevertheless, the equivalent models can be extracted using Babinet's principle. The equivalent circuit of a shorted CPW is a T-network comprised of three inductors [107], as depicted in Fig. 7.15a and c. This topology is complementary to the CPS gap discontinuity (Fig. 7.15b and d). Hence, using Babinet's principle the equivalent circuit of the CPS gap discontinuity is modeled with a Π-network comprised of three capacitors. The expressions of the parasitic capacitances are obtained by [111]

$$C_{shunt} = \frac{\varepsilon_{eff}}{(120\pi)^2} L_{series} \quad and \quad C_{series} = \frac{\varepsilon_{eff}}{(120\pi)^2} L_{shunt} \qquad (7.9)$$

where, $\varepsilon_{eff}=(\varepsilon_r+1)/2$, ε_r is the dielectric constant of the substrate, and L_{shunt}/L_{series} are the inductances of the CPW short discontinuity that depend on the geometrical features of the structure and are given by [107]

$$L_{shunt} = W_{track}\left(log_{10}\left(\frac{1+k}{p}\right)+p-k\right), p = G/4W_{track} \quad (7.10a)$$

$$L_{series} = \frac{L_{sc}}{1.2193e^{-5.687t}+2.3921e^{-1.0937t}+1.65653e^{-0.0423t}} \quad (7.10b)$$

where the process of calculating t and L_{sc} is thoroughly detailed in [107].

The CPS parasitic capacitances exhibit the same trends versus the gap size (G), as in the series CPW case (Fig. 7.5a); thus, the switching performance is expected to deteriorate for small gap values.

The graphene patches placed in the gaps of the series GL-CPS switch are modeled with a resistor ($R_{graphene}$), as shown in Fig. 7.16. The proposed model shows very good agreement when compared with full-wave simulations for various switch parameters, as depicted in Fig. 7.17.

The switching performance with respect to the various parameters {G, N, Z_0} follows similar trends to the results presented for the series GL-CPW switch (see Fig. 7.8), thus not presented.

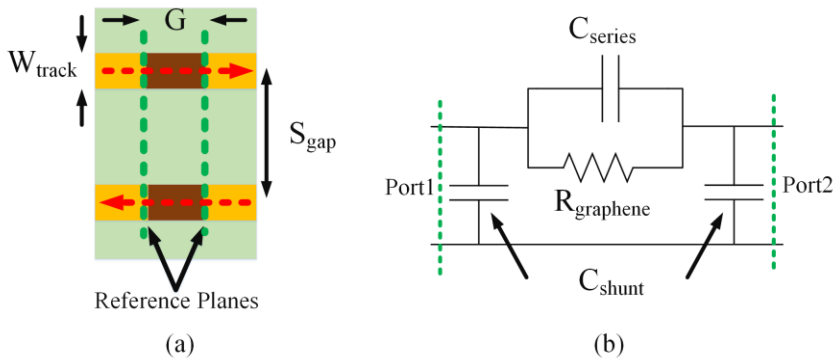

Fig. 7.16 (a) The series GL-CPS switch configuration (top-view) and (b) the equivalent circuit.

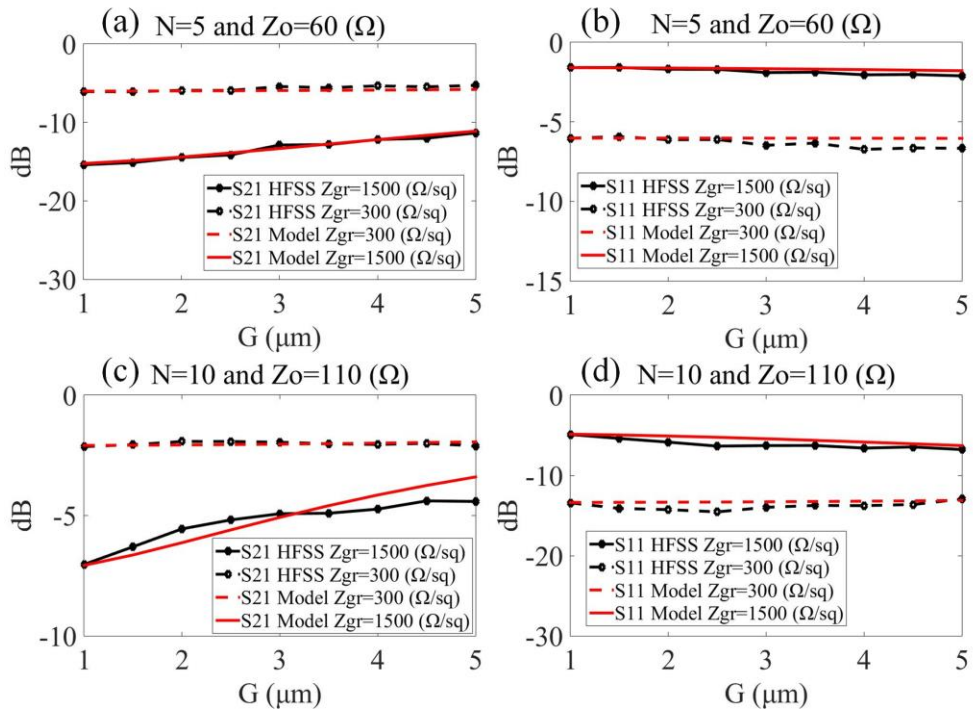

Fig. 7.17 The S_{21} and S_{11} comparison between the proposed series GL-CPS switch model and full-wave simulations for various configurations.

In Fig. 7.18, the S_{21} ON/OFF ratios are presented for two values of insertion loss.

When compared to the same switch parameters of the series CPW topology (see Fig. 7.10),

the series CPS S_{21} ratio falls off slower for larger G values and can have a potential advantage when gap minimum-dimensions are limited.

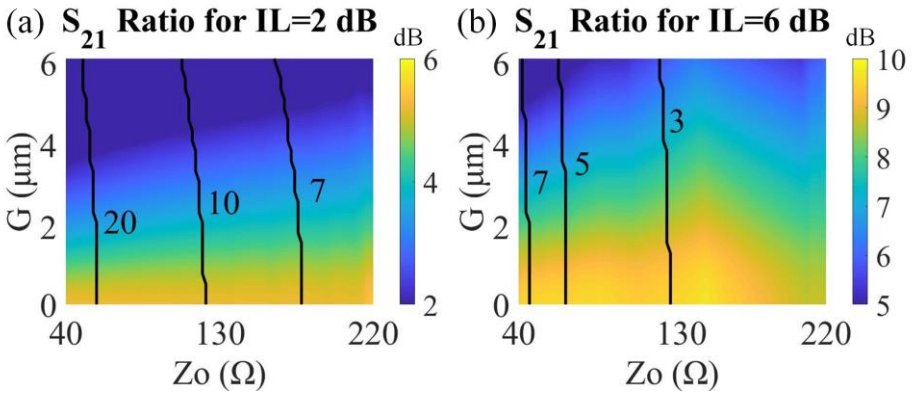

Fig. 7.18 The series GL-CPS switch 2D maps of the ON/OFF ratio for fixed IL. With black contour, the number of squares is noted.

B. Shunt CPS topology

In the shunt GL-CPS switch topology, the graphene is placed in the gap between the signal and the ground traces, as is illustrated in Fig. 7.19a. The expressions for the distributed components are given in (7.7). In this case, the graphene is modeled by a distributed admittance as $\Delta G_{gr}=NL/Z_{gr,sheet}$. The ABCD parameters are obtained using (6.8). The comparison between the full-wave simulations and the proposed model is depicted in Fig. 7.20, in which a very good agreement is observed.

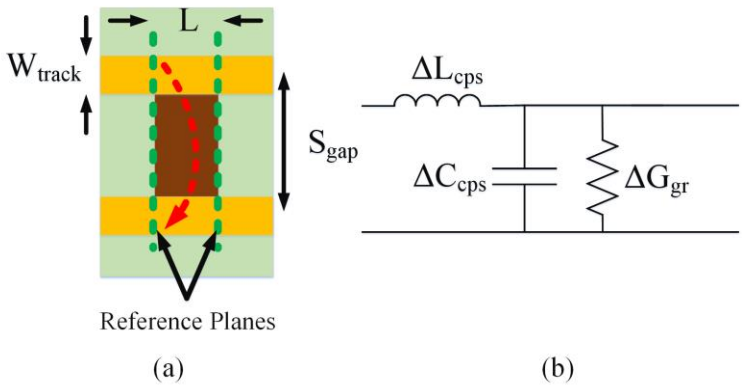

Fig. 7.19 (a) The shunt GL-CPS switch configuration (top-view) and (b) the equivalent circuit.

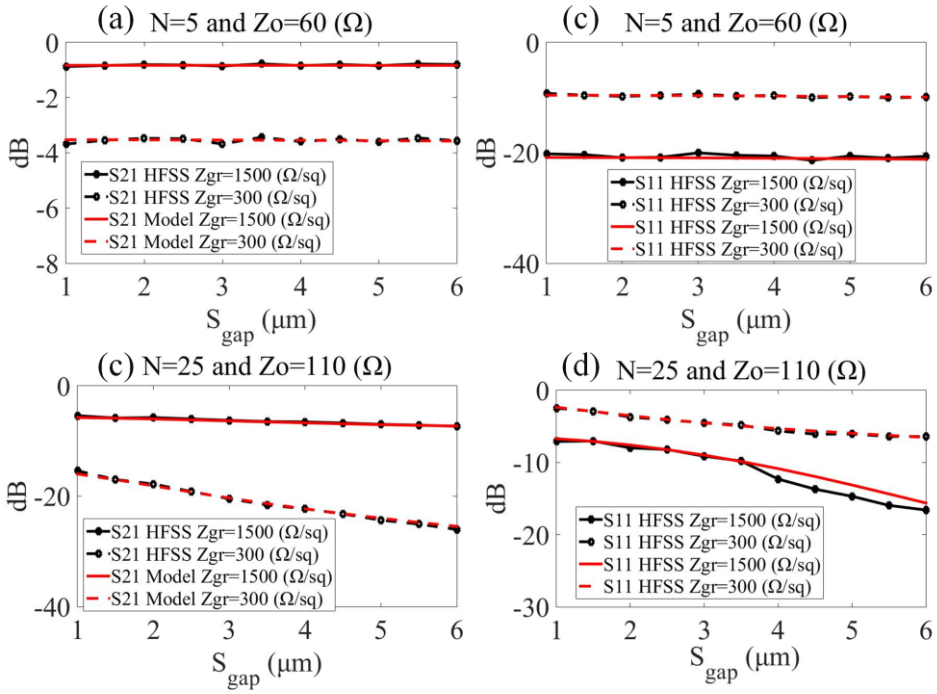

Fig. 7.20 The S_{21} and S_{11} comparison between the proposed shunt GL-CPS switch model and full-wave simulations for various configurations.

Similarly, to the series case, the switching performance trends with respect to the configuration parameters $\{W_{gap}, N, Z_0\}$, are similar to the shunt CPW switch (see Fig. 7.12),

thus not presented. Finally, in Fig. 7.21 the S_{21} ON/OFF ratios are given for various ILs. These graphs reveal that the shunt CPS switch has a very similar performance with the respective CPW switch.

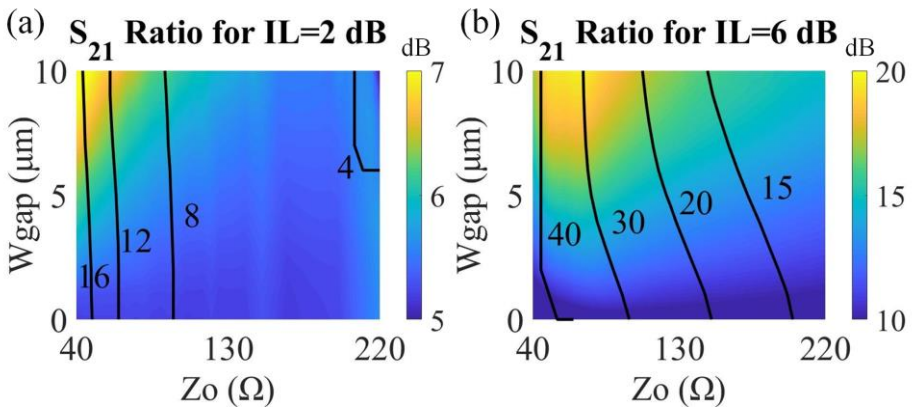

Fig. 7.21 The shunt GL-CPS switch 2D maps of the ON/OFF ratio for fixed IL. With black contour, the number of squares is noted.

V. Improving the performance of graphene switches

The theoretical models proposed in this Chapter are used to investigate the performance of mmWave/THz graphene-loaded switches realized on coplanar transmission line topologies. The presented results reveal the trends between the different series/shunt topologies with respect to geometrical parameters and suggest that the shunt switches are dominant over the series in terms of switching performance (IL and ON/OFF ratio). However, these models can be easily adjusted to other graphene sheet impedance ratios. Specifically, graphene is expected to have a sheet impedance biased/unbiased ratio between 4-10. In this Chapter, a ratio of 5 is chosen based on the previous experiments in

the 220-330 GHz band (Chapter 6). However, if the fabrication process is optimized, the impedance ratio will increase. In addition, instead of monolayer graphene, the thin-film could be comprised of graphene flakes that exhibit a higher ratio. For example, considering a ratio of 10 (R_{biased}=*150 Ω/□* and $R_{unbiased}$=*1500 Ω/□*), the switching performance increases significantly both for the series and the shunt case, as shown in Fig. 7.22 (CPW topology). Namely, for the series GL-CPW switch, if the graphene sheet impedance ratio is 5, for an IL=2 dB, the design parameters are Z_0=*50 Ω*, and *G=5 μm*, and the maximum switching ON/OFF ratio is 6 dB. Contrary, for an impedance ratio of 10, the respective ON/OFF switching ratio is 12 dB. To compare with existing configurations, at 275 GHz, VO_2 switches can achieve an ON/OFF ratio of 9 dB for an insertion loss of 2 dB [72].

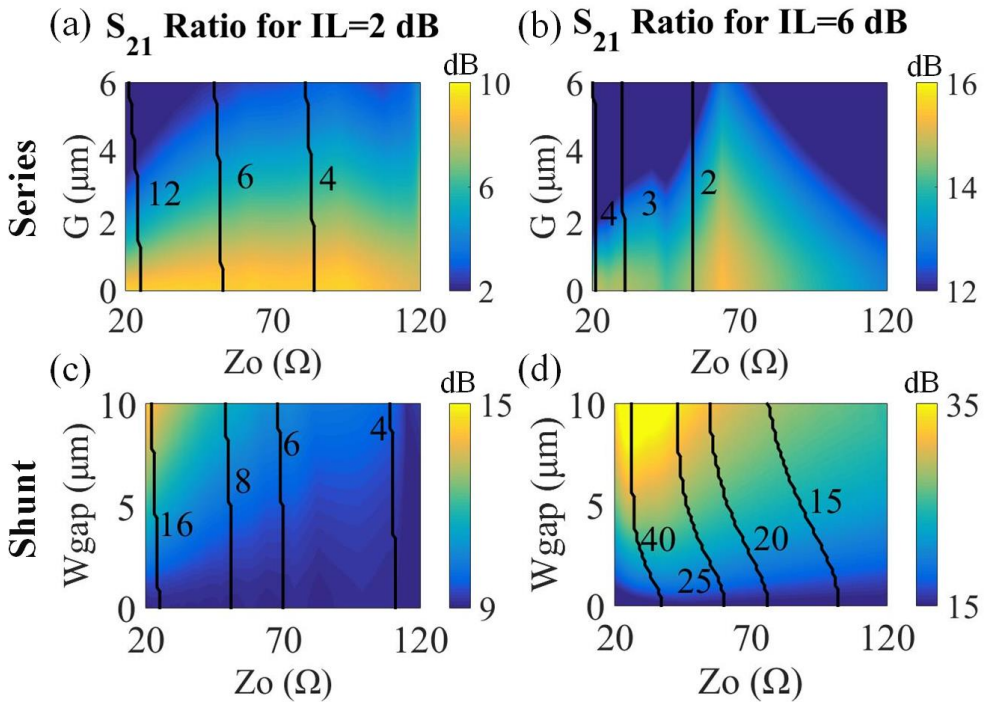

Fig. 7.22 The series and shunt GL-CPW switch 2D maps of the ON/OFF ratio for fixed IL. These results are obtained for an impedance ratio of 10, instead of 5 as the rest of the Chapter. The black contour indicates the number of squares (*N*).

Moreover, the presented models incorporate graphene as a distributed sheet impedance in Ω/□; hence, they can be exploited for other loaded topologies that use materials characterized by sheet impedance (e.g. VO_2, MoS_2, etc.). Additionally, the proposed models can be used for rapid optimization processes or in conjunction with machine learning algorithms, where the generation of many design points is required. For example, machine learning algorithms are leveraged to optimize the antenna topology under certain constraints (e.g. gain, VSWR, return loss, etc.) as shown in [114]; these algorithms could now be extended for graphene-actuated reconfigurable antennas with embedded switches, which could be modeled as proposed herein.

Finally, a compilation of all the available mmWave/THz switches is presented in Table 7.1, where a high switching performance is observed with "traditional" technologies (e.g., SiGe and CMOS) that require advanced/high-cost technology nodes. Conversely, graphene switches offer good performance without residing in the use of complex and costly fabrication techniques.

Table 7.1

Comparison of existing mmWave/THz switches

Technology	Frequency (GHz)	Insertion Loss (dB)	ON/OFF ratio (dB)	Ref.
0.13 μm SiGe BiCMOS	170	3.5	20	[115]
65-nm CMOS	275	3.5	17	[62]

Fraunhofer IAF 50 nm mHEMT	275	2.5	15	[63][66]
35-nm InGaAs mHEMT	275	1	25	[64]
800 nm InP DHBT	275	4	33	[65]
Shunt Graphene (ratio 10)	275	2	12	This work
Vanadium Dioxide	275	2	10	[72][73]

VI. Conclusions of Chapter 7

In this Chapter, an in-depth analysis of mmWave/THz graphene loaded switches for coplanar waveguide topologies (CPW and CPS) was presented. The study was carried out using equivalent models both for the series and shunt CPW and CPS configurations with respect to various parameters including scaling, characteristic impedance, and graphene size. Moreover, the results of the proposed equivalent models are validated using a FEM solver achieving good agreement between model and full-wave simulations. Besides, the proposed models were used to obtain the s-matrices and identify the trends between the IL and ON/OFF ratios both for series and shunt GL- CPW and CPS switches. Alongside the theoretical models of the switches, the series CPS discontinuity equivalent circuit is presented for the first time using Babinet's principle. The acquired data suggest that the shunt topology outmatches the series in terms of switching performance (both IL and ON/OFF ratio), both for the CPW and CPS topologies. This study would be impossible

without the use of the proposed equivalent models, since, more than 2,400,000 s-matrices were calculated both for the CPW and CPS cases. The proposed methodology constitutes a roadmap for the design of thin-film mmWave/THz switches and can be extended for other types of transmission lines (e.g. slotlines).

The graphene switching topologies presented in this Chapter could enable wavefront modulation both in coded phased arrays and reconfigurable reflective surfaces, as the ones presented in Chapter 2-II. In Chapter 8-10, the graphene switches presented herein, are integrated with printed antennas that form large-format mmWave/THz RRSs that can serve both in communication and imaging applications.

CHAPTER 8

Graphene-Loaded Reconfigurable Reflective Surfaces

This Chapter presents the design process of single-bit reconfigurable reflective surfaces in the mmWave/THz bands. Specifically, tunable apertures form high-gain steerable beams without residing to the use of complex RF-front-end circuitry, as discussed in Chapter 2-II. As such, RRSs consist of multiple antenna elements with integrated switches that modulate the phase of the impinging waves, enabling beamforming to the desired direction. In this Chapter, the graphene-loaded switches presented in Chapter 7 are integrated with mmWave/THz printed patch antennas, forming low-cost and high-efficiency large-scale tunable apertures that are attractive in imaging and wireless communication applications.

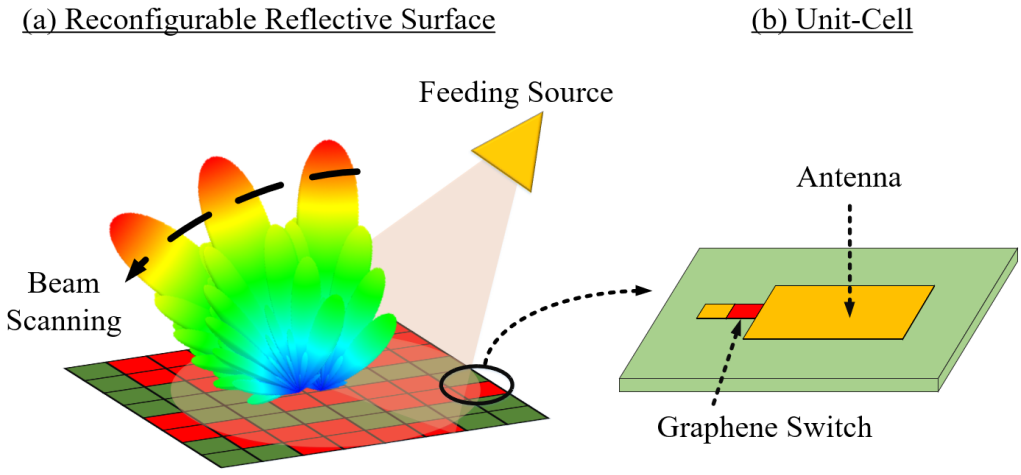

Fig. 8.1 The illustration of a graphene-loaded RRS with beamsteering capabilities.

I. Single-bit RRSs using ideal switches

As discussed in Chapters 6 and 7, mmWave/THz shunt graphene switches can exhibit significant ON/OFF ratios and low insertion losses. To achieve beamforming and steering, these switches can be integrated with RRSs comprising multiple patch antennas, as shown in Fig. 8.1. In this section, a prototype RRSs is presented consisting of a patch antenna with an integrated ideal switch to evaluate the overall expected performance of the design. Then, in section 8-II, a graphene-loaded switch is incorporated in the unit-cell and the design is optimized to carry out efficient beamforming.

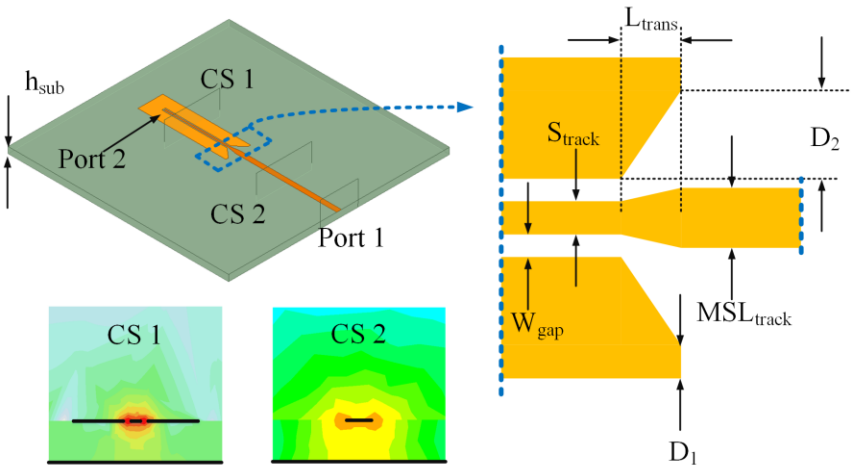

Fig. 8.2 The proposed CPW-to-MSL transition using a via-less approach.

A. Coplanar waveguide to microstrip line transition

As shown in Chapter 7, graphene switches perform better in shunt topologies and are easily integrated with coplanar transmission line topologies (e.g., CPW). Moreover, as the frequency of operation increases, the use of thick substates is prohibitive for reflective surfaces, due to the exhibited substrate modes that enhance the mutual coupling between

the antennas, leading to reduced radiation efficiency [116]. Several antenna configurations can be implemented on those thin substrates; however, printed patch antennas offer better performance, compared to other printed antenna configurations (e.g. dipoles), due to the impedance matching mechanism [2].

Typically, patch antennas are fed with the use of microstrip lines (MSLs) [2]. Therefore, to transition from the shunt CPW switch topology to the MSL, the via-less CPW-to-MSL transition of Fig. 8.2 is utilized [117]. This is a via-less transition, meaning that there is no need for RF vias that connect the MSL bottom ground with the coplanar CPW grounds. Explicitly, this transition was chosen since the design and implementation of RF vias is typically a challenging task that requires complex nanofabrication techniques [118] and results in additional RF losses. The transition is achieved by transforming the MSL quasi-TEM mode fields into the coplanar quasi-TEM mode of the CPW using a gradual transition, as shown in Fig. 8.2. As such, good signal coupling is achieved, as validated from the simulated S-parameters shown in Fig. 8.3a. Moreover, it is important to mention that the absence of RF vias, limits these transitions to CPW configurations that have W_{gap} smaller than the substrate thickness (h_{sub}). Namely, the small CPW gaps enable the fields of the MSL to couple to the coplanar CPW ground, instead of the bottom ground, forming the desired CPW coplanar quasi-TEM mode. In the case of greater CPW gaps, the MSL mode would remain unaltered and the coplanar grounds would act as parasitic metals. The design parameters of this CPW-to-MSL transition are given in table 8.1.

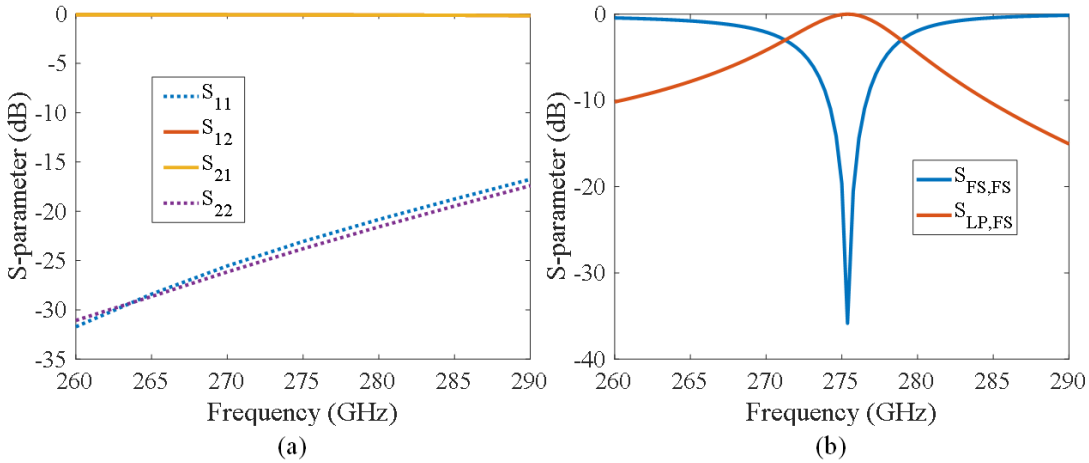

Fig. 8.3 The scattering paraments of: (a) the CPW-to-MSL transition and (b) the patch antenna placed in a periodic configuration (FS: free-space and LP: lumped port).

Table 8.1

Design Parameters of the Single-bit Unit-Cell

Variable	Value (μm)	Variable	Value (μm)
h_{sub}	20	L_{trans}	30
S_{track}	5	W	215
W_{gap}	3	L	151
MSL_{track}	15.3	W_g	10
D_1	8.4	y_o	65.5
D_2	25.8	λ_g (@ 275 GHz)	427

B. Patch antenna design of the RRS

The next step toward the implementation of the reconfigurable surface is the design of the radiating element (patch antenna). The patch antenna is fed from the radiating edges using an MLS, as illustrated in Fig. 8.4a. As such, the impinging waves from the free-space (FS), form fields on the patch antenna, and these fields are coupled to the MSL quasi-TEM mode using the inset feed scheme [2]. The impedance matching between the patch antenna and the MSL depends on the inset feed length (y_o) [2].

The goal of the unit-cell is to modulate the imping waves using an integrated switch. To ensure optimum modulation efficiency, the coupling between the imping waves (free-space) and the CPW line should be maximum. Therefore, the antenna is modeled in a unit-cell topology, where the antenna is placed in an infinite periodic configuration using periodic boundary conditions and a Floquet port (free-space) that illuminates the surface with an infinite plane wave, as shown in Fig. 8.4b. This periodic configuration represents the actual reconfigurable surface environment since it accounts for all the exhibited phenomena, including the mutual coupling between the antennas.

To test, the coupling between the Floquet-Port impinging waves and the CPW line, a lumped port is placed at the end of the CPW line, as shown in Fig. 7.4b. Moreover, the antenna dimensions are optimized to achieve maximum coupling between the Floquet-port (free-space) and the CPW line (lumped port) at 275 GHz, as shown in Fig. 7.3b. All the antenna design parameters are given in table 7.1.

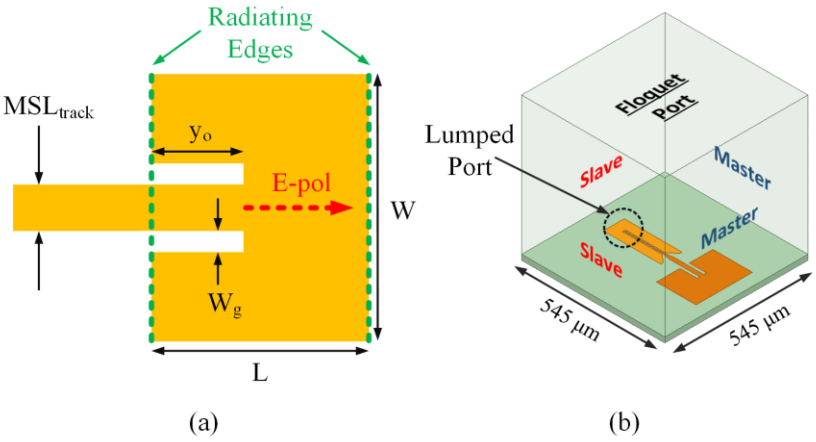

Fig. 8.4 The proposed radiator: (a) the top view of the antenna and (b) the periodic model used to simulate the coupling of the free-space imping waves to the CPW embedded lumped port.

C. Single-bit ideal unit-cell

After optimizing the antenna configuration, the integration of the switches is implemented. Initially, two ideal switching configurations are utilized, as illustrated in Fig. 8.5. Specifically, in the first design, a short-circuit (SC)/open-circuit (OC) switch is utilized to modulate the phase of the reflected waves, as shown in Fig. 8.6a. This configuration emulates the sheet impedance of an ideal switch (infinite ratio), using a simple shorting metallic patch. Though this design offers a compact solution, the open-ended CPW line – State-2 of the switch– is not an ideal open due to parasitics exhibited by open-ended CPW lines [107]; thus, the modulation of the phase is expected to be slightly mitigated, as shown in Fig. 8.6a. Moreover, as operating frequency increases, the effects of these parasitics are expected to further reduce the performance of the open-ended topology, since the RF signals will be coupled to the coplanar ground through the parasitic capacitance when the switch is tuned at State-2. To overcome this obstacle, the devices should be scaled to

smaller features that demand advanced nanofabrication techniques. The main advantage of this configuration is compactness; as such, the total real-estate of the device is almost $\lambda_0/4$, thus the mutual coupling between neighboring elements is expected to decrease. Besides, this design can be used in densely populated apertures.

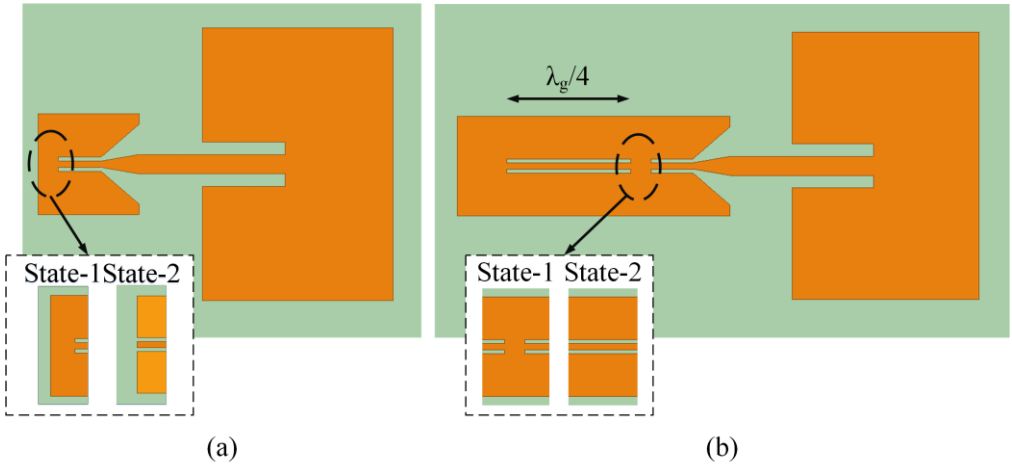

Fig. 8.5 The single-bit ideal unit-cell designs: (a) open-ended and (b) back-short.

On the other hand, to acquire a perfect 180^o of phase modulation, the same OC/SC switch could be integrated $\lambda_g/4$ away from a short-ended CPW line, as depicted in Fig. 8.5b. In this manner, when the switch is tuned at State-1 (grounded CPW trace), the reflection coefficient of the unit-cell is -1 (Fig. 8.6b). However, in the absence of the shorting patch (State-2), the S.C. is shifted by $\lambda_g/2$ (round-trip distance), leading to a phase difference of 180^o on the reflected waves, as shown in Fig. 8.6b. This back-short design has no limitation on the achieved modulation of the phase; however, the acquired phase difference is length depended, thus the BW would be limited compared to the open-ended design. Furthermore, this device is larger than the open-ended counterpart, thus an increase in the mutual coupling between neighboring antennas is expected. Finally, the back-short

design is suitable for Nyquist sampled configurations ($\lambda_0/2$) but not denser populated apertures.

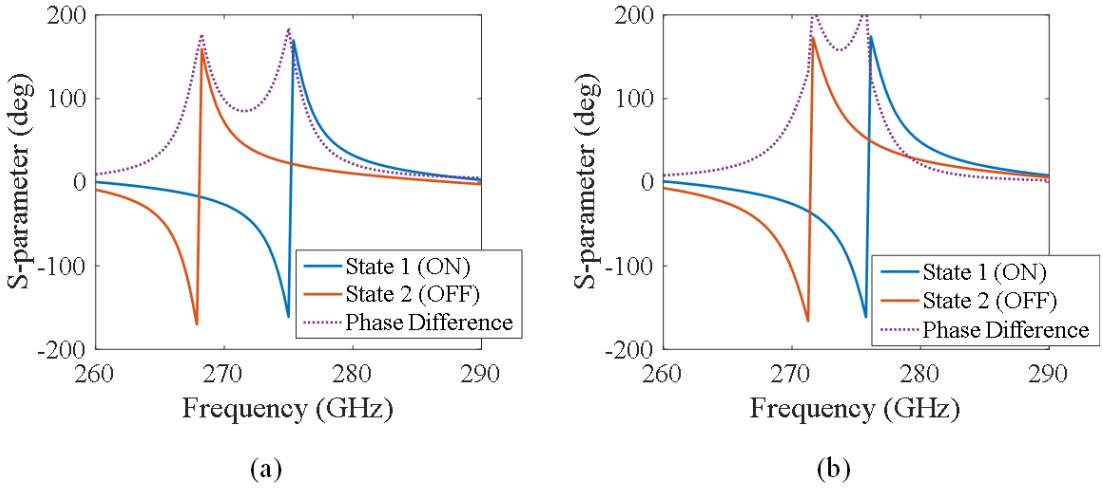

Fig. 8.6 The reflection coefficient phases of the ideal unit-cell designs of Fig. 8.5, obtained using full-wave simulations: (a) open-ended and (b) back-short.

To test the proposed single-bit designs, an exemplary 20-element linear RRS is modeled in a full-wave simulation tool [113], as shown in Fig. 8.7. In this case study, the surface is illuminated with an incident boresight plane-wave and the coding of the surface elements is chosen appropriately to steer the beam toward 30º. This coding profile is calculated using the scattered field analysis presented in Chapter 2-II –equations (2.5) to (2.10). Both arrays form a beam at 30º, however, a secondary main lobe at -30º is also present, due to the quantization errors of the single-bit scheme [35]. This parasitic radiation could be mitigated by using higher phase-bit quantization schemes and/or by incorporating randomization techniques on the antenna elements of the surface as discussed in Chapters 9 and 10, respectively.

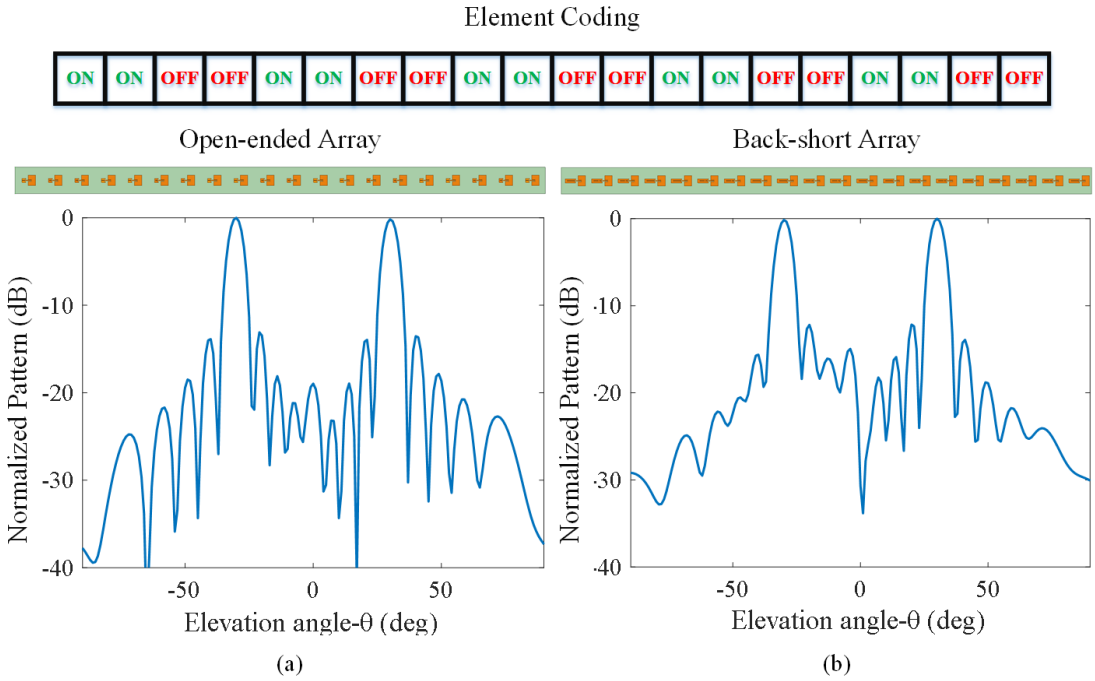

Fig. 8.7 The E-plane radiation patterns of the proposed ideal 20-element arrays: (a) open-ended and (b) back-short array.

Finally, the scope of most antenna systems, both in communication and imaging applications, is to offer beamforming and steering capabilities over a certain bandwidth and not a single frequency. Thus, the E-plane radiation patterns versus frequency are given in Fig. 8.8. These graphs are useful in determining the operation BW of the reconfigurable surfaces. As such, the BW is defined as the region in which a single beam is formed at the desired direction (30º at this case-study) and that the SLL is below -10 dB. The open-ended design exhibits a fractional BW of ~1.7% around 273 GHz, as shown in Fig. 8.8a. On the other hand, the back-short design offers a fractional BW of ~1.3%, as depicted in Fig. 8.8b. This drop in the back-short's BW is attributed to the fixed distance between the switch and the shorted CPW. As such, this electrical length is frequency-dependent causing a

reduction in the BW. Moreover, these small fractional BWs are typical for patch antennas printed on thin, high dielectric constant substrates [88].

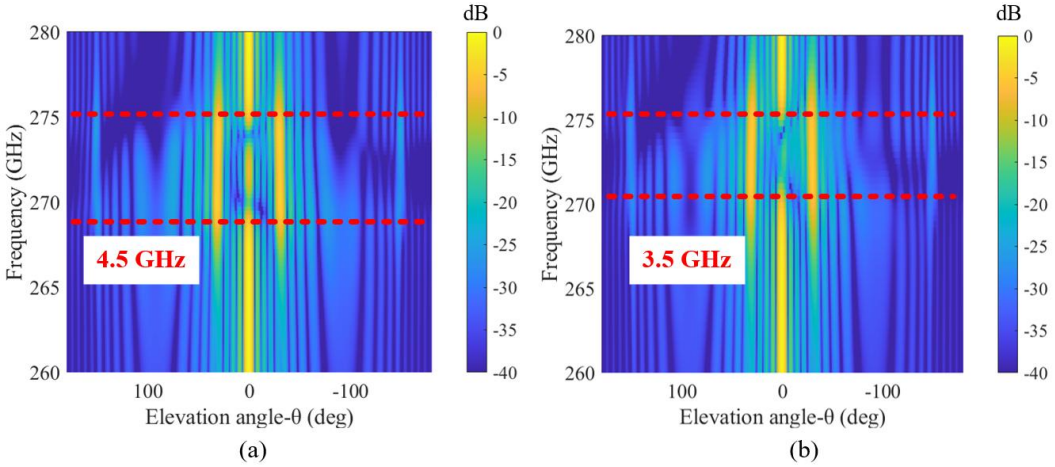

Fig. 8.8 The E-plane radiation patterns of the proposed ideal 20-element arrays versus frequency: (a) open-ended and (b) back-short array.

The results of this section demonstrate that the use of a perfect thin-film switch (infinite biased/unbiased sheet impedance ratio), integrated with patch antennas, leads to mmWave/THz reconfigurable surfaces with beamsteering capabilities.

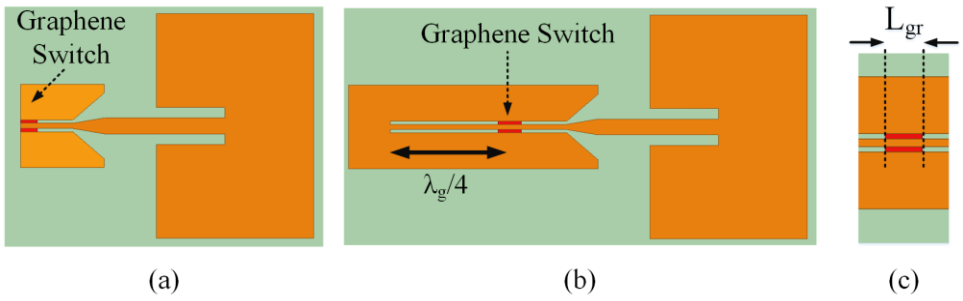

Fig. 8.9 The single-bit graphene-loaded unit-cell designs: (a) open-ended and (b) back-short. In (c) the integrated shunt graphene switch is presented.

II. Graphene-loaded single-bit RRSs

This section presents the expansion of the ideal unit-cells using graphene switches, as illustrated in Fig. 8.9. Namely, instead of a perfect metallic patch, a graphene sheet is placed between the ground and the signal conductors of the CPW. As the sheet impedance of the graphene monolayer is modulated between $Z_{gr,sh(biased)}=300\ \Omega/\square$ and $Z_{gr,sh(biased)}=1{,}500\ \Omega/\square$ (measured values presented in Chapter 6), the phase of the imping waves is expected to shift by 180^o, as in the ideal case. However, the biased/unbiased ratio of graphene is small and the modulation efficiency on the reflected waves is expected to decline.

A. Graphene unit-cell optimization

To study the performance of the graphene-loaded antennas the equivalent circuits of Fig. 8.10 are proposed. As such, the antenna is modeled as a Thevenin AC voltage source. Then, the transition from the antenna feed (MSL) to the CPW shunt switch is represented with a transmission line that has the same characteristic impedance as the source since the MSL is well-matched to the CPW line (Fig. 8.3a). After this transmission line, the shunt graphene switch is modeled with a loaded transmission line, with a complex $Z_{0,gr}$ and γ_{gr}, as discussed in Chapter 7-III-B. Both $Z_{0,gr}$ and γ_{gr} depend on the transmission line geometrical features including the characteristic impedance of the CPW, the gap size (W_{gap}-scaling factor), and the number of graphene squares ($N=L_{gr}/W_{gap}$ as shown in Fig. 8.9c). The W_{gap} of these designs is the same as in section 8-I (3 μm). After the graphene switch, a fixed load is placed consisting of a transmission line and a termination.

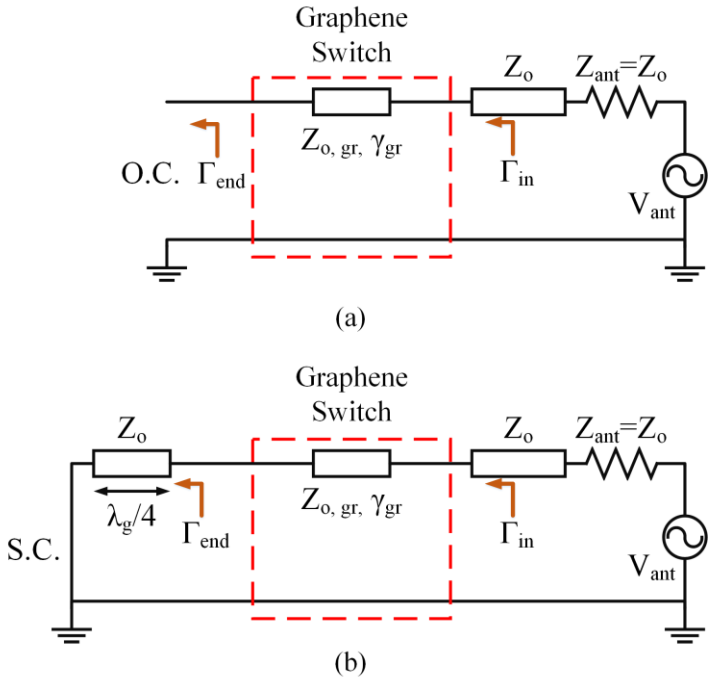

Fig. 8.10 The equivalent models of the single-bit ideal unit-cell designs of Fig. 8.9: (a) open-ended and (b) back-short.

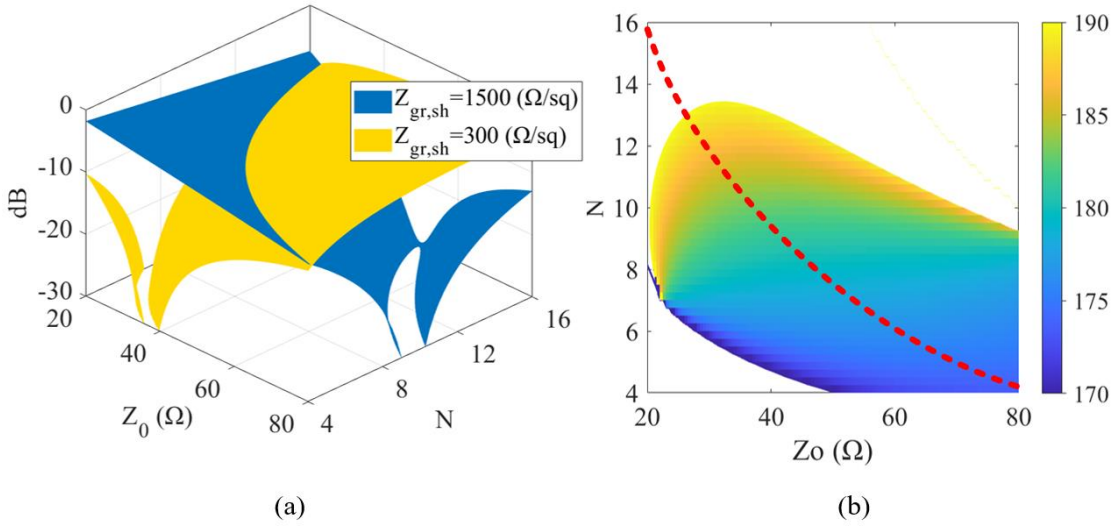

Fig. 8.11 (a) The reflection coefficient magnitude of the back-short unit-cell calculated using (7.1), and (b) the phase difference between the biased and unbiased cases (the red dotted line represents the equal reflection magnitude locus). Both configurations assume $W_{gap}=3\ \mu m$.

The free-space reflection coefficient of the unit-cell using the equivalent circuits of Fig. 8.10, is given by

$$\Gamma_{in,on/off} = S_{11,on/off} - \frac{S_{21,on/off}^2 \Gamma_{end}}{1 - S_{11,on/off}\Gamma_{end}} \qquad (8.1)$$

and

$$\Gamma_{end} = Ae^{-j2\theta} \qquad (8.2)$$

where $S_{ij,on/off}$ are the 2-port S-parameters of the graphene switch for the biased/unbiased cases, A is the amplitude of the CPW-end reflection coefficient ($A=1$ for O.C. and $A=-1$ for S.C.), and θ is the electrical length of the transmission line between the switch and the CPW-end ($\theta=0^o$ for Fig. 8.9a and $\theta=90^o$ for Fig. 8.9b). To ensure that the aperture efficiency of the reconfigurable surface is maximum, no amplitude modulation between the two states (biased/unbiased) of the unit-cell is required. Moreover, the phase difference between the states should be 180^o as in the ideal case of section 8-I. These two constraints are expressed as

$$Amplitude: \left|\Gamma_{in,on}\right| = \left|\Gamma_{in,off}\right| \qquad (8.3)$$

$$Phase: \left|ang(\Gamma_{in,on}) - ang(\Gamma_{in,off})\right| = 180^o \qquad (8.4)$$

By varying the CPW Z_0 and the graphene squares (N), for the back-short configuration of Fig. 8.9b (equivalent model of 8.10b), the results of Fig. 8.11 are obtained at 275 GHz. As such, the Γ_{in} magnitude varies with the number of graphene squares (N) and the CPW Z_0, both for the biased and unbiased graphene states (Fig. 8.11a). Thus, the condition of (7.3), is achieved only across a narrow range of $\{Z_0, N\}$ values. Alongside, the

phase difference between the two states of the unit-cell (biased/unbiased) is given in Fig. 8.11b. These two graphs suggest that a 180° phase difference is acquired, without any amplitude modulation on the reflected waves, when $Z_0 \approx 50\ \Omega$ and $N \approx 7$. Similar values occur for the open-ended design (Fig. 8.10a), thus not presented.

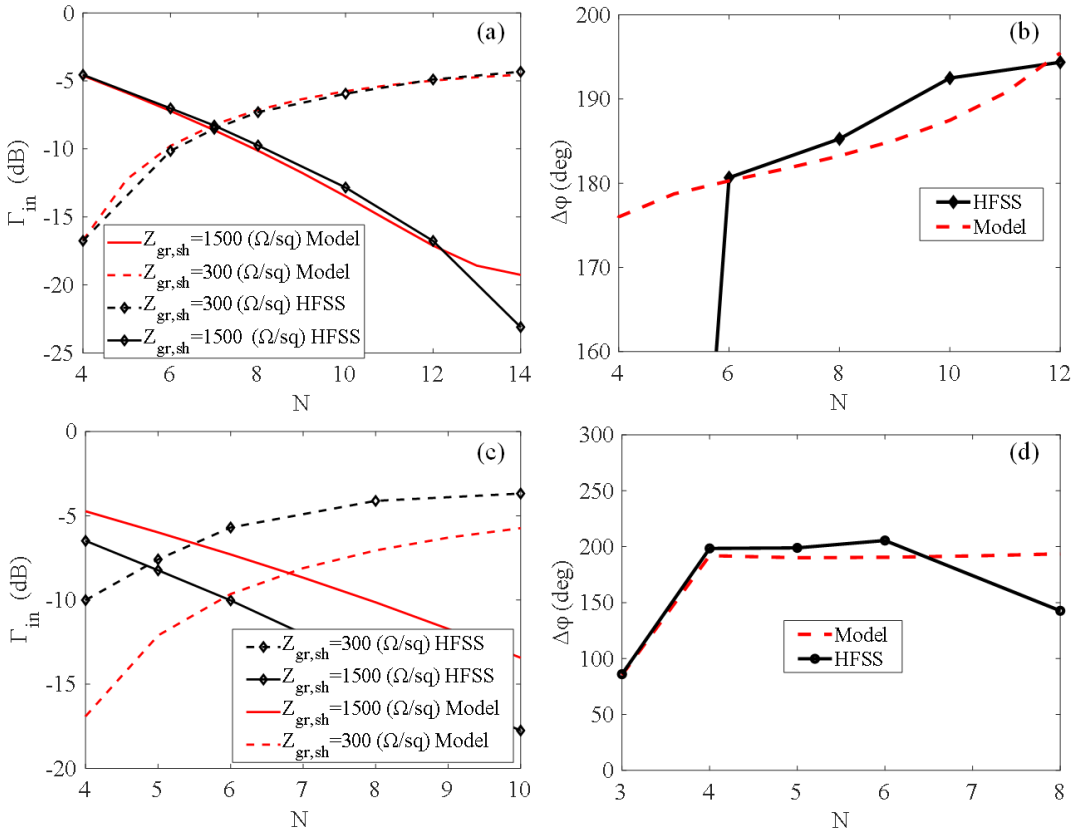

Fig. 8.12 (a) The reflection coefficients of the back-short unit-cell versus the number of squares. (b) the phase difference between the biased and unbiased cases of the back-short design. (c)-(d) the respective open-ended unit-cell results. All the depicted results are obtained at 275 GHz.

To validate the presented models, a comparison between the analytical and full-wave results is presented in Fig. 8.12. For the back-short design, a good agreement is observed between the full-wave unit-cell models and the proposed equivalent circuit, as shown in Fig. 8.12a-b. Conversely, the analytical results of the open-ended unit-cell design

exhibit a discrepancy with the respective full-wave models. This is attributed to the open-ended CPW that is not a perfect O.C. as accounted for in Fig. 8.10b. Such open-ended CPWs are modeled by a set of capacitors that couple the signal with the ground conductors of the CPW [107]. The effect of these capacitances is negligible in low RF bands, however, as the operating frequency increases the performance of the design is expected to decline, thus scaling to smaller geometrical features is necessary.

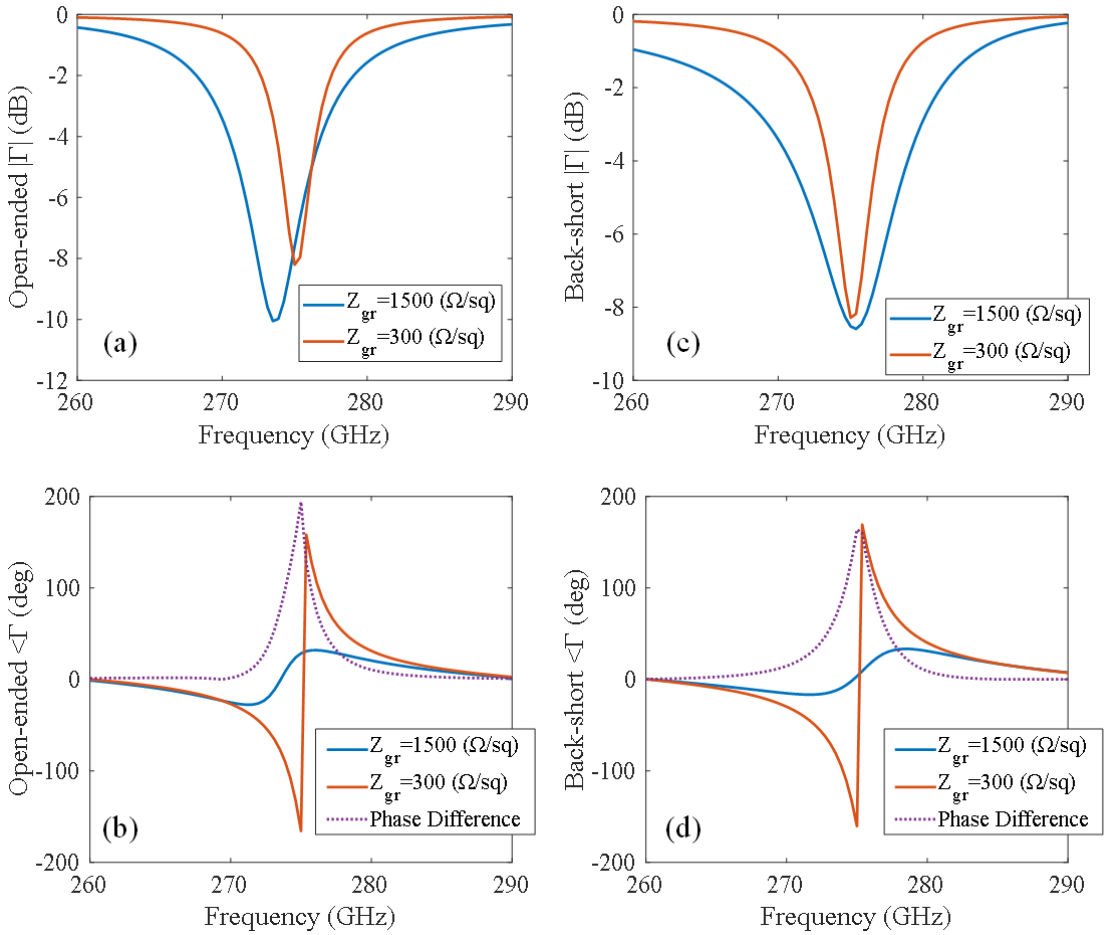

Fig. 8.13 The full-wave simulated reflection coefficients versus frequency for the open-ended (a)-(b) and the back-short (c)-(d) graphene-loaded unit-cells.

The unit-cells' optimization processes based on the reflection coefficient criteria of (8.3) and (8.4) reveal that minimum amplitude modulation and 180° of phase tuning are achieved when: 1) CPW $Z_o=50\ \Omega$ for both designs, and $N=5$ and 7 for the open-ended and back-short unit-cell, respectively. These results concern 275 GHz, however, as operating frequency varies, the reflection coefficient performance changes, as observed in the simulated results of 8.13. As such, (8.3) and (8.4) are met only at 275 GHz for the graphene-loaded unit-cells. Explicitly, the limited graphene sheet impedance ratio causes a mismatch between the graphene loaded CPW and the patch antenna, altering the phase tuning and leading to an amplitude modulation on the reflection coefficient. These effects are expected to mitigate the BW performance of the proposed unit-cells compared to their ideal counterparts, where there is no amplitude modulation (regardless of frequency) and a phase difference of 180° is achieved over a greater BW (Fig. 8.6).

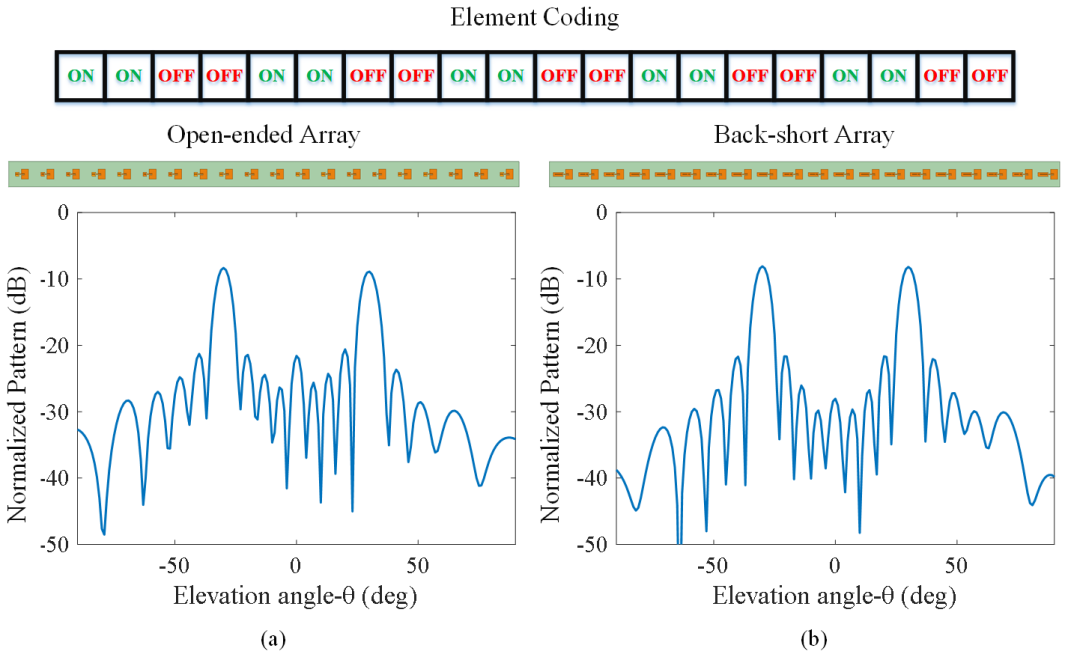

Fig. 8.14 The E-plane radiation patterns of the proposed graphene-loaded 20-element arrays: (a) open-ended and (b) back-short array.

B. Beamforming using graphene-loaded reflective surfaces

The previously detailed graphene-loaded unit-cells, offer phase reconfiguration on the reflected waves that can be leveraged to form high-gain steerable beams. To test the beamforming capabilities of the single-bit graphene loaded reflective surface, a 20-element array is used. As in section 8-I, the surface is illuminated with a boresight plane-wave and the beamforming is at 30^{o}, as shown in Fig. 8.14. The radiation patterns are normalized to the maximum gain of their respective ideal-switch counterparts. As such, the gain reduction of the graphene reconfigurable surfaces is 8 dB compared to the ideal designs. This value is equal to the unit-cell losses and it is attributed to the reduced biased/unbiased ratio of graphene. A more detailed discussion on the loss mechanisms of reflective surfaces is given in the next section.

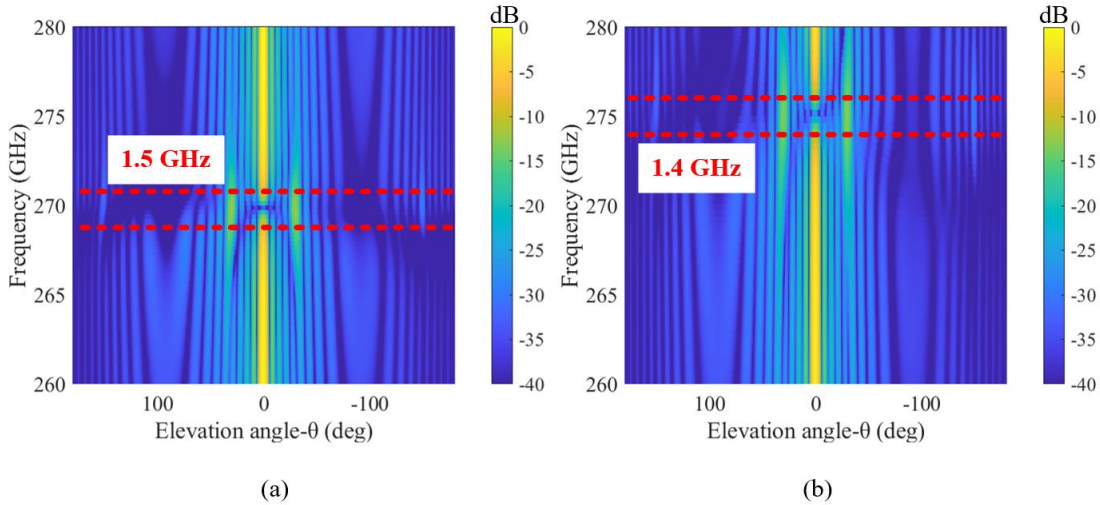

Fig. 8.15 The E-plane radiation patterns of the proposed graphene-loaded 20-element arrays versus frequency: (a) open-ended and (b) back-short array.

Finally, the BW performance of the proposed designs is evaluated using the E-plane radiation patterns versus frequency, as depicted in Fig. 8.15. As expected, the amplitude modulation exhibited by the graphene switches outside the center frequency reduces the exhibited BW compared to the ideal case.

C. Power efficiency analysis of graphene loaded RRSs

The radiation patterns of the graphene-loaded RRSs (Fig. 8.14), reveal that the total RF losses of the 20-element surface are the same as the unit-cell's (Fig. 8.13). Namely, the proposed graphene-loaded unit-cell designs exhibit 8 dB of losses compared to their ideal counterparts. These losses are independent of the number of antennas on the surface. Specifically, the power of the imping wave is assumed to be equally distributed between the surface antennas as P/N_{ele} (where P is the total power of the imping waves and N_{ele} is the number of antennas on the surface–$\lambda_0/2$ sampling). Each of these distributed waves is modulated by the respective antenna and the reflected waves, of each unit-cell, have a power of $L \cdot P/N_{ele}$ (where L represents the losses introduced by the graphene-loaded unit-cell). Afterward, the reflected waves are beamformed toward the desired direction by all the elements of the array and the maximum surface gain is N_{ele} due to the $\lambda_0/2$ sampling [2]; thus, the total power of the reflected waves is $L \cdot P$. Therefore, regardless of the number of elements, the introduced losses remain constant.

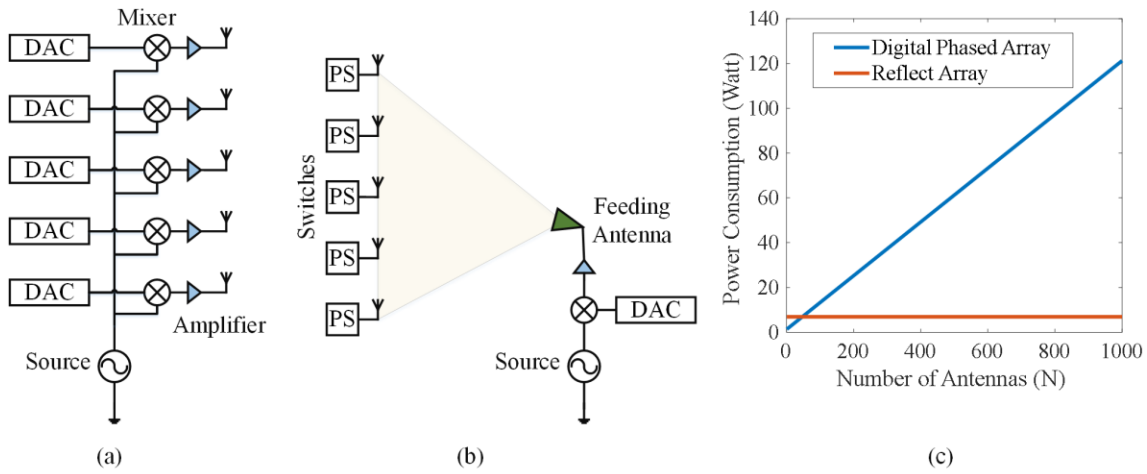

Fig. 8.16 The schematic of (a) a digital phased array and (b) a reflectarray system. In (c) the power consumption of these systems versus the number of integrated antennas.

This is the key advantage of RRSs compared to phased arrays, in which the RF losses and power consumption of the beamforming RF-front-end circuity are scaling as the number of elements increases [24]. Specifically, in a digital phased array, the power consumption is introduced by the mixers and amplifiers integrated at every RF chain, the baseband processing modules, and the RF source, as shown in Fig. 8.16a. As such, the total DC power consumption of this configuration is [24]

$$P_{total,dpa} = P_{bb} + NP_{rfc} + P_{tx}/e_{ap} \qquad (8.5)$$

where P_{bb} is the baseband processing power (e.g., DAC, switches, etc.) – P_{bb} is assumed constant since it is considerably smaller than the consumption of the RF components–, N is the number of antennas, P_{rfc} is the power required for every RF chain due to the integrated components (e.g., mixers, amplifiers, etc.), P_{tx} is the power of the source, and e_{ap} is the aperture efficiency.

On the other hand, for a reflectarray (Fig. 8.16b), the total DC power consumption is given by [24]

$$P_{total,ra} = P_{bb} + P_{rfc} + P_{tx}/\left(e_{ap}e_{us}\right) \qquad (8.6)$$

where e_{us} is the efficiency of the unit-cell. For the presented graphene-loaded unit-cells the efficiency is ~16% (-8 dB). To evaluate the power performance of a digital phased array versus a reflectarray the following are assumed:

1. Both systems have the same baseband processing power consumption (e.g., P_{bb}=200 mWatt, [24]),
2. Both systems use the same mixer and amplifier with P_{rfc}=120 mWatt [24],
3. Both systems use the same source, P_{tx}=1 Watt,
4. The digital phased array has an aperture efficiency of 95 % [24], while the reflectarray has 41 % due to the single-bit phase modulation [35].
5. Finally, the power efficiency of the RRS is 16 % due to the non-ideal switching.

With the aforementioned assumptions, the exhibited power consumption of a digital phased array and a reflectarray are calculated, versus the number of integrated antennas, as shown in Fig. 8.16c. As such, the power consumption of the reflectarray remains constant, while the digital phased array increases linearly with the number of antennas. Therefore, as the demand for large-scale systems increases both in communication and imaging applications, the use of reflectarrays is an attractive solution compared to power-hungry digital phased arrays.

III. Conclusions of Chapter 8

This Chapter presented reconfigurable graphene-loaded single-bit reflective surfaces. Initially, the design process was carried out using ideal switches to demonstrate the validity of the proposed configurations. Then, the graphene switches were incorporated in the designs obtaining the single-bit graphene-loaded unit-cells. These topologies offer single-bit phase reconfigurability with 8 dB of losses on the beamformed waves. These losses are independent of the number of incorporated antennas, as shown from the results of section 8-II-C. This constitutes a key factor toward the proliferation of large-scale mmWave/THz reconfigurable apertures that can be employed both in imaging and communication applications. Namely, apertures with hundreds or even thousands of antennas are expected to exhibit 8 dB of losses; however, their phased array counterparts would suffer from the intensive scaling of the RF-front-end hardware, leading to prohibitive RF losses. Finally, the main drawback of the proposed designs is the effect of quantization errors on the beamforming process that lead to parasitic radiation lobes and reduced power efficiency. These phase quantization issues could be mitigated with various techniques that are thoroughly discussed in the flowing Chapters 9 and 10 of this dissertation.

CHAPTER 9

Multi-Bit Reconfigurable Reflective Surfaces

This Chapter presents RRS topologies that employ multiple phase quantization bits to improve the aperture efficiency of the single-bit RRSs that were detailed in Chapter 8. Moreover, by utilizing multi-bit phase modulation on the impinging waves, the proposed RRSs eliminate the pronounced parasitic quantization lobes that pose a roadblock in wireless communication (IRS) and imaging applications. To acquire multiple phase bits, the presented RRSs incorporate multiple SPST switches in the unit-cell, instead of a single switch. In this manner, by manipulating the states (ON/OFF) of the various switches many combinations occur in the unit-cell's reflection phase, providing the required phase states. For every integrated switch, an extra phase bit is enabled, thus retaining a single-switch-per-bit constraint (up to 4 bits– 16 phase states). By meeting this criterion, the devised RRSs have lower RF losses and simpler/scalable designs. This is the first time in the known literature that 3 or more phase quantization bits are provided with SPST switches. In the following sections, the proposed designs are thoroughly presented alongside a series of theoretical and full-wave simulation results for validation.

I. Multi-bit RRS topologies

As described in Chapter 8, RRSs typically feature single-bit phase modulation on the incident waves, thus compromising beamforming performance (aperture efficiency) due to quantization errors. As such, SPST switches (e.g., graphene switches) are integrated on the antenna elements, and by manipulating their states (e.g., biased-ON/unbiased-OFF), the

phase of the impinging waves is modulated leading to electronic beamforming. To steer the waves toward the desired direction, a unique phase profile is required on the surface, and the reflection phases of each antenna element vary continuously within the [- π, π] region- equation (2.10). However, in realized surfaces, these continuous values are quantized based on the available phase states due to hardware limitations (e.g., for 1-bit– the unit-cell's phase can only take the values π and 0). Thus, the errors caused during the phase quantization process, lead to reduced aperture efficiency, coarse beam steering, and higher side lobe level (SLL). These drawbacks can be alleviated by using multi-bit configurations with finer phase quantization.

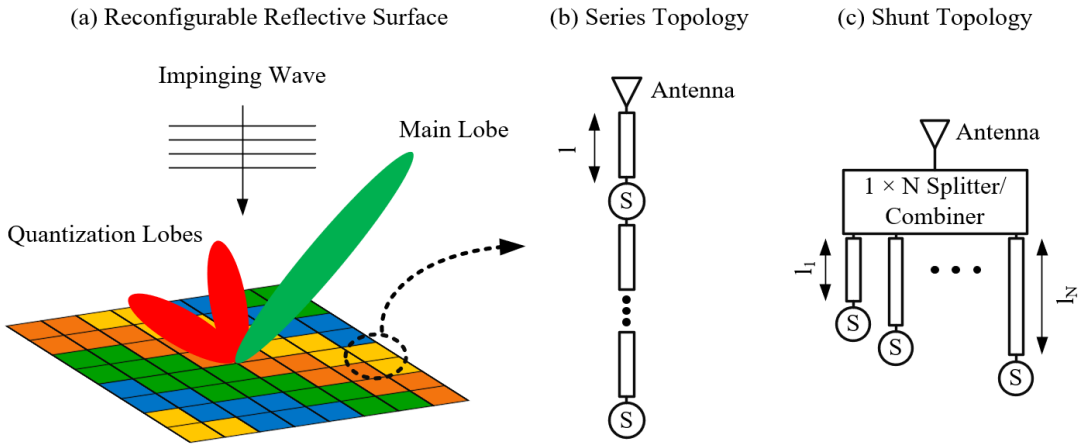

Fig. 9.1 (a) In multi-bit RRSs, the quantization lobes are suppressed due to the higher phase sampling within each unit-cell, compared to the single-bit designs (Chapter 8). The unit-cell topologies that provide the required multi-phase switching mechanism can be implemented using either (b) series or (c) shunt configurations.

In microwaves, such multi-bit configurations are realized either by integrating multi-state tunable switches (e.g., varactors) on the antennas [30], or by incorporating multiple SPST switches (e.g., PIN diodes) in the unit-cell design [28]. The first approach

is currently impractical in mmWave/THz bands since the availability of low-loss tunable switches (e.g., varactors) is limited in the microwave region (up to 30 GHz) and the use of mmWave/THz tunable materials (e.g., liquid crystals), requires high variable voltage, increasing the biasing network complexity [38]. Therefore, this Chapter focuses on RRS designs that integrate multiple SPST switches (Fig. 9.1) that can be implemented in the mmWave/THZ bands by leveraging the graphene switches presented in Chapters 6 and 7.

In multi-bit RSS topologies that integrate multiple SPST switches, the unit-cell's equivalent circuit can be classified into series and shunt topologies, as shown in Fig. 9.1b-c. In the series topology, the switches are separated by delay lines, thus the reflected signal's phase is controlled by changing the effective length of the transmission line, thus controlling the phase of the reflected waves [31]. However, in the series configuration, the number of switches is 2^B-*1* (*B* is the number of bits) and increases exponentially with the number of required bits, leading to amplitude modulation, insertion losses, and complex biasing networks. On the other hand, in a shunt topology, the received signal is equally split into parallel branches with different delay lines, as illustrated in Fig. 9.1c. Then the reflected waves from the branches constructively interfere forming the various phase states of the unit-cell [32].

Particularly, in the shunt topology, the antenna is integrated with a splitter/combiner forming a multi-port network that distributes the received signals to the parallel branches, as illustrated in Fig. 9.2a. In the case of 2-bit modulation, two SPST-switch-terminated branches are needed, as depicted in Fig. 9.2b. Each of the branches acts as a single-bit modulator, though, if the branches have an electrical length difference of 90^o (round trip), the combined signals on the antenna exhibit 4 different phase states depending on the state

of the respective switches (ON/OFF), as illustrated in the constellation diagrams of Fig. 9.2c-e. In this manner, the shunt topology retains a single switch-per-bit topology, thus keeping the biasing network complexity low, and mitigating amplitude modulation since the signals can be equally split between the identical switches. The main drawback of this configuration is the need for the bulky multi-port splitter/combiner that distributes the signals into the multiple branches. A few attempts to overcome this problem are found in the literature (e.g., [32]), though, none of the existing approaches achieves a single switch-per-bit topology for multi-bit reconfigurability.

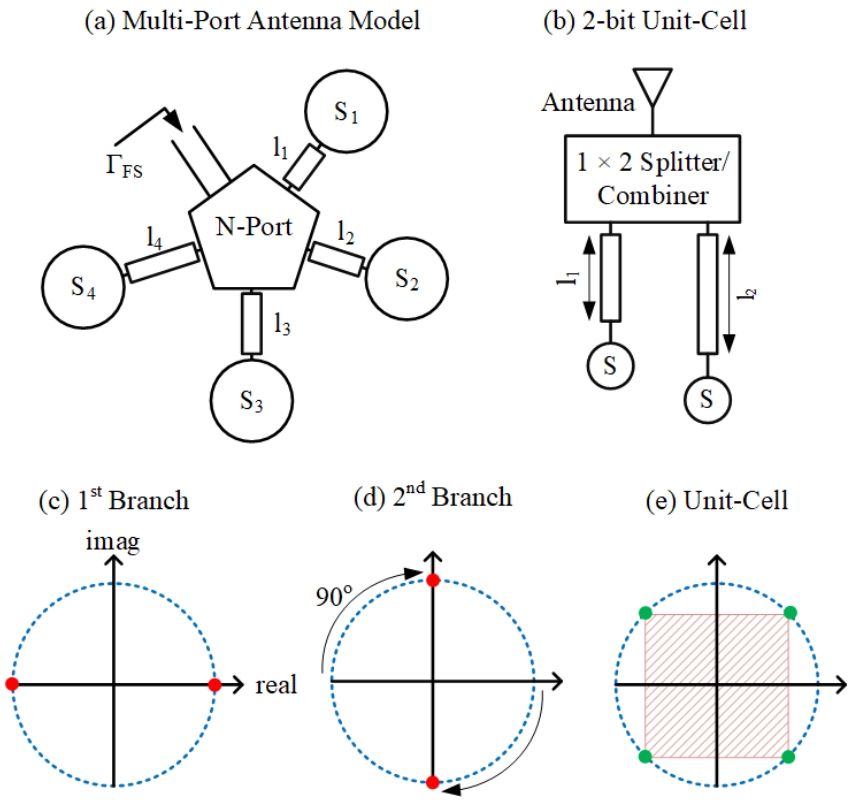

Fig. 9.2 (a) The equivalent network of the switch terminated multi-port antennas. The received signal is distributed between the SPST switches (S_i) through the respective delay lines (l_i). (b) The 2-bit shunt unit-cell topology and (c)-(e) the 2-bit shunt example, in which each of the SPST switches provides two states with a phase difference of 90°, leading to the 4-state constellation diagram in (e).

This Chapter presents high-efficiency multi-bit RRSs while retaining the single switch-per-bit constraint for minimum hardware complexity. Namely, by incorporating the bulky multi-port splitter/combiner into the antenna, the raised real-estate problems of the shunt topology are surmounted. In the presented designs, patch antennas are used, commonly employed in mmWave/THz RRSs, to achieve up to 4-bits of phase quantization, with a single switch-per-bit topology.

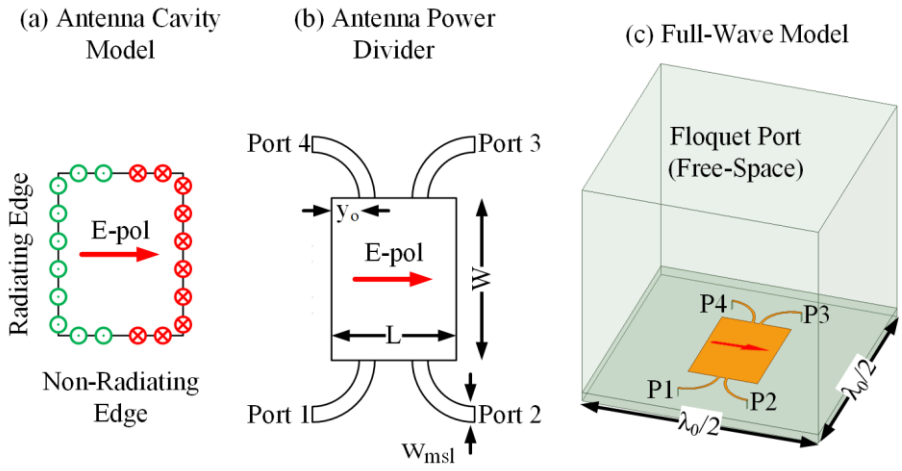

Fig. 9.3 The patch antenna as a power splitter: (a) the edge fields of the patch antenna TM_{001} cavity mode, (b) the multiple feed design to equally distribute the imping waves between the ports, and (c) the full-wave model of (b).

II. The patch antenna as a power splitter/combiner

One of the obstacles toward implementing multi-bit RRSs using the shunt topology (Fig. 9.1c) is the integration of the power splitter/combiner in the limited space of the unit-cell. To overcome this bottleneck, the splitter/combiner is incorporated within the patch antenna, as illustrated in Fig. 9.3. As such, assuming that the patch antenna is a resonating cavity (TM_{001} mode, [2]) 4 symmetric feeding lines are incorporated from the non-radiating

edges. Each of these lines feeds the same cavity mode (TM_{001}), thus the fields from the imping waves are coupled to all 4 ports. The distance (y_o) of the feeding points from the radiating edge impacts the impedance matching, as explained in [2], and is optimized to achieve equal power splitting between the ports.

The antenna is fed from the non-radiating edges, instead of inset feeding, to reduce the mutual coupling between the ports as demonstrated in Fig. 9.4. Furthermore, the coupling between the ports is pronounced as the distance between the inset microstrip feeding lines decreases. Additionally, the inset feeding alters the current flow on the patch antennas (due to the inset cuts), reducing the radiation efficiency, especially in the case of multiple inset feeds.

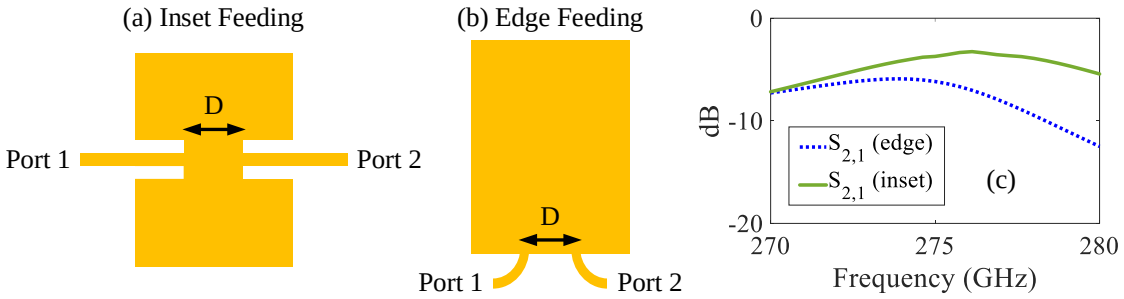

Fig. 9.4 Examples of dual-fed patch antennas: (a) inset feeding and (b) edge-feeding. (c) The coupling between the ports (substrate height is 20 µm, $\varepsilon_r=11.9$, and $D=90\ \mu m$).

To evaluate the proposed topology, the antenna-splitter/combiner configuration, shown in Fig. 9.3c, is modeled using an infinite periodic array of $\lambda_0/2$ spacing. As such, a Floquet port is assigned on the upper boundary of the unit-cell and lumped ports at the edges of the transmission lines and calculate the signal coupled from the Floquet-port (free-

space- FS) to the antenna ports. The substrate used is silicon (ε_r=*11.9* and *h=20 μm*) and the design frequency is 275 GHz. All the design parameters are given in table 9.1.

Table 9.1

Unit-Cell Design Parameters

Variable	Value (μm)	Variable	Value (μm)
W	215	y_o (1-bit)	50
L	147	y_o (2-bit)	57.5
h_{sub}	20	y_o (3-bit)	62.5
w_{msl}	5	y_o (4-bit)	65

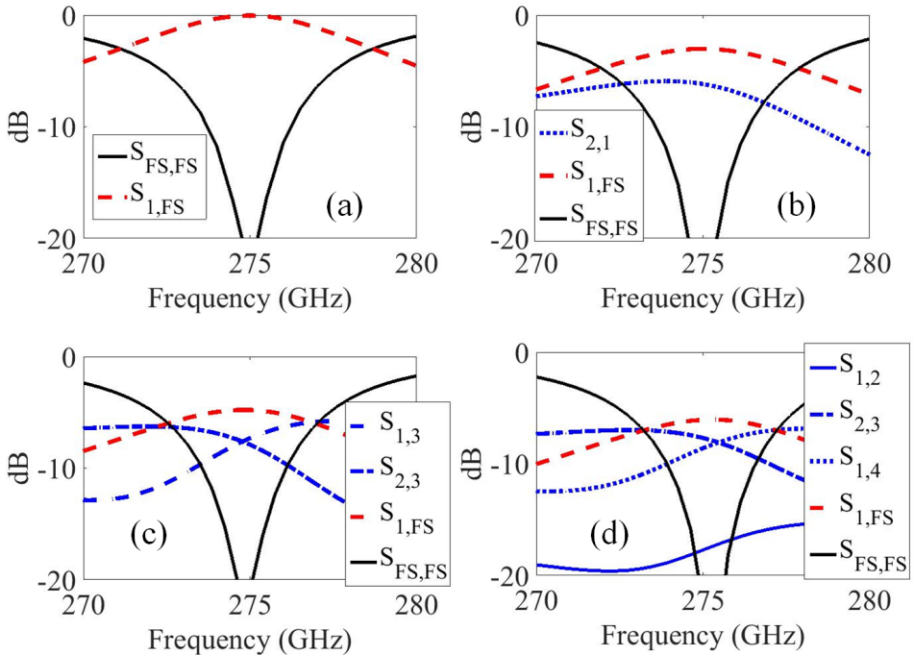

Fig. 9.5 The full-wave simulated scattering parameters of the multi-port antenna configurations of Fig. 9.3. With FS the free space (Floquet port) is denoted.

When a single port is used, all the incident power couples to that antenna port from free space, as shown in Fig. 9.5a. As the number of ports increases, the incoming wave is equally split at the respective ports (Fig. 9.5b-c). Therefore, using the proposed design equal power splitting is achieved between the antenna ports in the limited space of the unit-cell, without using any bulky components (e.g., external power splitters). Moreover, the phase difference between ports 1/4, and, 2/3 is 180^{o} since the mode fields have opposite directions (Fig. 9.3a). Finally, the isolation between the different ports is always 3 dB smaller than the power splitting.

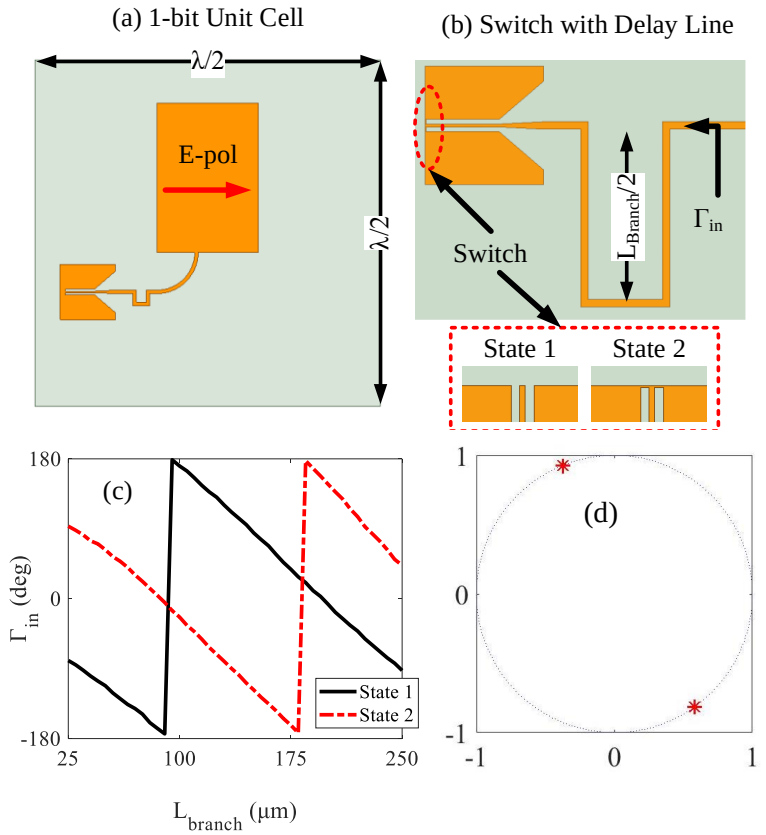

Fig. 9.6 (a) The single-bit unit-cell, (b) the integrated ideal planar CPW switch with the incorporated delay line, (c) the reflection phases of the unit-cell for various delay lengths at 275 GHz, and (d) the constellation diagram of the proposed single-bit unit-cell at 275 GHz for L_{branch}=25 μm.

III. Multi-bit unit-cell design

The singe-bit unit-cell topology that is used as the baseline for the multi-bit configurations is given in Fig. 9.6a. As such, the unit-cell is comprised of a patch antenna with an integrated ideal switch connected at the non-radiating edge. For this case study, an ideal CPW shunt switch is used consisting of a perfect electric conductor (PEC), as shown in Fig. 9.6b. When the PEC is shorting the signal and ground conductors of the CPW, the reflection coefficient is $\Gamma=-1$ (S.C.); on the contrary, in the absence of the PEC, the open-ended CPW is approximated by an open circuit [107], thus $\Gamma=1$ (O.C.). Instead of the PEC, 2D material that exhibits a tunable sheet resistance (e.g., graphene) can be integrated as presented in section 9-V.

To couple the signals from the coplanar-waveguide switch to the microstrip line, a via-less CPW to microstrip transition is implemented as the one used in the topologies of Chapter 8.

As mentioned in section 9-I, to achieve multi-bit reconfiguration, multiple SPST switches need to be integrated with the antenna, where each requires an individual delay line with respect to the feeding point. For that purpose, a microstrip delay line is incorporated in the switch design, as shown in Fig. 9.6b. The goal of this delay line is to shift the reference of the reflected signals as discussed in section 9-I (Fig. 9.2c-d). As shown in Fig. 9.6c, the unit-cell reflection coefficient between the two states (O.C./S.C.), acquired using full-wave simulations [113], remains close to 180^o for various delay lengths. The unit-cell reflection phase is -54^o when the switch is S.C. and 117^o for the O.C., leading to a phase difference of 171^o, close to the ideal 180^o, as depicted in the constellation

diagram of Fig. 9.6d. The defined performance metric for the single-bit unit-cell is the ratio of the achieved phase difference (171°) over the ideal single-bit phase difference (180°), leading to *a 95% ideality*. The phase deviation from the ideal 180° is mainly attributed to the parasitic capacitances of the open-ended CPW [107].

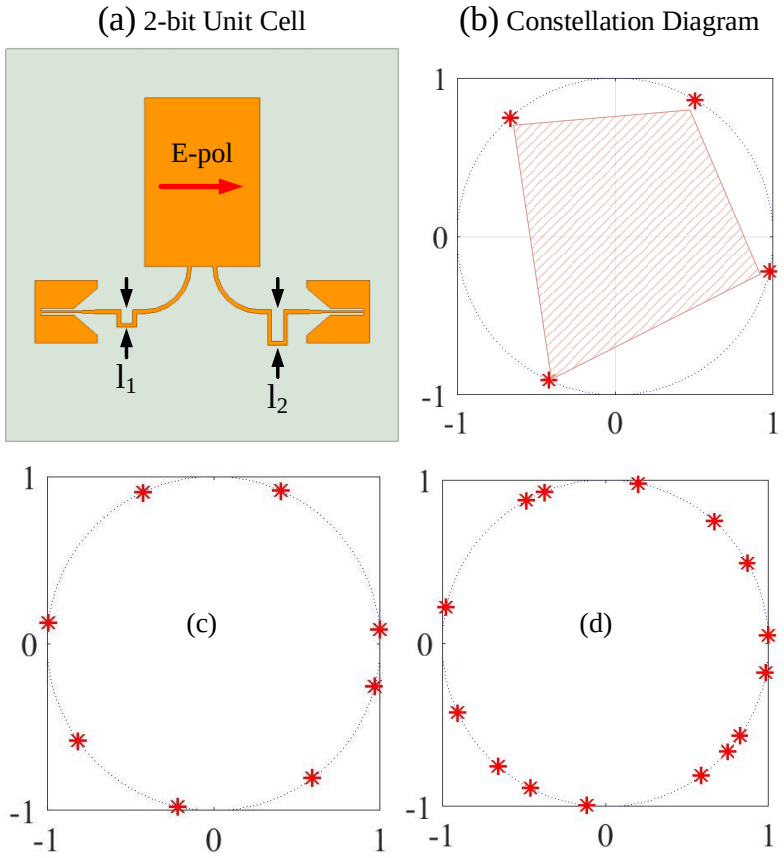

Fig. 9.7 (a) The 2-bit unit-cell design with two integrated SPST switches, (b)/(c)/(d) the full-wave simulated 2/3/4-bit unit-cell constellation diagrams at 275 GHz, respectively.

The 2-bit unit-cell consists of two CPW based SPST switches integrated at each port of the dual-feed antenna as depicted in Fig. 9.7a. Varying the states of the two switches between S.C. and O.C., four different phase states are acquired, hence 2 bits. The distribution of the four phase states alongside the unit-circle depends on the lengths of the

two delay lines since these control the required phase difference as explained in section 9-I (Fig. 9.1c and Fig. 9.2b-e). However, the multi-port antenna exhibits mutual coupling between the ports (Fig. 9.5), altering the expected performance. Thus, to find the optimal reflection phase constellation diagram, the delay branch lengths of each switch are varied between 25-250 μm, and the inscribed polygon area, defined by the unit-cell's reflection coefficients, is observed, as shown in Fig. 9.7b. When the area of the polygon is maximized, all the reflection coefficient points are close to equispaced (ideal distribution), thus providing the optimal branch lengths. This optimization is performed by mathematically combining the scattering parameter matrices of the multi-port antennas (acquired by full-wave simulations) and the reflection coefficients of the ideal switches with the delay lines (acquired by full-wave simulations), as depicted in Fig. 9.2a since the full-wave optimization of the unit-cell is a computationally-intensive process. The optimized branch length values are given in table 9.2. Afterward, the optimal delay lengths are used to design the unit-cells in the full-wave simulator and acquire unit-cell's reflection coefficients tabulated in table 9.3. The ideality of the phase states' distribution is 93% and is given by the ratio of the full-wave simulated polygon area (Fig. 9.7b) over the ideal polygon area (Fig. 9.2e).

Table 9.2

Multi-Bit Unit-Cell Branch Lengths and Ideality

Configuration	l_1 (μm)	l_2 (μm)	l_3 (μm)	l_4 (μm)	Ideality
1-bit	25	-	-	-	95 %
2-bit	25	61	-	-	93 %

3-bit	82	187.5	127.5	-	95 %
4-bit	61	36	96	126	97 %

Similarly, the 3- and 4-bit unit-cells are devised by integrating SPST switches with different delay lines at each port of the multi-port antenna. Each of the single-bit switches behaves as an S.C. or O.C. termination, leading to 8 and 16 reflection phase states for the 3- and 4-bit unit-cells, respectively. The lengths of the delay branches are optimized to acquire the maximum area of the inscribed polygon (as in the 2-bit case) and the optimal values are given in table 9.3. The simulated unit-cell reflection phase states (constellation diagram) for the 3- and 4-bit schemes are shown in Fig. 9.7c-d; the exact unit-cell reflection coefficients values are tabulated in table 9.3. Likewise, the ideality of the acquired constellation diagrams is computed by calculating the ratio of the inscribed area of the optimized polygon over the ideal, leading to a 95% and 97% ideality for the 3- and 4-bit unit-cells, respectively.

Table 9.3

The Multi-Bit Phase States in Degrees (at 275 GHz)

State Number	1-bit (deg)	2-bit (deg)	3-bit (deg)	4-bit (deg)
1	-54	-114	-144	-155
2	117	-12	-102	-155
3		59	-53	-131

4		131	-14	-117
5			4	-96
6			66	-54
7			115	-41
8			172	-34
9				-10
10				2
11				29
12				48
13				78
14				111
15				118
16				167

Table 9.4

Phase Distribution of the 21-element RRS for Beam Steering at +30^{o}

Antenna	1-bit	2-bit	3-bit	4-bit
1	-54^{o}	-12^{o}	4^{o}	2^{o}
2	-54^{o}	-114^{o}	-53^{o}	-96^{o}
3	117^{o}	-114^{o}	-144^{o}	-155^{o}

4	117º	131º	115º	118º
5	-54º	59º	66º	48º
6	-54º	-12º	-14º	-10º
7	117º	-114º	-102º	-96º
8	117º	-114º	-144º	-155º
9	117º	131º	115º	111º
10	-54º	59º	4º	29º
11	-54º	-12º	-53º	-41º
12	117º	-114º	-102º	-117º
13	117º	131º	172º	167º
14	117º	59º	115º	78º
15	-54º	-12º	4º	2º
16	-54º	-12º	-53º	-54º
17	117º	-114º	-144º	-131º
18	117º	131º	172º	167º
19	-54º	59º	66º	78º
20	-54º	-12º	-14º	-10º
21	-54º	-114º	-102º	-96º

IV. Multi-bit RRS design

In this section, the scattering properties of linear multi-bit RRSs are analyzed. As such, full-wave simulations are used to evaluate the performance of the proposed multi-bit RRSs when mutual coupling (e.g., surface waves) is also considered among the elements.

To demonstrate the performance of the proposed RRSs, the multi-bit unit-cells are used to devise 21-element linear RRSs ($\lambda_0/2$ spacing at 275 GHz) that are illuminated by boresight far-field plane-waves and redirect the waves at 30 degrees. The phase coding profile for each bit configuration is derived by quantizing (2.10) to the available phase states and resulting RRS phase coding profiles are given in table 9.4. The simulated RCS patterns of the four arrays, alongside their calculated patterns using (2.6), are given in Fig. 9.8a-d. As clearly shown by these figures, (2.6) is accurately capturing the shape of the main lobe and the maximum side-lobe level (SLL), but the sidelobe positions and shape differ since the coupling between the neighboring antennas results in surface waves that alter the surface field's profile. Moreover, all the simulated radiation patterns are given in Fig. 9.9, normalized to the 4-bit case. As expected, the greater the number of bits, the smaller the quantization errors, leading to higher gain and smaller SLL level.

The simulated aperture efficiencies ($e_{ap,sim}$) of these arrays are given in table 9.5. As such, the aperture efficiency is acquired by comparing the maximum RCS response of the RRS with respect to a PEC plate of the same size illuminated by a boresight plane wave. In the presented RRSs, the boresight impinging waves are reflected toward 30^o, unlike the PEC reference plate where waves are back-reflected toward the boresight direction. This discrepancy causes the RRS to appear physically smaller than the PEC plate due to the

oblique projection angle, thus the calculated aperture efficiencies are normalized by a factor of cos(30°)≈0.87 to account for this effect.

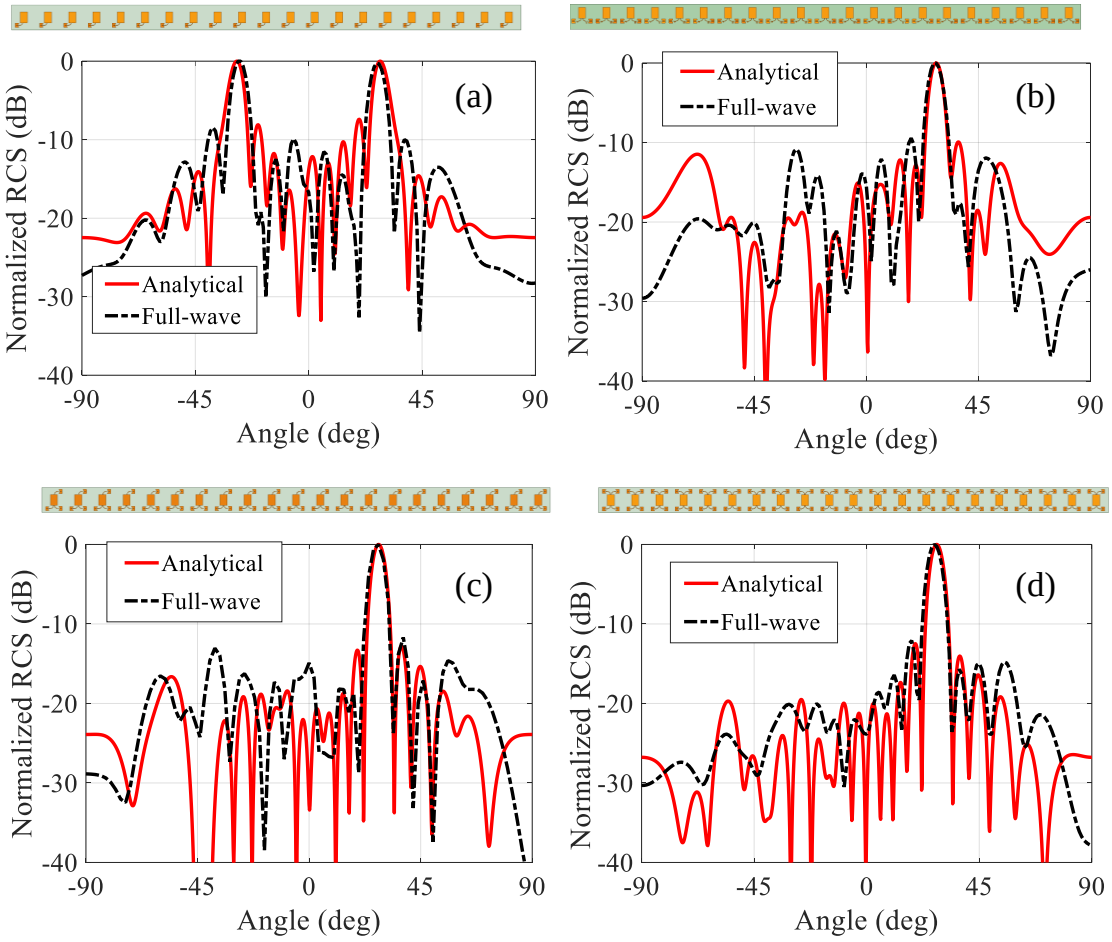

Fig. 9.8 The full-wave E-plane RCS patterns of the 21-element RRS at their respective center frequency versus the calculated using (3), for the 1,2,3, and 4- bit topologies in (a)-(d), respectively. On the top of each graph, the top-view of the full-wave model is given.

All the aforementioned results and discussions concern the center frequency of each array configuration given in table 9.5; however, all antenna systems are required to exhibit a reasonable performance over a specific bandwidth (BW) both for imaging and communication applications. Such thin, high dielectric constant substrates are common in mmWave/THz bands and are typically fabricated, using silicon-on-insulator (SOI) wafers.

The use of a thin silicon substrate reduces the 10 dB bandwidth (BW) of the patch antenna close to 1.5 % [2]. On the other hand, the designed patch antennas are not used as receivers or transmitters, though as single/multi-port power splitters/combiners (Fig. 9.5). Here the BW definition is expressed in terms of radiation characteristics. As such, the BW of the RRS is defined as the frequency range in which the SLL is below -10 dB, while the impinging waves are redirected at the desired angle (same as Chapter 8).

Table 9.5

Multi-Bit RRS Performance

Configuration	fc (GHz)	BW (%)	$e_{ap,sim}$
1-bit	273.25	1.5	0.41
2-bit	274.65	1	0.68
3-bit	274.55	0.9	0.88
4-bit	276.7	0.8	0.94

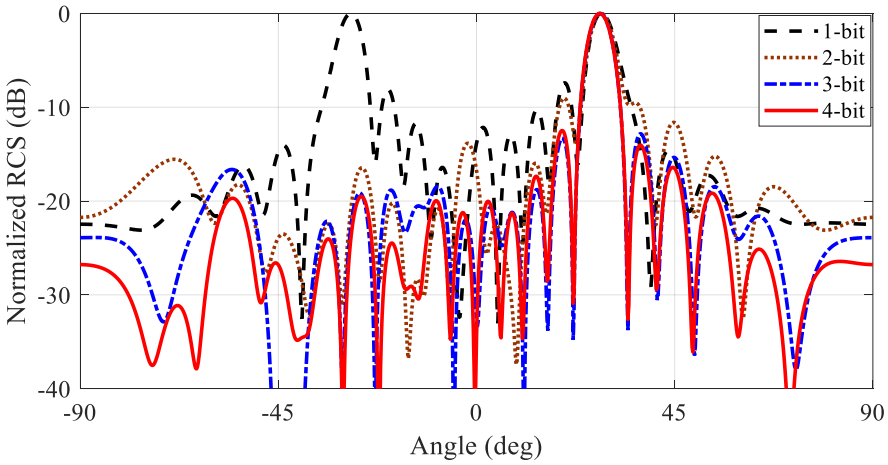

Fig. 9.9 The E-plane RCS patterns of the 21-element RRSs for all four configurations (full-wave), normalized to the maximum gain of the 4-bit design.

The simulated (FEM) RCS patterns of the 21-element multi-bit reflective arrays versus frequency are given in Fig. 9.10, where the frequency range in which the SLL remains below -10 dB is denoted. Noticeably the BW of the proposed multi-bit RRSs slightly reduces as the number of bits increases. This is attributed to the frequency-depended phase delay introduced by the different branches at each port, leading to alterations in reflection phase constellation diagrams of the unit-cells. The simulated BWs and the respective center frequencies are given in table 9.5, where the reduction in the fractional BW versus the number of utilized bits is observed. Moreover, the center frequency of the designs is slightly shifted when modeled in the full-wave simulator due to mutual coupling effects, hence optimization is necessary to align the center frequencies toward fabrication. though it constitutes part of the future work.

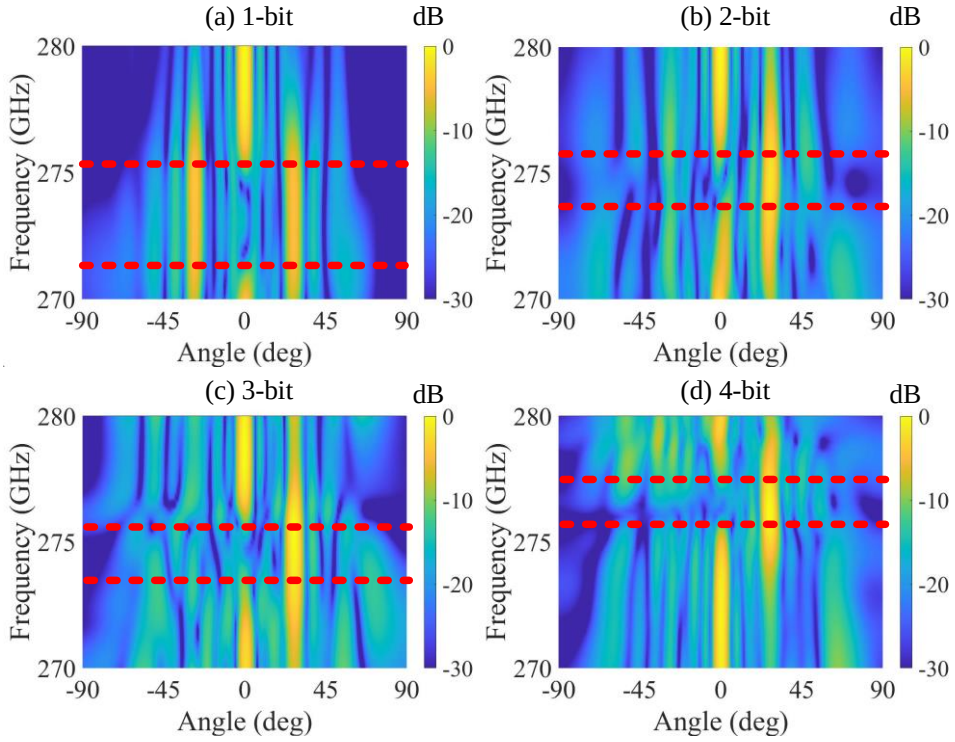

Fig. 9.10 The E-plane RCS patterns of the proposed RRSs versus frequency. With red dotted lines, the upper and lower operating frequencies are denoted.

To emphasize the novelty of the proposed designs, in table 9.6, a comparison of the existing multi-bit RRSs is presented. All the tabulated designs utilize multi-bit reconfiguration of the reflected waves with the use of SPST switches (e.g., PIN diodes).

Table 9.6

Multi-Bit Reflective Surfaces with SPST Switches

Ref.	fc (GHz)	Topology	Number of Bits	Switch-per-bit
[31]	3.2	Series	2	1.5
[32]	7.3	Shunt	2	1
[33]	2.3	Unspecified	2	2.5
[36]	15.5	Unspecified	2	1
[37]	36.5	Unspecified	2	4
This Work	275	Shunt	4	1

V. 2-bit Graphene RRS

In the previous sections of this Chapter, multi-bit unit-cell topologies for mmWave/THz RRSs were thoroughly presented. However, the previous case studies incorporated ideal CPW (S.C/O.C) switches that offer low RF losses simplifying the design process. As such, to optimize the multi-bit unit-cell designs and acquire the constellation diagrams, the inscribed polygon area formed by the various reflection states was observed. This process is adequate when lossless switches are used, however, in an implementation scenario where lossy switches (e.g., graphene) are incorporated, then the reflection states

of the unit-cell are expected to move not just radially around the unit circle but also within, leading to amplitude variation between the phase states, as shown in Fig. 9.11a. Namely, these are the phase states of the 2-bit graphene loaded unit-cell, illustrated in Fig. 9.12a. If the aforementioned optimization process is followed, both constellations of Fig. 9.11a could be used since they have the same inscribed area. However, the constellation of Area-2 (black) has severe amplitude variation between the four states, though the concentration of Area-1 (red) has a more uniform amplitude variation.

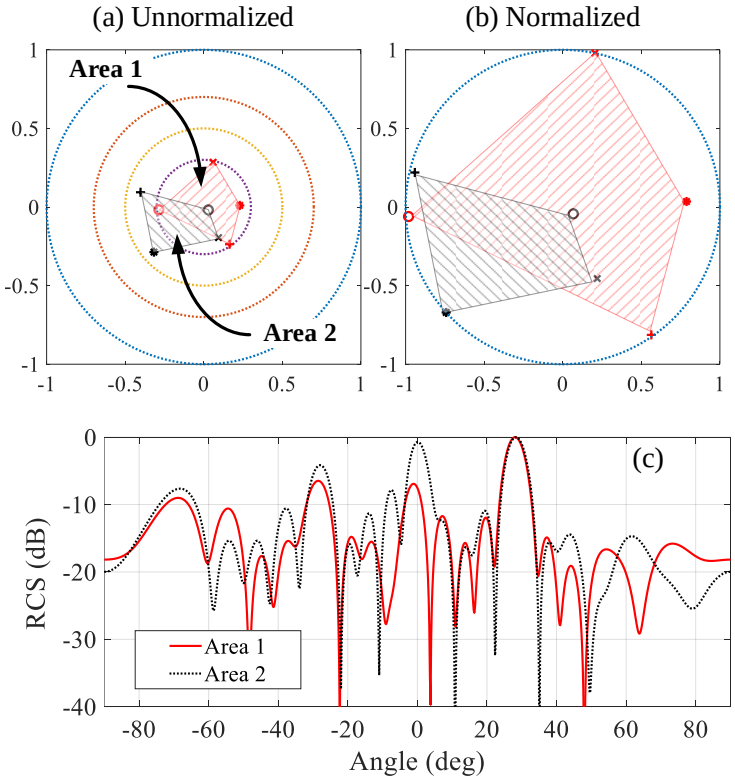

Fig. 9.11 (a) Two unnormalized constellation diagrams of the 2-bit graphene unit-cell that exhibit the same inscribed area. (b) the normalized constellation diagrams of (a), and (c) the normalized RCS patterns of a 20-element RRS with the two different coding schemes at 275 GHz.

To overcome this issue, during the optimization process, all the acquired phase states are normalized to their respective maximum, and then the inscribed areas are

calculated, as shown in Fig. 9.11b. In this manner, the more uniform (less amplitude variation) constellation diagram is chosen. The effect of the normalization process is evident in Fig. 9.11c, where the two different 2-bit configurations are used to form a linear RRS with 21-elements at 275 GHz. The calculated RCS patterns (using 2.6) show that using the Area-1 constellation leads to severe grating lobes due to the amplitude modulation, unlike the case in which the Area-2 (no amplitude modulation) constellation diagram is chosen.

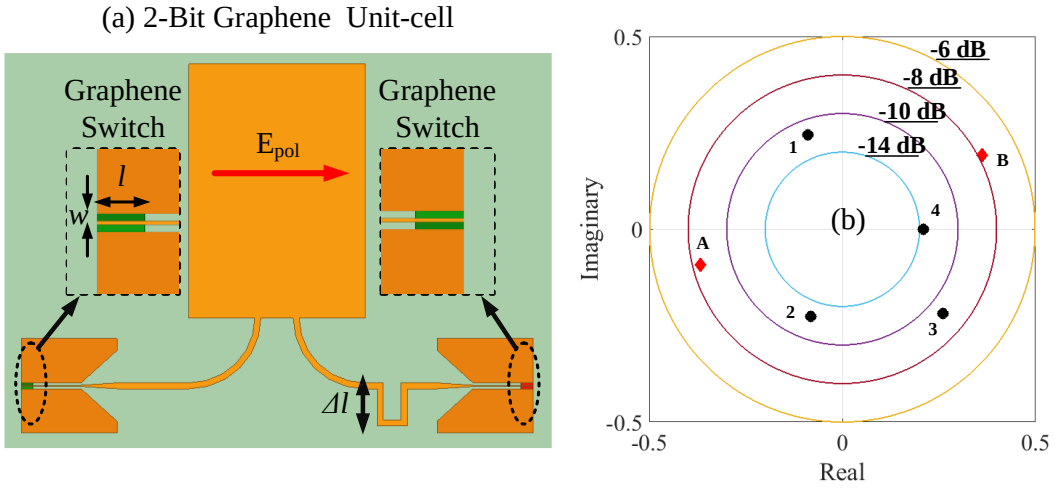

Fig. 9.12 (a) The proposed 2-bit graphene unit-cell and (b) the constellation diagrams of the 1-bit and 2-bit configurations at 275 GHz. {For the 2-bit design: *Δl =50 μm (~λg/8)*}

The constellation diagram of the two-bit graphene unit-cell alongside its 1-bit counterpart of Chapter 8, is given in Fig. 9.12b and tabulated in table 9.7. Specifically, from Fig. 9.12b, it is observed that the 2-bit implementation leads to more unit-cell losses compared to the 1-bit designs. These extra losses are attributed to the crosstalk between the two antenna ports with the integrated graphene switches. However, the quantization

efficiency is expected to increase due to the more phase states. As such, using 2-bits, suppresses the quantization lobes of the linear 21-element RRS, as shown in Fig. 9.13.

Table 9.7

The Phase States of the 2-bit Graphene Unit-Cell (at 275 GHz)

State	$\|\Gamma\|$	$\angle\Gamma$ (degrees)
1	0.37	142
2	0.45	-136
3	0.37	-56
[36]	0.33	43

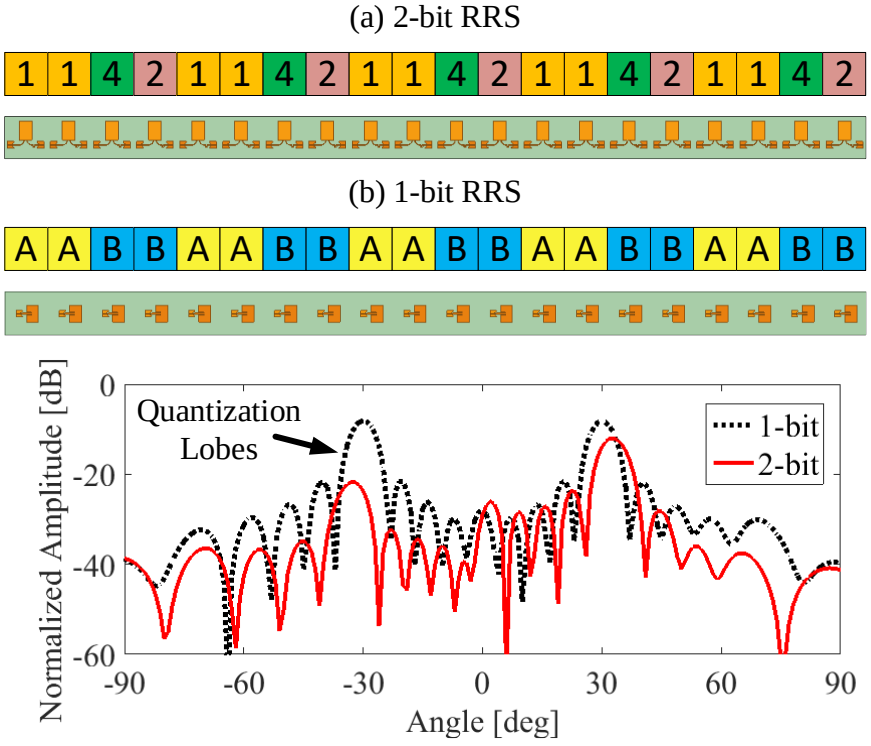

Fig. 9.13 The normalized RCS patterns of the graphene-reconfigured 21-element RRSs.

The RF unit cell losses in the 1-bit case are 8 dB, though for the 2-bit unit-cell the losses are increasing to almost 12 dB. This seems as a bottleneck, however, the 2-bit not only offers a single main beam that is crucial for imaging and wireless communication applications, but also outperforms digital phased arrays, as shown in Fig. 9.14. Namely, using (8.6) the total power consumption of the 2-bit graphene RRS is calculated and overlayed with the 1-bit RRS and digital phased array results (Fig. 8.16). From the presented data, it is obvious that the proposed 2-bit design outperforms the digital phased arrays in all configurations that use more than 100 antenna elements, thus emphasizing the overall efficacy of the proposed topologies.

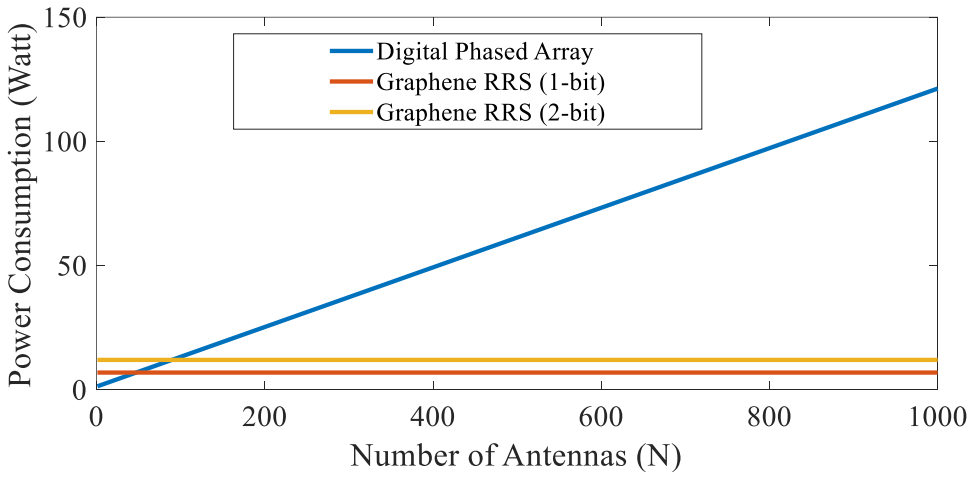

Fig. 9.14 The power consumption of the graphene reconfigurable RRSs and a digital phased array versus the number of integrated antenna elements.

VI. Conclusions of Chapter 9

In this Chapter, for the first time, a multi-bit (up to 4-bits) RRS design achieving single switch-per-bit schemes was presented. The reconfigurable multi-bit topologies incorporate the necessary power splitter/combiner in the unit-cell leveraging the cavity

model theory of the patch antenna, thus overcoming the real-estate constraints arising in such compact designs. Using these novel multi-port antennas, the impinging waves are split into the different ports and by modulating the state of the integrated SPST switches (one per port) multi-bit reconfigurability up to 4 bits (16 phase states) is achieved. The performance of the presented designs, with respect to the ideal multi-bit, is more than 93% for all the proposed configurations. The proposed topologies are validated through full-wave simulations showing a good agreement between the calculated and simulated RCS patterns. Using the presented approach, a significant improvement of the aperture efficiency of the single-bit reconfigurable surface from 41 % to 94 % for the 4-bit is acquired. This improvement arises from the elimination of quantization errors due to the use of multi-bit designs.

All the presented multi-bit RRS designs of this Chapter, incorporate more than one SPST switch to increase the aperture efficiency and eliminate the strong parasitic quantization lobes. However, in certain scenarios, a single SPST switch is preferable to retain a simple design and reduce the implementation cost. In that case, the undesired parasitic lobes should be eliminated to acquire single beam RCS patterns from the low-bit RRS. Thus, in the next Chapter, a method that eliminates the quantization lobes in low-bit RRSs is detailed.

CHAPTER 10

Mitigating Quantization Lobes in Low-bit Reconfigurable Reflective Surfaces

This Chapter presents a technique for the suppression of quantization lobes in low-bit RRS. As such, the multi-bit RRS topologies presented in Chapter 9 require the integration of multiple SPST switches within the limited space of the unit-cell; additionally, more switches translate to higher RF and DC losses, system complexity, and cost. Therefore, the question that arises is can an RRS retain the advantages of the multi-bit configurations, while alleviating the undesired system complexity?

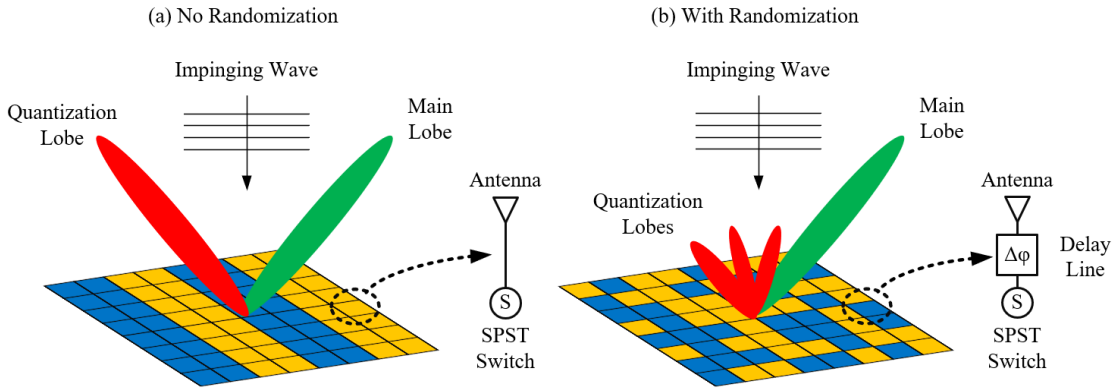

Fig. 10.1 Beamsteering with (a) 1-bit non-randomized RRS results in parasitic quantization lobe (as in Chapter 8). Adding random phase delays in the unit-cells (b) suppresses the undesired lobe.

This question has a twofold answer; on the one hand, the aperture efficiency of a single-bit RRS cannot exceed 50 % due to the high-quantization errors. On the other hand, the single lobe performance of the multi-bit RRS can be achieved with a single-bit RRS as

presented in this Chapter. Specifically, to suppress the high-level quantization lobes the unit-cell of the single-bit RRS can be modified accordingly by incorporating a delay line. These delays differ for every unit-cell and help abolish the symmetric phase profile of the reflected waves over the RRS, suppressing the quantization lobes that occur due to symmetry. In this Chapter, the mathematical approach of this method is presented along with a series of theoretical and measurement results of single-bit RRSs with single lobe performance.

I. Background on quantization lobe suppression in low-bit RRSs

The previous Chapters 2, 8, and 9 have proved that by applying a series of progressive phase shifts over an RRS, the main reflected beam can be steered to the desired direction. However, to acquire a single lobe RCS pattern from the RRS multi-bit quantization schemes should be employed that require multi-switch designs as the ones presented in Chapter 9. Though, in some implementations, 1-bit RRSs are preferable owing to their design simplicity and lower implementation cost when compared to the higher-bit quantization schemes. However, under plane wave illumination, the quantized coding techniques introduce grating lobes due to the periodicity of the errors resulting from the limited number of bits used in the phase rounding quantization as presented in Chapters 2 and 8. These undesired lobes or quantization lobes appear in addition to the main lobe, as shown in Fig. 10.1a. The issue is particularly aggravated in a 1-bit quantization scheme where the quantization lobe has the same power as the main lobe. Thus, to exploit the advantages of a 1-bit quantization scheme, it is critical to break the periodicity of the phase rounding quantization error and suppress the quantization lobes.

Accordingly, this Chapter presents a technique to mitigate the quantization lobes, in planar, single-layer 1-bit RRSs, that appear when illuminated with plane waves as in the IRS systems. Specifically, the principles of random phasing are adopted. This technique was originally proposed in multi-bit phased array systems [119] to break the periodicity of the phase rounding quantization error and thereby mitigate the quantization lobes in RRSs. The technique is realized by incorporating a randomized phase delay in each unit-cell of the RRS, as shown in Fig. 10.1b. A similar procedure was recently employed to mitigate the quantization lobes in 1-bit designs using a two-layer reflective metasurface excited by normally incident plane waves at 39 GHz [120]. A stacked-layer implementation with two substrate layers and three metal layers is employed with one metal layer acting as the tunable antenna element and the other as the delay. However, such multi-layer implementation can result in increased design complexity and possibly more losses when scaling to higher frequencies. With multiple dielectric layers, the fabrication complexity also increases due to misalignment between layers, airgaps, and bows and/or warpages in the individual wafers.

The presented technique to mitigate quantization lobes introduces random phase delays in a single layer RRS with 1-bit quantization that does not require stacked wafers or RF vias, thus reducing the issues arising in existing designs.

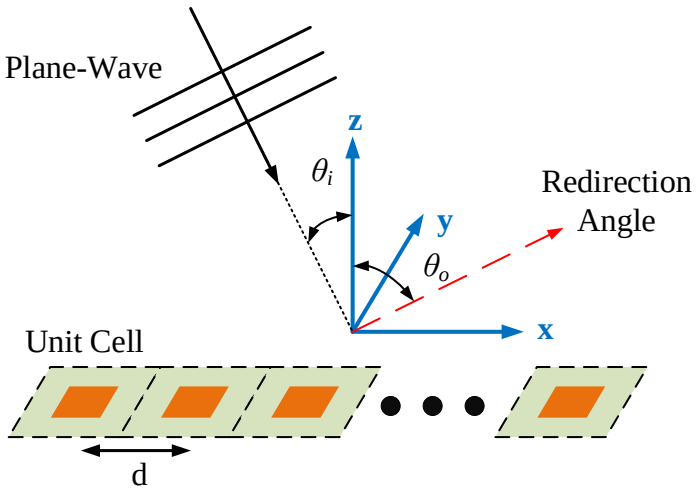

Fig. 10.2 A linear RRS illuminated by a plane wave.

II. Mitigation of quantization lobes in RRSs using random phasing

This section presents a comprehensive study of the random phasing technique employed to suppress the quantization lobes appearing in 1-bit RRS designs.

Let us consider a two-dimensional planar 1-bit RRS consisting of $M\times N$ radiating elements arranged on the **x-y** plane and illuminated by a plane wave from (θ_i,ϕ_i) direction (Fig. 2.4b). To steer the reflected main beam to the desired direction (θ_o,ϕ_o), the modulation phase induced on the currents of the il^{th} unit-cell is given by (2.10) and can be rewritten as

$$\Phi_{mod(i,l)} = \Phi_{RRS(i,l)} - \Phi_{illum(i,l)} \quad (10.1)$$

where $\Phi_{RRS(i,l)}$ is the phase delay required by the RRS elements to deflect the main beam in the (θ_o,ϕ_o) direction, $\Phi_{illum(i,l)}$ is the phase distribution of the element currents induced by a plane wave impinging from (θ_i,ϕ_i).

Considering a 1-bit quantization scheme, all the phase values are rounded off to 0^o or 180^o, and the periodicity of the errors resulting from this quantization scheme leads to the generation of quantization lobes in traditional RRSs. To suppress such lobes, random phase delays are added, $\Phi_{rand(i,l)}$ at every unit-cell using physical delay lines, as shown in Fig. 10.1b. Thus, the continuous excitation phase of the ilth element given by (10.1) becomes

$$\Phi_{mod(i,l)} = \Phi_{RRS(i,l)} - \Phi_{illum(i,l)} - \Phi_{rand(i,l)} \quad (10.2)$$

The random phase delays in (10.2) are obtained from a uniform pseudorandom number generator using

$$\Phi_{rand(i,l)} = rand(i,l) \cdot 180^o \quad (10.3)$$

where the function *rand* provides uniformly distributed random numbers between 0 and 1 [119]. A uniform distribution is required instead of a gaussian or a triangular distribution as the former gives the maximum achievable SLL when compared to the latter two distributions [119]. After calculating $\Phi_{mod(i,l)}$ the quantization process follows leading to $\Phi_{quant(i,l)}$.

To understand the effect of random phase delays in RRS designs, a 30-element linear 1-bit RRS under broadside plane wave illumination ($\Phi_{illum(i,l)}=0^o$) is considered (Fig. 10.2). Without randomization ($\Phi_{rand(i,l)}=0^o$), quantization errors due to phase rounding exhibit a periodic distribution across the RRS, leading to a periodic $\Phi_{quant(i,l)}$ profile, as shown in Fig. 10.3b. This spatial wave component results in a secondary lobe, as shown in the radiation pattern of Fig. 10.4a. This RCS pattern is calculated using (2.5). For this

specific example, the main lobe is designed to be at -30^o, while the undesired quantization lobe appears at +30^o. In general, under plane wave illumination, the quantization lobe level (QLL) is equal in magnitude to the main lobe and appears at a direction symmetrically opposite to that of the specular reflection angle as also seen in Chapter 8.

When a small range of randomization is introduced, for example, 0^o-60^o, then $\Phi_{rand(i,l)} \neq 0^o$, the random phase delays obtained from (10.3) are between 0^o and 60^o, as shown in Fig. 10.3c. Such a phase range is insufficient to break the periodicity of the quantization error. As such, the errors maintain a quasi-periodic distribution in $\Phi_{quant(i,l)}$, as shown in Fig. 10.3d. This is significantly more pronounced in smaller arrays due to a limited number of elements, and thus, there is only a slight reduction in the QLL (-0.9 dB), as shown in Fig. 10.4b. On the other hand, as the range of randomization is increased to 0^o-120^o, there is a noticeable change in the phase distribution that results in the QLL reduction by 3.6 dB, as depicted in Fig. 10.3e, 10.3f, and 10.4c respectively.

Finally, when the full range of randomization (0-180^o) is utilized to randomize the coding scheme (Fig. 10.3g-h) the quantization lobe reaches a minimum value (QLL = -11.6 dB), as shown in Fig. 10.4c. Table 10.1 summarizes the SLLs achieved for various RRS sizes.

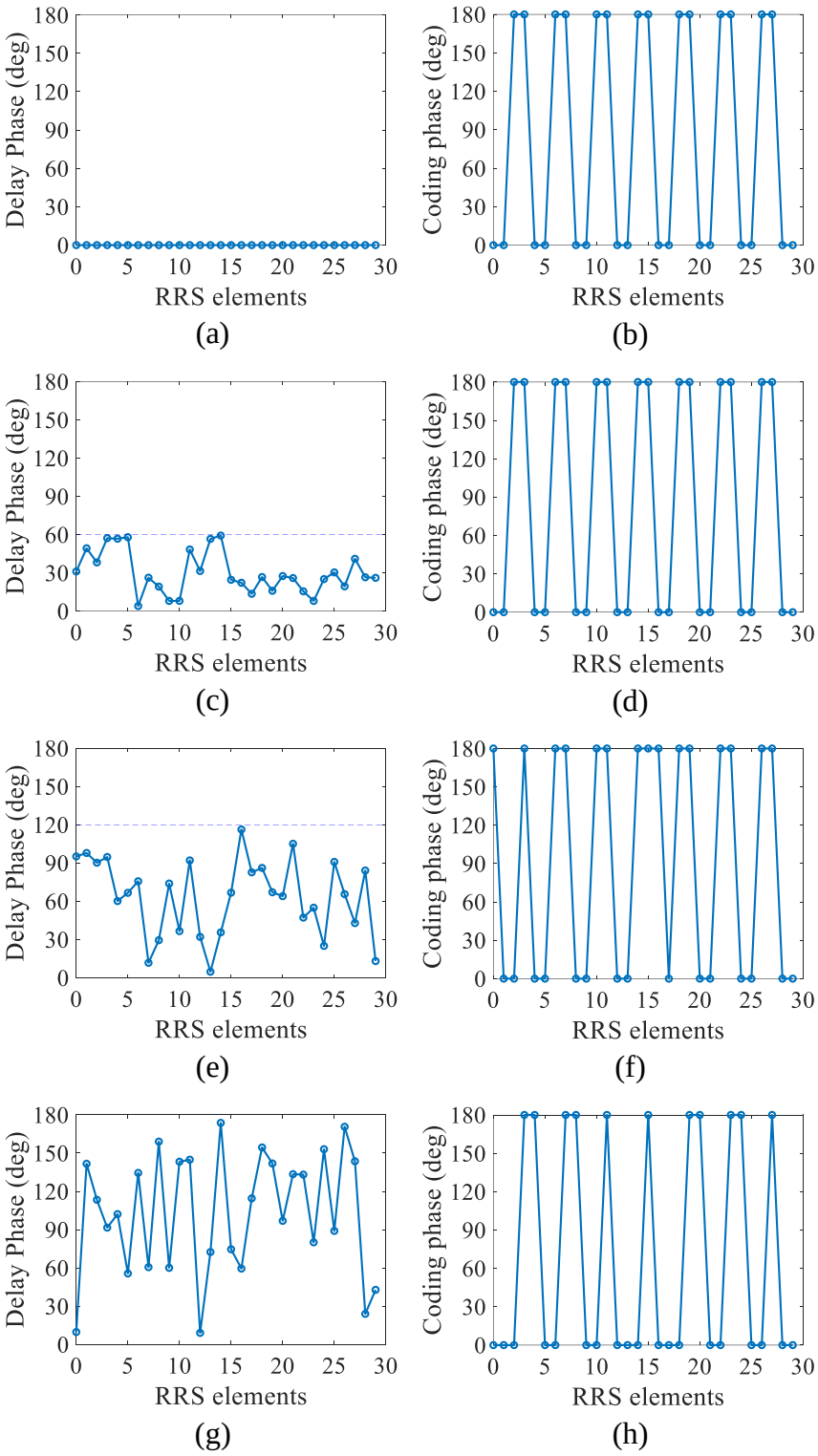

Fig. 10.3 Randomly generated delay phases with varying range of randomization (left) and corresponding quantized binary phases (right) of 30-element (linear) 1-bit RRS. (a), (b) 0º (no randomization), (c), (d) randomization range of 0º-60º, (e), (f) 0º-120º, and (g), (h) 0º-180º.

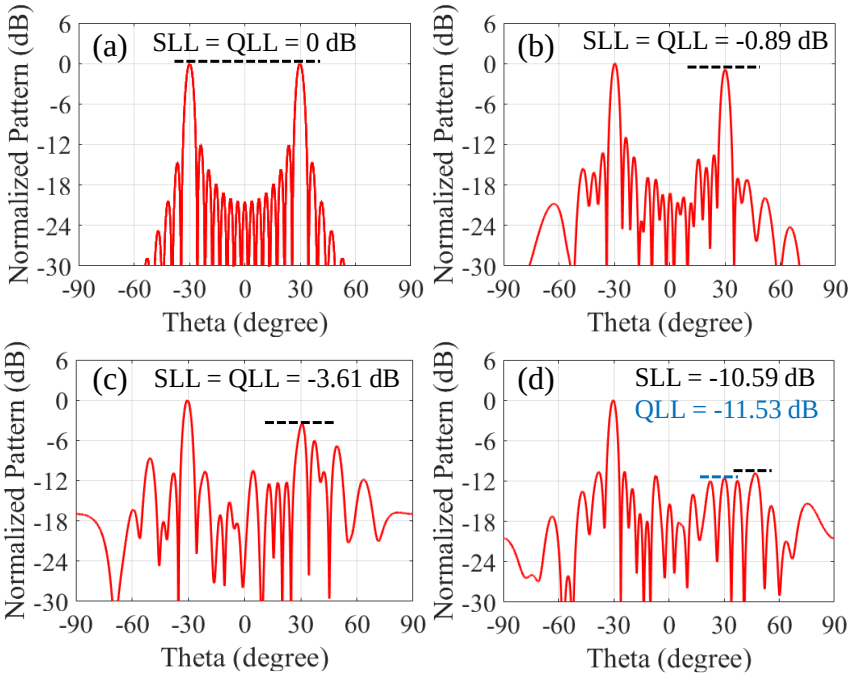

Fig. 10.4 Normalized radiation patterns of 30-element (linear) 1-bit RRS with (a) 0º (no randomization), (b) randomization range of 0º-60º, (c) 0º-120º, and (d) 0º-180º.

Table 10.1

Sidelobe level versus phase randomization

	SLL (dB)			
RRS size/ Randomization Range	0º	0º-60º	0º-120º	0º-180º
30×1	0	-0.9	-3.6	-10.6
200×1	0	-0.6	-7.4	-11.4
30×30	0	-0.8	-6	-15.4

Further to demonstrate the robustness of the proposed randomization technique, the normalized radiation patterns of a 30-element linear 1-bit RRS for various main beam directions are plotted in Fig. 10.5. From the plots, it is evident that altering the direction of the main beam does not impact the quantization lobe reduction. All the radiation patterns are calculated using (2.6).

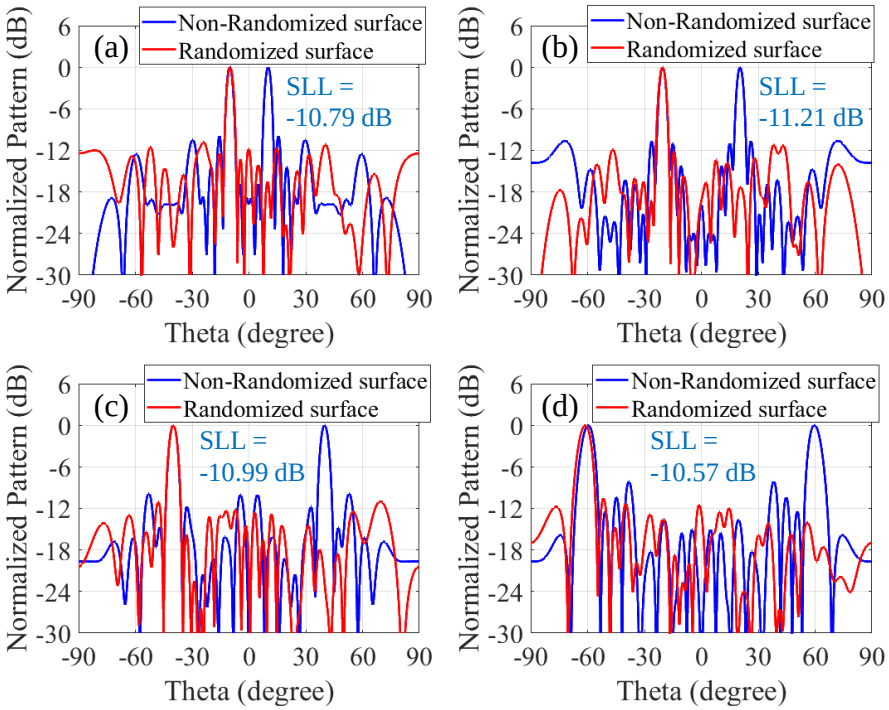

Fig. 10.5 Normalized radiation patterns of 30-element (linear) 1-bit randomized RRS with main beam directed towards (a) -10º, (b) -20º, (c) -40º, and (d) -60º.

Further, to demonstrate the robustness of the proposed randomization technique, the normalized radiation patterns of a 30-element linear RRS excited by obliquely incident plane waves, are plotted in Fig. 10.6. In these examples, the incident plane-waves are arriving from 20º and 30º, while the main beams are redirected toward -10º and -60º, respectively.

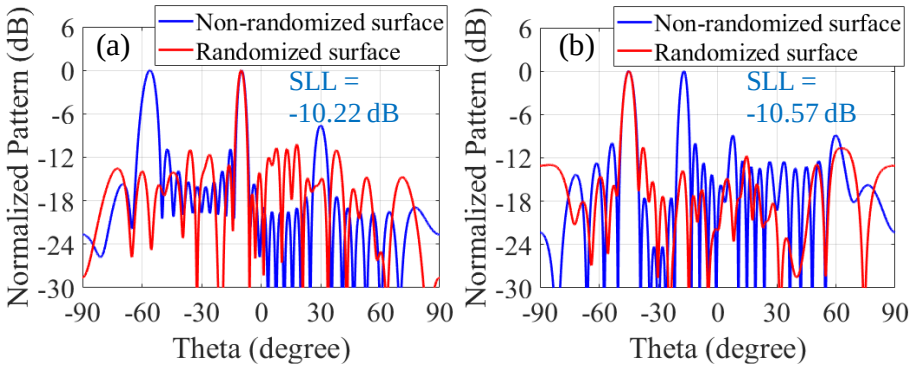

Fig. 10.6 Normalized radiation patterns of 30-element (linear) 1-bit randomized RRS excited by obliquely incident plane wave and the main beam directed towards (a) -10^o (incidence of 20^o) and (b) -60^o (incidence of 30^o).

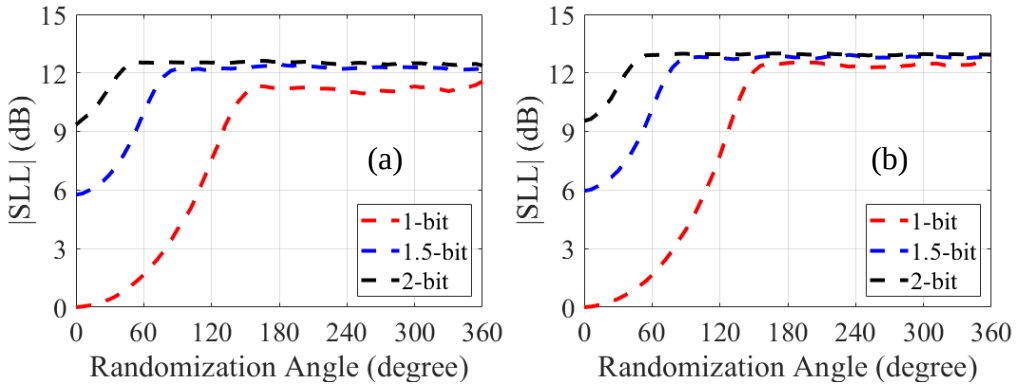

Fig. 10.7 Variation of the |SLL| versus the range of randomization for (a) 200-element linear RRS and (b) 900-element linear RRS.

To understand the effect of the range of phase delays on the acquired SLL, a comparison is carried out for apertures of various sizes and bit configurations. As such, the results of the analytical simulations for a 200-element and a 900-element linear RRS, are depicted in Fig. 10.7, for 1-, 1.5-, and 2-bit quantization schemes. It is observed that the range of randomization required for minimum SLL should be at least [0^o, 180^o] for 1-bit quantization, [0^o, 120^o] for 1.5-bit, and [0^o, 90^o] for 2-bit. This range of randomization also

guarantees the lowest SLL achievable for each configuration. Moreover, it is noticed from the radiation patterns of Fig. 10.4 that the average SLL is also impacted by the random phase delays. Namely, as randomization is increased, the average SLL also increases. This is attributed to the random redistribution of the quantization lobe power to other directions.

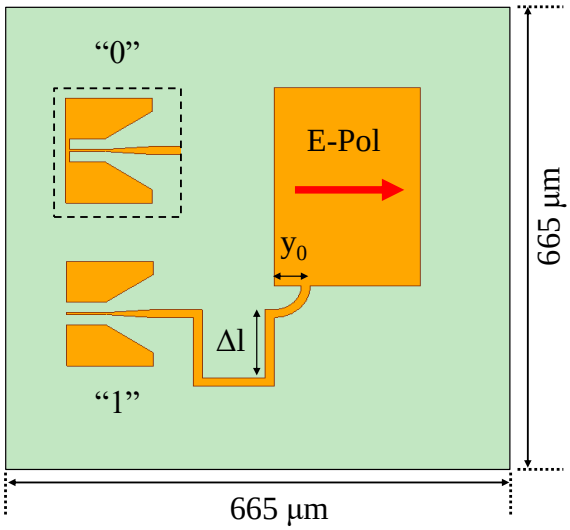

Fig. 10.8 The unit-cell design of the presented RRS.

III. Design of RRS with suppressed quantization lobes

The architecture of the proposed randomized RRS is shown in Fig. 10.1b and its unit-cell consists of an additional randomized delay phase along with the antenna and the SPST switch. The delays are implemented through microstrip lines. The corresponding implementation of the single bit unit-cell proposed in this Chapter is depicted in Fig. 10.8 and it is the basis of the multi-bit configurations presented in Chapter 9. As such, the patch antenna is linearly polarized, and at the non-radiating edge, a transmission line is embedded along with the CPW ideal (O.C./S.C.) switch. The feed position $y_0 = 40\ \mu m$ is optimized

to offer maximum signal coupling between the antenna and the transmission line. The dimensions of the patch are 284 μm × 185 μm, and it is designed to resonate at 222.5 GHz. By varying the length of the feed line branch Δl, the necessary random phase delays can be implemented for each unit-cell, while retaining the 180^o phase difference in the reflection coefficients between the two states (O.C./S.C.), as described in Section 9-III. The total size of the unit-cell is 665 μm × 665 μm, which is approximately $\lambda_0/2$ at 222.5 GHz.

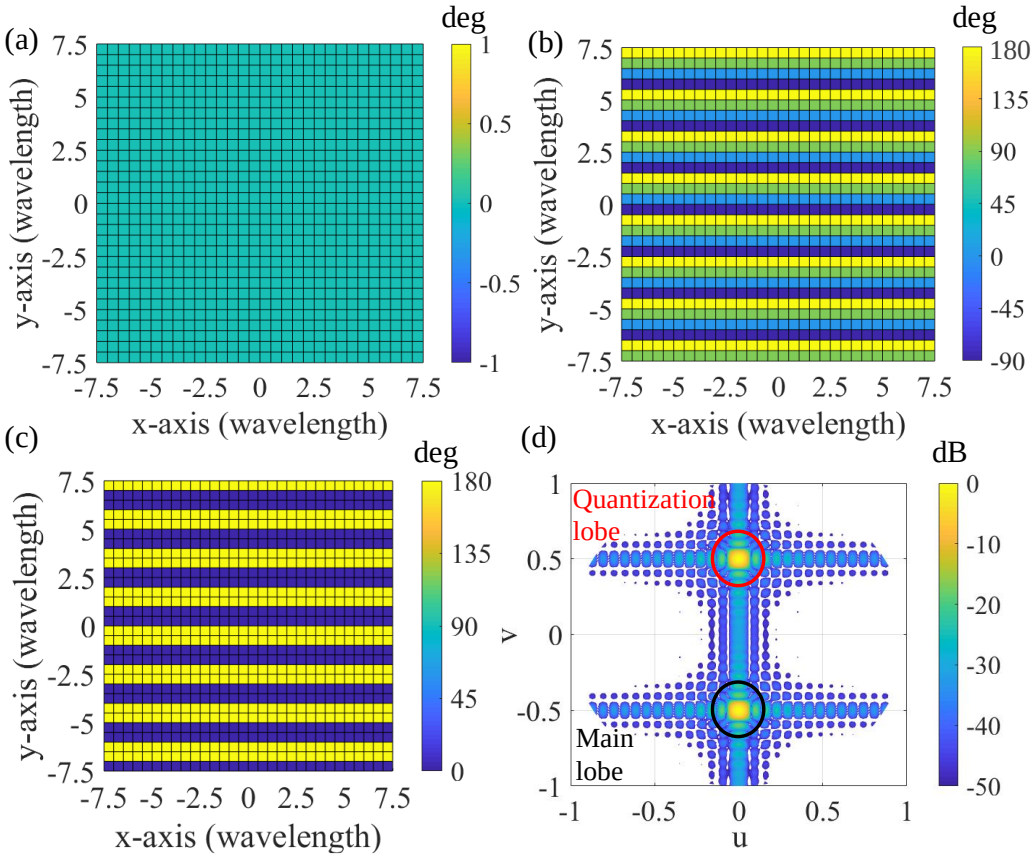

Fig. 10.9 The 30×30 2D non-randomized RRS design: (a) delay phase $\Phi_{rand(i,l)}=0^o$, (b) modulation phase $\Phi_{mod(i,l)}$ obtained from (10.2), (c) quantized phase profile $\Phi_{quant(i,l)}$ based on 1-bit quantization scheme, and (d) normalized 3D radiation pattern in the u-v plane obtained from (2.5).

The randomized and non-randomized RRS designs are compared through numerical analysis. For the non-randomized case, $\Phi_{rand(i,l)}=0^o$, and thus, the phase delays are zero, as shown in Fig. 10.9a. Consequently, the corresponding continuous RRS modulation phase obtained from (10.1) and shown in Fig. 10.9b results in a repetitive quantized coding scheme, as shown in Fig. 10.9c. The resulting radiation pattern has both the desired main lobe along the -30^o and an undesired quantization lobe along +30^o, as shown in Fig. 10.9d. This quantization lobe has the same magnitude as the main lobe, and thus, the QLL is 0 dB.

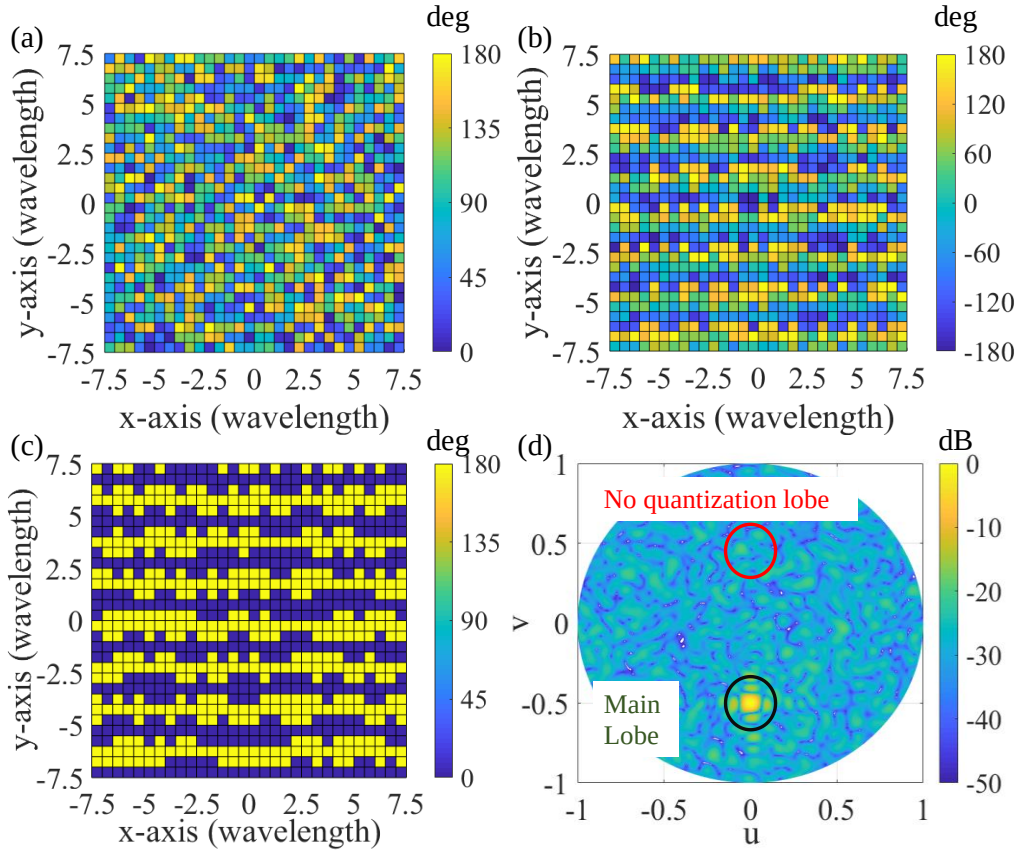

Fig. 10.10 The 30×30 2D randomized RRS design: (a) delay phase $\Phi_{rand(i,l)}\neq 0^o$, (b) modulation phase $\Phi_{mod(i,l)}$ obtained from (10.2), (c) quantized phase profile $\Phi_{quant(i,l)}$ based on 1-bit quantization scheme, and (d) normalized 3D radiation pattern in the u-v plane obtained from (2.5).

In contrast, for the case of randomized RRSs, $\Phi_{rand(i,l)} \neq 0^o$, the pseudorandom phase delays are generated from (10.3) and given in Fig. 10.10a. These phase delays correspond to the physical lengths of the microstrip feed line, Δl. Using (10.2), the calculated continuous element phases are shown in Fig. 10.10b. Consequently, the periodicity of the corresponding RRS modulation phase is perturbed as shown in Fig. 10.10c, resulting in a single main lobe at -30°, as depicted in Fig.10.10d. Finally, the two RRS topologies' RCS patterns at the $\phi = 90^o$ elevation plane are compared in Fig. 10.11, where it is observed that the random phase delay scheme eliminates the QLL.

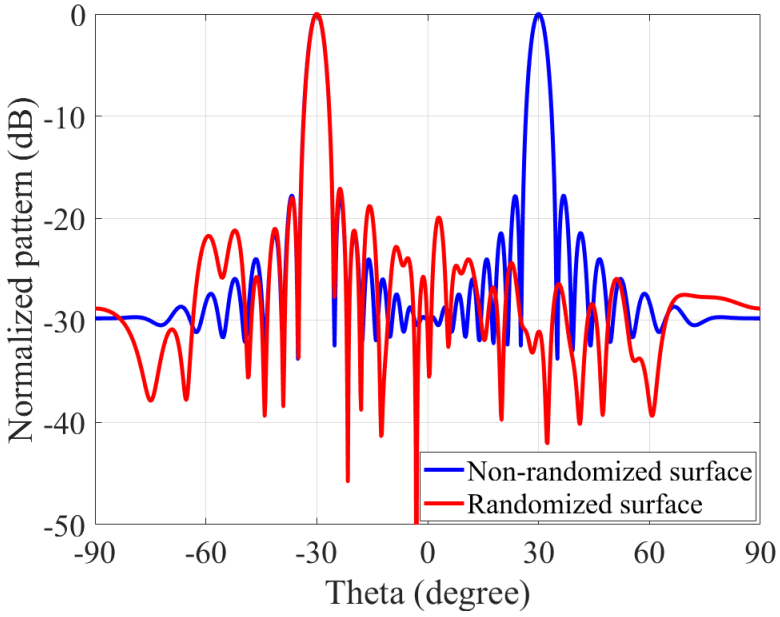

Fig. 10.11 Normalized 2D radiation pattern of the 30×30 reflective surface in the $\phi = 90^o$ plane, comparing the designs with no randomization and full randomization (0-180°).

IV. The fabrication process of a sub-mmWave RRS

The process used for the fabrication of the two single-layer 30×30 planar 1-bit RRSs, one employing full phase randomization (0°-180°) and the other employing no

randomization, are detailed in this section. The single-layer implementation reduces the fabrication complexities when compared to the existing methodologies used for fabricating reflective surfaces that produce single beam radiation patterns.

Both the non-randomized and the randomized RRSs are fabricated side-by-side on a 2" diameter, 45 μm thick alumina ribbon ceramic wafer. The wafer's dielectric properties are $\varepsilon_r=10$ and $tan\delta=0.8e\text{-}3$. The alumina ribbon ceramic wafer is semi-transparent and flexible owing to its fine grain, dense microstructure, and low thickness of 45 μm, so it was bonded to a 2" diameter, 500 μm thick quartz wafer to impart the sturdiness required by the alumina wafer for further fabrication steps. The steps used in the fabrication process are illustrated in Fig. 10.12. Initially, a 30 nm thick Ti layer followed by a 300 nm thick Al layer was deposited on one side of the alumina ribbon ceramic wafer. This layer serves as the ground plane for the radiating structures. Then the metalized side of the alumina ribbon ceramic wafer was permanently bonded with the carrier quartz wafer.

The bonded wafer was spin-coated with photoresists and exposed to UV through the photolithography step to develop the antenna patterns. Then a second metallization step is used to deposit Al for radiating structures, followed by a lift-off process, to obtain the final patterns as shown in Fig. 10.12a. In Fig. 10.12b, a high-magnification image of an individual fabricated unit-cell and in Fig. 10.12c the finished alumina ribbon ceramic wafer with two RRSs, are depicted, respectively.

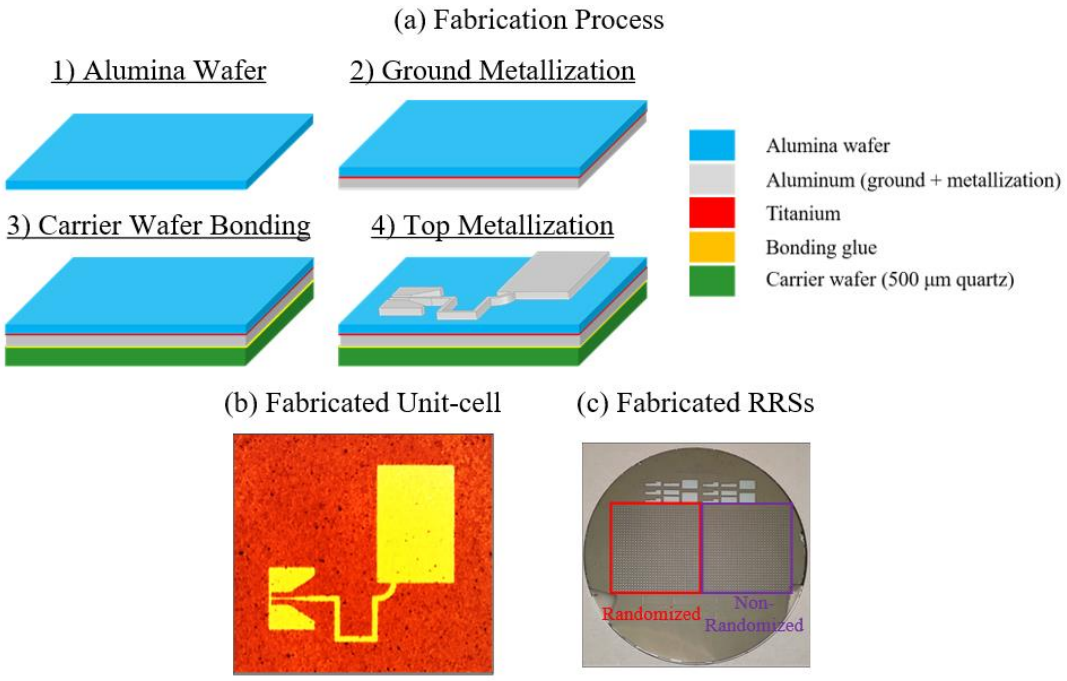

Fig. 10.12 (a) Fabrication process flow for the on-wafer development of the proposed RRSs, (b) a high-magnification image of a unit-cell of the fabricated RRSs, and (c) finished alumina ribbon ceramic wafer with the two RRS prototypes.

V. Characterization of the sub-mmWave RRS

The RCS characteristics of the fabricated RRS prototypes are measured using a quasi-optical setup (Fig. 10.13) consisting of two vector network analyzer (VNA) extenders, a transmitting, and a receiving horn antenna, 2 collimating lenses, and the prototype wafer, all mounted on an optical breadboard. The signal from the VNA is upconverted to 222.5 GHz using the VNA extender on the transmitter side and focused on the wafer. The Teflon lens in front of the transmitting horn antenna is used to collimate the diverging beam from the horn and provides an illumination beam of radius 1 cm on the reflective surfaces. The wafer is mounted on a sliding pedestal so that the RRS under test is aligned with the transmitter beam at boresight ($\theta_i = 0^o$). To measure the scattered fields,

the receiver is rotated radially around the center of each RRS covering the [-20^o, -80^o] and [+20^o, +80^o] angle ranges, only restricted by the geometrical limitations of the setup. Nevertheless, a single point RCS measurement at $\theta_d=0^o$ (monostatic RCS) is carried out to ensure that there is no significant reflection in the broadside direction.

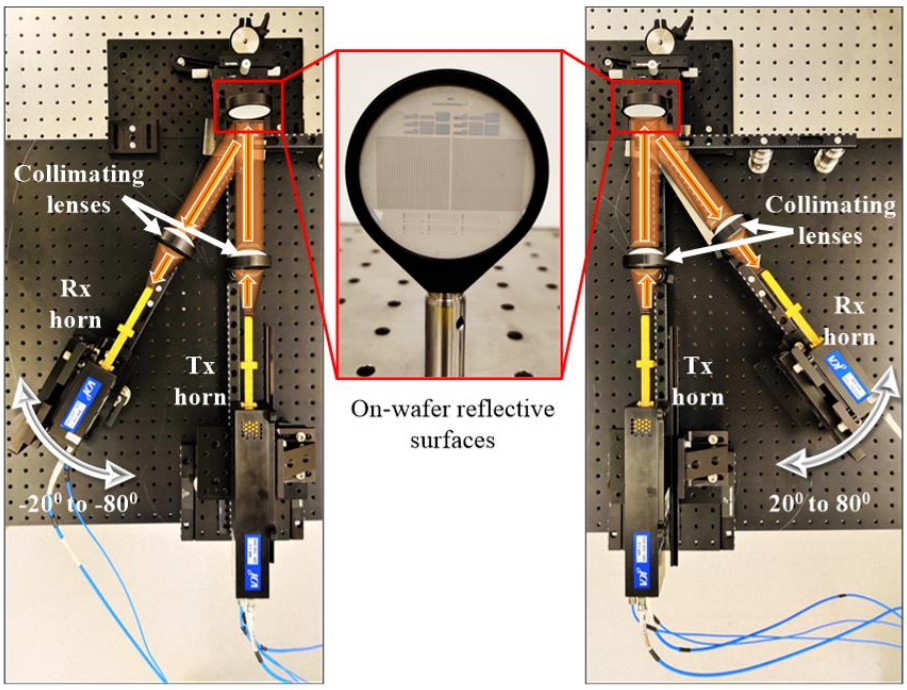

Fig. 10.13 Quasi-optical measurement setup used for the characterization of the fabricated reflective surfaces.

The measured RCS patterns of the non-randomized and randomized RRSs at 222.5 GHz have been plotted along with the analytical results, for both the surfaces in Fig. 10.14a and b, respectively. A good agreement is achieved between the measured and analytical bistatic RCS calculated by (2.5). The non-randomized RRS radiates at both -30^o and +30^o, indicating the presence of an undesired quantization lobe, while the randomized RRS radiates only at -30^o, which confirms that the quantization lobe is eliminated by

incorporating of phase randomization in the feed network of the RRS unit-cells. From the measurements, a QLL below -18 dB is achieved.

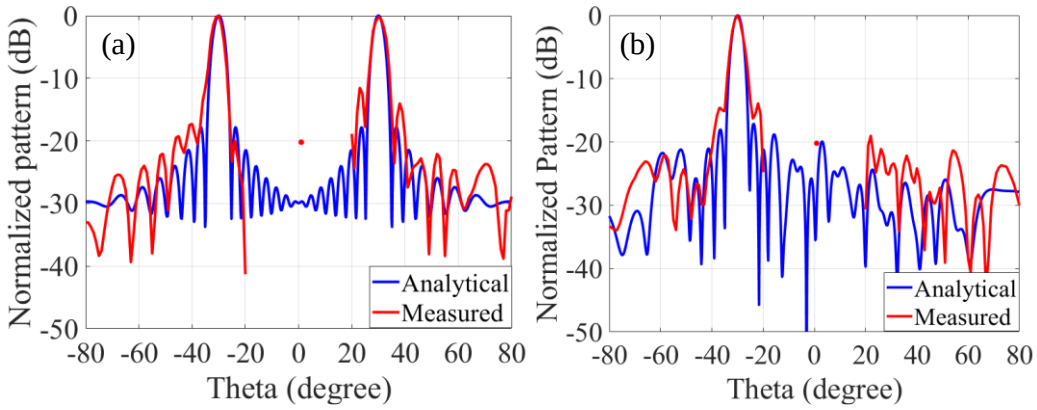

Fig. 10.14 Normalized RCS as a function of the scan angle theta at 222.5 GHz for (a) non-randomized RRS and (b) randomized RRS.

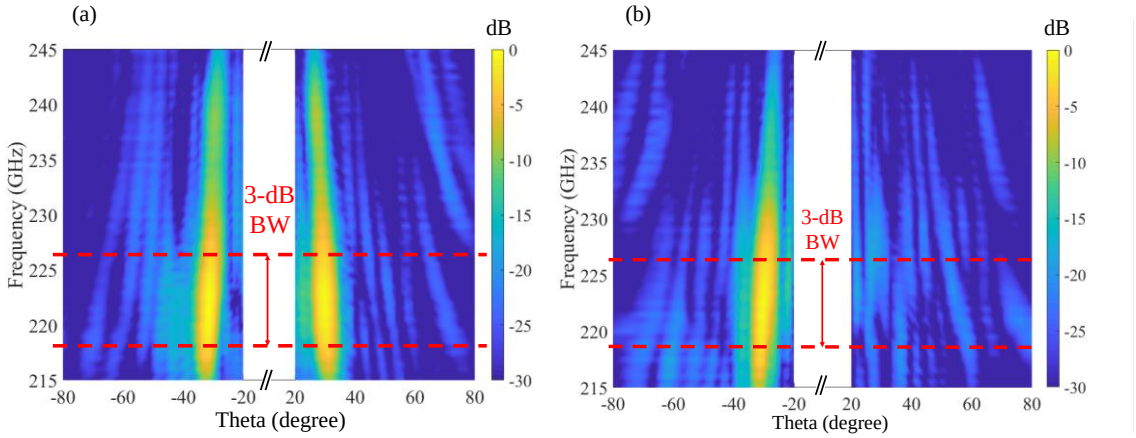

Fig. 10.15 Normalized RCS as a function of frequency and scan angle theta for (a) non-randomized RRS and (b) randomized RRS.

Furthermore, to evaluate the bandwidth of operation, the RCS is plotted as a function of frequency and scan angle theta, as shown in Fig. 10.15a and b. For both non-

randomized and randomized RRSs, the 3-dB bandwidth is approximately 8.5 GHz, which corresponds to a fractional bandwidth of 3.8%.

The afore presented measured RCS results, emphasize the loss mechanisms of the implemented RRSs. To calculate the losses, the measured S_{21} parameter at -30°, where both RRSs have their maximum RCS, is given versus frequency in Fig. 10.16. Alongside the RRSs' RCS values, the monostatic reflection (S_{11}) measurement from an aluminum-coated wafer is also plotted. As such, at 222.5 GHz, the RCS of the RRSs peaks since at that frequency the boresight imping waves are better coupled to the desired direction (-30°). As the frequency deviates from 225.5 GHz the bistatic RCS of the RRSs drops rapidly since the limping waves are back-reflected to the boresight direction –S_{11}– (the RRS acts like a mirror). On the other hand, the monostatic RCS (S_{11}) of the aluminum mirror is -3.9 dB across all frequencies and this loss is attributed to the discrepancies in the alignment and mirror planarity as well as losses from the lenses.

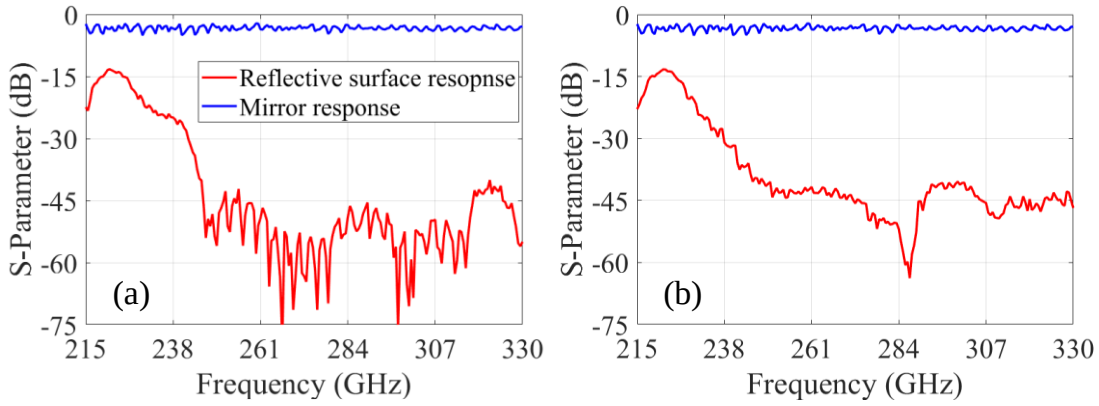

Fig. 10.16 RCS as a function of frequency at θ_o=-30° for (a) non-randomized and (b) randomized RRS.

The mechanisms leading to the additional RRS losses are listed below:

1) Quantization Loss: It results from the 1-bit quantization scheme employed in this work. It contributes to an additional loss of -3 dB.
2) Aperture Loss: It results from the choice of the main beam direction. Since θ_o=-30^o is chosen as the main beam direction, an aperture loss of 20log(cos(-30^o))=-1.25 dB is expected.
3) Surface Waves Loss: It is due to the coupling between the antenna elements and the surface waves excited in the alumina substrate. To characterize this loss, full-wave simulations of the 1-bit RRS are carried out with no conductor and dielectric losses and are compared with the full-wave results of an ideal 1-bit RRS, which is modeled using PEC-PMC boundaries as unit-cells (1.8 dB).
4) Dielectric Loss: Free-space measurements using a quasi-optical reflectometer setup estimated the loss tangent of alumina ribbon ceramic wafer as $tan\delta=0.8\times10e\text{-}3$. Full-wave simulations show that the dielectric loss contributes an additional 0.17 dB of loss.
5) Conductor Loss: The losses due to the finite conductivity and roughness of aluminum metallization result in an estimated 3.37 dB loss.

To estimate the prototype's efficiency, the loss mechanisms not present in an ideal 1-bit reflective surface comprised of PMC and PEC unit-cells designed for beam deflection at θ_o=-30^o are accounted; namely, surface wave, dielectric, and conductor losses are only considered. These losses summing up to 5.34 dB resulting in an efficiency of 30%.

Finally, in table 10.2 a comparison of the performance of the proposed design with the existing designs in the literature that employ plane wave illumination and 1-bit phase

quantization is provided. [114], [21], and [22] utilize a single layer design but consist of one or more quantization lobes. Pre-phasing technique is employed in [23] to suppress the quantization lobes and achieve an SLL of about -13 dB. However, as multi-layer design is adopted, it is unsuitable for sub-mmWave and THz implementations. In contrast, the single layer design proposed in this Chapter is well suited for sub-mmWave and THz implementations and achieves a single beam pattern with a QLL of -18 dB.

Table 10.2

Comparison of the proposed 1-bit randomized RRS with existing designs

Reference	Illumination	Frequency	Design	Quantization lobe level
[121]	Plane-wave	10.0 GHz	Single-layer	0 dB
[122]	Plane-wave	11.1 GHz	Single-layer	0 dB
[123]	Plane-wave	90.0 GHz	Single-layer	0 dB
[120]	Plane-wave	39.0 GHz	Multi-layer	-13 dB
This work	Plane-wave	222.5 GHz	Single-layer	-18 dB

VI. Conclusions of Chapter 10

This Chapter presented a robust technique for mitigating quantization lobes in sub-mmWave single-layer 1-bit RRSs under plane wave illumination using random phase delays. Specifically, the technique is realized by introducing randomized physical delay lines in the feed network of the individual unit-cells to break the periodicity of the

quantization error and mitigate the quantization lobes. A comprehensive study explaining the effect of introducing varied degrees of randomization in a traditional RRS is presented along with the analytical results. Leveraging these results, the condition for choosing the range of randomization required to achieve the lowest SLL is stipulated for the first time. Adopting the proposed range of randomization, a 30×30 single-layer 1-bit randomized RRS at 222.5 GHz is designed to radiate along -30^{o} direction. Also, a non-randomized RRS with similar specifications is designed to carry out a comparative analysis. Both surfaces are fabricated side-by-side on a 2" diameter, 45 μm thick alumina ribbon ceramic substrate from Corning Inc. The RCS of the fabricated reflective surfaces is characterized by a quasi-optical measurement setup, and the results confirm that the quantization lobes in randomized RRS are suppressed with a QLL below -18 dB. To demonstrate the proof-of-concept of the proposed technique, the fabricated prototype is implemented with permanent, ideal switches using open and short terminations. All the measured results verify the presented technique.

In the following last Chapter, the conclusions, innovations, and future work of this dissertation are summarized.

CHAPTER 11

Conclusions and Future Work

The methods and results presented in this dissertation, pave the way toward large-format mmWave/THz reconfigurable reflective surfaces that offer high-gain steerable beams and can serve both in wireless communication and imaging applications. As such, the contributions of the present work are summarized below.

Firstly, in Chapter 4, a domain decomposition technique that enables the study of large-format mmWave/THz imaging systems was presented. Namely, these electrically large configurations lead to resource-hungry models when studied with the use of full-wave simulators, due to the small wavelengths of these frequencies. The proposed approach decouples the imaging system and the targets and simulates them individually using full-wave simulators that capture all the exhibited phenomena (e.g. scattering from multiple lossy materials). Then, the results are combined utilizing a conjugate field coupling method, accurately calculating the response of the systems in complex target scenarios, while improving the overall simulation time by more than 270 times.

In Chapter 5, a novel 3D radar imaging method was presented utilizing a single rotating linear antenna that forms a narrow steerable fan-beam. As the fan-beam is electronically scanned and the antenna is rotated, the information from the whole field-of-view is recorded. Then, the images are reconstructed using the projection slice theorem that is typically leveraged in CT systems. The proposed imaging approach offers a fast image acquisition speed with the combination of mechanical and electronic scanning and

can serve as an imaging sensor in applications that inherently offer rotational motions, including drones (e.g. quadcopters) and CubeSats. Moreover, the incorporated elements are significantly reduced by a factor of $N^{3/2}/2$ leading to low-complexity topologies.

Chapter 6 presented a novel nanofabrication method for the development of graphene-actuated switches over large apertures. As such, the proposed method utilizes a titanium sacrificial layer to protect the delicate graphene during the aggressive fabrication steps, achieving more than 92% yield over large areas. Moreover, in this Chapter, the on-wafer characterization of the fabricated graphene devices was carried out, obtaining the graphene sheet impedance in the 220-330 GHz bands. This fabrication technique alongside the mmWave/THz measurements, enable the accurate design of large-format reconfigurable apertures that can serve both in imaging and communication applications.

In Chapter 7, the measured graphene sheet impedance values are incorporated in various coplanar transmission line models to investigate the performance of SPST graphene CPW and CPS switches. Specifically, the measured graphene sheet impedance values of Chapter 5 were incorporated into accurate equivalent circuit models of the CPW and CPS switches. Then, the switching performance was obtained (insertion loss and the ON/OFF ratio) for various parameters, including characteristic impedance, scaling factor, graphene shape, and topology (series versus shunt). The acquired results suggest that the shunt CPW and CPS switches outmatch the series in terms of insertion loss and ON/OFF ratio. This is attributed to the parasitic effects of the series switch (e.g. coupling capacitances), that offer a better path for the high-frequency signals, mitigating the switch performance. This was the first time in the existing literature that such a comprehensive

study was carried out to identify the optimum switch topology of graphene-controlled switches.

In Chapter 8, the optimized SPST shunt graphene switches are integrated on printed patch antennas to form single-bit large-scale mmWave/THz RRSs. These apertures offer beam steering capabilities with the use of a simplified RF-front-end; however, the single-bit scheme leads to low aperture efficiency and pronounced parasitic lobes.

To improve the radiation period of the single-bit RRS, in Chapter 9, multi-bit mmWave/THz RRSs are presented that use multiple SPST switches to acquire up to 4 bits of phase quantization (16 phase states). To achieve such a high quantization scheme, multi-port patch antennas are employed with integrated SPST switches at each port. By optimizing the delay lines at each port (between the antenna feed point and the SPST switch), the reflection phases of the unit-cell can be equally distributed along with the unit-cell offering multiple phase states (multiple bits). The key advantage of the proposed topologies over the existing ones is the use of a single-switch-per-bit up to 4 bits of phase quantization. Enforcing this constraint to the presented designs, low system complexity is maintained thus lower RF losses and fabrication cost. This is the first time in the known literature that such a high quantization scheme is achieved (previous was 2 bits). Leveraging the presented designs, the aperture efficiency improves from 41 % (1-bit) to 94 % (4-bit) and the undesired parasitic lobes are eliminated. Alongside the ideal multi-bit RRS topologies, the design process for the 2-bit graphene actuated RRS is detailed, offering beam steering versatility and low parasitic lobes.

Finally, in Chapter 10, a single-bit RRS is presented that offers suppressed quantization lobes (single beam pattern) leveraging a phase randomization method. Specifically, when the RRS structure is illuminated by a plane wave, the quantized phase profile over the surface exhibits symmetries that lead to parasitic quantization lobes. One way to suppress these lobes is by employing more phase bits (as in Chapter 8), but this leads to high system complexity and RF losses. An alternative route is the suppression of the quantization lobes by employing a randomization scheme on the coded phase profile, breaking the unwanted symmetry. To achieve that effect, a delay line is integrated into every unit-cell between the antenna feed point and the SPST switch. These physical delay lines are randomized in the 0^o-180^o range for all elements of the RRS. Afterward, the RRS beamforming process is the same as the non-randomized RRS, however, these random delays create non-symmetries in the phase profile leading to the redistribution of the parasitic lobe energy to various directions. In this manner, the presented designs achieve a quantization lobe suppression of more than 10 dB offering a single lobe pattern. Alongside the theoretical and experimental data, the optimum delay range is identified for various low-bit schemes, for the first time in the known literature. Finally, the proposed designs are planar structures, alleviating the use of RF vias and multi-layer structures that further hinder the proliferation process of mmWave/THz RRSs due to the incorporated losses and fabrication complexity.

I. Future Tasks and Directions

The results presented in this dissertation suggest that multi-bit, efficient RRSs are feasible in the mmWave/THz bands, either by employing high-performance switches (e.g., diodes) or by employing low-cost graphene switches. However, several aspects of this

work could be further pursued. As such, the future directions of the presented work are detailed in the following paragraphs.

Firstly, the implementation of both the single-bit randomized or the multi-bit RRSs in the mmWave/THz bands using graphene switches constitutes a natural continuation of the presented work. Certain fabrication challenges need to be addressed in this effort including the graphene integration on the alumina wafers and the design of the biasing network. Through this process, any arising issues would be identified and addressed, enabling the proliferation of mmWave/THz RRSs.

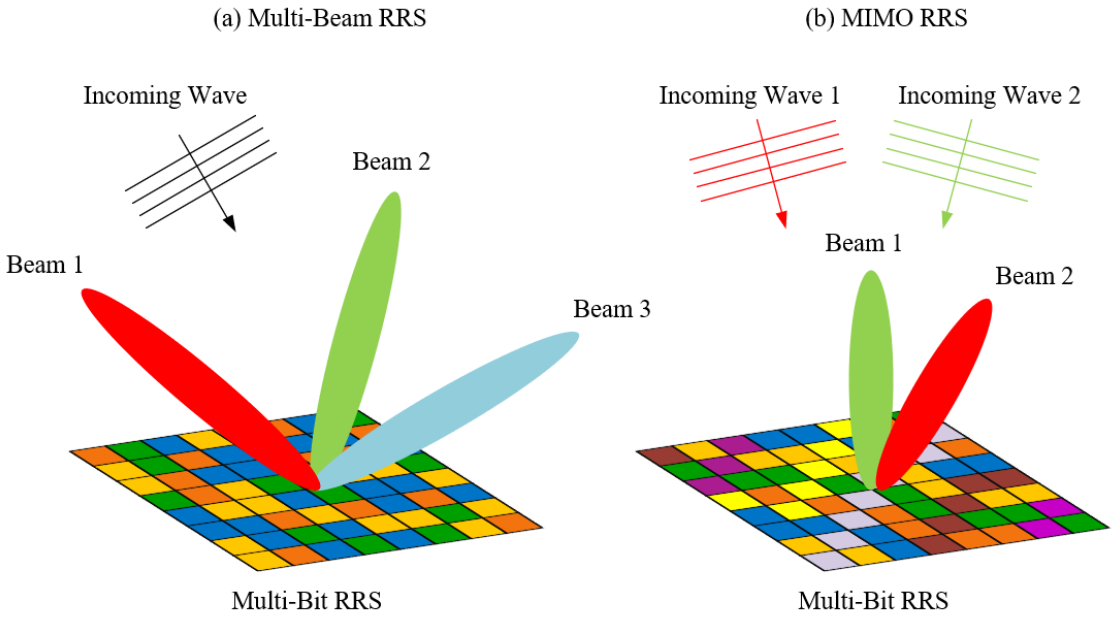

Fig. 11.1 (a) A multi-beam RRS that splits the impinging waves to various directions and (b) a multiple-input-multiple-output RRS that is illuminated by two different beams, steering each one to different directions.

Following the aforementioned goal, the graphene switches' development needs to be part of the future work, to ensure the improvement of the graphene RF performance

through the optimization of the nanofabrication process. Moreover, integrating graphene on other substrates (e.g., alumina, quartz, or silicon nitride) could offer better performance than silicon due to the less conductivity of these substrates (fewer impurities). Alternatively, different 2D materials that offer better sheet impedance ON/OFF ratios could be leveraged for SPST switches (e.g., vanadium dioxide), enabling the implementation of low-loss RRS designs.

Another part of the future work is the design of multi-beam RRS designs including the ones presented in Fig. 11.1. As such, RRSs are expected to be deployed as IRSs for wireless communication applications. These systems help redirect the scattered fields of the base station to non-line-of-sight users, enabling higher throughput and greater coverage range. Though, as expected, multiple users could lie in these areas, thus RRSs that serve more than one user are needed. To achieve that, the base station fields need to be split and redistributed toward the multiple users as shown in Fig. 11.1a. This was infeasible with the existing low-bit quantization schemes; however, it is now enabled by the development of the herein proposed multi-bit RRS designs and this beamforming needs to be thoroughly investigated.

Finally, the holy grail of RRSs that would establish them an inseparable part of modern 5G and beyond systems is the MIMO RRS, as depicted in Fig. 11.1b. The key concept of this topology is the phase modulation of the RRS that would enable the independent beam steering of two (or more) impinging waves to different directions with minimum crosstalk. As such, the unit-cell structure and coding of this conceptual RRS should be thoroughly investigated. The MIMO RRS would employ the spatial orthogonality of two (or more) coding profiles to enable the independent modulation of the

arriving waves. This concept has been demonstrated in metasurfaces that are excited by surface waves [124], however, the adaption of this concept in RRSs is a crucial part of the future work.

LIST OF PUBLICATIONS

During this research activity the following studies were published:

Journals:

1. **P. C. Theofanopoulos** and G. C. Trichopoulos, " Efficient Multi-Bit Millimeter-Wave and Terahertz Reconfigurable Reflective Surfaces," in IEEE Transactions on Antennas and Propagation, (under review)
2. B. G. Kashyap, **P. C. Theofanopoulos**, Y. Cui and G. C. Trichopoulos, "Mitigating Quantization Lobes in mmWave Low-bit Reconfigurable Reflective Surfaces," in IEEE Open Journal of Antennas and Propagation, (accepted), Sept. 2020
3. **P. C. Theofanopoulos** and G. C. Trichopoulos, "Modeling and Analysis of Terahertz Graphene Switches for On-Wafer Coplanar Transmission Lines," J. Infrared, mm, THz Waves, 2020
4. **P. C. Theofanopoulos**, et al., "High-yield fabrication method for high-frequency graphene devices using titanium sacrificial layers," J. Vac. Sci. Technol. B, vol. 37, no. 4, p. 41801, Jun. 2019
5. **P. C. Theofanopoulos**, M. Sakr, and G. C. Trichopoulos, "Multistatic Terahertz Imaging Using the Radon Transform," in IEEE Transactions on Antennas and Propagation, Jan. 2019
6. **P. C. Theofanopoulos** and G. C. Trichopoulos, "Modeling of mmW and THz Imaging Systems Using Conjugate Field Coupling," in IEEE Antennas and Wireless Propagation Letters, vol. 17, no. 2, pp. 213-216, Feb. 2018

Conferences:

1. **P. C. Theofanopoulos** and G. C. Trichopoulos, "Mitigating Quantization Lobes in Reconfigurable Reflective Surfaces," 2020 IEEE International Symposium on Antennas and Propagation and USNC-URSI Radio Science Meeting, Remote Conference, 2020 (in-print)
2. **P. C. Theofanopoulos** and G. C. Trichopoulos, "A Novel 2-Bit Graphene Reconfigurable Reflectarray," 2020 IEEE International Symposium on Antennas and Propagation and USNC-URSI Radio Science Meeting, Remote Conference, 2020 (in-print)
3. Y. Rong, **P. C. Theofanopoulos**, G. C. Trichopoulos and D. W. Bliss, "Cardiac Sensing Exploiting an Ultra-Wideband Terahertz Sensing System," 2020 IEEE International Radar Conference (RADAR), Washington, DC, USA, 2020, pp. 1002-1006

4. **P. C. Theofanopoulos** and G. C. Trichopoulos, "Toward Large-Scale Dynamically Reconfigurable Apertures Using Graphene," 2019 IEEE International Symposium on Antennas and Propagation and USNC-URSI Radio Science Meeting, Atlanta, GA, USA, 2019
5. **P. C. Theofanopoulos** and G. C. Trichopoulos, "Modeling of Sub-Millimeter Wave Coplanar Waveguide Graphene Switches," 2019 IEEE International Symposium on Antennas and Propagation and USNC-URSI Radio Science Meeting, Atlanta, GA, USA, 2019
6. **P. C. Theofanopoulos** and G. C. Trichopoulos, "On-Wafer Graphene Devices for THz Applications Using a High-Yield Fabrication Process," 2019 IEEE/MTT-S International Microwave Symposium - IMS, Boston, MA, June 2019
7. **P. C. Theofanopoulos** and G. C. Trichopoulos, "A Novel Fingerprint Scanning Method Using Terahertz Imaging," 2018 IEEE International Symposium on Antennas and Propagation & USNC/URSI National Radio Science Meeting, Boston, MA, 2018
8. **P. C. Theofanopoulos** and G. C. Trichopoulos, "A Terahertz Microscopy Technique for Sweat Duct Detection," 2018 IEEE/MTT-S International Microwave Symposium - IMS, Philadelphia, PA, 2018, pp. 864-867
9. **P. C. Theofanopoulos** and G. C. Trichopoulos, "A novel THz radar imaging system using the radon transform," 2017 IEEE International Symposium on Antennas and Propagation & USNC/URSI National Radio Science Meeting, San Diego, CA, 2017, pp. 1513-1514

The contents of these publications have been partially used to compile this dissertation.

REFERENCES

[1] T. S. Rappaport et al., “Wireless Communications and Applications Above 100 GHz: Opportunities and Challenges for 6G and Beyond,” IEEE Access, p. 1, 2019.

[2] C. A. Balanis, Antenna Theory: Analysis and Design, 3rd ed. Hoboken, NJ, USA: Wiley, 2005.

[3] C. E. Shannon, "A mathematical theory of communication," in The Bell System Technical Journal, vol. 27, no. 3, pp. 379-423, July 1948.

[4] S. V Thyagarajan, “Millimeter-Wave/Terahertz Circuits and Systems for Wireless Communication,” 2014.

[5] K. B. Cooper, R. J. Dengler, N. Llombart, B. Thomas, G. Chattopadhyay and P. H. Siegel, "THz Imaging Radar for Standoff Personnel Screening," in IEEE Transactions on Terahertz Science and Technology, vol. 1, no. 1, pp. 169-182, Sept. 2011.

[6] G. C. Trichopoulos, H. L. Mosbacker, D. Burdette and K. Sertel, "A Broadband Focal Plane Array Camera for Real-time THz Imaging Applications," in IEEE Transactions on Antennas and Propagation, vol. 61, no. 4, pp. 1733-1740, April 2013.

[7] B. Gonzalez-Valdes, Y. Alvarez, S. Mantzavinos, C. M. Rappaport, F. Las-Heras and J. A. Martinez-Lorenzo, "Improving Security Screening: A Comparison of Multistatic Radar Configurations for Human Body Imaging," in IEEE Antennas and Propagation Magazine, vol. 58, no. 4, pp. 35-47, Aug. 2016.

[8] S. S. Ahmed, A. Schiessl and L. P. Schmidt, "A Novel Fully Electronic Active Real-Time Imager Based on a Planar Multistatic Sparse Array," in IEEE Transactions on Microwave Theory and Techniques, vol. 59, no. 12, pp. 3567-3576, Dec. 2011.

[9] S. Nowok, R. Herschel, R. Zimmermann, A. Shoykhetbrod, S. A. Lang and N. Pohl, "3D imaging system based on a MIMO approach at 360GHz for security screening," 2016 Progress in Electromagnetic Research Symposium (PIERS), Shanghai, 2016, pp. 671-675.

[10] B. Baccouche; P. Agostini; S. Mohammadzadeh; M. Kahl; C. Weisenstein; J. Jonuscheit; A. Keil; T. Loeffler; W. Sauer-Greff; R. Urbansky; P. Haring Bolivar; F. Friederich, "3D Terahertz Imaging with Sparse Multistatic Line Arrays," in IEEE Journal of Selected Topics in Quantum Electronics, vol.PP, no.99, pp.1-1.

[11] J. J. Lynch, K. S. Kona, R. G. Nagele, G. L. Virbila, R. L. Bowen and M. D. Wetzel, "128 Element Coded Aperture Radar at 77 GHz," 2018 IEEE MTT-S International Conference on Microwaves for Intelligent Mobility (ICMIM), Munich, 2018, pp. 1-4.

[12] Trichopoulos, G.C., Sertel, K. Broadband Terahertz Computed Tomography Using a 5k-pixel Real-time THz Camera. J Infrared Milli Terahz Waves 36, 675–686 (2015).

[13] Tewari, P., Kealey, C. P., Bennett, D. B., Bajwa, N., Barnett, K. S., Singh, R. S., … Taylor, Z. D. (2012). In vivo terahertz imaging of rat skin burns. Journal of Biomedical Optics, 17(4), 040503.

[14] G. R. Lockwood and F. S. Foster, "Optimizing sparse two-dimensional transducer arrays using an effective aperture approach," 1994 Proceedings of IEEE Ultrasonics Symposium, Cannes, France, 1994, pp. 1497-1501 vol.3.

[15] K. Liu et al., "100 Gbit/s THz Photonic Wireless Transmission in the 350-GHz Band With Extended Reach," in IEEE Photonics Technology Letters, vol. 30, no. 11, pp. 1064-1067, 1 June1, 2018.

[16] C. Wang, Changxing Lin, Qi Chen, Xianjin Deng and Jian Zhang, "0.14THz high speed data communication over 1.5 kilometers," 2012 37th International Conference on Infrared, Millimeter, and Terahertz Waves, Wollongong, NSW, 2012, pp. 1-2.

[17] X. Yu et al., "400-GHz Wireless Transmission of 60-Gb/s Nyquist-QPSK Signals Using UTC-PD and Heterodyne Mixer," in IEEE Transactions on Terahertz Science and Technology, vol. 6, no. 6, pp. 765-770, Nov. 2016.

[18] Ericsson, “Advanced antenna systems for 5G networks,” White paper, 2018.

[19] https://www.microwavejournal.com/articles/27830-ibm-and-ericsson-announce-5g-mmwave-phase-array-antenna-module

[20] W. Tang et al., “Wireless Communications with Reconfigurable Intelligent Surface: Path Loss Modeling and Experimental Measurement.” 2019.

[21] E. Björnson and L. Sanguinetti, “Power Scaling Laws and Near-Field Behaviors of Massive MIMO and Intelligent Reflecting Surfaces.” 2020.

[22] C. S. Merola and M. N. Vouvakis, "An RF Beamforming Architecture for UWB Continuous Time-Delay Control," 2019 IEEE International Symposium on Phased Array System & Technology (PAST), Waltham, MA, USA, 2019, pp. 1-5.

[23] Hu, C. Wang and R. Han, "A 32-Unit 240-GHz Heterodyne Receiver Array in 65-nm CMOS With Array-Wide Phase Locking," in IEEE Journal of Solid-State Circuits, vol. 54, no. 5, pp. 1216-1227, May 2019.

[24] V. Jamali, A. M. Tulino, G. Fischer, R. Muller and R. Schober, "Scalable and Energy-Efficient Millimeter Massive MIMO Architectures: Reflect-Array and Transmit-Array Antennas," ICC 2019 - 2019 IEEE International Conference on Communications (ICC), Shanghai, China, 2019, pp. 1-7.

[25] http://europractice-ic.com/wp-content/uploads/2019/06/190517_MPW2019-general-v7.0.pdf

[26] J. J. Lynch, "Low latency digital beamforming radar using aperture coding," in IEEE Transactions on Aerospace and Electronic Systems, vol. 52, no. 2, pp. 918-927, April 2016.

[27] J. Huang and J.A. Encinar, Reflectarray Antennas, Piscataway, NJ; Hoboken, NJ: IEEE Press; Wiley, 2008.

[28] H. Kamoda, T. Iwasaki, J. Tsumochi, T. Kuki, and O. Hashimoto, "60-GHz Electronically Reconfigurable Large Reflectarray Using Single-Bit Phase Shifters," IEEE Trans. Antennas Propag., vol. 59, no. 7, pp. 2524–2531, 2011.

[29] D. Rodrigo, L. Jofre, and J. Perruisseau-Carrier, "Unit-cell for frequency-tunable beamscanning reflectarrays," IEEE Trans. Antennas Propag., vol. 61, no. 12, pp. 5992–5999, 2013.

[30] S. Costanzo, F. Venneri, A. Raffo, and G. Di Massa, "Dual-Layer Single-Varactor Driven Reflectarray Cell for Broad-Band Beam-Steering and Frequency Tunable Applications," IEEE Access, vol. 6, pp. 71793–71800, 2018.

[31] L. Li et al., "Machine-learning reprogrammable metasurface imager," Nat. Commun., vol. 10, no. 1, p. 1082, 2019.

[32] C. Huang, B. Sun, W. Pan, J. Cui, X. Wu, and X. Luo, "Dynamical beam manipulation based on 2-bit digitally-controlled coding metasurface," Sci. Rep., vol. 7, no. September 2016, pp. 1–8, 2017.

[33] L. Dai et al., "Reconfigurable Intelligent Surface-Based Wireless Communications: Antenna Design, Prototyping, and Experimental Results," in IEEE Access, vol. 8, pp. 45913-45923, 2020.

[34] Y. Han, W. Tang, S. Jin, C. Wen, and X. Ma, "Large Intelligent Surface-Assisted Wireless Communication Exploiting Statistical CSI," in IEEE Transactions on Vehicular Technology, vol. 68, no. 8, pp. 8238-8242, Aug. 2019.

[35] H. Yang et al., "A Study of Phase Quantization Effects for Reconfigurable Reflectarray Antennas," IEEE Antennas Wirel. Propag. Lett., vol. 16, pp. 302–305, 2017.

[36] X. Zhang, H. Zhang, J. Su, and Z. Li, "2-Bit programmable digital metasurface for controlling electromagnetic wave," 2017 Sixth Asia-Pacific Conference on Antennas and Propagation (APCAP), Xi'an, 2017, pp. 1-3.

[37] J. Rodriguez-Zamudio, J. I. Martinez-Lopez, J. Rodriguez-Cuevas, and A. E. Martynyuk, “Reconfigurable reflectarrays based on optimized spiraphase-type elements,” IEEE Trans. Antennas Propag., vol. 60, no. 4, pp. 1821–1830, 2012.

[38] G. Perez-Palomino et al., “Design and Demonstration of an Electronically Scanned Reflectarray Antenna at 100 GHz Using Multiresonant Cells Based on Liquid Crystals,” IEEE Trans. Antennas Propag., vol. 63, no. 8, pp. 3722–3727, 2015.

[39] P. F. Goldsmith, Quasioptical Systems: Gaussian Beam Quasioptical Propogation and Applications, 1st ed., Piscataway, NJ, USA: Wiley-IEEE Press, 1998.

[40] John D. Kraus Radio Astronomy, 2nd Edition, McGraw-Hill, 1966.

[41] Skolnik, M. I. (Ed.). Introduction to Radar (3rd ed.). New York, NY: McGraw Hill Book Company, 2002.

[42] J. W. Crispin and A. L. Maffett, "Radar cross-section estimation for simple shapes," in Proceedings of the IEEE, vol. 53, no. 8, pp. 833-848, Aug. 1965.

[43] M. Chen, M. Kuloglu and C. C. Chen, "Numerical study of pedestrian RCS at 76–77 GHz," 2013 IEEE Antennas and Propagation Society International Symposium (APSURSI), Orlando, FL, 2013, pp. 1982-1983.

[44] L. Pulido-Mancera, T. Fromenteze, T. Sleasman, M. Boyarsky, M. Imani, M. Reynolds, and D. Smith, "Application of range migration algorithms to imaging with a dynamic metasurface antenna," J. Opt. Soc. Am. B 33, 2082-2092 (2016).

[45] G. C. Trichopoulos, K. Topalli, and K. Sertel, "Imaging performance of a THz focal plane array," 2011 IEEE International Symposium on Antennas and Propagation (APSURSI), Spokane, WA, 2011, pp. 134-136.

[46] FEKO 14.1 Stellenbosch, South Africa, E. S. Systems. Available: http://www.feko.info

[47] A. C. Newell, "Error analysis techniques for planar near-field measurements," in IEEE Transactions on Antennas and Propagation, vol. 36, no. 6, pp. 754-768, Jun 1988.

[48] K. Wu, Y. J. Cheng, T. Djerafi and W. Hong, "Substrate-Integrated Millimeter-Wave and Terahertz Antenna Technology," in Proceedings of the IEEE, vol. 100, no. 7, pp. 2219-2232, July 2012.

[49] H. Wang, "Review of CMOS millimeter-wave radio frequency integrated circuits," 2015 IEEE MTT-S International Microwave and RF Conference (IMaRC), Hyderabad, 2015, pp. 239-242.

[50] A. Tang, T. Reck and G. Chattopadhyay, "CMOS system-on-chip techniques in millimeter-wave/THz instruments and communications for planetary exploration," in IEEE Communications Magazine, vol. 54, no. 10, pp. 176-182, October 2016.

[51] C. A. Wiley, “Fanbeam inversion radar,” US 4 739 332 A, April, 19 1988.

[52] A. C. Kak and M. Slaney, “Principles of Computerized Tomographic Imaging,” IEEE Press, 1988.

[53] D. C. Munson, J. D. O'Brien and W. K. Jenkins, "A tomographic formulation of spotlight-mode synthetic aperture radar," in Proceedings of the IEEE, vol. 71, no. 8, pp. 917-925, Aug. 1983.

[54] J. W. Goodman, Introduction to Fourier Optics (McGrawHill, New York, 1968).

[55] J. T. Caulfield, J. A. Wilson, and N. K. Dhar, "Spatial oversampling in imaging sensors: Benefits in sensitivity and detection," 2012 IEEE Applied Imagery Pattern Recognition Workshop (AIPR), Washington, DC, 2012, pp. 1-6.

[56] J. E. Fielding, "Beam overlap impact on phased-array target detection," in IEEE Transactions on Aerospace and Electronic Systems, vol. 29, no. 2, pp. 404-411, Apr 1993.

[57] H. Deng and B. Himed, "A VFBPual Antenna Beamforming (VAB) Approach for Radar Systems by Using Orthogonal Coding Waveforms," in IEEE Transactions on Antennas and Propagation, vol. 57, no. 2, pp. 425-435, Feb. 2009.

[58] S. Zhang, C. Guo, T. Wang, and W. Zhang, “ON-OFF Analog Beamforming for Massive MIMO,” IEEE Trans. Veh. Technol., vol. 67, no. 5, pp. 4113–4123, 2018.

[59] X. G. Zhang, W. X. Jiang, H. W. Tian, Z. X. Wang, Q. Wang and T. J. Cui, "Pattern-Reconfigurable Planar Array Antenna Characterized by Digital Coding Method," IEEE Transactions on Antennas and Propagation, 2019.

[60] A. Ç. Ulusoy et al., “A Low-Loss and High Isolation D-Band SPDT Switch Utilizing Deep-Saturated SiGe HBTs,” IEEE Microw. Wirel. Components Lett., vol. 24, no. 6, pp. 400–402, 2014.

[61] R. L. Schmid, A. Ç. Ulusoy, P. Song, and J. D. Cressler, “A 94 GHz, 1.4 dB Insertion Loss Single-Pole Double-Throw Switch Using Reverse-Saturated SiGe HBTs,” IEEE Microw. Wirel. Components Lett., vol. 24, no. 1, pp. 56–58, 2014.

[62] S. Lim, H. Koo, C. Kim, J. Kim, J. Rieh, and S. Hong, “290-GHz 17-dB ON-/OFF-Ratio Modulator With Resonance Control Varactors,” IEEE Microw. Wirel. Components Lett., vol. 29, no. 1, pp. 50–52, 2019.

[63] F. Thome, M. Ohlrogge, A. Leuther, M. Schlechtweg, and O. Ambacher, “An investigation of millimeter wave switches based on shunt transistors including SPDT SWITCH MMICs up to 300 GHz,” in 2016 IEEE MTT-S International Microwave Symposium (IMS), 2016, pp. 1–4.

[64] D. Müller et al., “A Novel Unit Cell for Active Switches in the Millimeter-Wave Frequency Range,” J. Infrared, Millimeter, Terahertz Waves, vol. 39, no. 2, pp. 161–176, 2018.

[65] T. Shivan et al., “220–325 GHz high-isolation SPDT switch in InP DHBT technology,” Electron. Lett., vol. 54, no. 21, pp. 1222–1224, 2018.

[66] F. Thome and O. Ambacher, “Highly Isolating and Broadband Single-Pole Double-Throw Switches for Millimeter-Wave Applications Up to 330 GHz,” IEEE Trans. Microw. Theory Tech., vol. 66, no. 4, pp. 1998–2009, 2018.

[67] J. D. Cressler et al., “SiGe Technology as a Millimeter-Wave Platform: Scaling Issues, Reliability Physics, Circuit Performance, and New Opportunities,” in 2016 IEEE Compound Semiconductor Integrated Circuit Symposium (CSICS), 2016, pp. 1–13.

[68] P. C. Theofanopoulos, C. S. Lavranos, K. E. Z0iros, G. C. Trichopoulos, G. Granet, and G. A. Kyriacou, “Investigation of Nonreciprocal Dispersion Phenomena in Anisotropic Periodic Structures Based on a Curvilinear FDFD Method,” IEEE Trans. Microw. Theory Tech., vol. 65, no. 1, pp. 36–49, 2017.

[69] M. Jost, R. Reese, M. Nickel, H. Maune, and R. Jakoby, “Fully dielectric interference-based SPDT with liquid crystal phase shifters,” IET Microwaves, Antennas Propag., vol. 12, no. 6, pp. 850–857, 2018.

[70] M. Kim, S. Park, A. Sanne, S. K. Banerjee, and D. Akinwande, “Towards mm-wave nanoelectronics and RF switches using MoS22D Semiconductor,” in 2018 IEEE/MTT-S International Microwave Symposium - IMS, 2018, pp. 352–354.

[71] H. Huang, B. Jiang, X. Zou, X. Zhao, and L. Liao, “Black phosphorus electronics,” Sci. Bull., vol. 64, no. 15, pp. 1067–1079, 2019.

[72] C. Hillman, P. A. Stupar, and Z. Griffith, “VO2 Switches for Millimeter and Submillimeter-Wave Applications,” in 2015 IEEE Compound Semiconductor Integrated Circuit Symposium (CSICS), 2015, pp. 1–4.

[73] C. Hillman, P. Stupar, and Z. Griffith, “Scaleable vanadium dioxide switches with submillimeterwave bandwidth: VO2 switches with impoved RF bandwidth and power handling,” in 2017 IEEE Compound Semiconductor Integrated Circuit Symposium (CSICS), 2017, pp. 1–4.

[74] H. Madan et al., “26.5 Terahertz electrically triggered RF switch on epitaxial VO2-on-Sapphire (VOS) wafer,” in 2015 IEEE International Electron Devices Meeting (IEDM), 2015, pp. 9.3.1-9.3.4.

[75] D. Fadil et al., “2D-Graphene Epitaxy on SiC for RF Application: Fabrication, Electrical Characterization and Noise Performance,” in 2018 IEEE/MTT-S International Microwave Symposium - IMS, 2018, pp. 228–231.

[76] Z. Miao et al., “Widely Tunable Terahertz Phase Modulation with Gate-Controlled Graphene Metasurfaces,” Phys. Rev. X, vol. 5, no. 4, p. 41027, Nov. 2015.

[77] J. Liu et al., “Flexible terahertz modulator based on coplanar-gate graphene field-effect transistor structure,” Opt. Lett., vol. 41, no. 4, pp. 816–819, Feb. 2016.

[78] N. Kakenov, M. S. Ergoktas, O. Balci, and C. Kocabas, “Graphene based terahertz phase modulators,” 2D Mater., vol. 5, no. 3, p. 035018, May 2018.

[79] M. Dragoman et al., “Coplanar waveguide on graphene in the range 40 MHz–110 GHz,” Appl. Phys. Lett., vol. 99, no. 3, p. 33112, Jul. 2011.

[80] H.-J. Lee, E. Kim, W.-J. Lee, and J. Jung, “RF transmission properties of graphene monolayers with width variation,” Phys. status solidi – Rapid Res. Lett., vol. 6, no. 1, pp. 19–21, Jan. 2012.

[81] L. Pierantoni et al., “Broadband Microwave Attenuator Based on Few Layer Graphene Flakes,” IEEE Trans. Microw. Theory Tech., vol. 63, no. 8, pp. 2491–2497, 2015.

[82] Y. Wu, M. Qu, and Y. Liu, “A Generalized Lossy Transmission-Line Model for Tunable Graphene-Based Transmission Lines with Attenuation Phenomenon,” Sci. Rep., vol. 6, p. 31760, Aug. 2016.

[83] J. Judek, M. Zdrojek, J. Sobieski, A. Przewłoka, and J. K. Piotrowski, “Characterization of the CVD Graphene Monolayer as an Active Element of a One-Port Microwave Device,” IEEE Trans. Electron Devices, vol. 64, no. 10, pp. 4340–4345, 2017.

[84] R. Heyrovska, “Atomic Structures of Graphene, Benzene and Methane with Bond Lengths as Sums of the Single, Double and Resonance Bond Radii of Carbon.” 2008.

[85] A. Fallahi and J. Perruisseau-Carrier, “Design of tunable biperiodic graphene metasurfaces,” Phys. Rev. B, vol. 86, no. 19, p. 195408, Nov. 2012.

[86] C. A. Joiner, T. Roy, Z. R. Hesabi, B. Chakrabarti, and E. M. Vogel, “Cleaning graphene with a titanium sacrificial layer,” Appl. Phys. Lett., vol. 104, no. 22, p. 223109, Jun. 2014.

[87] N. C. Wang, E. A. Carrion, M. C. Tung, and E. Pop, “Reducing graphene device variability with yttrium sacrificial layers,” Appl. Phys. Lett., vol. 110, no. 22, p. 223106, May 2017.

[88] D. M. Pozar, Microwave Engineering, 2nd ed. (Wiley, New York, 1998).

[89] J. Golden, H. Miller, D. Nawrocki, and J. Ross, “Optimization of bi-layer lift-off resist process,” in CS Mantech, Technical Digest, (MicroChem, 2009).

[90] T. Betancourt and L. Brannon-Peppas, “Micro- and nanofabrication methods in nanotechnological medical and pharmaceutical devices,” Int. J. Nanomedicine, vol. 1, no. 4, pp. 483–495, 2006.

[91] H. Taghvaee, A. Cabellos-Aparicio, J. Georgiou and S. Abadal, "Error Analysis of Programmable Metasurfaces for Beam Steering," in IEEE Journal on Emerging and Selected Topics in Circuits and Systems, vol. 10, no. 1, pp. 62-74, March 2020.

[92] K. T. Rim, K. H. Koo, and J. S. Park, “Toxicological Evaluations of Rare Earths and Their Health Impacts to Workers: A Literature Review,” Saf. Health Work, vol. 4, no. 1, pp. 12–26, 2013.

[93] D. B. Warheit, C. M. Sayes, K. L. Reed, and K. A. Swain, “Health effects related to nanoparticle exposures: Environmental, health and safety considerations for assessing hazards and risks,” Pharmacol. Ther., vol. 120, no. 1, pp. 35–42, 2008.

[94] Y. Xu et al., “Inducing Electronic Changes in Graphene through Silicon (100) Substrate Modification,” Nano Lett., vol. 11, no. 7, pp. 2735–2742, Jul. 2011.

[95] X. Xi, J. Shi, S. Maghsoudy-Louyeh, and B. R. Tittmann, “CHARACTERIZATION OF SILICON WAFER SURFACES AFTER HYDROPHILIC AND HYDROPHOBIC TREATMENTS BY ATOMIC FORCE MICROSCOPY,” AIP Conf. Proc., vol. 1211, no. 1, pp. 1493–1498, 2010.

[96] M. Lafkioti et al., “Graphene on a Hydrophobic Substrate: Doping Reduction and Hysteresis Suppression under Ambient Conditions,” Nano Lett., vol. 10, no. 4, pp. 1149–1153, Apr. 2010.

[97] Y. Chen, X.-L. Gong, and J.-G. Gai, “Progress and Challenges in Transfer of Large-Area Graphene Films,” Adv. Sci., vol. 3, no. 8, p. 1500343.

[98] https://www.acsmaterial.com/materials/graphene-series.html

[99] Q. H. Wang et al., “Understanding and controlling the substrate effect on graphene electron-transfer chemistry via reactivity imprint lithography,” Nat. Chem., vol. 4, p. 724, Aug. 2012.

[100] https://www.vadiodes.com/en/products/vector-network-analyzer-extension-modules

[101] http://www.ggb.com/PdfIndex_files/Model325B.pdf

[102] D. Rytting, “Network analyzer error models and calibration methods,” White Paper, Sep. 1998.

[103] Jeffrey L. Hesler, "From GHz to THz: The Essentials of Very High-Frequency Signal Measurements," Virginia Diodes Inc., Agilent Technologies Inc., 2012.

[104] K. Yau, E. Dacquay, I. Sarkas and S. P. Voinigescu, "Device and IC Characterization Above 100 GHz," in IEEE Microwave Magazine, vol. 13, no. 1, pp. 30-54, Jan.-Feb. 2012.

[105] D. F. Williams et al., "Calibrations for Millimeter-Wave Silicon Transistor Characterization," in IEEE Transactions on Microwave Theory and Techniques, vol. 62, no. 3, pp. 658-668, March 2014.

[106] L. Galatro and M. Spirito, "Millimeter-Wave On-Wafer TRL Calibration Employing 3-D EM Simulation-Based Characteristic Impedance Extraction," in IEEE Transactions on Microwave Theory and Techniques, vol. 65, no. 4, pp. 1315-1323, April 2017.

[107] N. Dib, "Comprehensive study of CAD models of several coplanar waveguide (CPW) discontinuities," in IEE Proceedings - Microwaves, Antennas and Propagation, vol. 152, no. 2, pp. 69-76, 8 April 2005.

[108] P. Bevington and K. Robinson, Data Reduction and Error Analysis for the Physical Sciences. 2003.

[109] H. S. Skulason et al., “110 GHz measurement of large-area graphene integrated in low-loss microwave structures,” Appl. Phys. Lett., vol. 99, no. 15, p. 153504, Oct. 2011.

[110] H. Yuan, H. Shimotani, A. Tsukazaki, A. Ohtomo, M. Kawasaki, and Y. Iwasa, “High-Density Carrier Accumulation in ZnO Field-Effect Transistors Gated by Electric Double Layers of Ionic Liquids,” Adv. Funct. Mater., vol. 19, no. 7, pp. 1046–1053, 2009.

[111] W. J. Getsinger, “Circuit Duals on Planar Transmission Media,” in 1983 IEEE MTT-S International Microwave Symposium Digest, 1983, pp. 154–156.

[112] Rainee N. Simons, Coplanar Waveguide Circuits, Components, and Systems, 1st ed. New York, NY, USA: Wiley, 2001.

[113] ANSYS Electronics Desktop available at: https://www.ansys.com/products/electronics/ansys-electronics-desktop

[114] B. Liu, H. Aliakbarian, Z. Ma, G. A. E. Vandenbosch, G. Gielen, and P. Excell, “An Efficient Method for Antenna Design Optimization Based on Evolutionary Computation and Machine Learning Techniques,” IEEE Trans. Antennas Propag., vol. 62, no. 1, pp. 7–18, 2014.

[115] A. Ç. Ulusoy et al., “A Low-Loss and High Isolation D-Band SPDT Switch Utilizing Deep-Saturated SiGe HBTs,” IEEE Microw. Wirel. Components Lett., vol. 24, no. 6, pp. 400–402, 2014.

[116] D. Pozar, "Considerations for millimeter wave printed antennas," in IEEE Transactions on Antennas and Propagation, vol. 31, no. 5, pp. 740-747, September 1983

[117] Guizhen Zheng, J. Papapolymerou and M. M. Tentzeris, "Wideband coplanar waveguide RF probe pad to microstrip transitions without via holes," in IEEE Microwave and Wireless Components Letters, vol. 13, no. 12, pp. 544-546, Dec. 2003.

[118] S. J. Bleiker et al., "High-Aspect-Ratio Through Silicon Vias for High-Frequency Application Fabricated by Magnetic Assembly of Gold-Coated Nickel Wires," in IEEE Transactions on Components, Packaging and Manufacturing Technology, vol. 5, no. 1, pp. 21-27, Jan. 2015.

[119] M. Smith and Y. Guo, "A comparison of methods for randomizing phase quantization errors in phased arrays," in IEEE Transactions on Antennas and Propagation, vol. 31, no. 6, pp. 821-828, November 1983.

[120] J. Yin, Q. Wu, Q. Lou, H. Wang, Z. N. Chen and W. Hong, "Single-Beam 1 Bit Reflective Metasurface Using Prephased Unit-cells for Normally Incident Plane Waves," in IEEE Transactions on Antennas and Propagation, vol. 68, no. 7, pp. 5496-5504, July 2020.

[121] S. Liu and T. J. Cui, “Concepts, working principles, and applications of coding and programmable metamaterials,” Adv. Opt. Mater., vol. 5,no. 22, p. 1700624, 2017.

[122] H. Yang, X. Cao, F. Yang, J. Gao, S. Xu, M. Li, X. Chen, Y. Zhao, Y. Zheng, and S. Li, “A programmable metasurface with dynamic polarization, scattering and focusing control,” Sci. Rep., vol. 6, p. 35692, 2016.

[123] M. K. T. Al-Nuaimi, Y. He, and W. Hong, “Design of 1-bit coding engineered reflectors for EM-wave shaping and RCS modifications,” IEEE Access, vol. 6, pp. 75 422–75 428, 2018.

[124] S. Ramalingam, C. A. Balanis, C. R. Birtcher and H. N. Shaman, "Polarization-Diverse Holographic Metasurfaces," in IEEE Antennas and Wireless Propagation Letters, vol. 18, no. 2, pp. 264-268, Feb. 2019.